UNIVERSITY OF BATH

PHD

CW Stimulated Raman Scattering Generation and Phase-Locking of Raman Comb using Hypocycloid-shaped Kagome HC-PCF

Alharbi, Meshaal

Award date:
2014

Awarding institution:
University of Bath

[Link to publication](#)

CW Stimulated Raman Scattering Generation and Phase-Locking of Raman Comb using Hypocycloid-shaped Kagome HC-PCF

Mehsaal Obaid Alharbi

A thesis submitted for the degree of Doctor of Philosophy

University of Bath

Department of Physics

August 2014

COPYRIGHT

Abstract

This thesis presents several milestones towards the development of an all-fibre photonic waveform synthesiser. The synthesiser design relies on the generation of multiple-octave wide coherent Raman comb in hydrogen confined in hollow-core photonic crystal fibres (HC-PCF), with the ultimate aim to generate the comb of continuous wave (CW) spectral components, thus paving the way to optical wave synthesis with a comparable control as in electronics. The milestones achieved in this thesis entitle the development of new state-of-the-art HC-PCF, the first demonstration of intra-pulse waveform synthesis using transient stimulated Raman scattering (SRS), strong Stokes generation in the CW regime and finally a report on novel dynamics of the hydrogen molecules that enabled the generation of high power Stokes with ultra-narrow linewidth.

Within the continuous endeavour in the group of GPPMM, the development of hollow core photonic crystal fibres (HC-PCF) is an essential key element towards the realisation and the development of an optical waveform synthesiser based on the generation and the synthesis of optical frequency combs using stimulated Raman scattering (SRS) process in gas filled HC-PCF.

Two types of HC-PCF are developed and fabricated for this objective. The first type is the photonic bandgap (PBG) HC-PCF that is used as a host for selective generation of rotational first-order Stokes in the first stage of the waveform synthesis process due to its low optical loss and narrow transmission bandwidth. The second type is the Kagome lattice HC-PCF, which is used in the second stage of waveform synthesis due to its ultra-broadband transmission. The guidance mechanism of this type of fibre, known as Inhibited Coupling (IC), is examined, through the study of the effect of the newly introduced hypocycloid core shape on confinement loss theoretically and experimentally. A reduction in optical loss figures from a typical value of ~100 dB/km down to

~17 dB/km is achieved by enhancing the negative curvature of the core-contour. In addition, a systematic theoretical and experimental study on the effect of the number of cladding rings upon the confinement and bending loss in Kagome HC-PCF is performed to gain a thorough understanding of the IC guidance mechanism.

The two developed fibres have enabled the development of an all-fibre based system, where the generation of intra-pulse periodic train pulse waveform with 17.6 THz repetition rate and ~ 26fs pulse duration are demonstrated. This was achieved by generating a Raman comb using a compact HC-PCF based system and a micro-chip pulsed laser. The experimental parameters were engineered so the Raman process is in a highly transient regime so to amplify from the quantum noise only a single spatio-temporal mode (STM) to the macroscopic level. We experimentally demonstrated the role of this STM amplification in enhancing the phase-locking of the comb spectral components, and subsequently the intra-pulse optical waveform generation. Furthermore, the results show a long lived persistence of the Raman coherence, thus hinting to a possible pulse-to-pulse mode locking. Such findings make this novel Raman excitation an ideal possible alternative to high harmonic generation (HHG) in gases for the field of attoscience.

Towards the aim of generating ultra-broad comb in the CW regime, we generated first rotational Stokes in the CW regime with output power higher than 50 W. The Stokes laser power stability and the thermal distribution along the coupled fibre are reported. In addition, the linewidth measurements of the forward and backward Stokes are presented. A novel mechanism of stimulated Raman scattering is reported. The model is based on optically induced nanostructured Raman gain, whereby the population difference is saturated but in 1D periodic sub-wavelength sections over a long interaction length. The results show a multi-watt forward and backward Stokes emission with structured spectrum, and linewidth as narrow as ~ 10 kHz (>5 orders of

magnitude shorter than the Raman linewidth as expected from conventional SRS). Observation of rich dynamics that include Rabi splitting, molecular motional sideband and inter-sideband four wave mixing, and finally AC stark induced molecule acceleration is reported.

Acknowledgements

First and foremost, I would like to thank my supervisor Fetah Benabid for offering me the opportunity to study for my PhD under his supervision. This thesis would not have been possible without his guidance, support and encouragement.

I would also like to thank the past and present members of the Gas Phase Photonics Group and the Gas Phase Photonics and Microwave Materials Group. Specific mention should go Tom Bradley whom I have worked with the last few years in Limoges.

I would like to thank Francois Couny and Yingying Wang for their support in my first year. I greatly appreciate the support of Brian Mangan , Frederic Gerome and Benoit Debord for their support for making fibre fabrication during my PhD study. I would like to thank Anton Husakou for help and support.

I would also like to thank Benoit Beaudou, Jean-Marc Blondy, Madhou Dontabactouny, Katell Gadonna, Ekaterina Ilinova, Muhammad Adnan, Ximeng Zheng, Abhilash Amsanpally and the rest of the photonics department members in XLIM Research Institute in France.

Special thanks should go to Mohamed Saleh Abeih for his help and support during my stay at Limoges in the last years.

Finally, but by no means least, my most sincere thanks as always, to my parents, brothers, sisters and to my wife for their continued support encouragements all the time.

Table of Contents

Publication list

Journal Publications

B. Debord, <u>M. Alharbi</u>, T. Bradley, C. Fourcade-Dutin, Y. Wang, L. Vincetti, F. Gérôme, and F. Benabid, "Hypocycloid-shaped hollow-core photonic crystal fiber Part I: Arc curvature effect on confinement loss," Opt. Express 21, 28597-28608 (2013).

<u>M. Alharbi</u>, T. Bradley, B. Debord, C. Fourcade-Dutin, D. Ghosh, L. Vincetti, F. Gérôme, and F. Benabid, "Hypocycloid-shaped hollow-core photonic crystal fiber Part II: Cladding effect on confinement and bend loss," Opt. Express 21, 28609-28616 (2013).

B. Debord, <u>M. Alharbi</u>, L. Vincetti, A. Husakou, C. Fourcade-Dutin, C. Hoenninger, E. Mottay, F. Gérôme, and F. Benabid, "Multi-meter fiber-delivery and pulse self-compression of milli-Joule femtosecond laser and fiber-aided laser-micromachining," Opt. Express 22, 10735-10746 (2014).

Y. Y. Wang, <u>M. Alharbi</u>, T. D. Bradley, C. Fourcade Dutin, B. Debord, B. Beaudou, F. Gerôme and F. Benabid (2013). Hollow-core photonic crystal fibre for high power laser beam delivery. High Power Laser Science and Engineering, 1, pp 17-28. doi:10.1017/hpl.2013.3

A. Nampoothiri, A. Jones, C. Fourcade-Dutin, C. Mao, N. Dadashzadeh, B. Baumgart, Y. Wang, <u>M. Alharbi</u>, T. Bradley, N. Campbell, F. Benabid, B. Washburn, K. Corwin, and W. Rudolph, "Hollow-core Optical Fiber Gas Lasers (HOFGLAS): a review [Invited]," Opt. Mater. Express 2, 948-961 (2012).

B. Beaudou, F. Gerôme, Y. Wang, <u>M. Alharbi</u>, T. Bradley, G. Humbert, J. Auguste, J. Blondy, and F. Benabid, "Millijoule laser pulse delivery for spark ignition through kagome hollow-core fiber," Opt. Lett. 37, 1430-1432 (2012).

Y. Wang, X. Peng, <u>M. Alharbi</u>, C. Dutin, T. Bradley, F. Gérôme, M. Mielke, T. Booth, and F. Benabid, "Design and fabrication of hollow-core photonic crystal fibers for high-power ultrashort pulse transportation and pulse compression," Opt. Lett. 37, 3111-3113 (2012).

Conference Publications

M. Alharbi, B. Debord, M. Dontabactouny, F. Gérôme, and F. Benabid, "17.6 THz waveform synthesis by phase-locked Raman sidebands generation in HC-PCF," in CLEO: 2014, OSA Technical Digest (online) (Optical Society of America, 2014), paper SF2N.6.

B. Debord, M. Alharbi, A. Benoît, M. Dontabactouny, J. Blondy, F. Gérôme, and F. Benabid, "Ultra low-loss hypocycloid-core kagome hollow-core photonic crystal fiber for the green spectral-range applications," in CLEO: 2014, OSA Technical Digest (online) (Optical Society of America, 2014), paper SM1N.3.

A. Benoit, B. Beaudou, M. Alharbi, B. Debord, F. Gerome, F. Salin, and F. Benabid, "Generation of Raman comb over two octaves with picosecond pulse laser in hydrogen-filled Kagome HC-PCF," in CLEO: 2014, OSA Technical Digest (online) (Optical Society of America, 2014), paper SM3N.2.

V. Nampoothiri, W. Rudolph, B. Debord, M. Alharbi, F. Gérôme, and F. Benabid, "CW Hollow Core Optically Pumped Fiber Gas Laser," in CLEO: 2014, OSA Technical Digest (online) (Optical Society of America, 2014), paper SM3N.3.

A. Benoit, B. Beaudou, M. Alharbi, B. Debord, F. Gerome, F. Salin, and F. Benabid, "Dual strong picoseconds laser emissions at 1.8 and 2 µm," in CLEO: 2014, OSA Technical Digest (online) (Optical Society of America, 2014), paper SM3N.5.

B. Beaudou, A. Bhardwaj, T. Bradley, M. Alharbi, B. Debord, F. Gerôme, and F. Benabid, "Macro Bending Losses in Single-Cell Kagome-Lattice Hollow-Core Photonic Crystal Fibers," J. Lightwave Technol. 32, 1370-1373 (2014).

B. Debord, M. Alharbi, C. Hoenninger, E. Mottay, F. Gérôme, and F. Benabid, "Optics-free kagome fiber-aided laser micro-machining," in CLEO: 2014, OSA Technical Digest (online) (Optical Society of America, 2014), paper AM2L.4.

E. Ilinova, T. Bradley, M. Alharbi, J. Mac Ferran, B. Debord, F. Gérôme, and F. Benabid, "Ultra-long lived atomic polarization of Rb confined in hypocycloidal Kagome HC-PCF," in CLEO: 2014, OSA Technical Digest (online) (Optical Society of America, 2014), paper FTh3B.5.

B. Debord, F. Gérôme, M. Alharbi, C. Hoenninger, E. Mottay, A. Husakou, and F. Benabid, "High energy pulse compression regimes in hypocycloid-core kagome hollow-core photonic crystal fibers," in CLEO: 2014, OSA Technical Digest (online) (Optical Society of America, 2014), paper SF2N.4.

M. Alharbi, T. Bradley, B. Debord, C. Fourcade-Dutin, D. Ghosh, L. Vincetti, F. Gérôme, and F. Benabid, "Cladding effect on confinement and bend losses in hypocycloid-core Kagome HC-PCF," in CLEO: 2013, OSA Technical Digest (online) (Optical Society of America, 2013), paper CTu2K.7.

T. Bradley, Y. Wang, M. Alharbi, B. Debord, C. Fourcade-Dutin, B. Beaudou, F. Gerome, and F. Benabid, "Optical Properties of Low Loss (70dB/km) Hypocycloid-CoreKagome Hollow Core Photonic Crystal Fiber for Rb and Cs BasedOptical Applications," J. Lightwave Technol. 31, 3052-3055 (2013).

B. Debord, M. Dontabactouny, M. Alharbi, C. Fourcade-Dutin, C. Hoenninger, E. Mottay, L. Vincetti, F. Gérôme, and F. Benabid, "Multi-meter fiber-delivery and compression of milli-Joule femtosecond laser and fiber-aided micromachining," in Advanced Solid-State Lasers Congress, G. Huber and P. Moulton, eds., OSA Technical Digest (online) (Optical Society of America, 2013), paper ATh1A.6.

M. Alharbi, A. Husakou, and F. Benabid, "Sub-natural Raman linewidth and high power CW Raman-Stokes laser in hydrogen filled HC-PCF," in CLEO:2011 - Laser Applications to Photonic Applications, OSA Technical Digest (CD) (Optical Society of America, 2011), paper QThS4.

T. Bradley, M. Alharbi, Y. Wang, C. Dutin, and F. Benabid, "Optical properties of low loss (70dB/km) Kagome hollow core photonic crystal fiber for Rb and Cs based optical applications," in Conference on Lasers and Electro-Optics 2012, OSA Technical Digest (online) (Optical Society of America, 2012), paper CM3N.1.

Y. Wang, X. Peng, M. Alharbi, C. Dutin, T. Bradley, M. Mielke, T. Booth, and F. Benabid, "Low loss Kagome hollow-core photonic crystal fiber for high power fast laser beam transportation and pulse compression," in Conference on Lasers and Electro-Optics 2012, OSA Technical Digest (Optical Society of America, 2012), paper JTh3I.6.

B. Beaudou, F. Gerome, Y. Wang, M. Alharbi, T. Bradley, G. Humbert, J. Auguste, J. Blondy, and F. Benabid, "Milli-Joule laser pulse delivery for spark ignition through kagome fiber," in Conference on Lasers and Electro-Optics 2012, OSA Technical Digest (online) (Optical Society of America, 2012), paper CM3N.4.

Y. Wang, X. Peng, M. Alharbi, C. Dutin, T. Bradley, M. Mielke, T. Booth, and F. Benabid, "Low loss Kagome hollow-core photonic crystal fiber for high power fast laser beam transportation and pulse compression," in Conference on Lasers and Electro-Optics 2012, OSA Technical Digest (online) (Optical Society of America, 2012), paper JTh3I.6.

B. DEBORD, <u>M. Alharbi</u>, T. Bradley, C. Fourcade-Dutin, Y. Wang, L. Vincetti, F. Gérôme, and F. Benabid, "Cups curvature effect on confinement loss in hypocycloid-core Kagome HC-PCF," in CLEO: 2013, OSA Technical Digest (online) (Optical Society of America, 2013), paper CTu2K.4.

Y. Y. Wang, Xiang Peng, <u>M. Alharbi</u>, C. F. Dutin, T. D. Bradley, Michael Mielke, Timothy Booth and F. Benabid, "Design and fabrication of hollow-core photonic crystal fibers for high power fast laser beam transportation and pulse compression", Proc. SPIE 8269, 826907 (2012).

T. D. Bradley, Y. Y. Wang, <u>M. Alharbi</u>, C. Fourcade Dutin, B. J. Mangan, N. V. Wheeler and F. Benabid, "Progress in hollow core photonic crystal fiber for atomic vapour based coherent optics", Proc. SPIE 8273, 82730O (2012).

Chapter 1

Introduction

In this opening chapter, we review the prior work that underlies the scope of the present thesis. Stimulated Raman scattering (SRS) and hollow core photonic crystal fibre (HC-PCF) are discussed. Furthermore, the principle of optical waveform synthesis through the Raman route is reviewed. An emphasis on transient SRS in HC-PCF and the spatio-temporal mode description of the quantum noise generated Stokes field is made. We discuss how the recent developments in transient SRS in HC-PCF made it as a possible alternative to other technique for ultra-short pulse generation. Finally, we review the key features of the long-term goal of developing HC-PCF based ultra-broad Raman comb generator optical waveform synthesiser in the CW regime

1.1 Stimulated Raman Scattering and HC-PCF

Raman scattering can be defined simply as a two-photon inelastic scattering of an incident laser beam by the molecular excitation of the Raman medium, resulting in a frequency down-converted (Stokes line (ω_S)) or up-converted (anti-Stokes line (ω_{AS})) photon shifted from the pump frequency by Raman transition frequency ω_R of the molecular system [1]. In contrast to its simple definition, Raman scattering is extremely versatile and carries a rich set of physical phenomena, and underpins applications spanning from nonlinear optics to quantum information. For example, it is used as an efficient tool in spectroscopy and microscopy for imaging and molecular tracing [2]. In nonlinear optics, stimulated Raman scattering is used as Raman gas lasers [3], a frequency conversion means, or more recently as an ultra-short pulse synthesiser [4], [5]. In quantum information, Raman scattering has been found to be an excellent way to devise quantum memories and buffers [6], [7]. The diversity of these applications stems from their difference in how the Raman medium is excited and the regime of the Raman dynamics.

For example, the most common configuration is Raman scattering generation with a single laser pump. In this case the scattering occurs independently of the laser frequency, as it is an off-resonance process. However, the scattered Stokes spectral and temporal content strongly depend on the pump laser intensity, duration and spectral content. Given the relevance of the Stokes spectral-temporal properties to the scope of this thesis, we recall some basics related to the Stokes amplification in the case where the medium is excited by a pulsed laser. Within the quantum mechanics framework, Raymer and co-workers considered the generation and propagation dynamics of Raman scattering generation, and identified three different regimes for Raman scattering in the case of a pulsed laser pump [8]. The Raman scattering can be either spontaneous, transient stimulated or steady-state scattering. The boundaries of these regimes and their specific properties are outlined below:

Spontaneous regime: this regime is reached when the pulse duration, τ, is shorter than a characteristic time $\tau_1 = 1/G\Gamma$. Here, Γ is the collisional linewidth (HWHM), and is related to the molecular relaxation time T_2 by $\Gamma = 1/T_2$, L is the interaction length of the laser with the Raman medium. G is the Raman net gain. This is given by $G = (\tilde{g}/\Gamma)P(L/A_{eff})$, with $\tilde{g} = (4\pi\kappa_1\kappa_2)/c$, P is the pump laser power, A_{eff} is the effective area of the pump laser beam and L is the interaction length between the pump laser and the medium $\tilde{g}$ can be considered as the intrinsic Raman coefficient gain of the Raman medium, whilst the tabulated Raman gain coefficient is $g = \tilde{g}/\Gamma$. Here, κ_1 and κ_2 are coupling constants related to molecular polarisability of the medium, given by:

$$\kappa_1 = \sqrt{\frac{1}{2m\hbar\omega_R}}\left(\frac{\partial\alpha}{\partial Q}\right) \tag{1.1}$$

$$\kappa_2 = \frac{2\pi N\omega_S\kappa_1^*}{n_S c} \tag{1.2}$$

here, m is the effective mass of the excitation of Raman medium and n_S is the Raman medium index at the Stokes frequency. $\left(\dfrac{\partial\alpha}{\partial Q}\right)$ is the molecular polarisability change with the ro-vibrational coordinates. Q is the molecular ro-vibration complex amplitude. N is the medium density.

It is noticeable through the expression of the net gain that τ_1 is set by both the Raman medium dephasing time, by the molecule Raman transition strength through $\tilde{g}$, on the laser intensity and pulse duration, and on the interaction configuration through L and the effective area of the laser beam. We notice as well that the larger the net gain the shorter the pump laser duration where the spontaneous scattering occurs. This characteristic time boundary is shown in

Figure 1.1(b) by the dashed line τ_1, where this regime falls underneath this line.

The Stokes amplification in this regime follows a linear amplification with the net gain in contrast with the exponential amplification in the stimulated regime. In this situation, the intensity of the Stokes is given by:

$$I_S^{SP}(L,\tau) = \frac{\hbar\omega_S \Gamma G}{2} \tag{1.3}$$

Finally, the net gain also determines the threshold above which the stimulated scattering occurs. This threshold is set by $G = G_{th} = 15 - 20$.

Steady state regime: this is a stimulated regime in the sense that the Stokes goes through an exponential rise. It is achieved for a pulse duration larger than that of the characteristic time $\tau_2 = GT_2$ (i.e. $\tau \geq \tau_2$). Furthermore, the Stokes intensity in this regime is given by:

$$I_S^{SS}(L,\tau) = \frac{\hbar\omega_S \Gamma e^G}{2\sqrt{\pi G}} \tag{1.4}$$

This characteristic time boundary is shown in Figure 1.1(a) by the dashed line τ_2, where this regime falls above this line.

Transient regime: For pump pulse duration between τ_1 and τ_2 ($\tau_1 < \tau < \tau_2$), the amplification regime is transient. This means that the Stokes generation time is shorter than the molecular dephasing time T_2. We will get back to this point below. The generated Stokes in this case is highly dependent on the pump temporal structure, and its intensity is given by:

$$I_S^{tr}(L,\tau) = \frac{\hbar\omega_S e^{2\sqrt{2gL\Gamma\tau} - 2\Gamma\tau}}{8\pi\tau} \tag{1.5}$$

Here, the pulse duration of the pump in this regime is long enough to initiate the SRS process, but the gain is sufficiently high so the Stokes is generated

within a time duration that is shorter than the collisional dephasing time. Thus, at this regime, the Stokes produced during the interaction has a high level of molecular coherence, and the Stokes pulse approaches that of a transform limited pulse. A more detailed account on the implication of such a regime on the SRS dynamics and on the generation of coherent Raman comb is given below. The use of this regime is restricted traditionally to pulses with a duration shorter or equal to the molecular dephasing time T_2. Such a situation can be explained by the required peak power for SRS. As mentioned above for SRS to happen the net gain must be larger than G_{th}, which translates as

$P > G_{th} \dfrac{1}{g} \left(\dfrac{L}{A_{eff}} \right)^{-1}$. In free-space configuration, we have $\dfrac{L}{A_{eff}}$ with λ being the

laser wavelength (see below), and the minimum peak power required for SRS

generation being $P > \dfrac{G_{th}\lambda}{2g}$. In the case of hydrogen with $g \sim 0.3 cmGW^{-1}$, and a

pump wavelength of 1µm, the pump peak power must be larger than the MW power-level.
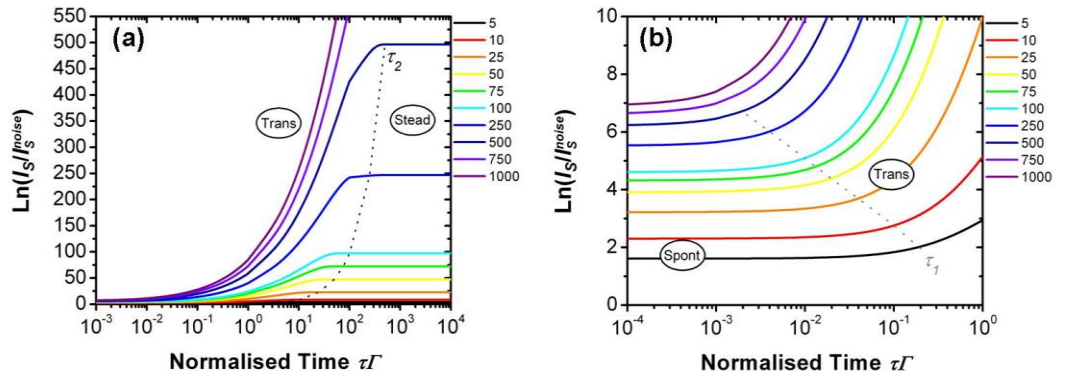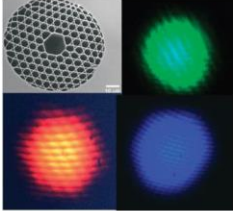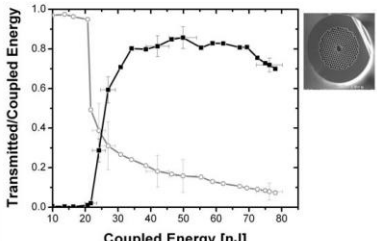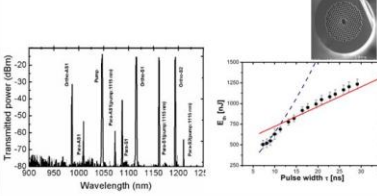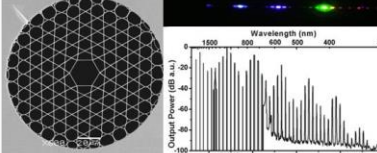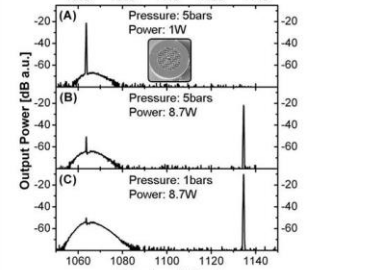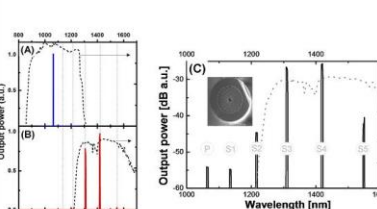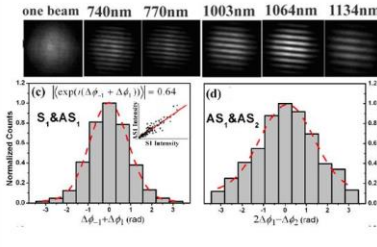
Figure 1.1: Normalised Stokes intensity evolves as function of normalised pump pulse duration $\tau\Gamma$ for different value of gL for (a) high value and (b) low value of $\ln\left(I_S / I_S^{noise}\right)$ illustrating the three different Raman amplification regimes. The dotted lines in (a) and (b) represent passage time τ_1 and τ_2 [9].

However, this constraint on the pump power can be lifted by increasing the net gain G through extending the effective propagation length and decreasing the effective area. From this perspective, the advent of hollow core photonic crystal fibre (HC-PCF), and the first demonstration of ultra-low threshold SRS in hydrogen [10] created a paradigmatic shift in gas-laser interaction by providing a platform where nonlinear optical phenomena in gas-phase media could be excited with very low light-levels.

Since this seminal work, several results have been achieved in our group using H_2-filled HC-PCF. Among these we count (1) rotational SRS generation in H_2-filled photonic bandgap HC-PCF with a million-fold reduction in SRS pulse energy threshold compared to conventional excitations, and suppression of vibrational SRS [11]; (2) novel physical phenomena related to the Stokes amplification dynamics whereby transient SRS is observed with large pulses, and generation of rotational Raman comb [12]; (3) CW SRS in hydrogen [13]; (4) selective generation of higher order Stokes [14]; (5) multi-octave Raman comb generation [15]; and (6) the demonstration of the mutual coherence of the Raman comb spectral components [16]. Table 1.1 illustrates these results along with the experimental conditions and the HC-PCF used.

The work of the present thesis is the continuation of this effort with the long-term aim to synthesise optical waveform in the same manner as in electronics. Of particular relevance to the present thesis is firstly the result related to the coherence of the Raman comb [16], [17], and secondly the CW SRS [13] results. Consequently, in order to set the context for the following chapters of the thesis, we review how the SRS dynamics in the transient regime could explain the generation of coherence Raman comb despite the Stokes being amplified from the quantum noise. Secondly, we conclude the present section on how we are planning to proceed for Raman comb generation using CW SRS.

Table 1.1: Development of SRS in gas filled HC-PCF

2002 [10]		**First demonstration of SRS in gas-filled HC-PCF** • Laser: 532nm, 6 ns pulse duration • Fibre :7 cell Kagome , Loss : ~ 1 dB/m, core diameter: 15µm • Broad transmission bandwidth • SRS: Vibrational SRS in H_2 • Conversion efficiency of ~ 30%
2004 [11]		**Quantum-limited conversion in pure rotational SRS** • Single laser at 1064nm, 0.8 ns pulse duration • Fibre: 7 cell PBG, Loss : ~ 70dB/km , core diameter: 7.2µm • SRS: Rotational SRS in H_2 and suppression of vibrational SRS • Power Conversion efficiency of ~ 92% from pump to first rotational Stokes
2005 [12]		**Raman comb generation and demonstration of transient SRS with large pulses** • Single laser at 1047nm, 14 ns pulse duration • Fibre: 7 cell PBG, Loss : ~ 70dB/km , core diameter: 7µm • Rotational SRS in H_2 • Higher order Raman sidebands generated in the transient regime
2007 [17]		**Multi-octave Raman comb** • Single laser at 1064nm, 12 ns pulse duration • Fibre: 7 cell Kagome, Loss : ~ 500 dB/km , core diameter: 20µm • Generation of multi-octave Raman lines spanning from 325nm to 2300 nm.
2007 [14]		**Quantum-limited conversion in CW rotational SRS** • Single laser at 1064nm, CW • Fibre: 7 cell PBG , Loss : ~ 100 dB/km, core diameter: 5µm • Rotational SRS in H_2 • Conversion efficiency of ~ 99.99% from pump to first rotational Stokes • Observation of CW SRS with pressure as low as 1bar
2010 [16]		**Selective conversion to a specific rotational SRS order** • Single laser at 1064nm, 12 ns pulse duration • Fibre: 7 cell PBG , Loss : ~ 100 dB/km , core diameter: 8µm • First ultra- long tapered PBG HC-PCF filled with H_2 • Shifting the PBG spectral location • Conversion efficiency of ~ 82%
2010 [18]		**Self-coherence and mutual-coherence demonstration in Raman comb** • Single laser at 1064nm, 12 ns pulse duration • Fibre: 7 cell Kagome, Loss : ~ 500 dB/km, core diameter: 20µm • comb generated through spontaneously emitted Stokes • Demonstration of high self and mutual moherence of the Raman comb components

In order to understand how one can obtain a coherent Raman comb from quantum noise, we introduce a coherent mode picture [8] whereby the spontaneously emitted Stokes field or equivalently the collective molecular excitation can be considered as a sum of coherent but statistically independent spatial and temporal modes (STM) [14, 16, 17]. Within this framework, the electronic field operator at the output of the Raman medium can be expanded using a Karhunen-Loeve expansion [13, 18]:

$$\widetilde{E}_S^{(-)}(\rho, L, \tau) = \sqrt{(2\pi\hbar\omega_S n_S / c)} \left(\sum_n \left(\sum_k \hat{b}_k^{(n)} \Psi_k(\tau) \right) \sqrt{\beta_n} \Phi_n(\rho) \right) \tag{1.6}$$

Here the mode functions are orthonormal, $\int \Psi_k(\tau)\Psi_l^*(\tau)d\tau = \delta_{kl}$ and $\int \Phi_k(\rho)\Phi_l^*(\rho)d\rho = \delta_{kl}$. The $\hat{b}_k$ operators are statistically uncorrelated $\langle \hat{b}_k^* \hat{b}_l \rangle = \lambda_k \delta_{kl}$ where $\lambda_k = \langle \hat{b}_k^* \hat{b}_k \rangle$ is the average number of photons emitted into the "temporally coherent mode" $\Psi_k(\tau)$. β_n is seen to be the fraction of photon emitted into the spatial mode $\Phi_n(\rho)$, and thus we have $\sum_n \beta_n = 1$.

Within this description the Raman generation regimes mentioned above take an additional perspective, which is illustrated in Figure 1.2. In the case of spontaneous regime (i.e. $\tau < T_2/G$), all the uncorrelated spatial and temporal modes can be amplified with equal probability. The result is an amplified spontaneous emission with no phase or spatial coherence between the photons constituting the Stokes pulse. In the case of steady-state SRS ($\tau > GT_2$), the pulse duration is sufficiently long that several Stokes photons with different temporal modes $\Psi_k(\tau)$ are amplified. Consequently, the SRS generated Stokes pulse does not contain a deterministic phase, but an average over the different uncorrelated amplified STM. Remarkably, when $T_2/G < \tau < GT_2$, i.e. transient regime, the high gain and the short pulse duration conspire to amplify only a few of the coherent temporal modes. These modes are those which have the

highest Raman gain. Furthermore, if the gain is high enough, only one single temporal mode is amplified to the macroscopic level. The combination of high gain and short pulse duration acts as a temporal filter feeding back the filtered modes to the amplification process. The larger the ratio GT_2/τ the higher the number of filtered-out temporal modes, and thus the fewer temporal modes amplified. Furthermore, if the interaction is taking place in a photonic structure that allows only a few spatial modes, a similar filtering and amplification process takes places for the spatial modes. The net result is that one single STM is amplified, and the Stokes pulse is a phase and spatially coherent and transform-limited pulse. This wave packet, called the dominant-STM, corresponds to the highest Raman gain and is reproducibly created on each laser shot (different phase for different shot) [19]. In other words, it has the form of a transform-limited wave packet with a single overall phase and peak amplitude that are random from one pump pulse to another.
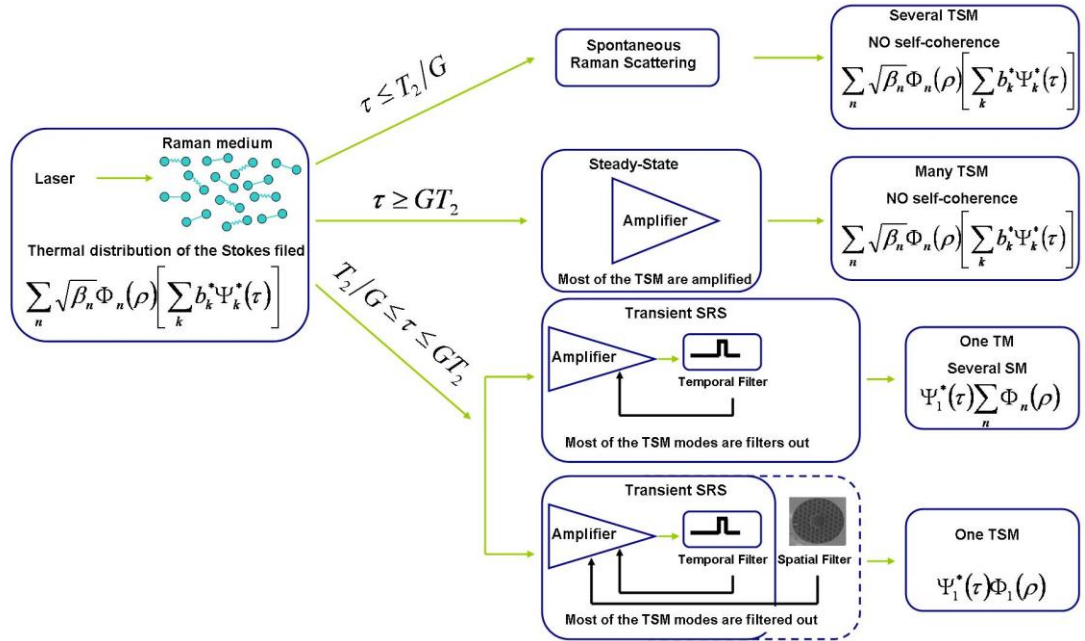
Figure 1.2: A modal picture for self-coherence of different regimes of SRS [18]

This is the case of HC-PCF when it is used as a host for SRS. By providing a very high gain (even for a pump pulse duration larger than T_2 and single mode guidance), it enables generation of a highly coherent transform-limited

(self-coherence) Stokes pulse. A detailed account of the properties of HC-PCF that enabled such a situation is given below in this section. Furthermore, this is experimentally demonstrated in [16], [19] within the framework of generating coherent Raman comb in the transient regime. This STM amplification and filtering bears resemblance with cavity-quantum electrodynamic (QED), wherein a single molecular excitation is strongly coupled to a single cavity mode [20]. However, the difference in the present configuration is that spontaneous emission is not strongly modified as in the case of cavity-QED, but instead, and owing to the optical guiding property of the fibre and the high-gain and highly transient regime of the Raman amplification, only a single TSM (a coherent pulse) is *selected* from the multimode vacuum field. Finally, once the generation of a transform-limited Stokes is achieved, the higher order Stokes and anti-Stokes are generated via a parametric process between the pump, the first order Stokes and anti-Stokes to form an ultra-broad optical comb (see Figure 1.3).
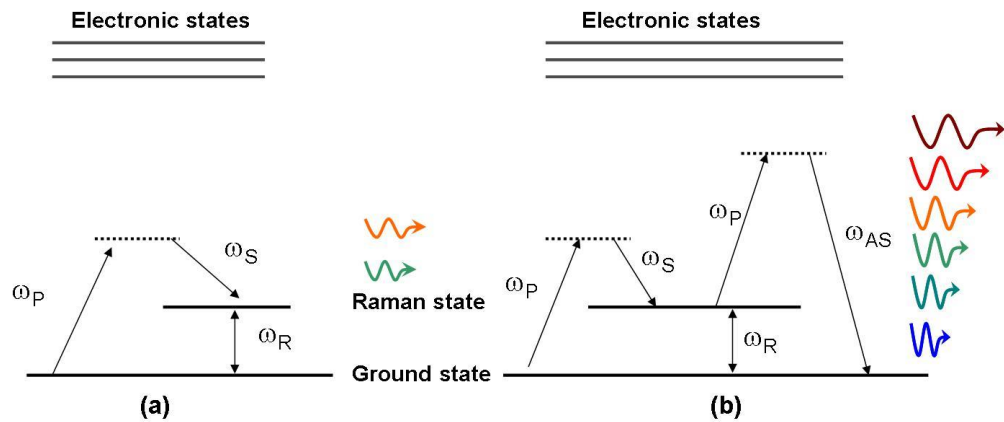
Figure 1.3: Energy levels diagram showing the generation of (a) Stokes photon and (b) Stokes and Anti-Stokes photon during Raman scattering.

Such a configuration opened a new route towards multi-octave comb generation and waveform synthesis, including attosecond pulse generation. In Chapter 4 and Chapter 5 we report on a new result confirming the promise that this technique holds, with the first demonstration of waveform synthesis using phased-locked Raman comb generation in HC-PCF. Also, the demonstration of

molecular coherent survival for a period that is much longer than the dephasing time T_2.

A further exciting development would be to generate such an ultra-broad Raman comb but one pumped with CW lasers. However, because of the high power threshold required to generate SRS, CW SRS in gas-phase media has been a real challenge. It is this challenge that we are taking by exploiting the useful properties of HC-PCF. Below, we briefly review the properties of HC-PCF that are relevant to SRS generation.

Today, we mainly count two types of HC-PCF: photonic bandgap (PBG) HC-PCF and inhibited-coupling (IC) HC-PCF as being important. In the former the cladding structure provides a photonic bandgap at the guidance indices and wavelengths (see Chapter 2), whereas in the latter, the cladding is "populated" with a continuum of modes that are strongly phase-mismatched with the core modes (see Chapter 3). Both fibres exhibit the ability of micro-confining together gas-phase materials and light over large distances. These attributes have led to a broad range of novel applications including enhanced nonlinear effects in gases [11] and particle guidance [20] to mention a few. Owing to the micro-meter scale core size and long interaction length of several metres, light and matter can interact in theses fibres with a very high efficiency, which makes these fibres an ideal host for gas phase nonlinear optics. As a matter of fact, these fibres have created a new paradigm in laser-gas or liquid interaction. The laser-matter interaction enhancement in hollow-core fibre is the key issue of this report. Indeed, in endeavouring to generate a waveform synthesiser via SRS processes, we require the ability to have an ultra-broad bandwidth and/or to selectively excite a specific high order Raman line in the most effective way. For this the ideal fibre should exhibit low propagation loss, a small effective area and tailored transmission bandwidth (see the last section of the chapter relating to the system architecture for the CW SRS comb generation). Within this context, the triangular lattice PBG HC-PCF and the Kagome lattice IC

HC-PCF exhibit complementary properties. Indeed, the PBG HC-PCF has a narrow transmission bandwidth and was proven to generate a given Raman line and suppress others [11], whilst Kagome HC-PCF exhibits an ultra-broad transmission window which is amenable for multi-octave comb generation [21]. One should also take into account the optical power handling of each fibre in the case where high-power SRS generation is required. In addition, the transmission loss, which determines the effective length in laser-matter interaction, and the effective area are important parameters in devising the appropriate HC-PCF as they set the efficiency of the laser-gas interaction. This is quantified by the following figure-of-merit (FOM):

$$FOM = \frac{L_{int}\lambda}{A_{eff}} \tag{1.7}$$

where L_{int} is the effective interaction length. In HC-PCF, L_{int} is related to the attenuation loss α by simply $L_{int} \sim \alpha^{-1}$. λ is the wavelength and A_{eff} is the effective area. Typically in conventional free-space experiments, the interaction is maximised by tightly focusing the laser beam Figure 1.4 (a). However, the main drawback of this method is that the laser remains focused only for a short distance (which is twice the Rayleigh length): $L_{int} = 2\pi\omega_0^2/\lambda$. Thus, the effective interaction only occurs over this distance. Moreover, using this method limits the laser intensity level to avoid high power non-linearity [22]. Thus, high FOM in a free space configuration is difficult to achieve. Another common configuration to improve FOM is the use of a single hollow capillary. In this technique, the interaction length becomes longer and the FOM value is improved to being 10 times more efficient than the free space technique. However, this technique has a limited interaction length (usually ~ 1m) and a high loss figure ~ 0.13 dB/m for 1 mm bore [23]. To enhance the interaction efficiency to a value much more than that, one needs to turn to HC-PCF technology. The FOM of HC-PCF takes the following form:

$$FOM_{HC-PCF} = \frac{\lambda}{a^2 \alpha \pi}$$ (1.8)

where α is the attenuation of the fibre (in m^{-1}) and a is the core radius.

The HC-PCF offers the long interaction length associated with a small effective area to achieve a high FOM compared to other configurations. Figure 1.4 illustrates how the FOM compares with each of the above configurations. It can be seen that the FOM for capillary waveguides becomes very low once the core radius reaches 15 μm. With the introduction of the HC-PCF, the FOM increased significantly up to 10^7 times, as is shown in Figure 1.4 (d). Different types of HC-PCF have different FOM depending on core diameter and propagation loss, but still have high FOM even with fibre with high propagation loss reaching the level of ~ 1dB/m. The coloured regions in Figure 1.4 (d) represent the FOM for the two types of HC-PCF (PBG and Kagome). The SEM images of such fibres are illustrated in Figure 1.4 (c). The maxima FOM values are achieved using the 7 cell and the 19 Cell PBG HC-PCF. The FOM of Kagome HC-PCF occurs at a lower level compared with the PBG. This can be seen due to the fact that this type of HC-PCF has a larger core radius. In order to reach a higher level of FOM, one needs to have low loss Kagome HC-PCF comparable to PBG HC-PCF, which will be introduced in Chapter 3.
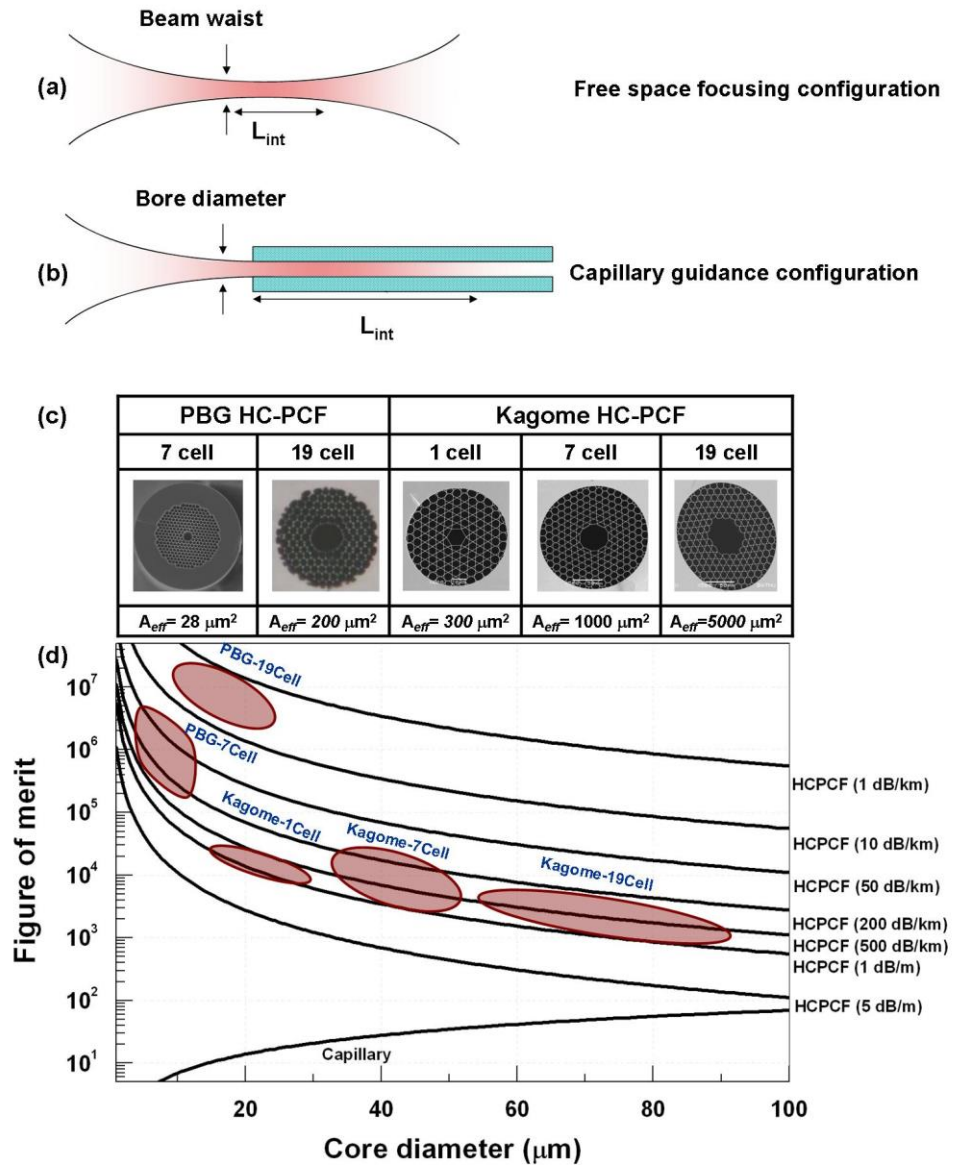
Figure 1.4: (a) Focused laser beam in free-space. (b) Capillary guidance. (c) SEM images of different HC-PCF (d) FOM of capillary guidance and HC-PC. Red shaded regions correspond to prior art to this work.

In the present section, we have seen some key properties of transient SRS in HC-PCF, and the advantage of these fibres in endeavouring to multi-octave coherent and synthesisable optical comb both in the pulsed regime and in CW. It is noteworthy that this aim is part of a broader context where several techniques are used or currently being developed to harness optical waves. The following section describes the current landscape of the different techniques in generating optical comb and the synthesis of pulses or waveform.

1.2 Raman and Waveform Synthesis

In a similar way to the principle operation of an electronic function generator, optical waveform synthesis operates via Fourier synthesis. The most effective way of generating an arbitrary waveform is to have a sufficiently broad spectral comb. Indeed, with such a spectrum, which by definition is comprised of discreet spectral lines equally spaced in frequency, i.e. each line has its frequency in the form of $\omega_C \pm n\omega_R$, where n is an integer, ω_R is modulation frequency, and ω_C is the central frequency of the comb, a waveform can be generated by controlling the phase and the amplitude of each spectral line independently. Such a broad coherent comb means that the temporal profile of the output light can be synthesised to practically any waveform leading to a train of attosecond pulses, by controlling the magnitude and the relative phase of a selective comb component. Figure 1.5 shows an example of how a simple comb comprising spectral components enables us to have a different waveform shape by changing the number of combs generated. Figure 1.6 simply illustrates the generation of deferent forms of signals by controlling the amplitude and the phase for different spectral components.

In the optics or photonics field, the generation of an arbitrary waveform is still on the "wish list" of the scientific community as this would require multi-octave combs with CW spectral components where amplitude and phase could be controlled with the same degree of flexibility as in electronics. This was thought until very recently an impossible goal, and that is the reason why the term of waveform synthesis in optics is synonymous with pulse shaping, as the synthesis of the waveform is still constrained to pulses.
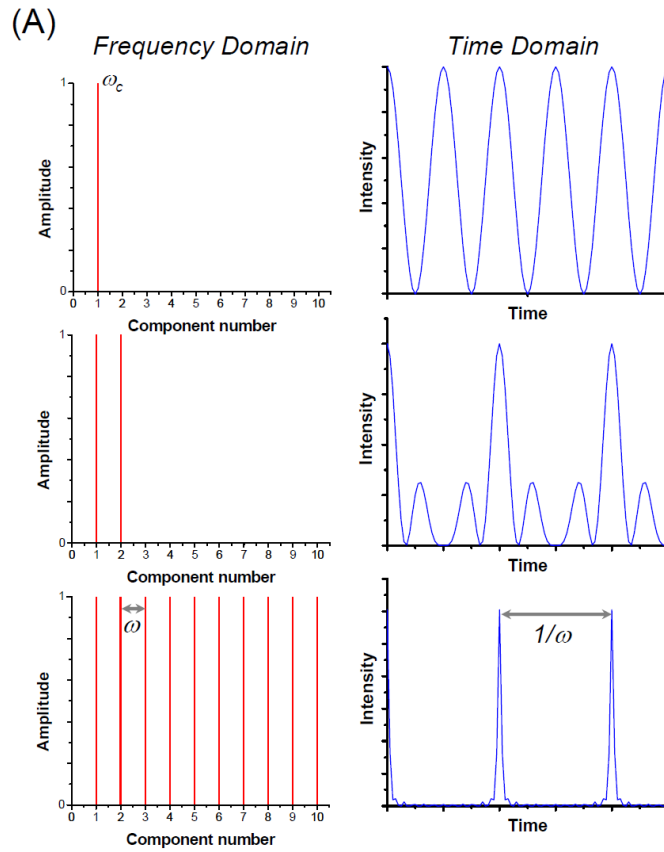
Figure 1.5: Frequency domain (left) and temporal domain for signal with different components number [9].
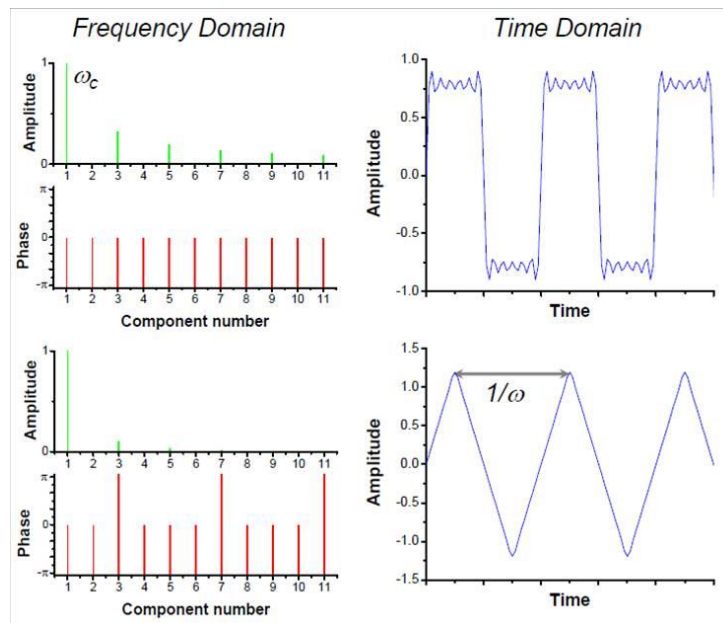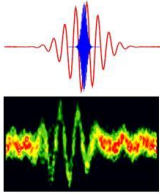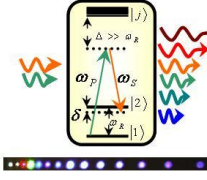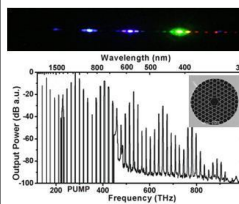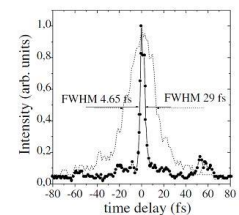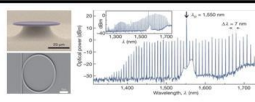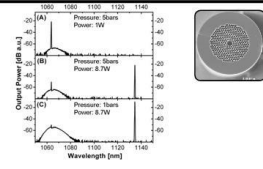
Figure 1.6: Frequency domain (left) and temporal domain for signal with different amplitudes and phases [9].

Within this context, a strong drive was focused on the generation of shorter and shorter pulses, which subsequently requires techniques to generate multiple octave optical combs. This drive is motivated by both scientific and technological quests. For example, the ability to generate ultrashort pulse lasers with adequate temporal resolution has yielded new interesting fields such as a femtochemistry field [24] and the emergence of an attoscience field [25], [26]. Recent developments in the attosecond area have shown the ability to study electron dynamics in atoms [27]. This is achieved via the high harmonic generation (HHG) method using femtosecond lasers [28], [29] where pulses in the extreme ultraviolet (XUV) and soft X-ray regions are generated which leads to pulse shaping. Although these pulses act as unique gadgets, they are difficult to control due to intrinsic concerns of X-ray transmission through optics. Furthermore, a major limitation of HHG is the low photon conversion efficiency (typically 10^{-6}). In addition, the need to use ultra-short pulses with high peak power (10^{15} Watt/cm^2) for noble gases excitation and engineering difficulties of this method have led to the exploration of new alternative methods to overcome these constraints. Several techniques have been proposed and demonstrated in the last 15 years. Table 1.2 summarises these techniques, which are divided into two families to illustrate which technique can be a good candidate for waveform synthesis. This classification is based on whether the generated comb is generated with excitation pulsed or CW laser. This in turn, determines whether the synthesis is prescribed to pre-determined pulses (pulse shaping) or not.

Among the pulsed techniques, we count high-order stimulated Raman scattering (HSRS) in hydrogen or deuterium as a promising alternative method for the generation of ultrabroad light spectrum with high photon conversion efficiency and low nonlinear threshold [30]–[33]. Up to now, there are three methods for this Raman rout: impulsive Raman method, molecular modulation method and transient Raman method. The first technique was proposed by

Nazarkin *et al.* [31] where they illustrate experimentally the generation of high order Stokes and anti-Stokes sidebands in impulsively excited medium. This is done by exposing the medium to an intense femtosecond laser pulse with a duration shorter than the dephasing time T_2. Following that, a second weak delayed pulse propagating in the excited medium experiences scattering due to the modulation of its refractive index by molecular vibration. This technique has been able to produce pulses as short as 3.8 fs in the near UV region [34]. However, its main drawback is that the generated Raman coherence is several orders of magnitude smaller than the maximal value (~ 0.5).

Table 1.2: Methods of comb generation

The second method is the molecular modulation method. In this regime the duration of the laser pulses is much longer than the dephasing time T_2. This technique is considered to be the most promising technique for generating an ultra-broad spectrum with high photon conversion efficiency. It was originally suggested and demonstrated by Harris and co-workers [35], where they

prepared adiabatically the molecular medium coherent by driving it with two high power lasers (at the nanosecond pulse duration) whose frequency is slightly detuned from the Raman transition ω_R. Subsequently, the material refractive index is modulated, which in turn, generates collinear and mutually coherent combs [4], [35]. However, this scheme suffers from some limitations such as; needing a pair of high intensity lasers and limited interaction length and intensity achieved due to free-space configuration. Finally, the third method is the transient method. This technique is usually applicable when the laser pulse duration is comparable to or shorter than the dephasing time (T_2) of the Raman medium [32], [33], [36]. This is experimentally executed using a megawatt power transform limited sub-picosecond laser pulse. In parallel to this, and due to the development of HC-PCF, it was demonstrated in [12] that Raman comb generation with ~ 70 THz bandwidth in PBG HC-PCF could be accomplished in transient SRS with large pulses. This was followed shortly after by the report of a multi-octave Raman comb generation using Kagome HC-PCF [15]. A further development in this regime was achieved by Wang *et al*. in 2010 [16], where they demonstrated a high self-coherence and mutual coherence by comb generated through spontaneously emitted Stokes. This scheme is quite new and part of the aim of this thesis is to further explore the transient SRS and continue the above mentioned work which enables the ability of Fourier synthesis of these comb spectral components to generate ultrashort optical pulses including pulses with attosecond pulse duration.

The second part in Table 1.2 is the comb generation in the CW regime where a coherent frequency CW comb and a broad spectrum (~ 1000 THz) are one of the key requirements for the realisation of an optical waveform synthesiser. However, such methods, thus far, come at the cost of using either high peak power of ultrashort pulsed lasers or multiple pump lasers that require a cumbersome setup procedure. One of the methods for CW comb generation is based on microresonator via Kerr nonlinearity [37] and silicon nitride ring

resonator on silicon via optical parametric oscillator [38]. However, those methods are restricted to limited power handling and limited bandwidth. In the Raman route, such a coherent comb could be achieved either by using a high finesse Fabry Perot cavity [3], [39], [40] or HC-PCF [12], [13] as hosts for Raman active medium. The former was the first demonstration of CW SRS generation. However, this technique suffers from some limitations such as, low bandwidth, poor conversion efficiency, output power scale-up, and cavity stabilisation problems. On the other hand, the latter technique showed the ability to overcome the limitations mentioned above. The HC-PCF offers the possibility of having quantum-limited conversion in CW rotational SRS [13]. This scheme was founded and developed in our group and work is ongoing towards the realisation of an optical waveform synthesiser through coherent SRS (see section 1.3). This thesis is a continuation of this effort where work on the HC-PCF architecture and SRS in the transient and CW regimes are the essence of this thesis and include a major part on the optical waveform synthesiser project.

1.3 HC-PCF based Raman waveform synthesiser

Recent developments have been made to HC-PCF enabled generation of an ultra-broad optical comb of phase-locked and collinear spectral Raman sideband components spaced by an extremely high frequency (> 10 THz). The coherence of these broad spectral components raises the possibility of synthesising optical waveforms. Although waveform synthesis via HHG [41], [42] or by molecular modulation [4] has been recently demonstrated, it is limited to isolated short pulses and restricted to ultra high power transform limited nanosecond pulsed lasers. Thus, the synthesis has been restricted by the temporal profile of the isolated nanosecond pump pulses and, hence it is more appropriate to consider here pulse shaping rather than waveform synthesis. In

order to achieve an optical waveform synthesiser with a high degree of control similar to the electronic function generator, one must operate and generate optical components in the continuous wave (CW) regime. In this regime, the pump and the Stokes beams are sufficiently intense. The driving CW lasers (pump and Stokes) need to have a narrow linewidth in order to reach the maximum coherence. Fortunately, this condition can now be met thanks to the recent development made in high power CW fibre lasers [43]. These lasers are commercially available and can operate at a single frequency with a linewidth of only tens of kilohertz (kHz). In addition, the interaction length needs to be sufficiently long in view of the fact that the efficiency of the generation of Raman process is proportional to the product of the gas density and the interaction length [44]. This is achieved by integrating the new developed low loss HC-PCF to the scheme as a host for nonlinear optics in gases. Thus, the conditions on adiabaticity and maximum coherence of the system are accomplished easily.

These developments have led Prof. Fetah Benabid to propose all-fibre based CW Raman sidebands via the molecular modulation technique to achieve a stable and compact optical waveform synthesiser [45]. This proposal is considered to be the first CW-based optical waveform synthesiser and attosecond pulse generator in an integrated all-optical system based on hollow-core photonic crystal fibre (HC-PCF) filled with hydrogen gas. The device would generate and synthesise almost any optical intensity waveform with a frequency as high as several tens of THz and with any central wavelength from UV to IR. It would be able to generate ultra-short laser pulses with tuneable duration from a few femtoseconds down to a few hundreds of attoseconds. This device would be able to generate a wide range of coherent laser sources. The proposed system has the potential to open new regimes in a wide variety of fields, including ultra-high resolution spectroscopy, quantum optics and computing, and ultra-fast optical processing.

The suggested experimental setup for the coherent CW Raman sidebands is illustrated in Figure 1.7. Device 1 is the proposed setup for the generation of the first rotational Stokes through SRS process in hydrogen filled PBG HC-PCF using part of the CW pump laser output. This stage has been already achieved and reported in [46] , with first Stokes output of 55 Watts (see chapter 6). The remaining power from the CW pump laser and the new generated Stokes act as a two-pump laser source for the next stage. The output from this two-pump source is coupled to device 2 to either a chain of gas filled PBG HC-PCF, as shown in Figure 1.7 (A), or to a single gas filled Kagome HC-PCF to generate the Raman sideband spectrum (Figure 1.7 (B)). The former, is limited in terms of transmission bandwidth to ~ 70 THz. For this reason in order to cover a broader bandwidth one needs to operate many gas filled PBG HC-PCF with different transmission bandwidth locations. Whereas the latter can cover a much broader bandwidth up to ~ 1000 THz. Furthermore, the recent progress on Kagome development means the use of this type of HC-PCF is more favourable.
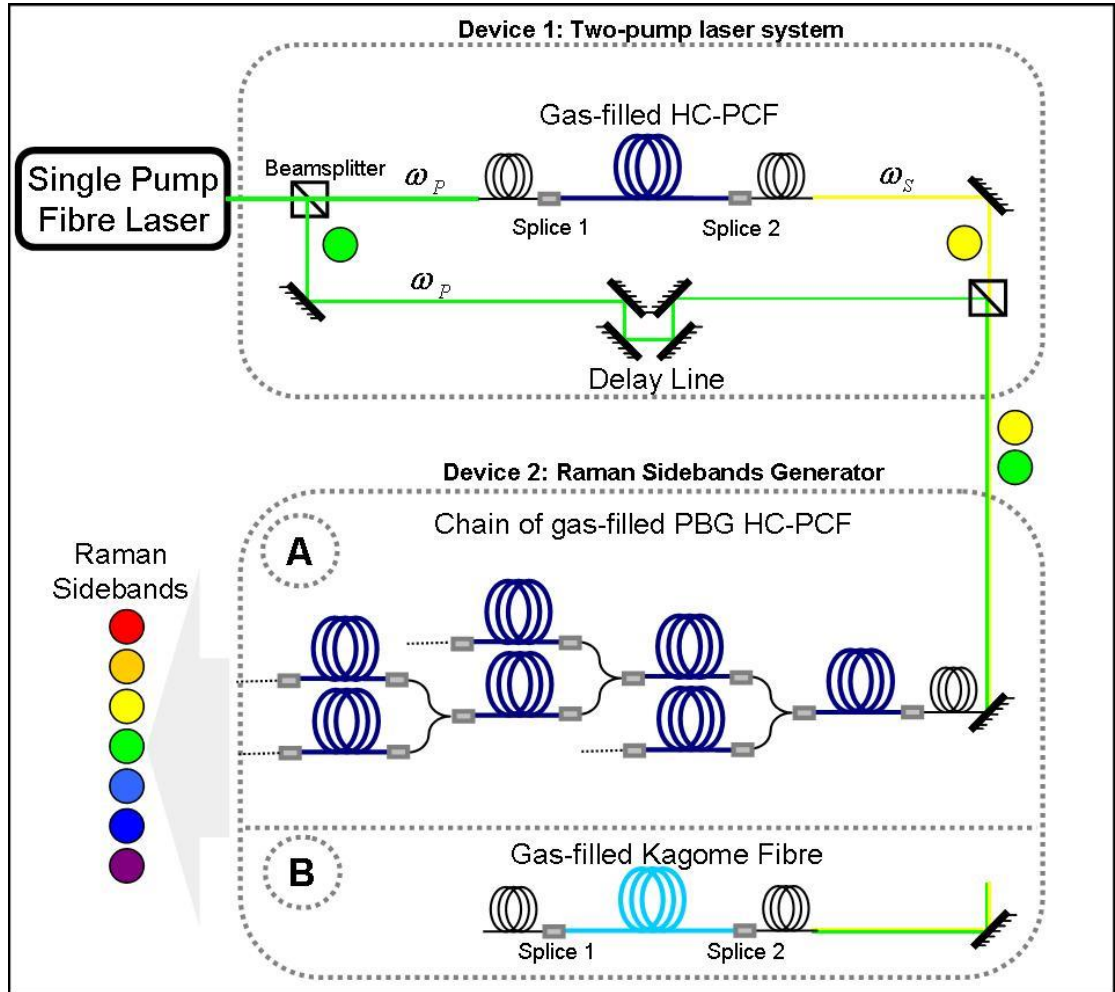
Figure 1.7: Schematic of proposed Raman sidebands generator based on gas-filled HC-PCF. A single laser is coupled into Device 1 to generate the required Stokes radiation. The resulting two-pump laser system is then coupled onto Device 2 for the generation of the sidebands by (A) a chain of gas filled PBG HC-PCF, (B) a single Kagome-lattice HC-PCF [9], [45].

1.4 Thesis outline

Based on the above, this thesis covers a further investigation of the IC mechanism of Kagome HC-PCF and of Raman frequency generation and coherence in pulsed and CW regimes. The thesis contains three parts.

Part 1 is the prior knowledge and development of HC-PCF presented in two chapters:

- Chapter 2 presents a review of PBG HC-PCF and highlights the guidance mechanism physics using the photonic tight binding model. Furthermore, it covers the fabrication of this type of fibre and its role as one of the key elements for some results achieved in this thesis.

- Chapter 3 presents a review of Kagome HC-PCF and emphasises the guidance mechanism through IC mechanism. This chapter is one stage of many ongoing stages to have a deeper understanding of IC, and hence better fibre performances. This chapter covers recent developments in the design and fabrication of ultra-low loss IC HC-PCF and the effect of cladding numbers on the confinement and bend loss.

Part 2 covers the Raman frequency comb and coherence based on pulsed and SRS generation in the transient regime. This part consists of two chapters:

- Chapter 4 presents the recent results about spatiotemporal mapping of Raman coherence in HC-PCF filled with H_2, where the molecule coherence persists for duration larger than the dephasing time of Raman transient.

- Chapter 5 is a demonstration of waveform synthesis with a repetition rate of 17 THz and pulse duration of ~ 26 fs using intra-pulse phase-locked Raman comb generation in HC-PCF filled with H_2 and pumped with a half nanosecond pulse duration laser. The role of the quantum

noise initiated Stokes seed is demonstrated. Furthermore, the chapter covers results on the Raman coherence survival after the pump pulse passage, and the possibility of developing pulse-to-pulse Raman based mode-lock laser.

Part 3 presents the recent efforts towards the realisation of an optical waveform synthesiser in the CW regime using the HC-PCF. This part contains two chapters:

- Chapter 6 is a review of recent results for CW Raman first rotational Stokes generated using HC-PCF filled with H_2 and pumped by a high power single frequency fibre laser. Furthermore it covers the generation of >50 W Stokes power and its stability.

- Chapter 7 presents an original study about high power sub-natural linewidth Stokes emission through velocity selective SRS and saturation in confined H_2 molecules inside HC-PCF.

Finally, in chapter 8 a summarisation of the thesis and proposal of future work especially regarding the optical waveform synthesis are presented.

References

[1]   N. Shen, Y. R. and Bloembergen, "Theory of Stimulated Brillouin and Raman Scattering," *Phys. Rev.*, vol. 137, no. 6A, p. A1787, 1964.

[2]   J. Cheng and X. S. Xie, "Coherent Anti-Stokes Raman Scattering Microscopy: Instrumentation, Theory, and Applications," *J. Phys. Chem. B* no. 108, pp. 827–840, 2004.

[3]   L. S. Meng, P. a Roos, and J. L. Carlsten, "Continuous-wave rotational Raman laser in H(2).," *Opt. Lett.*, vol. 27, no. 14, pp. 1226–8, Jul. 2002.

[4]   S. E. Harris and A. V Sokolov, "Subfemtosecond Pulse Generation by Molecular Modulation," *Phys. Rev. Lett.*, vol. 81, no. 14, pp. 2894–2897, Oct. 1998.

[5]   H.-S. Chan, Z.-M. Hsieh, W.-H. Liang, A. H. Kung, C.-K. Lee, C.-J. Lai, R.-P. Pan, and L.-H. Peng, "Synthesis and Measurement of Ultrafast Waveforms from Five Discrete Optical Harmonics," *Sci.* , vol. 331 , no. 6021 , pp. 1165–1168, Mar. 2011.

[6]   M. G. Raymer and J. Mostowski, "Stimulated Raman scattering: Unified treatment of spontaneous initiation and spatial propagation," *Phys. Rev. A*, vol. 24, no. 4, pp. 1980–1993, Oct. 1981.

[7]   I. A. Walmsley and M. G. Raymer, "Observation of Macroscopic Quantum Fluctuations in Stimulated Raman Scattering," *Phys. Rev. Lett.*, vol. 50, no. 13, pp. 962–965, Mar. 1983.

[8]   I. A. Raymer, M.G. Walmsley, "The quantum coherence properties of stimulated Raman scattering." *E. Wolf, Progress in Optice*. Vol 28, 1990.

[9]   F. Couny, "Photonic Solutions towards Optical Waveform Synthesis," *University of Bath*, 2008.

[10]   F. Benabid, J. C. Knight, G. Antonopoulos, and P. S. J. Russell, "Stimulated Raman scattering in hydrogen-filled hollow-core photonic crystal fibre.," *Science*, vol. 298, no. 5592, pp. 399–402, Oct. 2002.

[11]   F. Benabid, G. Bouwmans, J. Knight, P. Russell, and F. Couny, "Ultrahigh Efficiency Laser Wavelength Conversion in a Gas-Filled Hollow Core Photonic Crystal Fibre by Pure Stimulated Rotational Raman Scattering in Molecular Hydrogen," *Phys. Rev. Lett.*, vol. 93, no. 12, p. 123903, Sep. 2004.

[12] F. Benabid, G. Antonopoulos, J. Knight, and P. Russell, "Stokes Amplification Regimes in Quasi-cw Pumped Hydrogen-Filled Hollow-Core Photonic Crystal Fibre," *Phys. Rev. Lett.*, vol. 95, no. 21, p. 213903, Nov. 2005.

[13] F. Couny, F. Benabid, and P. Light, "Subwatt Threshold cw Raman Fibre-Gas Laser Based on H2-Filled Hollow-Core Photonic Crystal Fibre," *Phys. Rev. Lett.*, vol. 99, no. 14, p. 143903, Oct. 2007.

[14] B. Beaudou, F. Couny, Y. Y. Wang, P. S. Light, N. V Wheeler, F. Gérôme, and F. Benabid, "Matched cascade of bandgap-shift and frequency-conversion using stimulated Raman scattering in a tapered hollow-core photonic crystal fibre.," *Opt. Express*, vol. 18, no. 12, pp. 12381–90, Jun. 2010.

[15] F. Couny, F. Benabid, P. J. Roberts, P. S. Light, and M. G. Raymer, "Generation and photonic guidance of multi-octave optical-frequency combs.," *Science*, vol. 318, no. 5853, pp. 1118–21, Nov. 2007.

[16] Y. Y. Wang, C. Wu, F. Couny, M. G. Raymer, and F. Benabid, "Quantum-Fluctuation-Initiated Coherence in Multioctave Raman Optical Frequency Combs," *Phys. Rev. Lett.*, vol. 105, no. 12, p. 123603, Sep. 2010.

[17] F. Couny, F. Benabid, P. J. Roberts, P. S. Light, and M. G. Raymer, "Generation and photonic guidance of multi-octave optical-frequency combs.," *Science*, vol. 318, no. 5853, pp. 1118–21, Nov. 2007.

[18] Y. Wang, "Quantum-Fluctuation-Initiated Coherent Raman Comb in Hydrogen-Filled Hollow-Core Photonic Crystal Fibre," *University of Bath*, 2011.

[19] C. Wu, M. G. Raymer, Y. Y. Wang, and F. Benabid, "Quantum theory of phase correlations in optical frequency combs generated by stimulated Raman scattering," *Phys. Rev. A*, vol. 82, no. 5, p. 053834, Nov. 2010.

[20] F. Benabid, J. C. Knight, and P. S. J. Russell, "Particle levitation and guidance in hollow-core photonic crystal fibre," *Opt. Express.* vol. 10, no. 21, pp. 1195–1203, 2002.

[21] F. Couny, F. Benabid, P. J. Roberts, P. S. Light, and M. G. Raymer, "Generation and photonic guidance of multi-octave optical-frequency combs.," *Science*, vol. 318, no. 5853, pp. 1118–21, Nov. 2007.

[22] G. Agrawal, *Nonlinear fibre optics.* Academic Press, London. 2001.

[23] Y. Matsuura, M. Miyagi, K. Shihoyama, and M. Kawachi, "Delivery of femtosecond pulses by flexible hollow fibres," *J. Appl. Phys.*, vol. 91, no. 2, p. 887, 2002.

[24] A. H. Zewail, "Laser Femtochemistry," *Sci.* , vol. 242 , no. 4886 , pp. 1645–1653, Dec. 1988.

[25] N. A. Papadogiannis, B. Witzel, C. Kalpouzos, and D. Charalambidis, "Observation of Attosecond Light Localization in Higher Order Harmonic Generation," *Phys. Rev. Lett.*, vol. 83, no. 21, pp. 4289–4292, 1999.

[26] P. Corkum, "Attosecond pulses at last," *Nature*, vol. 403, no24 FEBRUARY, pp. 845–846, 2000.

[27] M. Uiberacker, T. Uphues, M. Schultze, a J. Verhoef, V. Yakovlev, M. F. Kling, J. Rauschenberger, N. M. Kabachnik, H. Schröder, M. Lezius, K. L. Kompa, H.-G. Muller, M. J. J. Vrakking, S. Hendel, U. Kleineberg, U. Heinzmann, M. Drescher, and F. Krausz, "Attosecond real-time observation of electron tunnelling in atoms.," *Nature*, vol. 446, no. 7136, pp. 627–32, Apr. 2007.

[28] M. Hentschel, R. Kienberger, C. Spielmann, G. A. Reider, N. Milosevic, T. Brabec, P. Corkum, U. Heinzmann, M. Drescher, and F. Krausz, "Attosecond metrology," *Nature*, vol. 414, no. 6863, pp. 509–513, Nov. 2001.

[29] P. M. Paul, E. S. Toma, P. Breger, G. Mullot, F. Auge, P. Balcou, H. G. Muller, and P. Agostini, "Observation of a train of attosecond pulses from high harmonic generation.," *Science*, vol. 292, no. 5522, pp. 1689–92, Jun. 2001.

[30] a V Sokolov, D. R. Walker, D. D. Yavuz, G. Y. Yin, and S. E. Harris, "Raman generation by phased and antiphased molecular states.," *Phys. Rev. Lett.*, vol. 85, no. 3, pp. 562–5, Jul. 2000.

[31] A. Nazarkin, G. Korn, M. Wittmann, and T. Elsaesser, "Generation of Multiple Phase-Locked Stokes and Anti-Stokes Components in an Impulsively Excited Raman Medium," *Phys. Rev. Lett.*, vol. 83, no. 13, pp. 2560–3, Sep. 1999.

[32] H. Kawano, Y. Hirakawa, and T. Imasaka, "Generation of high-order rotational lines in hydrogen by four-wave Raman mixing in the femtosecond regime," *IEEE J. Quantum Electron.*, vol. 34, no. 2, pp. 260–268, 1998.

[33] E. Sali, K. J. Mendham, J. W. G. Tisch, T. Halfmann, and J. P. Marangos, "High-order stimulated Raman scattering in a highly transient regime driven by a pair of ultrashort pulses," *Opt. Lett.*, vol. 29, no. 5, pp. 495–497, 2004.

[34] N. Zhavoronkov and G. Korn, "Generation of Single Intense Short Optical Pulses by Ultrafast Molecular Phase Modulation," *Phys. Rev. Lett.*, vol. 88, no. 20, p. 203901, May 2002.

[35] S. E. Harris and a. V. Sokolov, "Broadband spectral generation with refractive index control," *Phys. Rev. A*, vol. 55, no. 6, pp. R4019–R4022, Jun. 1997.

[36] H. Kawano, Y. Hirakawa, and T. Imasaka, "Generation of more than 40 rotational Raman lines by picosecond and femtosecond Ti:sapphire laser for Fourier synthesis," *Appl. Phys. B Lasers Opt.*, vol. 65, no. 1, pp. 1–4, Jul. 1997.

[37] P. Del'Haye, a Schliesser, O. Arcizet, T. Wilken, R. Holzwarth, and T. J. Kippenberg, "Optical frequency comb generation from a monolithic microresonator.," *Nature*, vol. 450, no. 7173, pp. 1214–7, Dec. 2007.

[38] J. S. Levy, A. Gondarenko, M. A. Foster, A. C. Turner-foster, A. L. Gaeta, and M. Lipson, "CMOS-compatible multiple-wavelength oscillator for on-chip optical interconnects," *Na Photon,* vol. 4, no. 1, December, pp. 37–40, 2009.

[39] J. K. Brasseur, K. S. Repasky, and J. L. Carlsten, "Continuous-wave Raman laser in H_2.," *Opt. Lett.*, vol. 23, no. 5, pp. 367–9, Mar. 1998.

[40] J. T. Green, J. J. Weber, and D. D. Yavuz, "Continuous-wave, multiple-order rotational Raman generation in molecular deuterium.," *Opt. Lett.*, vol. 36, no. 6, pp. 897–9, Mar. 2011.

[41] P. Antoine, a L'Huillier, and M. Lewenstein, "Attosecond Pulse Trains Using High-Order Harmonics.," *Phys. Rev. Lett.*, vol. 77, no. 7, pp. 1234–1237, Aug. 1996.

[42] Y. Mairesse, a. de Bohan, L. Frasinski, H. Merdji, L. Dinu, P. Monchicourt, P. Breger, M. Kovačev, T. Auguste, B. Carré, H. Muller, P. Agostini, and P. Salières, "Optimization of Attosecond Pulse Generation," *Phys. Rev. Lett.*, vol. 93, no. 16, p. 163901, Oct. 2004.

[43] IPG. Photonics, [Online]. Available: www.ipgphotonics.com.

[44] A. V. Sokolov, M. Y. Shverdin, D. R. Walker, D. D. Yavuz §, a. M. Burzo, G. Y. Yin, and S. E. Harris, "Generation and control of femtosecond pulses by molecular modulation," *J. Mod. Opt.*, vol. 52, no. 2–3, pp. 285–304, Jan. 2005.

[45] F. Benabid, "Optical Wave Generator," Patent : GB 0615541.02006.

[46] F. Couny, B. J. Mangan, A. V. Sokolov, and F. Benabid, "High Power 55 Watts CW Raman Fibre-Gas-Laser," *Conf. Lasers Electro-Optics (CLEO)*, p. CTuM3, 2010.

Part 1

Design and Fabrication of HC-PCF

This part covers the design, fabrication and characterisation of HC-PCFs that are used in the different experiments on the generation of high-order stimulated Raman scattering. Two types of HC-PCF were fabricated and used as the essential building blocks for the experiments reported in the present thesis. The first one is based on photonic bandgap (PBG) guidance with narrow bandwidth and small effective area. The second fibre is based on inhibited coupling guidance and exhibits a very large bandwidth.

The part is divided into two chapters. Chapter 2 presents a brief review on the guidance mechanism of photonic bandgap, the photonic tight binding model to explain intuitively the formation of PBG, and the current state-of-the-art in such a fibre, with an emphasis on those that guide around 1 μm and 532 nm. We then quickly review the fibre fabrication process before presenting a fabricated 1μm PBG HC-PCF whose bandwidth and transmission loss figures are within the current state-of-the-art range. Chapter 3 covers a body of work in designing and developing a new type of Kagome HC-PCF. The novel fibre relies on hypocycloid-like (negative curvature) core-contour to enhance the inhibited coupling (IC). A profound and systematic experimental and theoretical investigation on the guidance mechanism of Kagome HC-PCF was conducted to elucidate the role of the negative curvature and the cladding ring number in the confinement loss. A work that led to new state-of-the-art in HC-PCF transmission loss illustrated in the 17 dB/km loss around 1 μm.

Chapter 2

Photonic Bandgap HC-PCF

This chapter covers a review of PBG guiding HC-PCF and the underlying physics of the PBG formation using the photonic tight binding model. The chapter covers fabrication of PBG HC-PCF especially designed for a Stokes laser which is an important element of the HC-PCF waveform synthesiser.

1.1 Introduction

Optical fibres, which can guide light via total internal reflection (TIR), are one of the key technological achievements of the 20th century. The development of this technology has led to many applications (telecommunication and non-telecommunication applications). However, this kind of fibre suffers from limitations such as optical loss, nonlinearity and dispersion, due to light confinement in the solid glass medium which forms the core of such fibres. These effects might be overcome when light is guided in an air core. Such an air optical guide has the advantage of reducing the effect of Rayleigh scattering and material absorption. Moreover, it has the ability to deliver high optical power. Nevertheless, the light in such a core cannot be guided through TIR. The idea of guiding light through a hollow core instead of silica opens the door for a great number of interesting applications and phenomena, some of which the present thesis explores.

The concept of photonic bandgap (PBG) within photonic crystal materials was suggested for the first time by Yablonovitch [1] and John [2] . This PBG rises in periodic structures where it is defined as a forbidden region where no electromagnetic wave can travel in a given wave vector-frequency space. This concept at its beginning was mainly focused on "in-plane" propagation in periodic dielectric structures. In 1991, Russell [3] extended the PBG concept to include the "out-of-plane" by suggesting that light through an air-core fibre could be realised by having a photonic crystal cladding around the air core. In 1995, a theoretical demonstration of out-of-plane PBG was reported by Birks *et al*. [4] where they suggested that PBG regions could be identified. In 1999, Cregan *et al.* [5] demonstrated the first hollow core photonic crystal fibre (HC-PCF) based on bandgap guidance. Although this type of fibre has overcome the constraint that limits the use of conventional optical fibres in many applications due to its solid core, its loss figure (~ 1.2 dB / km) is still one

order of magnitude higher than that of a conventional optical fibre (~ 0.16 dB/km). Having said that, this fibre found several uses in nonlinear optical applications. Figure 2.1 shows an example of this type of HC-PCF.
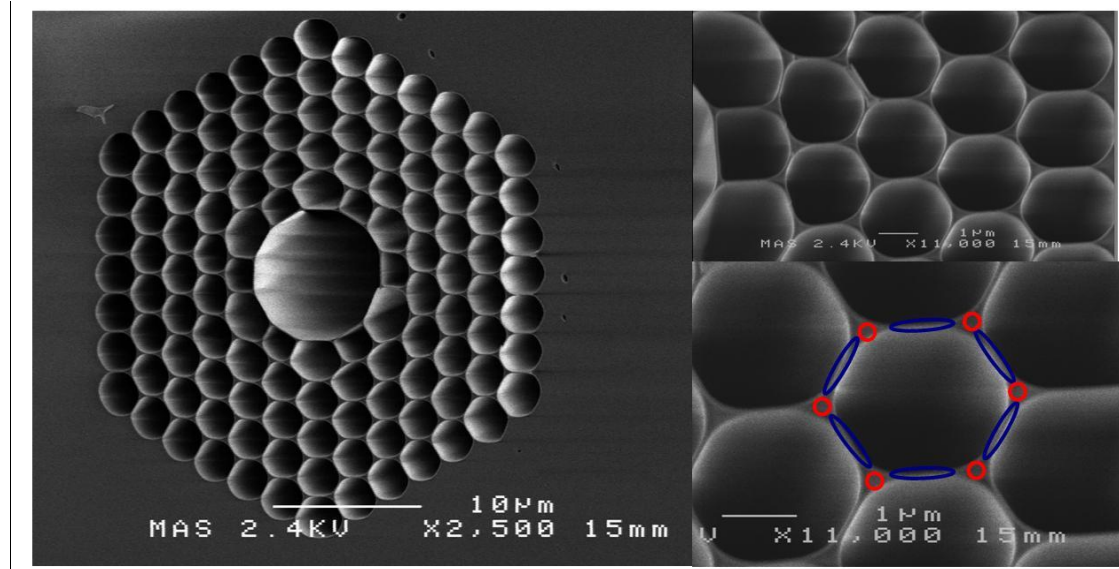
Figure 2.1: Scanning electron micrograph (SEM) image of a PBG HC-PCF specially designed to guide at 1064nm. The red circles are the apexes and the blue circles are the struts of a unit cell.

2.2 Photonic bandgap guidance concept

The guidance of this type of fibre relies on the confinement of light in the air core. The cladding structure is designed to exhibit what is known as an out-of-plane photonic bandgap (PBG) in the transverse plane, where no optical modes over a specified range of frequencies are supported [5]. Inside such a structure, the dielectric function n of the cladding structure and the free-space wavenumber k are linked to the propagation constant β through Maxwell-Helmholtz equation:

$$\left(\nabla^2 + k^2 n^2\right)h + \nabla\left(\ln n^2\right)\times\left(\nabla\times h\right) = \beta^2 h \tag{2.1}$$

Where k is the free-space wavenumber, n is the dielectric function of the cladding structure, h is the transverse component of the magnetic field, and β is

the propagation function. By considering propagation out-of-plane for infinite PCF lattice, Birks *et al.* [4] identified specific spectral regions where no solution exists for Eq. (2.1). The generated result is a propagation diagram of the cladding structure, as in Figure 2.2, plotted against both normalised wave vector magnitude ($k\Lambda$) and normalised axial wave vector ($\beta\Lambda$), where Λ is the pitch of the structure, k is the wave vector magnitude (i.e. it is related to the frequency by $k = \omega/c$) and is β the propagation constant.
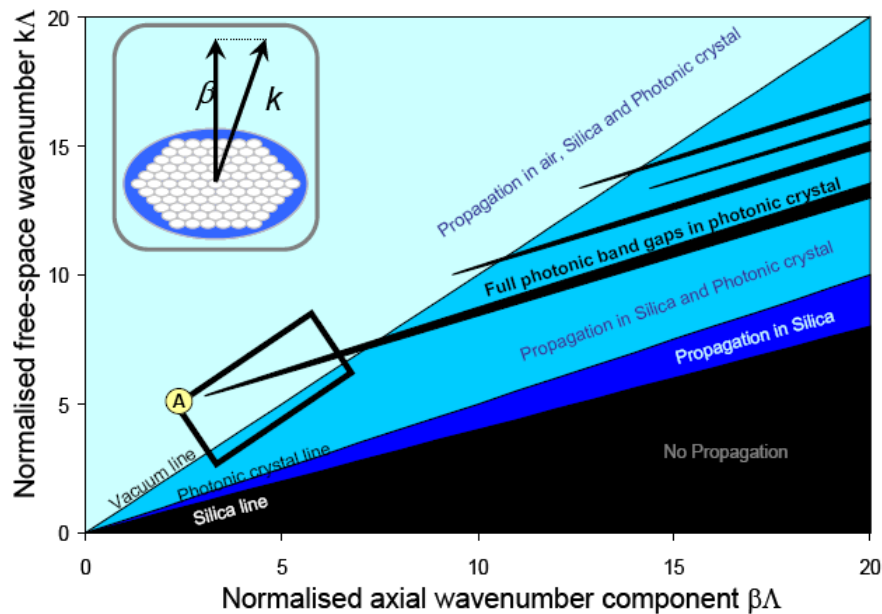
Figure 2.2: Band-edge diagram illustrating the position of photonic bandgaps in terms of normalised wave vector [6].

Figure 2.2 shows schematically the position of full photonic bandgaps (black regions) in the $\beta\Lambda - k\Lambda$ space, and which is related to the $\beta\Lambda - k\Lambda$ pair for which no solution exists to Eq. (2.1), or equivalently, light is excluded from being guided in the photonic crystal. The diagram also shows several diagonal lines. These are the boundary (i.e. cut-off) between allowed and forbidden propagation in different materials constituting the photonic structure. In the example taken in this diagram, the materials are air and silica, which are the most common in PCF. When a defect is introduced in the photonic crystal, thus breaking the transverse periodicity of the structure, light becomes effectively

trapped inside and guided provided the introduced defect supports guided mode within the PBG $\beta\Lambda - k\Lambda$ range. The diagram shows that this defect (i.e. the fibre core) can have a refractive index lower than that of the cladding. If one or more of these PBG regions extends above the vacuum dispersion line (air-line $k = \beta$), air-core guidance becomes possible over a particular frequency range (rectangle A in Figure 2.2). For $\beta\Lambda - k\Lambda$ band diagram of real structure, density of photonic state (DOPS) of the structure, which is the number of electromagnetic modes per unit of frequency (Δk) (and propagation constant $(\Delta\beta)$, is usually plotted. In this case, the $\beta\Lambda - k\Lambda$ regions where DOPS is not nil correspond to the cladding modes, whilst when DOPS drops to zero, the region is said to be photonic bandgap. Below, we reconsider the above-mentioned diagram in light of the simple and intuitive picture of photonic tight binding model.

2.3 Photonic tight binding Model

Several models have been developed to explain the transmission characteristics and modal properties of hollow fibres and give physical insight on how light is confined in bandgap guiding PCF, thus providing predictive tools in designing these photonic structures. Among the models that have developed in the last decade we count the anti-resonant reflective optical waveguide (ARROW) model [7], the cellular method (CM) [4] and finally the photonic tight binding model (PTBM) [6]. The ARROW model was an extension to PCF structures of the ARROW model proposed by Duguay *et al.*[8] to design planar waveguides with a low-index core region sandwiched between two thin glass sheets. This work was also an extension from Fabry-Perot interferometry whereby a configuration is said to be anti-resonant when a signal is extracted from the reflected light off the interferometer.
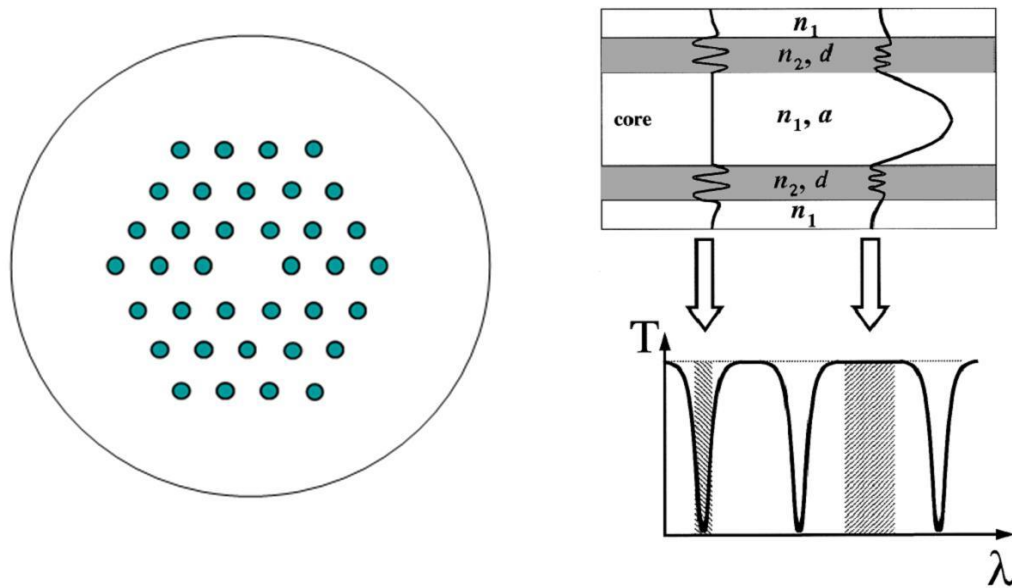
Figure 2.3: Microstructure optical fibre with low core refractive index surrounded with high index inclusions [7].

The main insight in the ARROW model when applied to PCF was to identify the spectral regions where guided modes are in resonance with the constituent features of the cladding structure. It is noteworthy that ARROW is by definition a necessary condition in any low index core. Furthermore, when this model is applied to the structure shown in Figure 2.3 [7], they found that when the pitch is much larger than the operating wavelength the transmission band edges are independent of the pitch. The MC introduced by Birks *et al.*[4] is more complete than the ARROW in the sense that it takes into account electromagnetic coupling between each high index inclusion of the cladding structure mentioned above. Furthermore, it has the useful feature of reducing the simulation of a photonic structure to a single cell using a semi-analytical method. The model identifies the band-edges of band gaps in the same single inclusion cladding structure mentioned above. This model is analogous to the cellular method used in solid-state physics.

The photonic tight binding model (PTBM), proposed by Benabid, and reported in Couny *et al.* [6] is a further completion of the above model by explaining both the origin of the bandgap formation more generally, including HC-PCF, and

the nature of allowed states in the cladding structures. The model is the photonic equivalent of the well-known tight binding model in condensed matter [9]. This is used to describe the origin of allowed and forbidden electronic bands. Here the model describes the electronic bands in the crystal are the result of bringing together isolated and identical atoms. As the isolated atoms are brought closer, a spatial overlap between the atomic orbitals occurs and the discreet and degenerate electronic levels split to form allowed bands of energy levels with a bandgap in between. Similarly, in a photonic crystal structure, the atoms are replaced by high index waveguiding features and the electronic energy levels are replaced by high index waveguide dispersion. When the waveguiding features get sufficiently close (small pitch), overlap of the waveguide fields is achieved, and the modes split forming photonic bands in the cladding structure. To illustrate the PTBM, Benabid *et al.* [10] considered a 1-dimensional array of silica rod waveguides. The top graph in Figure 2.4 shows the dispersion curves of the fundamental LP_{01} and higher order LP_{11} modes of an isolated rod with diameter "*d*". For a 1-dimension array of identical rods (lower graph Figure 2.4), the dispersion curves may be calculated by considering the coupling between rods. The figure shows the calculated curves for rods of diameter $d=0.45\Lambda$, where Λ is the pitch of the array. It is calculated for an array of 1000 rods. The rods assumed to have a Gaussian refractive index profile and to couple only the nearest-neighbour rods. It is observed that the allowed frequencies for a single rod broaden into allowed bands for the array. An observation of the band diagram shows that for larger pitch (i.e. $\Lambda >> \lambda$) the allowed photonic bands remain very narrow and do not deviate from the dispersion of a single rod. This trend is the same as the conclusion for the ARROW model regarding the band edges evolution at large pitch.
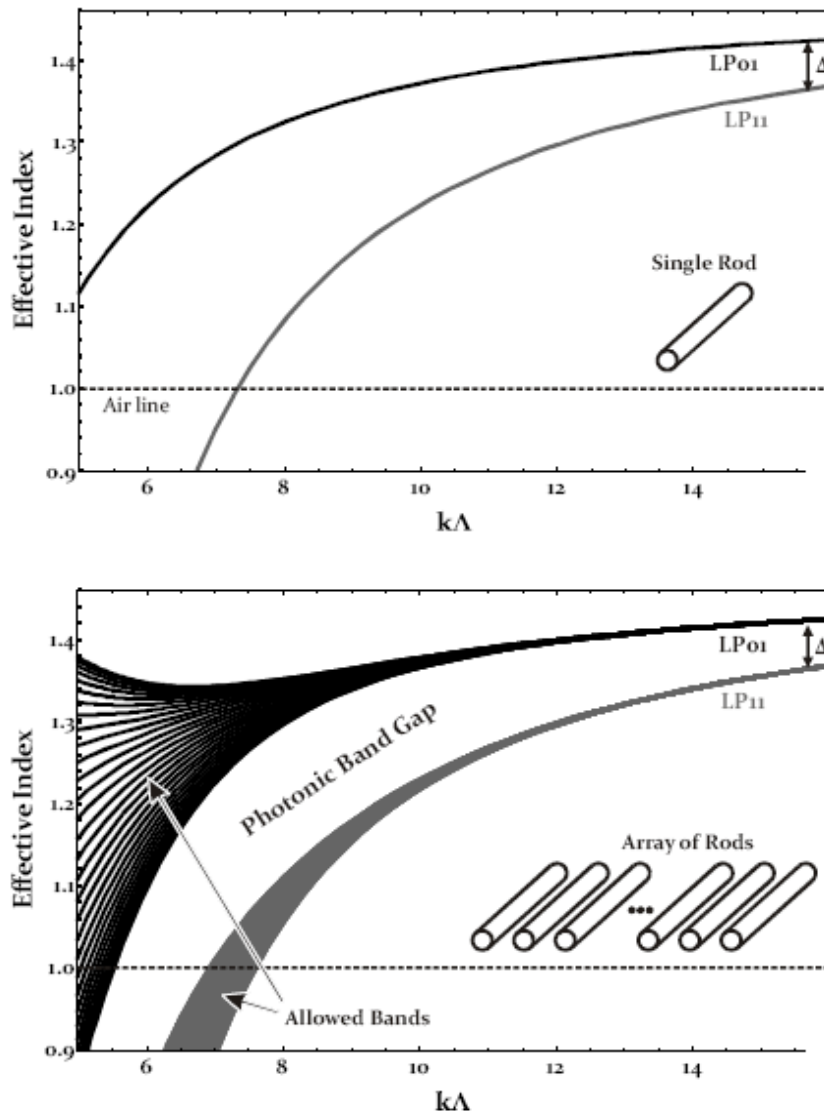
Figure 2.4: Top: dispersion curves of the fundamental and first higher-order modes of an isolated silica rod. Bottom: For an array of identical rods spaced by pitch Λ the dispersion curves broaden to form allowed bands[10].

This TPBM model was successfully applied to real HC-PCF despite the complexity of the structure compared to the single inclusion structure mentioned above [6]. Indeed, because of the interconnected struts and apexes in PBG guiding HC-PCF cladding structure (see Figure 2.1), the identification of the wave guiding responsible for the formation of the allowed band and bandgap is challenging. The demonstration of the TPBM in HC-PCF was achieved by examining theoretically and experimentally the field profile of cladding modes, and was concluded that the cladding DOPS was the result of

three waveguiding features: the silica apexes, silica struts and air holes. Figure 2.5 shows the DOPS diagram over a large normalised frequency range [3]. The yellow shaded region indicates the spectral and effective-index range where light in the hollow core is possible. A zoom-in of this DOPS diagram is illustrated in Figure 2.6, with the aim of identifying the field distribution of representative Bloch modes on the allowed photonic bands. The coloured lines added to the figure illustrate key modes that define the boundary of the bandgap. The upper edge of the bandgap, the red line, is defined by modes which are localised in the interstitial apex of the cladding, whilst the lower edge, the green and blue lines, is formed by two modes of different symmetry, one being guided predominantly in the air holes (green line), the other guided predominantly within and close to the silica struts which join the neighbouring apices (blue line).

Figure 2.6 C shows the calculated profiles of these three types of cladding resonators. Consequently, one can easily identify the structural features behind each photonic band. Through this understanding, it is possible to optimise the PBG bandwidth and the fibre attenuation by, for example, increasing the air filling fraction (AFF) of the cladding, which is defined using the ratio of hole diameter D to the pitch Λ (or between apex size and strut thickness), can broaden the bandgap and move its location to a higher frequency . Figure 2.7, shows an example of predicted bandgap broadening with the increase of AFF[10] .
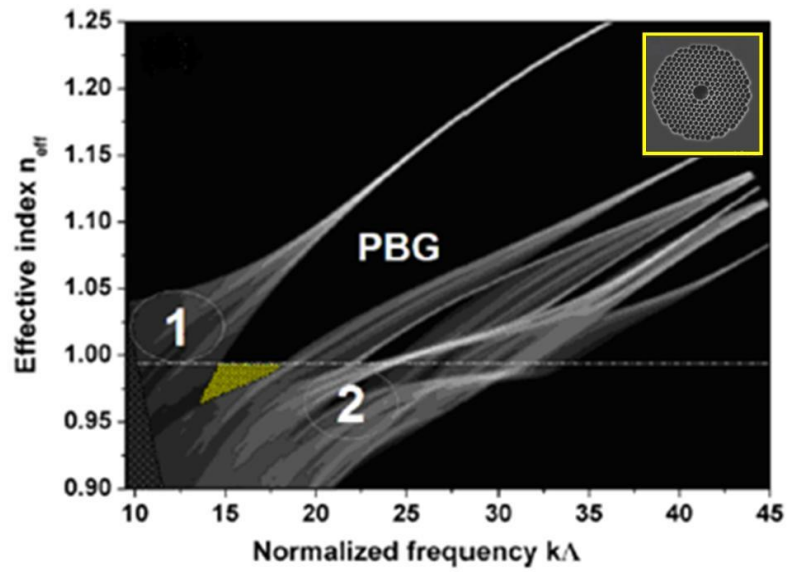
Figure 2.5: Calculated density of the photonic state plot for PBG HC-FCF [12].
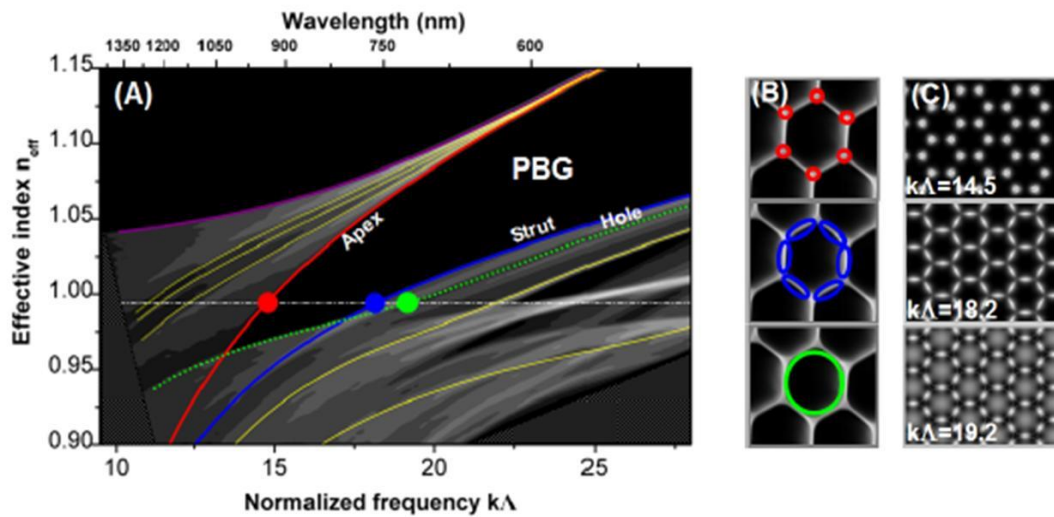
Figure 2.6: (A) Detail of the calculated density of state plot around the PBG region falling below the vacuum line. (B) Detail of the three resonators identified in the triangular structure. (C) Their calculated near-fields, at position indicated by the dots [6].
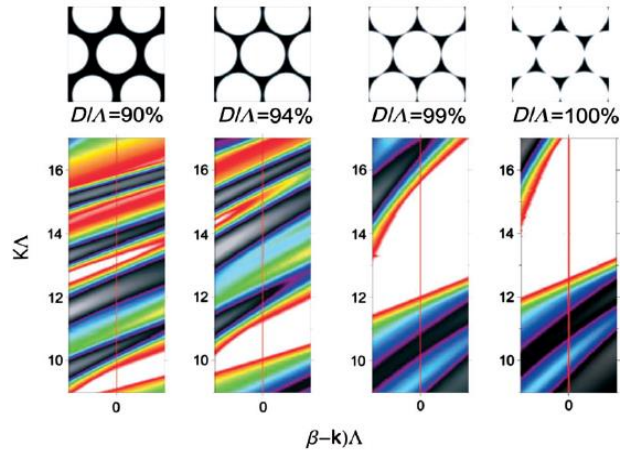
Figure 2.7: Band structure for a triangular lattice with different D/Λ [10].

The introduction of a defect into the photonic crystal cladding structure (i.e. the core of a HC-PCF) introduces a guided mode within the defect. Within the PBG, the lowest order mode of the hollow core defect (fundamental mode) is the mode with the highest propagation constant β and thus the closest to the air line (HE_{11} in Figure 2.8). The modal content of the core can be controlled by either setting the core size or by engineering the cladding structure. For example, with a larger core diameter, high order air-guided modes (HOM) can propagate at lower n_{eff} because all the n_{eff} of the core-guided modes are shifted towards the air line. Within the PBG boundaries, the dispersion of these air-guided modes is flatter than that of silica-guided cladding modes, and their trajectory in the DOPS diagram is near-horizontal line in Figure 2.8 limited on either side by the continuum of modes creating the PBG edges. Near to these boundaries, the core modes couple to the continuum, leading to high loss and increased dispersion. This limits the transmission bandwidth of the HC-PCF to a narrow range. Therefore, the pitch Λ of the fibre has to be chosen so that the fibre guides at a given wavelength.
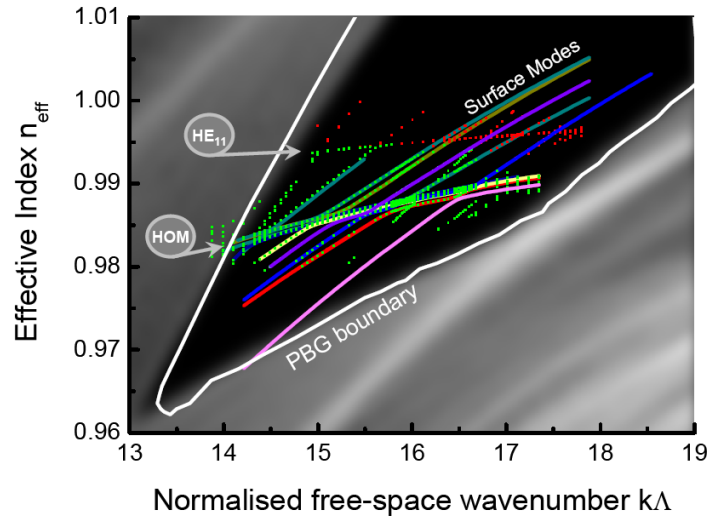
Figure 2.8: DOPS diagram of the region of the PBG falling below the vacuum line. The trajectory of the core-guided fundamental (HE$_{11}$) mode and other high order modes (HOM) are identified (dashed lines). The solid line represents the surface mode [6].

In addition to the PBG bandwidth limitation, another restriction to the bandwidth is imposed by the interaction between the air-guided modes and the surface modes. These surface modes can be seen as another type of defect mode. They originate at the interface between the photonic crystal cladding and the core defect. The dispersion of these modes has a sharper slope than the air-guided modes and can intersect with them inside the PBG. If the surface and the core mode have the same β, an "anti-crossing" occurs where the dispersion curves of the modes repulse each other leading to an increase in the transfer of energy from the core mode to the high attenuation surface mode. These high attenuation regions at the frequency of these anti-crossings further reduce the operational bandwidth and affect the overall transmission of the HC-PCF [13].

However, the location of these anti-crossing events can be shifted to the edge of the transmission spectrum by controlling the shape of the core which is demonstrated theoretically [14] and experimentally [15]. Wang *et al.* [16] also illustrated a technique to tailor these events by reducing the core ring thickness using an etching method.

2.4 PBG HC-PCF for Raman

Based on the physical background of how PBG guiding HC-PCF guides light, we designed and fabricated a PBG HC-PCF that favourably guides at 1064 nm and ~1135 nm, which correspond to the first order Stokes in hydrogen rotational SRS. The outstanding features offered by PBG HC-PCF, such as a small effective area and low loss over long lengths, make it an ideal candidate for selective conversion SRS. The introduction of such a host has enabled remarkable progress in the field of SRS in molecular gases, where in order to reach the Raman threshold using conventional methods one needs to operate at a high power laser. Using this novel technique, Benabid *et al.* in 2004 [12] reported on the generation of first Stokes with a photon conversion reaching the quantum limit and pump power threshold reduction (down to ~ 3nJ) to around one million lower than the lowest values reported for SRS generation in free space [17], [18]. In 2005 [19] the generation of a few higher order rotational Raman sidebands using this type of fibre was demonstrated, where the Raman generation was achieved in the transient regime at a modest power level (~ 150 nJ) with a pulse duration of ~ 14 ns. Couny *et al.* in 2007 [20], demonstrated on a single pass CW Raman laser using this kind of fibre, with around 99.99% conversion from pump to first rotational Stokes. This very high conversion efficiency is difficult to accomplish using the Kagome lattice HC-PCF. Therefore, the PBG HC-PCF is selected, here in this thesis, as the best candidate for converting pump to its first Stokes line, which will be used as a second pump for the realization of optical waveform synthesis, as described previously in Chapter 1. This is an essential part in the progress made in Chapter 5 and Chapter 7 of this thesis.

Below, we report on a 7 cell PBG HC-PCF which is designed and fabricated to guide specifically at pump single-frequency laser (1064 nm) and ~1135 nm. This

will be done by having the shortest bandwidth possible whilst still guiding at the pump range and 1st order Stokes wavelengths.

2.4.1 Fabrication of PBG HC-PCF

The technique used for fabricating HC-PCF is called "stack-and-draw"[5]. This is illustrated schematically in Figure (2.9). This is basically based on drawing hundreds of capillaries (with ~ 1mm diameter and ~ 1m long) using a silica tube (~ 20mm diameter) with a chosen wall thickness Figure 2.9(i). These capillaries are then "stacked" manually in a specific arrangement according to the design. The stack is then inserted into a chosen jacket tube to form the final "stack", where the gaps between the stack and the tube are filled carefully with packing capillaries and rods Figure 2.9(ii). This stack is then fused and drawn to many "canes" (with ~ 3 mm diameter) ~ 1 m long, Figure 2.8(iii). The final step is to draw the cane, after inserting it inside a ~ 10 jacket tube, into fibre Figure 2.8 (iv). During drawing of the fibre at the final stage, pressure is applied to the core and cladding regions to avoid any deformation to the structure and to control the air-filling fraction (AFF) of the fibre.
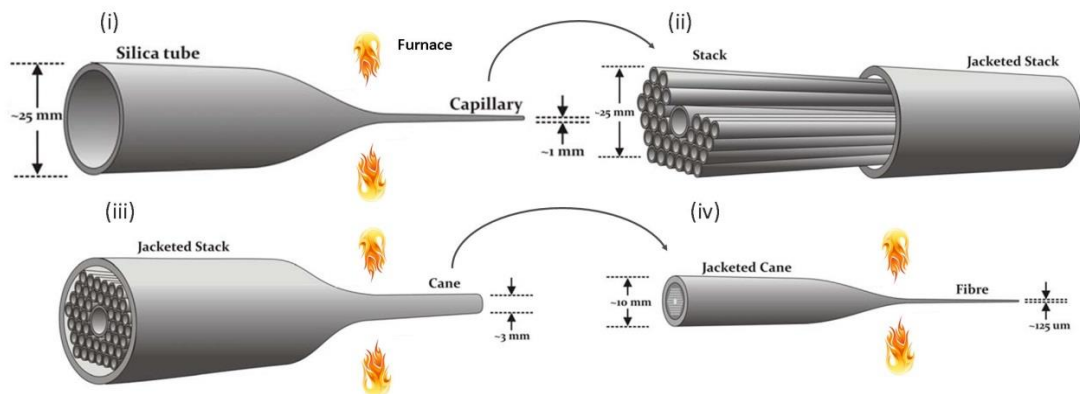
Figure 2.8: Stack-and-draw technique procedure (i) Capillary fabrication, (ii) Capillaries and then inserted in a jacket tube, (iii) Drawing jacketed stack to ~ 1 m long canes, (iv) Cane fitted in a jacket tube and then drawn to fibre.

2.4.2 Fabrication Results

Using the fabrication method, as mentioned above, a 7cell PBG HC-PCF fibre is fabricated. Figure (2.9) shows a scanning electron micrograph (SEM) image of the fabricated fibre. The optical properties of this fabricated fibre are illustrated in Figure (2.10), where the core diameter was set to 7 μm with pitch of 2.7 μm. Figure 2.10(A) illustrates the transmission spectra of a 100 m (blue curve) and 50 m long segment respectively. The loss spectrum is illustrated in Figure 2.10(B) with a minimum loss figure of ~ 75 dB/km at ~ 1090 nm. This is recorded using the cutback method using a white light source. The transmission bandwidth spans from 1018 nm to 1203 nm. The location of the transmission bandwidth is especially tailored to guide light at 1064 nm and the first rotational Stokes at wavelength 1135 nm. This is important practically for experiments performed in Chapter 5 and Chapter 7.
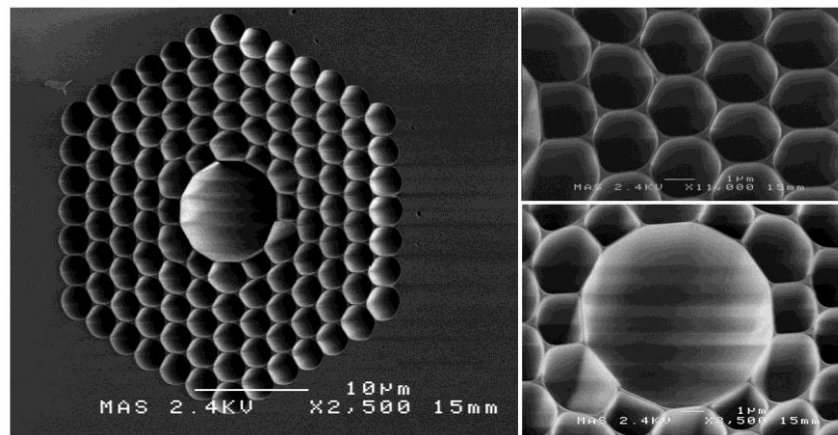
Figure 2.9: SEM of fabricated PBG HC-PCF guides at 1064 nm.
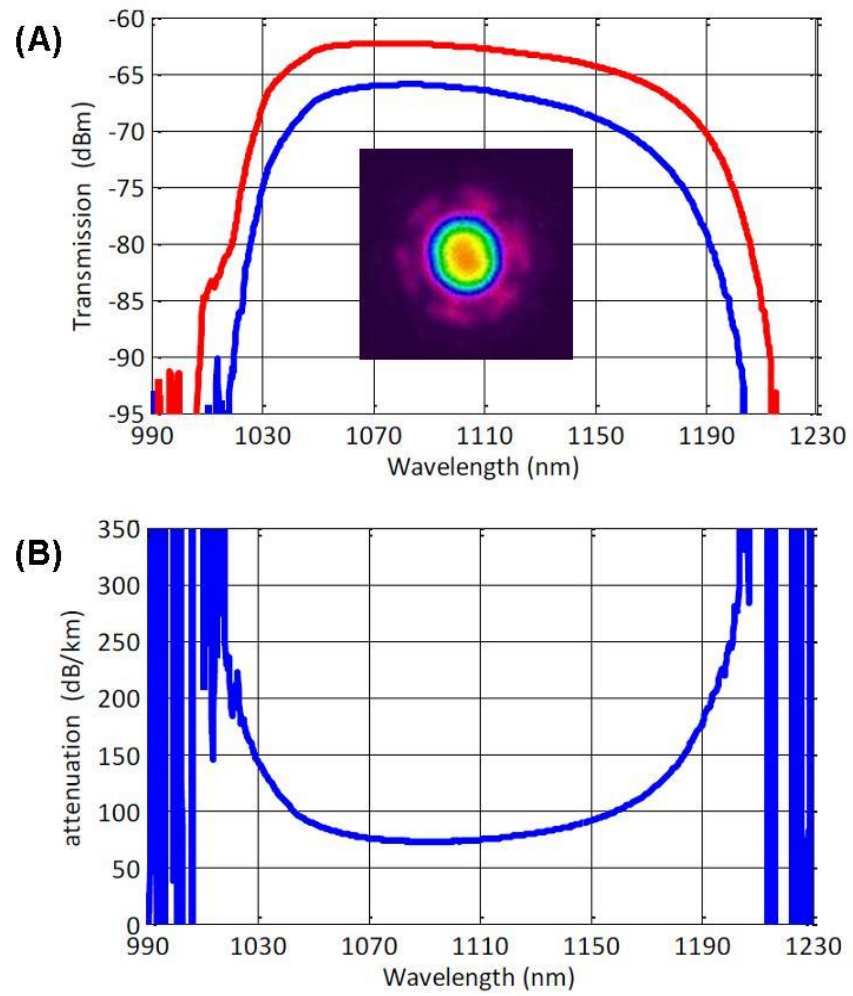
Figure 2.10: (A) Fabricated fibre transmission for 100 m (blue curve) and 50 m (red curve), inset illustrates the recorded modal content profile. (B) The measured loss from the fabricated PBG HC-PCF.

2.5 Summary

The guidance mechanism of PBG HC-PCF using the photonic tight binding model has been reviewed. In this Chapter we covered the fabrication process of PBG HC-PCF and showed results achieved for fabricating specially designed fibre to guide at the pump and the first order Stokes line which is an important element of the HC-PCF waveform synthesiser as demonstrated in Chapter 5 and Chapter 7.

References

[1] E. Yablonovitch, "Inhibited Spontaneous Emission in Solid-State Physics and Electronics," *Phys. Rev. Lett.*, vol. 58, no. 20, pp. 2059–2062, May 1987.

[2] S. John, "Strong localization of photons in certain disordered dielectric superlattices," *Phys. Rev. Lett.*, vol. 58, no. 23, pp. 2486–2489, Jun. 1987.

[3] P. St. J. Russell, private paper (1991).

[4] T. J. Birks, T.A. Roberts, P.J. Tussell, P.St.J Atkin, D.M. and Shepherd, "Full 2-D photonic bandgaps in silica/air structures - Electronics Letters," *Electron. Lett.*, vol. 31, no. 22, pp. 1941–1943, 1995.

[5] R. F. Cregan, B. J. Mangan, J. C. Knight, T. A. Birks, P. St. J. Russell, P. J. Roberts, and D. C. Allan, "Single-Mode Photonic Band Gap Guidance of Light in Air," *Science*, vol. 285, no. 5433, pp. 1537–1539, Sep. 1999.

[6] F. Couny, F. Benabid, P. J. Roberts, M. T. Burnett, and S. A. Maier, "Identification of Bloch-modes in hollow-core photonic crystal fiber cladding," *Opt. Express*, vol. 15, no. 2, pp. 325–338, 2007.

[7] N. M. Litchinitser, A. K. Abeeluck, C. Headley, and B. J. Eggleton, "Antiresonant reflecting photonic crystal optical waveguides," *Opt. Lett.*, vol. 27, no. 18, pp. 1592–1594, 2002.

[8] M. A. Duguay, Y. Kokubun, T. L. Koch, and L. Pfeiffer, "Antiresonant reflecting optical waveguides in SiO2- Si multilayer structures," *Appl. Phys. Lett.*, vol. 49, no. 13, 1986.

[9] N. D. Ashcroft, Von N. and Mermin, "Solid State Physics. Holt, Rinehart and Winston, New York 1976, XXII," *Phys. unserer Zeit*, vol. 31, no. 1, p. 33, 1978.

[10] F. Benabid, "Hollow-core photonic bandgap fibre: new light guidance for new science and technology.," *Philos. Trans. A. Math. Phys. Eng. Sci.*, vol. 364, no. 1849, pp. 3439–62, Dec. 2006.

[11] F. Benabid, "Hollow-core photonic bandgap fibre: new light guidance for new science and technology.," *Philos. Trans. A. Math. Phys. Eng. Sci.*, vol. 364, no. 1849, pp. 3439–62, Dec. 2006.

[12] F. Benabid, G. Bouwmans, J. Knight, P. Russell, and F. Couny, "Ultrahigh Efficiency Laser Wavelength Conversion in a Gas-Filled Hollow Core Photonic Crystal Fiber by Pure Stimulated Rotational Raman Scattering in Molecular Hydrogen," *Phys. Rev. Lett.*, vol. 93, no. 12, p. 123903, Sep. 2004.

[13]   F. Couny and F. Benabid, "Optical frequency comb generation in gas-filled hollow core photonic crystal fibres," *J. Opt. A Pure Appl. Opt.*, vol. 11, no. 10, p. 103002, Oct. 2009.

[14]   R. Amezcua-Correa, N. G. Broderick, M. N. Petrovich, F. Poletti, and D. J. Richardson, "Optimizing the usable bandwidth and loss through core design in realistic hollow-core photonic bandgap fibers.," *Opt. Express*, vol. 14, no. 17, pp. 7974–85, Aug. 2006.

[15]   R. Amezcua-Correa, F. Gerome, S. G. Leon-Saval, N. G. R. Broderick, T. A. Birks, and J. C. Knight, "Control of surface modes in low loss hollow-core photonic bandgap fibers," *Opt. Express*, vol. 16, no. 2, pp. 1142–1149, 2008.

[16]   Y. Y. Wang, P. S. Light, and F. Benabid, "Core-Surround Shaping of Hollow-Core Photonic Crystal Fiber Via HF Etching," *Photonics Technology Letters, IEEE*, vol. 20, no. 12. pp. 1018–1020, 2008.

[17]   R. J. Heeman, H. P. Godfried, and W. J. Witteman, "Threshold and conversion experiments on seeded stimulated Raman scattering," *Appl. Phys. B*, vol. 60, no. 5, pp. 479–484, 1995.

[18]   F. De Tomasi, D. Diso, M. R. Perrone, and M. L. Protopapa, "Stimulated rotational and vibrational Raman scattering by elliptical polarized pump radiation," *Phys. Rev. A*, vol. 64, no. 2, p. 23812, Jul. 2001.

[19]   F. Benabid, G. Antonopoulos, J. C. Knight, and P. S. J. Russell, "Stokes amplification regimes in quasi-CW pumped hydrogen- filled hollow-core PCF." *Phys. Rev. Lett.*, vol. 95, no. 21, p. 123903, Sep. 2005.

[20]   F. Couny, F. Benabid, and P. Light, "Subwatt Threshold cw Raman Fiber-Gas Laser Based on H2-Filled Hollow-Core Photonic Crystal Fiber," *Phys. Rev. Lett.*, vol. 99, no. 14, p. 143903, Oct. 2007.

Chapter 3

Enhanced Inhibited Coupling Kagome Hollow Photonic crystal Fibre

In this chapter, the recent development made towards the understanding of the guiding mechanism of Kagome lattice hollow core photonic crystal fibre (HC-PCF) via Inhibited Coupling (IC) is presented. A record loss Figure of ~ 17 dB/km at 1 μm has been achieved. The effect of the hypocycloid core shape on confinement loss theoretically and experimentally is presented. A systematic theoretical and experimental study on the effect of the number of cladding rings upon the confinement and bending loss in Kagome HC-PCF is presented[1].

---

[1] This work was a team effort. The author was involved in the fibre fabrication, characterisation and data processing.

3.1 Introduction

Although the triangular-lattice PBG guiding HC-PCF has outstanding transmission performance, it suffers from some drawbacks such as narrow transmission bandwidth, strong optical overlap between core-guided modes and the cladding silica, and the presence of surface modes. Such limitations exclude the implementation of PBG HC-PCF for a large number of applications requiring, for example, broadband guidance, guidance in the visible or UV or single modedness over a reasonably modest spectral bandwidth (e.g. over 10 nm). An example of such a restriction is one of the aims of this work, which is to generate and guide a multi-octave optical comb.

In 2002, and in parallel to the report of low loss PBG HC-PCF by Corning, an alternative HC-PCF, based on a large pitch Kagome lattice, has been reported by Benabid *et al*. [1]. This fibre guides over extended frequency ranges and its lattice structure consists of tessellating hexagons and triangles as shown in Figure 3.1 This type of structure has been shown to support low-loss guidance over a broad spectral range, with a typical loss in the order of 1 dB/m in the near-IR and below 2 dB/m in the visible [2]. These loss figures unfortunately remain high for efficient SRS, especially when the aim is to have an ultra-broad spectrum.

Despite the outstanding transmission bandwidth obtained using large pitch fibre, the cladding structure does not exhibit photonic bandgaps. Instead, the guidance in such fibres is attributed to the "inhibited coupling" between the core modes and cladding modes. The model proposed by Benabid, was reported only in 2007 [3]. Here, the guidance occurs with the cladding no longer requiring bandgap in the core mode $k\Lambda - n_{eff}$ space, but the structure and its dimension are engineered such that the cladding supports a continuum of modes whose overlap integrals (i.e. transverse phase matching) with the core modes is strongly reduced. In the case of air-silica HC-PCF, this situation can

occur if the cladding modes are strongly confined in the cladding thin silica-web and exhibit very fast transverse oscillations (i.e. high azimuthal-like number) [7]. In the sense that a fibre PBG is defined by the absence of phase-matched cladding modes to transfer light outward from the core, the surrounding cladding of IC guiding fibres acts as a quasi-PBG over the core mode $k\Lambda - n_{eff}$ space. It is noteworthy that such a strong mismatch can occur even if the cladding-mode and core-mode have the same effective index [7]. This model is akin to that of a bound or quasi-bound state in a continuum predicted by Von Neumann and Wigner within the context of quantum mechanics or condensed matter physics [4] Consequently, Kagome HC-PCF is the first photonic manifestation of a bound or quasi-bound state in a continuum.
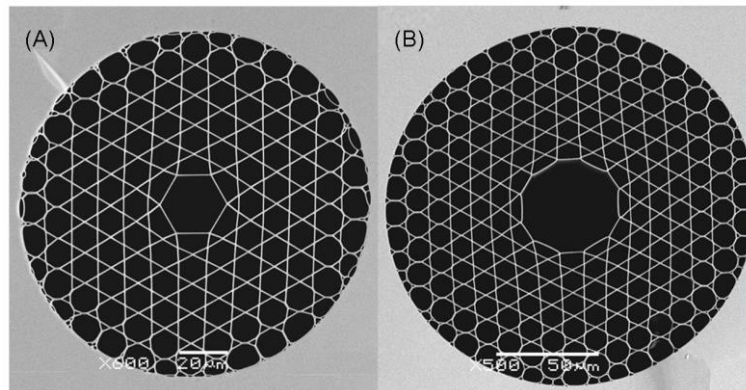
Figure 3.1: Scanning electron micrograph (SEM) for Kagome lattice HC-PCF (A) 1 cell, (B) 7 cell defect fibre.

Figure 3.2 illustrates the above. The density of photonic state (DOPS) plot of Kagome lattice clearly illustrates the absence of a photonic bandgap for normalised frequency below 160. Instead, the cladding structure exhibits a relatively low DOPS shown in the two regions I and III in Figure 3.2 where the transmission was expected to be high. The guided core mode and the cladding modes in this structure can co-exist even at the same (kΛ, n_{eff}). This situation can be observed experimentally by the near-field of the transmitted white light through a few centimetres of fibre, as illustrated in Figure 3.4(B). At high and

low transmission bands, Figure 3.3 shows a calculated core mode, cladding modes and unit-cell mode based on an infinite cladding structure and without a core defect. The core mode, at the transmission bands, is very well localised in the core, and exhibits only 0.05% of optical overlap with the cladding, compared to ~1% for a PBG HC-PCF. The cladding modes with similar effective index are primarily localised at silica struts with fast decay into the surrounding air regions. This means that there is very low spatial overlap between core and cladding modes.
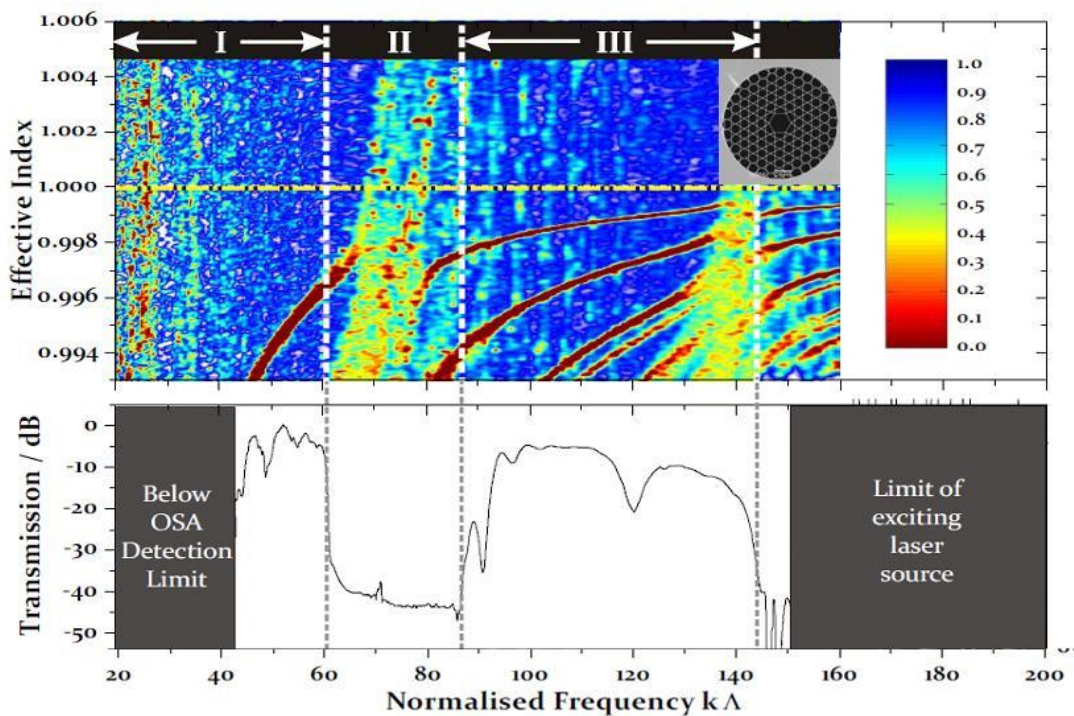
Figure 3.2: Top: Density of photonic states for Kagome lattice structure. The dashed line indicates the air line. (I) and (III) represent high transmission bands regions. (II) Represents low transmission band region. Bottom: Transmission spectrum of a fabricated Kagome lattice fibre of the same structure as simulation [5].

Finally and more importantly, these silica localised cladding modes exhibit very fast transverse oscillations (i.e. very large azimuthal-like number) enhancing thus the reduction in the overlap integral between the core and cladding modes by virtue of a strong transverse field mismatch between the fast phase oscillations observed within the glassy cladding field component and the slowly varying core field distribution, as illustrated in Figure 3.3. This

suggests the occurrence of bound or quasi-bound states (core modes) within a continuum (cladding modes), which is linked to a Von Neumann and Wigner proposal regarding the problem of electronic bound states at energies above the potential barriers [15].
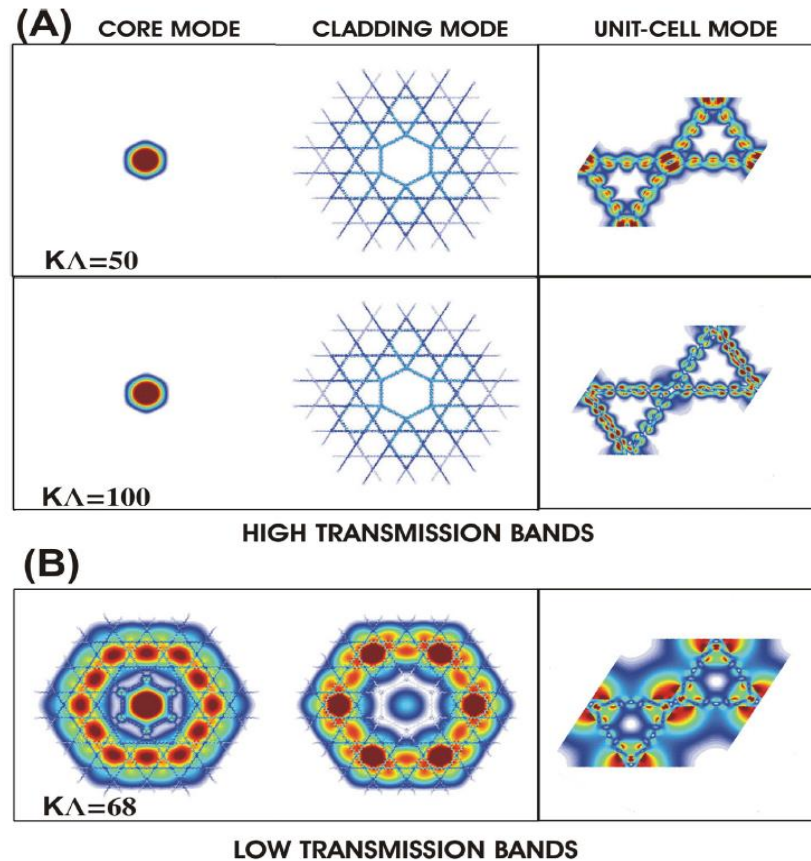
Figure 3.3: Nature of the Kagome lattice modes at (A) high transmission bands I and III where core and cladding modes are "inhibited" and (B) low transmission bands II with strong interaction between core and cladding modes [6].

3.2 IC in Hypocycloid core shape Kagome HC-PCF

The inhibited coupling (IC) guidance mechanism described above provided us with a predictive tool in designing HC-PC with better performance. Indeed, for a better transmission performance one needs photonic structures with overlap integral where a hollow core transverse field profile is minimised. This rule led

us to the development of a hypocycloid-like (or negative curvature) core-shape HC-PCF [7], [8].
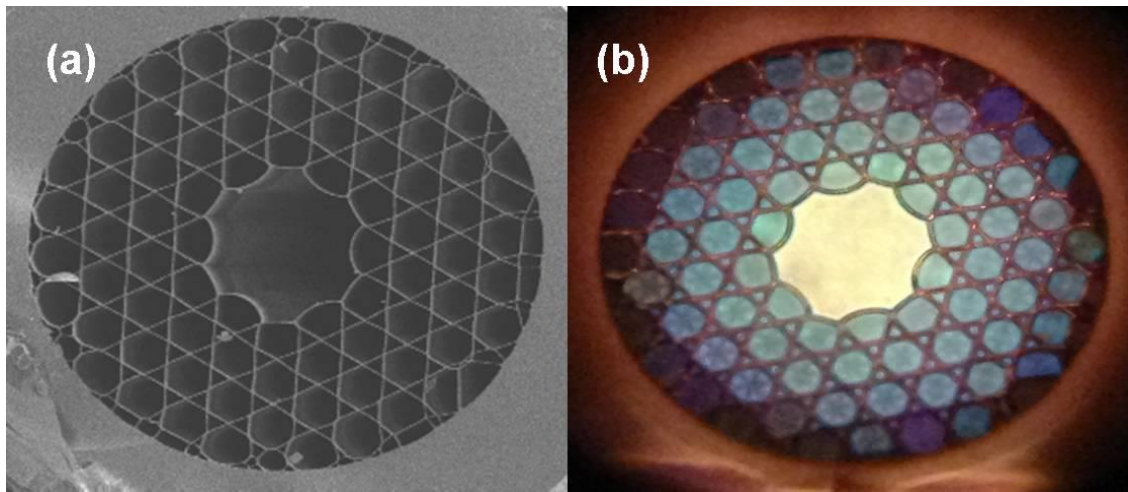
Figure 3.4: (A) Scanning electron micrograph (SEM) of hypocycloid core contour Kagome fibre, inset cladding lattice. (B) Optical micrograph.

Here, instead of having a conventional circular core shape, the core shape is modified to have a hypocycloid-shape (i.e. negative curvature) without causing any distortions to the first cladding ring (see Figure 3.4). This new approach has been very useful, whereby the transmission loss of this new design has been reduced by more than an order of magnitude (from ~ 1000 dB/km down to ~ 100 dB/km). Using this new design, a further reduction has been achieved where the loss dropped down to the level of ~ 30-40 dB/km [9].

Figure 3.5 schematically shows how the IC is enhanced in the case of a HC-PCF with a core-contour that has a hypocycloid-like shape compared to a circular-like contour, which was the shape for conventional 7-cell HC-PCF (see Figure 3.1 (B)). Here, the hypocycloid contour exhibits a set of alternating negative curvature cups with an inner radius R_{in} and an outer radius R_{out}. For this contour, the fundamental mode of the hollow core is that of HE_{11}, and whose mode-field diameter is that of a capillary or a circular core HC-PCF with a radius equal to R_{in} (see Figure 3.5 (b)). Based on this fact, it is readily noticeable that the overlap integral between the core-mode and the highly oscillating (i.e. high azimuthal-like number m) silica core-surround mode
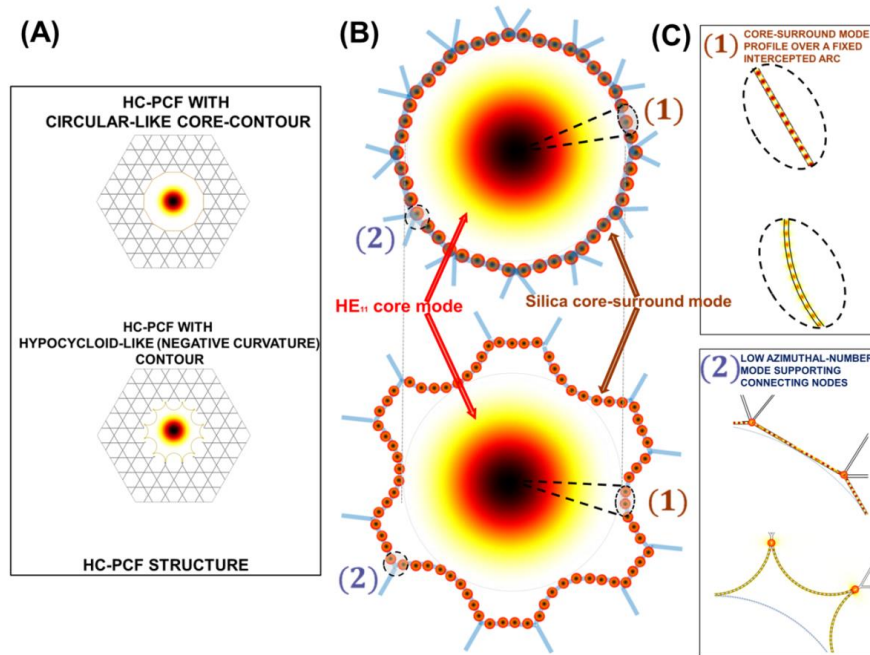
Figure 3.5: Schematic representation of the inhibited coupling enhancement for the case of hypocycloid (negative curvature) core-contour relative to the circular-like core-contour. (A) A circular core kagome HC-PCF (top) and a negative curvature core-contour kagome HC-PCF (bottom) supporting the same HE_{11} core mode. (B) Zoom-in of the fibre core highlighting the HE_{11} core mode, the silica core-surround mode with its fast transverse oscillations for both fibres. The circled and numbered regions are zoomed-in in (C). Region (1) shows the intensity transverse profile of the silica core-surround mode for both core-contour. Region (2) shows the connecting struts and their schematic low-azimuthal number modes and their position relative to the circle of radius Rin (blue dashed curve).

(cladding-mode) is strongly reduced via three avenues. Firstly, via a simple spatial overlap reduction argument. Indeed, at the circle of radius R_{in}, the core HE_{11} mode transverse profile intersects with only the tangent sections of the six inner-most cups for the hypocycloid contour whilst it intersects with the whole circle perimeter in the case of the circular contour. Secondly, the IC is enhanced by symmetry argument. Because of the larger perimeter of the hypocycloid, the silica core-surround modes exhibit higher m (see Figure 3.5 (c1)), and hence, by virtue of a stronger transverse phase-mismatch $\Delta\beta_{\perp} \propto m$ [7], the overlap integral between the core-mode and the cladding-mode is further reduced. Finally, the IC is enhanced by reducing the overlap between the core-mode with the low azimuthal number modes residing at the connecting nodes.

Indeed, the connecting nodes, which are inherent in HC-PCF structures and fabrication process (see Figure 3.5 (b) and Figure 3.5 (c2)), are "pushed away" from the core-mode in the case of hypocycloid contour. By this simple and intuitive picture, one can expect a further enhancement in IC and hence a stronger reduction in confinement loss.

This chapter covers an experimental and theoretical systematic study in designing a fabricating hypocycloid core contour Kagome HC-PCF with different core-contour negative curvatures and with different cladding ring numbers with the aim to firstly further corroborate the intuitive model described below. Secondly, to optimize the contour curvature for the lowest loss possible, and finally to further our understanding of IC by assessing the role of the cladding in the confinement loss.

3.3 Core-contour negative effect on IC

In this section we explore the effect of arc negative curvature of the hypocycloid core along with that of the cladding on the confinement loss in this Kagome HC-PCF. In this work, a detailed account on experimental and numerical work showing the influence of the arc curvature of the hypocycloid-core on the loss figure of the fibre and on its modal properties. In section 3.3.1, we define the arc curvature and present the theoretical and experimental loss spectra for different arc curvatures. In section 3.3.2, we show the evolution with arc curvature of the optical power overlap between the core mode with the cladding silica struts, and of the core modal content. Finally, we present the fabrication of fibre exhibiting the largest arc curvature and a record loss level of 17 dB/km at 1064 nm. This work is published at [11].

3.3.1 Loss evolution with the arc curvature

Figure 3.6 (a) shows a typical example of hypocycloid-like core HC-PCF with a Kagome lattice cladding. In the case considered here, the hypocycloid core contour results from 7 missing cells of a triangular arrangement of circular tubes. Consequently, the core contour is formed by two alternating arcs, which result in a small circle with radius R_{in} that is tangent with the 6 most inward arcs, and a larger circle with radius R_{out} that is tangent with the 6 most outward arcs. The curvature of the hypocycloid-like core is quantified through the parameter noted b (see Figure. 3.6 (b)). The latter is defined as $b=d/r$, where d is the distance between the top of the arcs and the chord joining the nodes connecting the inward arc to its two neighbouring ones and r is half the chord-length. With this definition, the "classical" Kagome fibre with a "quasi" circular core corresponds to $b=0$, whilst $b=1$ corresponds to a core contour with circular shaped arcs. For $0<b<1$ and $b>1$, the inward arcs have an elliptical shape whilst the outward ones are set to have a circular shape.
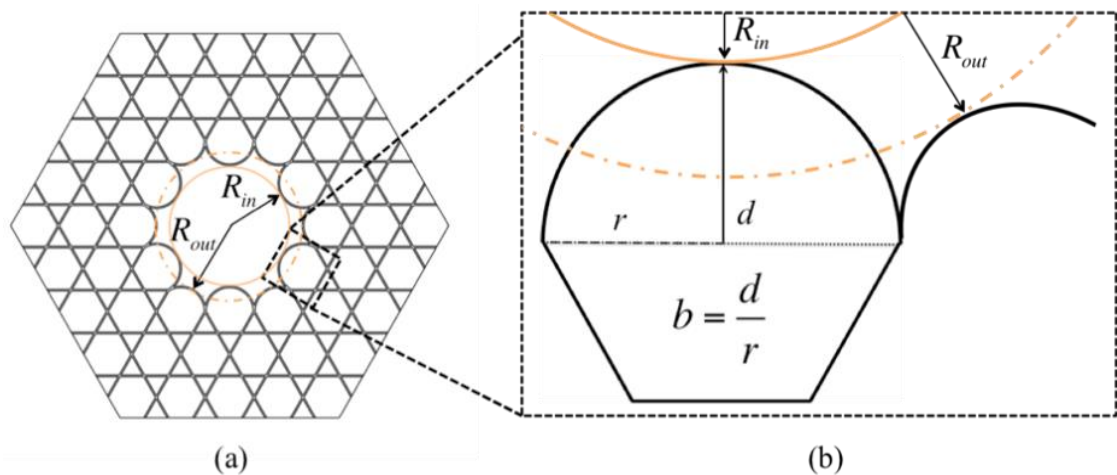
Figure 3.6: (a) Structure of a hypocycloid-like core HC-PCF. (b) Definition of the parameters quantifying the curvature of the core arcs [11].

Figure 3.7 (a) shows the calculated loss spectra of the HE_{11} core mode for a hypocycloid-like core Kagome-lattice HC-PCF with different arc curvatures. The numerical results have been obtained through the modal solver of the

commercial software Comsol Multiphysics 3.5 based on the finite-element method, with an optimized anisotropic phase-matching layer (PML) [12], and which was already successfully applied to the analysis of loss and dispersion properties of several IC HC-PCFs [13], [14]. In the simulations, all the HC-PCFs have a 7-cell core defect and a Kagome-latticed cladding of 3 rings, and with strut thickness t equal to 350 nm. The HC-PCF structure has been studied for core arcs varying from $b=0$ to $b=1.5$. Furthermore, the core inner diameter (i.e. $2 \times R_{in}$) has been kept constant and equal to 60 μm throughout (see Figure 3.7 (b)). Consequently, this has an effect on the pitch Λ of the cladding which changes by

$$\Lambda = \frac{\left[R_{in} + t\left(1 - \dfrac{b}{3}\right)\right]}{\sqrt{3} - \dfrac{b}{2}} \qquad (3.1)$$

The calculated spectra clearly show the strong influence of the inward arc curvature on the loss confinement, and where the loss level drops from ~1000 dB/km in the case of a "quasi" circular core (i.e. $b=0$) to lower than the 1 dB/km for hypocycloid core with $b \geq 1$. For a given structure, the loss spectrum exhibits a high loss spectral-region near 700 nm; corresponding to the resonance of the fundamental core-mode with the glass struts, and occurring at wavelengths λ_j given by the expression $\lambda_j = \left(\dfrac{1}{j}\right) 2t \sqrt{n_{gl}^2 - 1}$, where j is an integer, n_{gl} is the refractive index of the glass forming the cladding structure and t is the thickness of the glass web which is assumed to be uniformly constant throughout the cladding structure [6]. Outside these spectral regions (i.e. the spectral ranges where the silica cladding structure is anti-resonant), the confinement loss exhibits an exponential-like decrease with the increase in the curvature parameter b. Figure 3.7 (c) illustrates this trend for one wavelength in the first transmission band (λ_j = 1000 nm), and one wavelength at the second

order transmission window (λ_j = 500 nm). It is noteworthy that all the confinement loss spectra exhibit relatively strong oscillations. These are attributed to resonant structural cladding features such as corners[6], and in some cases are Fano resonances [15]. These oscillations, which are now a subject of ongoing work, are beyond the current scope of this thesis.
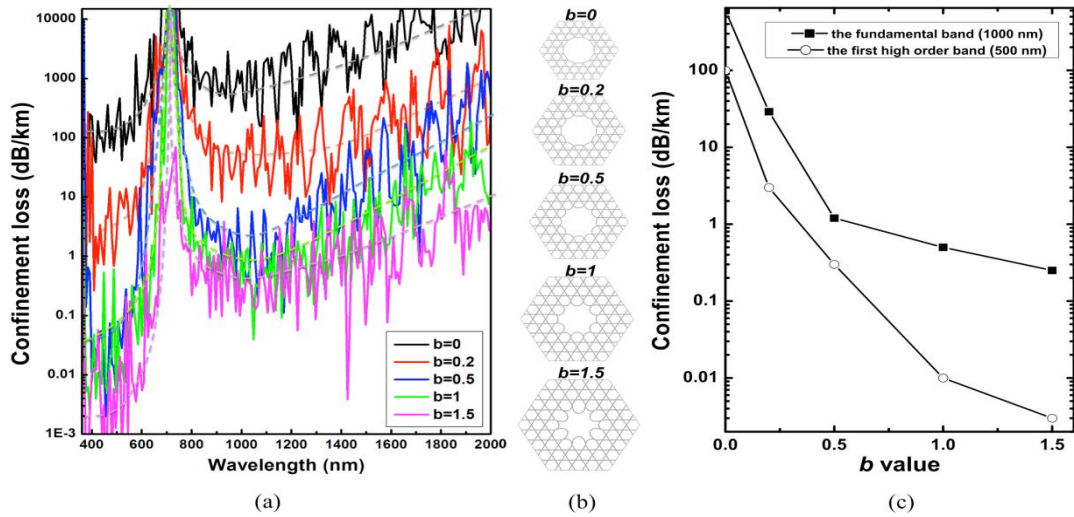
Figure 3.7: (a) Kagome-latticed HC-PCF computed confinement loss evolution with the arc curvatures (b=0, 0.2, 0.5, 1 and 1.5). The dashed lines are added for eye-guidance. (b) The fibre structure transverse profile for the different b values. (c) Evolution with b of the transmission loss Figures for 1000 nm (joined solid squares) and for 500 nm (joined open circles) wavelengths [11].

This trend of loss reduction with the increase in b has been experimentally confirmed with the fabrication of four Kagome-latticed fibres with different b. Figure 3.8 (a) shows scanning electronic microscope (SEM) images of the fibres around the fibre core. Figure 3.8 (b) shows the loss spectra in the fundamental band (i.e. for wavelengths longer than roughly twice the thickness of the silica struts [6]), obtained by a cutback measurement using a supercontinuum source, and fibre lengths were in the range of 50 to 70 m. The loss base-line level was found to be ~1300 dB/km for b=0, 400 dB/km for b=0.39, 200 dB/km for b=0.68, and 40 dB/km for b=0.75, which is in qualitative agreement with the theoretical calculations. Care was taken in the fibre design and fabrication so as to have all the fibres with the same strut thickness of 350 nm, core diameter of 60 μm and a

pitch of 21 μm within a measured relative uncertainty of less than 10%. Figure 3.8 (c) shows, for a given wavelength of 1500 nm, a comparison between the calculated confinement loss and the measured transmission loss when b is increased. The higher level in the measured loss relative to the numerical results is likely due to the cladding imperfections such as non-uniform strut thickness.
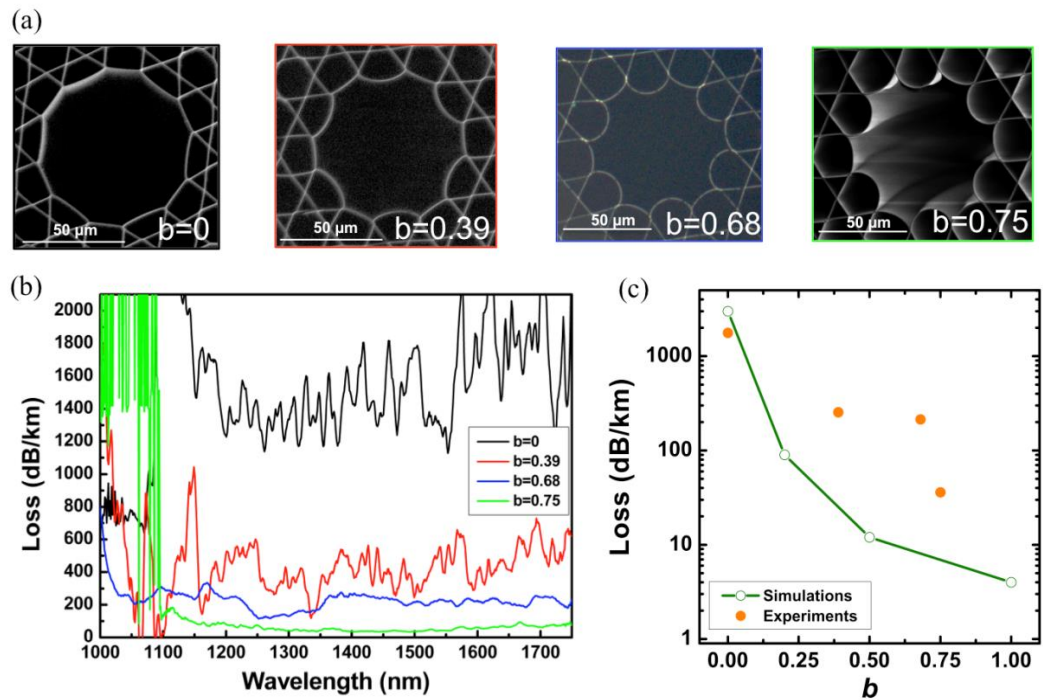
Figure 3.8: SEM images (a) and measured loss spectra (b) of fabricated hypocycloid-core Kagome-latticed HC-PCFs with different b. (c) Experimental and theoretical evolution of the transmission loss with the b at 1500 nm [11].

3.3.2 Power overlap and modal content "cleansing" with increasing "*b*"

Figure 3.9 shows the evolution of the mode profile for the core fundamental mode (FM) HE_{11} with the increase of *b*. As above, the inner radius of the fibre R_{in} is still kept constant at 30 μm throughout all the simulations. We observe that the change of the curvature does not affect the mode profile (see Figure. 3.9 (a)). More remarkably, the mode-field diameter MFD ($(1/e)^2$ diameter of the

modal transverse profile) shows little change when b is altered from 0 to 1.5. This is illustrated by the radial profile of the mode along the two axes of the core-symmetry (i.e. along the axes of R_{in} and R_{out} respectively (see Figure. 3.6)), and where the MFD radii are shown in a vertical dashed line.

In order to gain further insight into the properties of the HE_{11} in this hypocycloid-core Kagome HC-PCF, it is useful to compare its MFD to that of a dielectric circular capillary whose properties such as dispersion and guided field profile takes simple and analytical forms [16]. For example in the case of a dielectric capillary with a bore radius R_{cap}, and a dielectric index n_g, the effective index and the MFD of the fundamental core-mode HE_{11} are given by

$n_{eff} = \sqrt{n_g^2 - (\lambda \times (2.405/2\pi R_{cap}))^2}$ and $MFD_{cap} = 0.7285(2R_{cap})$ respectively [16]. Here λ is the wavelength.

Figure 3.9(b) shows the relative error, $(MFD_{cap} - MFD_{HCPCF})/MFD_{cap}$ when the hypocycloid-core Kagome HC-PCF mode field-diameter, MFD_{HCPCF}, is approximated to that of a capillary, MFD_{cap}, with its radius $R_{cap}=R_{in}$. Here, the MFD_{HCPCF} is deduced from the numerically calculated effective area A_{eff} by $MFD_{HCPCF} = 2\sqrt{A_{eff}/\pi}$.

The results indicate that within a maximum relative error of less than 7%, one could approximate the MFD of hypocycloid-core HC-PCF to that of a capillary with an effective radius equal to that of the inner radius of the hypocycloid. Similarly, the dispersion of the HE_{11} mode deviates little from that of the capillary when the curvature parameter b is increased from 0 to 1.5. Figure 3.9(c) shows the HE_{11} mode effective index spectra for different b along with that of a capillary with a bore radius of 30 µm. The dispersion traces show that the shorter the wavelength the closer the traces are. Furthermore, outside the resonance with the glass region, one could qualitatively approximate the effective index of hypocycloid-core Kagome HC-PCF fundamental mode to that

of a dielectric capillary of bore radius equal to the inner radius of the hypocycloid-core.
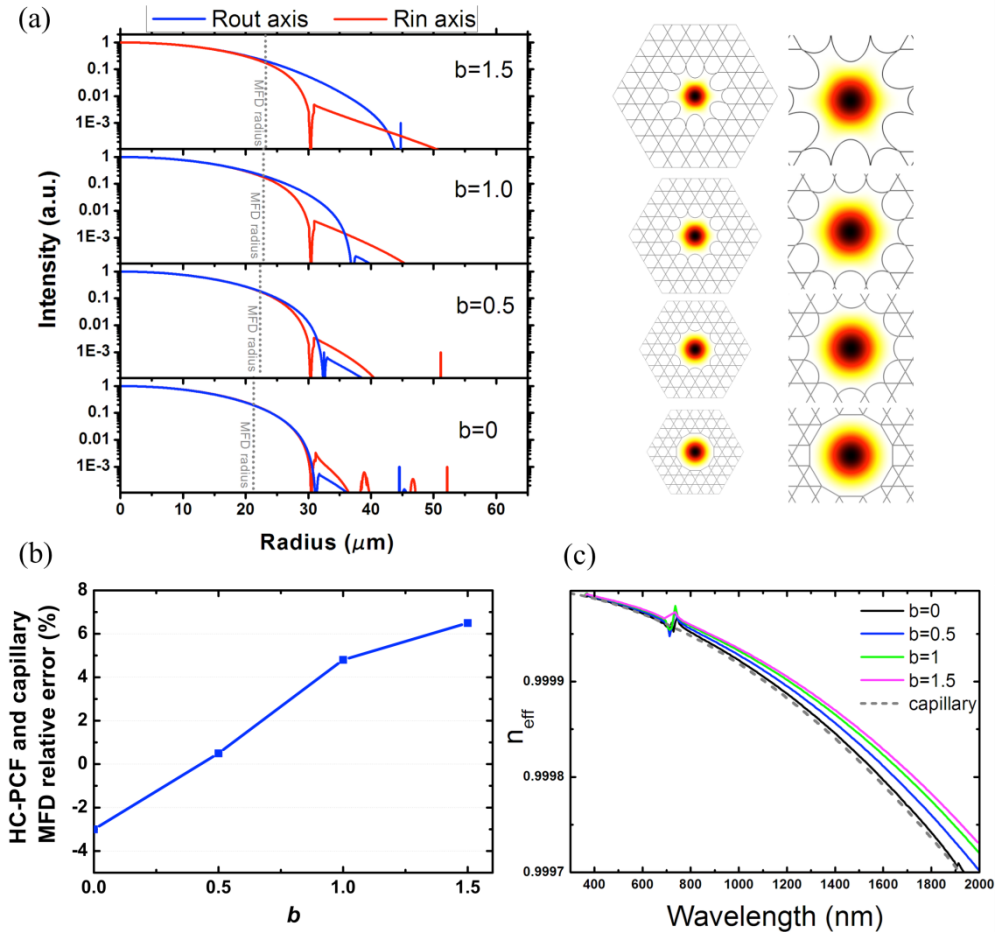
Figure 3.9: (a) Evolution with b of HE$_{11}$ mode profile at 1000 nm: Radial profile of the mode intensity along the two symmetry axes (lhs), and the 2D transverse intensity profile (rhs). (b) Evolution with b of the relative error in the MFD of hypocycloid-core Kagome HC-PCF when approximated to that of a capillary, at 1000 nm. (c) Effective index spectrum of a capillary with Rcap=30 µm (grey dashed curve), and for a 30 µm inner radius hypocycloid-core Kagome HC-PCF with different b (solid curves) [11].

A direct consequence of the above-mentioned properties of the hypocycloid-core Kagome HC-PCF fundamental core-mode is that its spatial optical power overlap (SPOPO) with the silica core-surround is reduced when the core shape is changed from a circular contour to one of a hypocycloid.. This is expected from a simple assessment of the geometrical overlap between the zero-order Bessel shaped HE$_{11}$ mode and the core-contour at radius R_{in} [9], [17]. A numerical corroboration is shown in Figure 3.10, which gives, for a

wavelength of 1 µm, the evolution with *b* of the fractional optical power residing in the cladding silica web for the core fundamental mode HE_{11} and the first four higher order modes (HOM) (represented only by one curve for better visibility as the curves for these four HOM are so closed to each other), which consist of the two polarizations of the HE_{21} mode, the TE_{01} and TM_{01} modes. The fractional power in silica η was deduced numerically using the following expression:

$$\eta = \frac{\iint_{S_{Si}} p_z ds}{\iint_{S_{\infty}} p_z ds} \tag{3.2}$$

where p_z is the longitudinal component of the Poynting vector, while S_{Si} and S_{∞} indicate integration over the silica region and the whole cross section, respectively. The results show that the relative power ratio for the HE_{11} decreases by a factor of ~10 when *b* is increased from 0 to 0.5, and then decreases at a lower rate when *b* is increased from 0.5 to 2. The HOM fractional power in silica follows the same trend for the b in the range of 0 - 1.5. However for *b*>1.5 the overlap with silica strongly increases. This is due to the coupling between the HOM core modes and the inner arc hole modes (HM), that is the modes confined inside the holes of the large arcs surrounding the core. Figure 3.9 (a) shows spectra of the effective index difference between the HOMs and the HM for *b* =1.0, *b* =1.5 and *b* =1.9. The curves clearly show that increasing *b* from 1 to 1.9 reduces the index difference between the HOM and the HM, thus favouring coupling between them by virtue of phase matching.

Indeed, as *b* increases, the whole size of the large arc increases, and thus the HM effective index increases and approaches that of the fibre core. This is also illustrated in the inset Figure 3.11 which shows the intensity profile evolution of one of the HOM core modes (here HE_{21} mode) at 1 µm for *b* =1.0, *b* =1.5 and *b* =1.9. For *b* =1.9, the HE_{21} intensity profile differs strongly from those in the case

of b =1.0 and b =1.5, and show a strong hybridization with the HM. This has already been experimentally observed in [6] and further investigated in [18], [19]. As a result, since the HMs are much less confined than the HOM, the hybridization causes an increase in both the fraction power in silica and the confinement loss of HOM. The coupling between the HOM and HM is also indicative of the strong coupling inhibition between the core modes and the silica strut modes [6]. The decrease of the SPOPO between the fundamental core modes and the silica core-surround in the case of the hypocycloid-shaped core HC-PCF corroborates the qualitative picture reported in [7], [9], [18]. This also explains the high power handling demonstrated recently in [20].
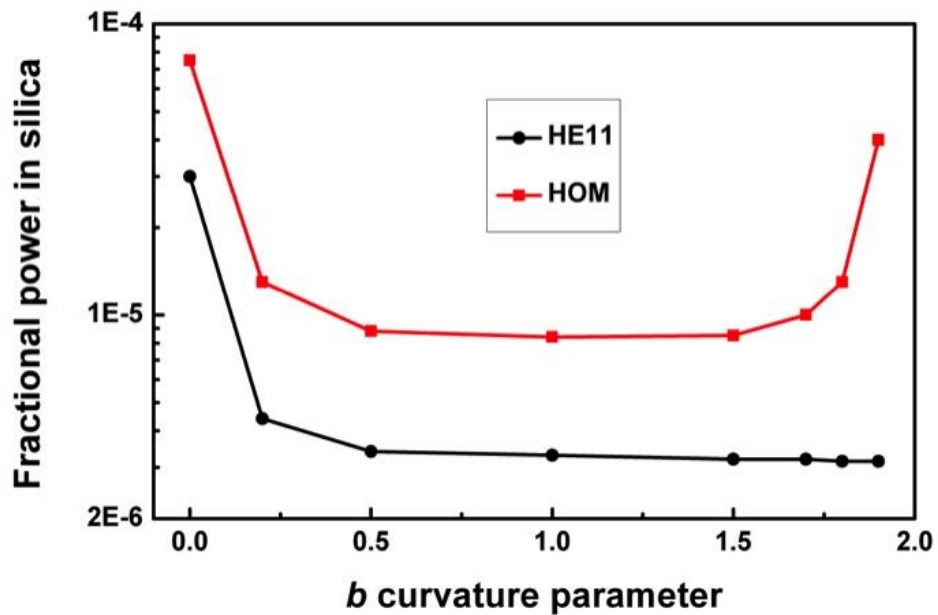
Figure 3.10: The fractional optical power residing in the cladding silica, for a wavelength of 1 μm, for the core fundamental mode HE_{11} (black trace) and for the first four higher order modes: the two polarizations of the HE_{21} mode, TE_{01}, TM_{01} (red curve)[11].
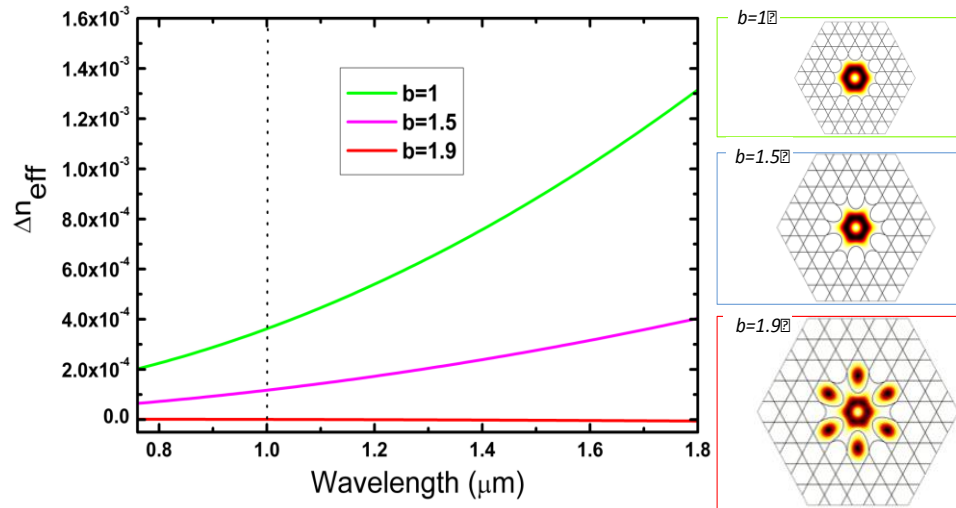
Figure 3.11:   Evolution with b of the effective index difference between the core first higher order modes (HOM), and the large arc mode (HMs) for b=1.0, b=1.5 and b=1.9. In inset: intensity profile of the HE_{21} mode at 1 µm for the different b values [11].

It is noteworthy, that the decrease in the spatial overlap between the core guided modes and silica core-surround is not the only mechanism behind the confinement loss decrease by increasing *b*. Indeed, this can be observed in the decrease rate difference between the strong confinement loss (Figure 3.7 (c)), and that of the SPOPO when b is increased above 0.5 (Figure 3.10). Furthermore, in addition to the SPOPO decrease between the core modes and those of the core silica-surround, the increase of *b* also results in a reduction of the overlap integral between the fibre core-modes and those of the silica core-surround via symmetry-mismatch (i.e. transverse phase-mismatch).

Figure 3.11 summarizes the evolution around 1 µm wavelength of a representative silica core-surround mode when b is increased from 0 to 1.9 whilst keeping R_{in} to 30 µm. Figure 3.11(a) shows the intensity profile of a mode with closest effective index to that of HE_{11} mode for different *b*. For each *b*, the profile shows the expected silica-residing mode with a fast-oscillating transverse-phase[6]. The latter is quantified by an azimuthal-like number *m*, which corresponds to the number of phase oscillations along the silica core-contour. Figure 3.11(b), which shows the evolution of *m* with *b* increase,

clearly indicates that as *b* is increased, *m* is increased exponentially, and subsequently the overlap integral between the core mode and the silica core-surround is strongly decreased. The increase in *m* with *b* results from the increase in the perimeter of the hypocycloid contour as *b* is increased, as is illustrated by the red trace in Figure 3.11(b). The net result of the azimuthal-like number increase is an enhanced coupling inhibition between the fundamental core mode and the cladding modes, and subsequently a decrease in the experimentally observed confinement loss.

(a)   (b)
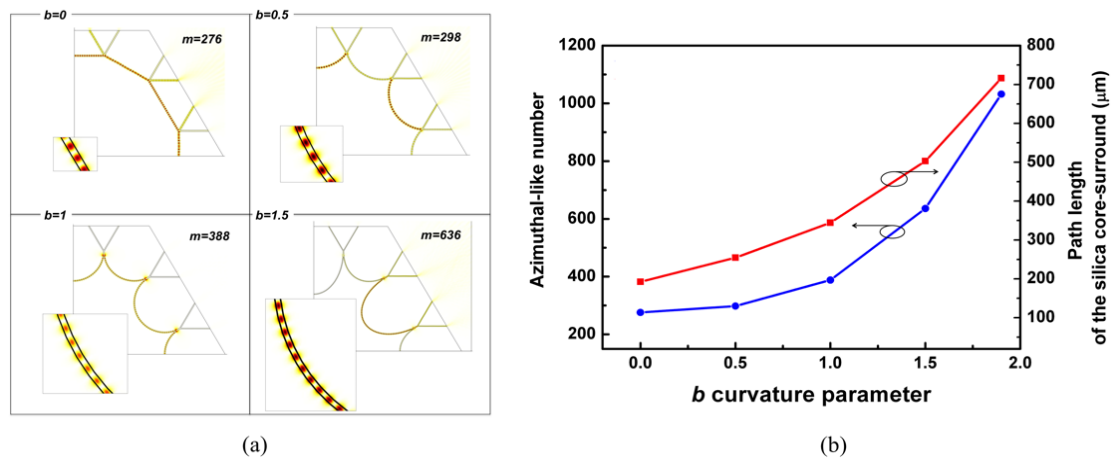
Figure 3.11: (a) Profile of a representative silica core-surround mode for *b*=0 (top left), *b*=0.5 (top right), *b*=1 (bottom left) and *b*=1.5 (bottom right) at 1 µm. In inset: zoom-in of the cladding profile on a small section of the first inner arc. (b) Evolution of the azimuthal-like number m and the perimeter of the silica core-surround contour with *b* [11].

Finally, the increase of *b* carries a third merit as it involves the suppression of the higher order modes via propagation loss enhancement. Figure 3.12(a) shows the spectra loss for the four HOMs versus *b* at 1 µm wavelength (represented only by one curve for better visibility as the curves for these four HOM are so closed to each other). Unlike the HE_{11} loss, which keeps decreasing with *b*, the HOM confinement loss shows an increase for *b* larger than 0.5, which is due to the coupling with the HM as mentioned above. This explains the single modedness observed in [20]. Furthermore, the confinement loss "extinction-ratio" between the HE_{11} mode and the HOM increases from 0 dB for *b*<0.5 to 7 dB for *b* =1, reaching the notable figure of >100 dB for *b*=1.9. These results clearly show that in order to have near single-mode guidance, *b* should

be much higher than 0.5. This is illustrated experimentally by inspecting the near-field and far field of the output of a 1064 nm laser beam using 3m-long of two fabricated HC-PCFs with a b =0.39 and b =1 (see Figure 3.12(b)).
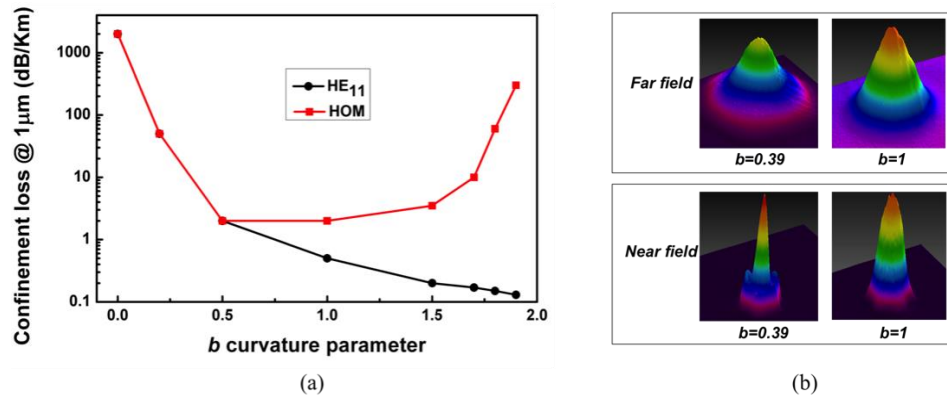
Figure 3.12: (a) Calculated spectra loss at 1 μm for the fundamental core-mode HE_{11} and for the first four higher order modes. (b) Measured fundamental core-mode near field and far field at 1064 nm for two fabricated fibres with b=0.39 and b=1 [11].

It is noteworthy that the HC-PCF with b =1 was obtained with a silica strut thickness of 1400 nm instead of t =350 nm, which is the thickness of all the fabricated fibres mentioned above. This was dictated by the difficulties in drawing thin strut HC-PCF with enhanced negative curvature. Indeed, in the above, the highest achieved b parameter without altering the desired structure was limited to 0.75. Furthermore, we experimentally observed that with such thin struts, the higher-order transmission bands exhibit stronger transmission loss (>1 dB/m) than what is numerically predicted [21]. We believe that this is due to an enhanced capillary wave effect, and hence the fibre core-wall surface roughness during the fibre draw. Further investigations are required to assess the source of the higher loss in the short wavelength (< 700 nm in the case of our 350 nm thick strut HC-PCF), and the feasibility of enhanced negative curvature with the stack-and-draw process used here.

In order to achieve higher values than this experimental limit whilst keeping the same fabrication process, a new design of fibre has been explored based on thicker struts so as to mitigate the induced surface roughness mentioned above,

and with the aim to optimize the loss for a wavelength around 1 μm. Numerical simulations show that ~1 dB/km loss-level could be obtained with thicker struts if b =1 could be experimentally achieved (see Figure 3.13(a)). The Figure shows calculated loss spectra for three different t values, t =350 nm, 800 nm and 1400 nm. Here the inner core radius has been set to be the same as the simulations above for the case of thinner struts (i.e. R_{in}=30 μm). An attenuation level of ~1 dB/km at 1 μm was numerically predicted for the three fibres but in the fundamental band for t =350 nm, in the second band for 800 nm and in the third for 1400 nm. It is noteworthy, that whilst thickening the struts would reduce the bandwidth of each transmission band, the fibre total bandwidth, unlike the PBG HC-PCF, remains unrestricted. Furthermore, this relative loss in bandwidth could be compensated by a more uniform strut thickness throughout the whole cladding structure, which narrows the high loss bands [6]. Figures 3.13(b) and 3.13(c) correspond to the loss spectra of two fabricated fibres with thicker struts t = 800 nm and 1400 nm respectively. A maximum arc curvature of 0.9 is obtained for t = 800 nm. In contrast with thin-strut fibres, which exhibit strong attenuation in the higher-order transmission band, a loss figure as low as 80 dB/km was achieved in the first high-order band. This result was further corroborated with the t = 1400 nm fibre in which the wavelength of 1 μm lies in the second higher-order band. With this fibre, an arc curvature as high as b =1 was successfully achieved, and a record loss fibre of 17 dB/km at 1064 nm was reached.
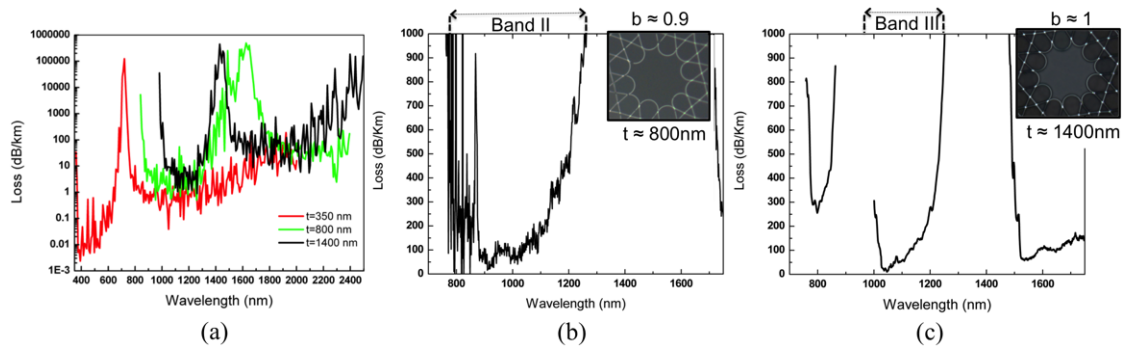
Figure 3.13: (a) Computed loss of Kagome-latticed HC-PCFs with arcs curvature b=1 for three strut thicknesses 350, 800 and 1400 nm; Measured loss of fabricated Kagome-latticed HC-PCFs with strut thickness (b) t=800 nm and (c) t=1400 nm. In inset, pictures of the core structures [11].

In order to put these results into perspective with the PBG guiding HC-PCF, Figure 3.14 compares the loss spectra of two hypocycloid Kagome HC-PCF with the same strut thickness (here 1400 nm) and same b (here 1) but with slightly different drawing parameters, with four state-of-art commercially available PBG guiding HC-PCF [22]. Three of the fibres set are 7-cell PBG guiding HC-PCF whose transmission window is centred at ~800 nm, 1000 nm and 1550 nm respectively (light grey filled curves). The fourth fibre is today's record 19-cell PBG guiding HC-PCF [23] (grey filled curve). The Figure shows that whilst one single IC guiding Kagome HC-PCF guides a much wider spectral window than PBG HC-PCF, its loss figures are comparable. As a matter of fact, the loss is lower for Kagome HC-PCF in the region near 1 μm and 800 nm, indicating thus that IC guiding HC-PCF could be a good alternative to PBG HC-PCF for ultra-low loss guidance HC-PCF.
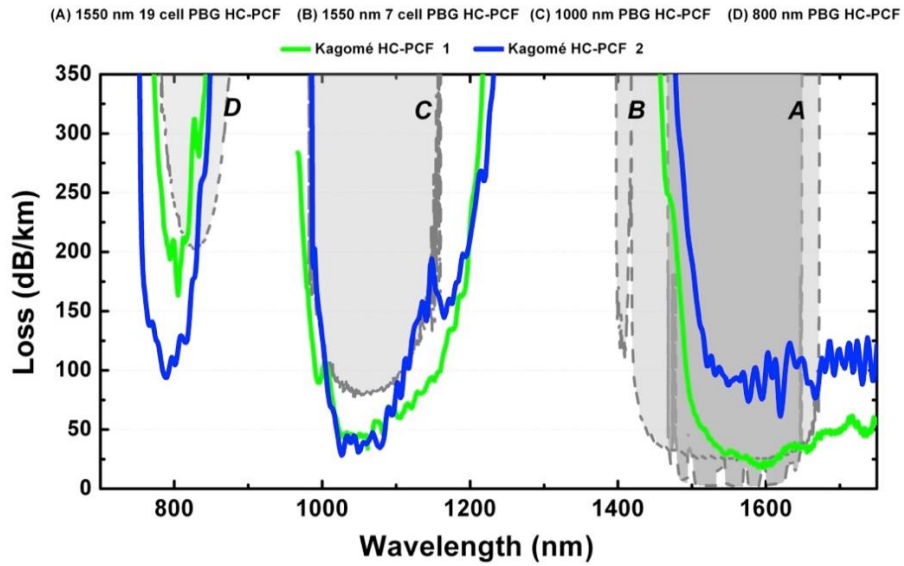
Figure 3.14: Comparison of the loss spectra of the current lowest loss 19-cell BPG HC-PCF centred at 1550 nm (A), and three state-of-art 7-cell PBG HC-PCF centred at 1550 nm (B), 1000 nm (C), and 800 nm (D) with the two different hypocycloid-core Kagome HC-PCF with b=1 (blue and green solid curves) [11].

3.4 Cladding number effect on confinement and bend loss

In this section an experimental and theoretical systematic study of the effect of the cladding ring number on confinement and bend losses in hypocycloid-core shaped Kagome cladding lattice HC-PCF is performed. Firstly, we report on how the transmission loss evolves with the cladding ring number in these fibres. Secondly, we investigate the bend loss dependence on the ring number, and finally we show how the cladding ring number affects the modal content and the physical mechanism underlying the bend loss. This work is published at [24].

3.4.1 Transmission loss evolution with cladding ring number

Figure 3.15(a) shows computed confinement loss (CL) spectra of Kagome cladding-lattice HC-PCF with different cladding ring-numbers. The fibres are taken to have a hypocycloid-shape core with a constant b curvature parameter of 0.3 (see section 3.3 for the definition of b), and a constant inner diameter of 32.5 μm. The thickness of the silica web forming the cladding is set to 450 nm and the pitch equal to 20 μm. The computation was carried out using a commercial software (COMSOL Multiphysics) based program on the finite-element-method (FEM) with an anisotropic perfectly matched layer [12], which was successfully applied to the analysis of loss and dispersion properties of several IC HC-PCFs [14]. The spectral range of the computed CL was limited to the first transmission band (i.e λ>900 nm) and spans from 900 nm to 2.4 μm. It is noteworthy that for a single ring structure the CL obtained with $b = 0.3$ negative-curvature core HC-PCF is lower than its circular single-ring counterpart (i.e. an anti-resonant ring) [20]. Indeed, here the loss in a single ring reaches a minimum of ~ 50 dB/km in the 1200-1400 nm spectral range, which is almost three orders of magnitude lower than that of a circular ring with comparable core-size and silica thickness [9]. This loss figure is in qualitative agreement with the ones experimentally observed in the fabricated single-ring hypocycloid-core HC-PCF [18], [25], and which was explained by the decrease of CL with increasing b [18]. Furthermore, the results show two distinct trends in the confinement loss evolution with the cladding ring number. Firstly, there is little overall variation in the confinement loss by increasing the cladding ring-number from two to four rings. This trend is similar to the one found with circular or hexagonal core Kagome HC-PCF [26]. For fibres with a ring-number of 2 or larger, the average base-line of the loss is about 20 dB/km in a 1200nm-1400nm spectral range. Secondly, the CL reduces significantly when the cladding ring number is increased from 1 (i.e. single-ring cladding fibre) to 2 (i.e. 2-ring fibre), with the average base-line loss figure dropping from 60 dB/km to 20 dB/km. In addition to these trends, the modulation depth of the peaks and dips that structure the CL spectrum is significantly increased with

the cladding ring-number. As a matter of fact some dips exhibit a CL of less than 2 dB/km, whilst for some peaks, the CL increases above 100 dB/km. Furthermore, the origin of such oscillations were attributed to the structural cladding features [6], and in some cases they exhibit behaviour akin to Fano resonances [15].
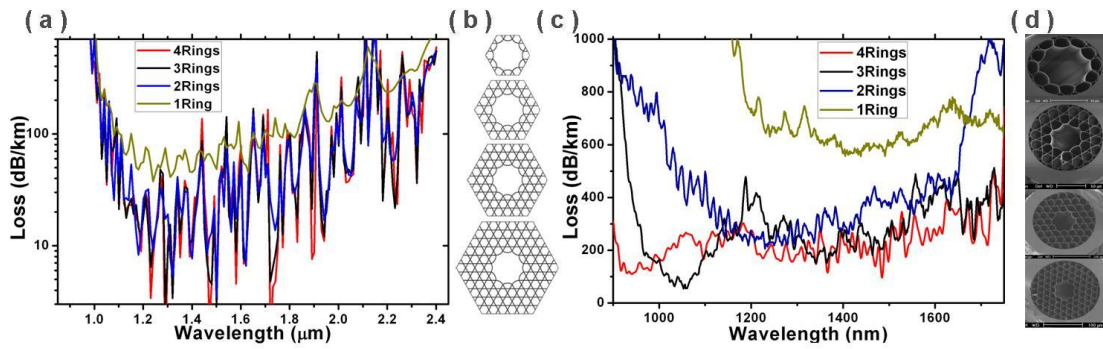
Figure 3.15: (a) Simulated loss spectra for four different cladding ring numbers; (b) Structure fibre profile, (c) Measured loss spectra for four fabricated hypocycloid-core Kagome HC-PCF (one, two, three and four cladding rings), and (d) corresponding SEM images [24].

The overall trends of the CL spectra are qualitatively corroborated experimentally. Figure 3.15(c) shows the measured loss spectra for four fabricated fibres with a ring-number varying from one to four. The fibres whose scanning electron micrographs are shown in Figure 3.15(d), were fabricated with similar pitch (~20 μm) to within a relative difference of less than 8%, and strut thickness (~450 nm), core diameter (~52 μm) and hypocycloid-core shape (b~0.45). Care was taken so the curvature of the hypocycloid-core arcs is kept the same for all the fibres and close to the computed one. Table 3.1 lists the physical parameters of each drawn fibre along with a representative loss figure measured at 1500 nm. The loss spectra of the fibres were obtained by a cut-back measurement on ~50 m long fibre. The curves of Figure 3.15(c) show that the four, three and two ring fibres present comparable loss figures; in the range of ~150 dB/km and 300 dB/km, which is in good qualitative agreement with the numerical results. Similarly, 600 dB/km loss level measured for the single-ring HC-PCF confirms the numerical results that the single-ring fibre contrasts with

the larger cladding ring-number fibres by a relatively higher transmission loss[9].

Table 3.1: Physical parameters of the fabricated hypocycloid-shaped core HC-PCF[24].

	b-curvature parameter	*Pitch (μm)*	*Silica thickness (nm)*	*Core inner diameter (μm)*	*Representative loss (@ 1500 nm) (dB/km)*
1-ring HC-PCF	0.45	19.5	480	58	610
2-ring HC-PCF	0.34	20.3	405	48	373
3-ring HC-PCF	0.52	19.2	450	55	251
4-ring HC-PCF	0.45	18.8	440	47	171

3.4.2 Bend loss and modal content evolution with cladding ring number

A further characterisation of these different cladding ring-number fibres is made by measuring the macro bending behaviour. Figure 3.16 shows the bend-loss spectra for different bend radii (5 cm, 4 cm, 3 cm and 2 cm) measured with the four fibre designs. The bend was carried out by coiling the fibre four turns for each measurement run.

For a bend radius of 5 cm, the loss spectra in the 1500nm-1750nm spectral range are comparable for the fibres with a cladding ring number of up to 3, all exhibiting a bend loss figure of ~ 2 dB/m. However, as the wavelength gets shorter towards the high-frequency transmission edge of the fundamental band, the loss in the single-ring fibre increases at a much higher rate than the rest of the fibres, indicating that the cladding layers act as a barrier to bend-induced mode-coupling between the core modes and radiation modes. This corroborated with the 4-ring fibre whose bend loss figure reaches ~0.1 dB/m level in the 1500nm - 1750nm spectral range. Furthermore, for radii shorter than

5 cm, the spectra clearly show that the bending loss decreases with the cladding ring number. For example in the case of a bend radius of 3 cm, the spectra show that fibres with more than two layers exhibit a bend loss lower than the single ring design by more than one order of magnitude.
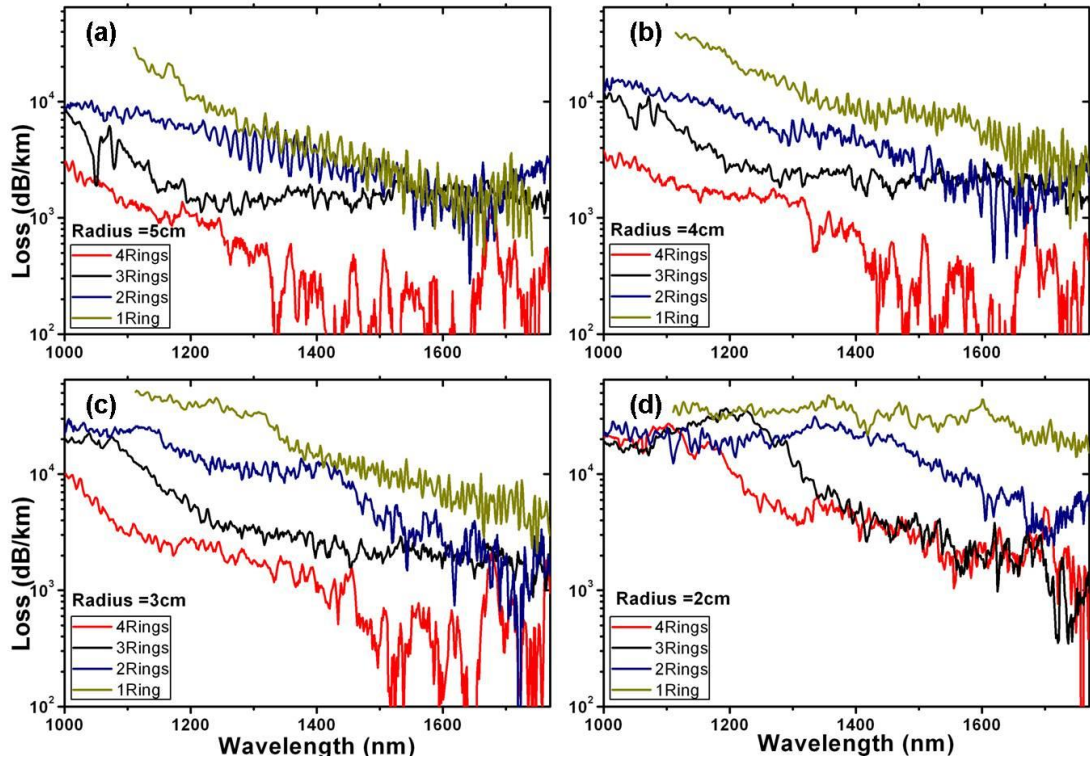
Figure 3.16: Bending loss spectrum measured for four hypocycloid-core Kagome HC-PCF (with one, two, three and four cladding rings) at different bending radii (a) 5 cm, (b) 4 cm, (c) 3 cm and (d) 2 cm [24].
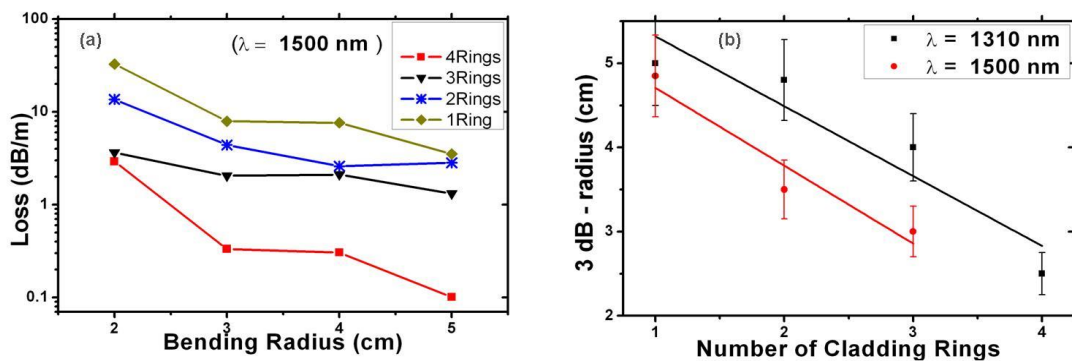
Figure 3.17: (a) Zoom-in of measured bending loss evolution at the particular wavelength 1500 nm. (b) Critical radius versus number of cladding rings at 1310 nm and 1500 nm [24].

Figure 3.17(a) shows the evolution of the bend loss at a representative wavelength from the centre of the transmission band (chosen to be 1500 nm) with the bend radius. The results show that when the fibres are bent with a bend radius of 5 cm, the bend loss is as low as 0.1 dB/m for a 4-ring HC-PCF, whilst it is ~ 50 dB/m for a single-ring fibre. Figure 3.17(b) shows the evolution of the deduced 3-dB radius (i.e. the bend radius at which the transmission is attenuated by 3dB upon a one full turn coil) at 1500 nm and at another wavelength from a spectral range that is closer to the short-wavelength transmission (chosen to be 1300 nm). For both wavelengths, the 3dB-radius is decreased by 1 cm per one ring addition to the cladding.
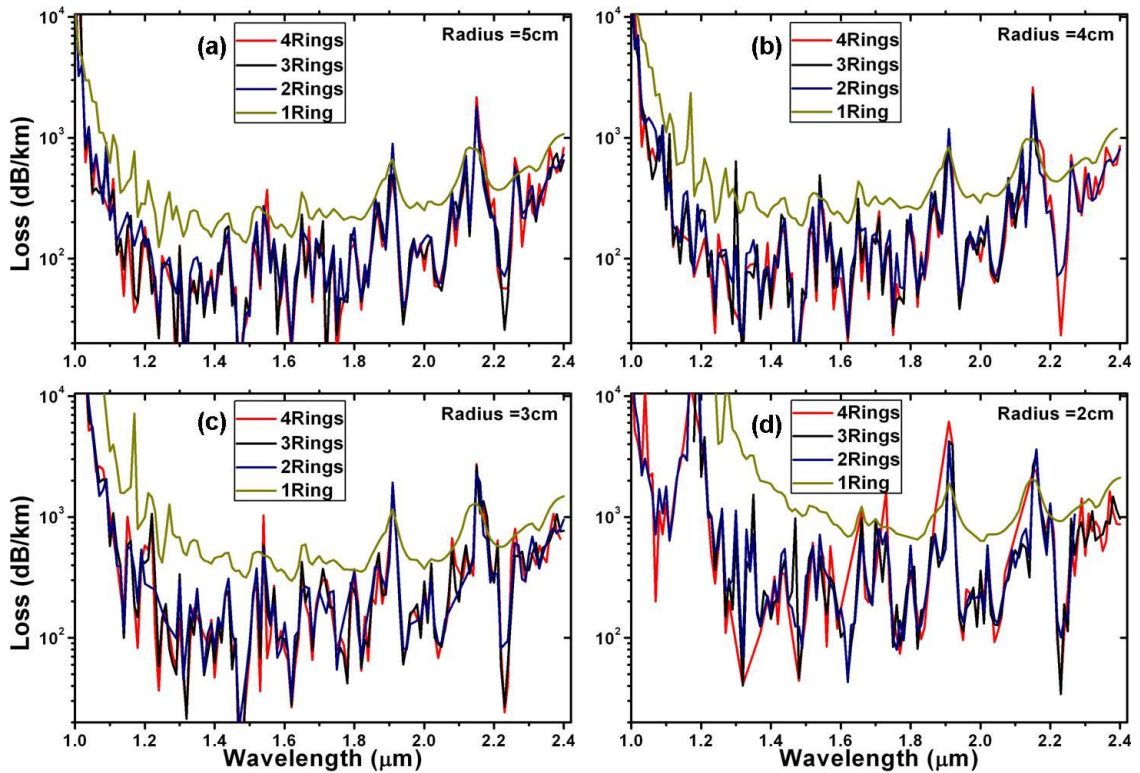
Figure 3.18: Calculated bend loss spectra for four fibres with different cladding ring numbers (1, 2, 3 and 4 rings) at different bending radii (5, 4, 3, and 2 cm) [24].

The trends of the above experimental results are qualitatively corroborated numerically. Figure 3.18 shows the computed bend loss spectra for four fibres with different cladding ring-numbers, varying from one to four rings, at different bending radii. The numerical results were obtained through joint use

of the FEM modal solver and of the conformal mapping technique [27], which allows the replacement of the bent fibre with refractive index $n(x, y)$ with a straight one having an equivalent index profile $n_{eq}(x, y) = n(x, y)e^{\xi/R_b}$ where $\zeta=$x,y is the transverse bending direction and R_b the bending radius. The combined use of the FEM and conformal mapping have already been successfully used to analyse bending loss in solid core step index fibres [28], microstructured fibres [29], and HC tube lattice fibres [30]. Similar to the experimental results, these results show that passing from one ring to two rings the confinement loss is significantly reduced, whereas a further increase in the number of cladding rings has a minor effect on the bend loss. This is confirmed by Figure 3.19, where the confinement loss versus the bend radius for two wavelengths (λ = 1.5 µm and λ = 1.55 µm) for different ring numbers are plotted. The discrepancy between the experimental data and the numerical data is likely due to micro-imperfections in the fabricated fibres and mechanical deformations that are not taken into account in the numerical model. Furthermore, the experimental results show stronger insensitivity to bend when the cladding ring-number is increased, indicating further the limit of our numerical model.

Furthermore, the evolution of the transmission loss with bend radius does not show a uniform decrease but exhibits a resonant loss for a bend radius at 1.16 cm, and an oscillatory behaviour shows a structured curve in the radial range of 2-8 cm. The loss resonant peaks are explained by the coupling between the fibre core HE$_{11}$ mode and that of cladding hole (see Figures. 3.19(c)-(f)) [18], [30]. The origin of the oscillatory behaviour near 2-8 cm radial range is more complicated to trace back. We believe that it is due to a bending dependence of the Fano resonances [31].
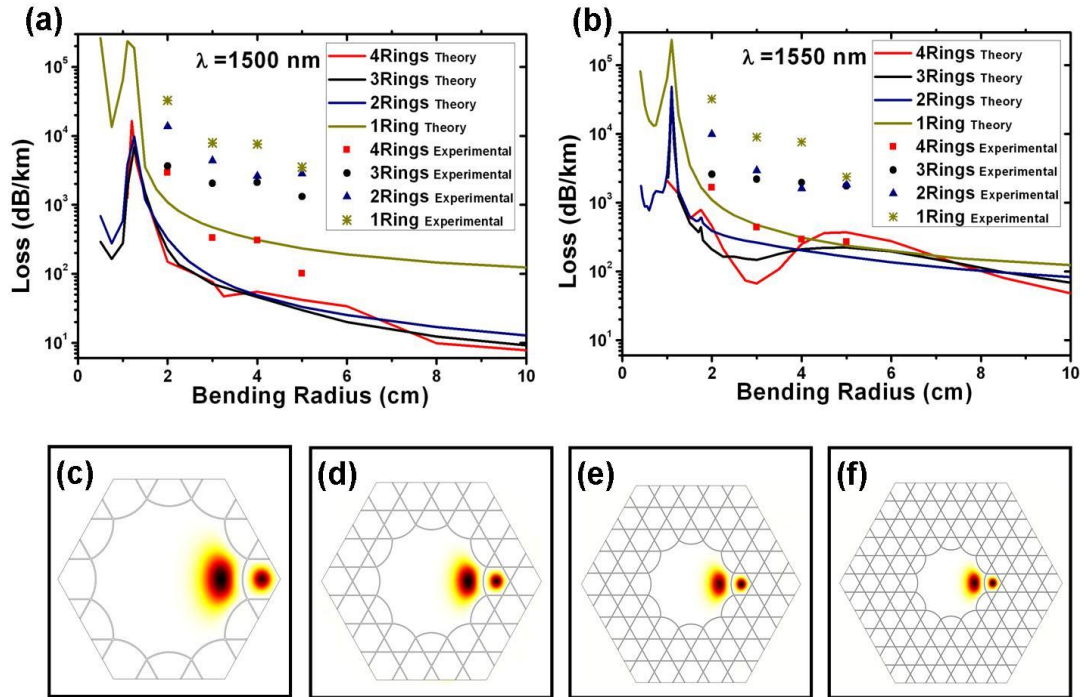
Figure 3.19: (a) and (b) Confinement loss versus the bend radius for two wavelengths (λ= 1.5µm and λ= 1.55µm) for different ring numbers. (c) - (f) Simulated fundamental mode profile at bend radius 1.1 cm at λ = 1.5µm [24].

Finally, we observed that the increase of the cladding ring-number affects the modal content of the fibre. Figure 3.20 shows a set of reconstructed near field images recorded, using a CCD camera, of the light output for the different 5m-long piece of fibres considered here and for different bend radii. A strong multimode guidance is found for the 1st ring design that contrasts with the other configurations. The coupling of the HE_{11} mode with the air-cladding modes is playing a key role as is demonstrated in Figures 3.19(c)-(f). Indeed, the loss level at the coupling point is strongly dependent on the distance between the first layer of the microstructure and the outer silica-cladding jacket. The results clearly show that an increase in cladding ring-number improves the modal content and lessens the fibre sensitivity to bend. This study is an original way to confirm the main role played by the inhibiting coupling mechanism in such micro-structured fibres.
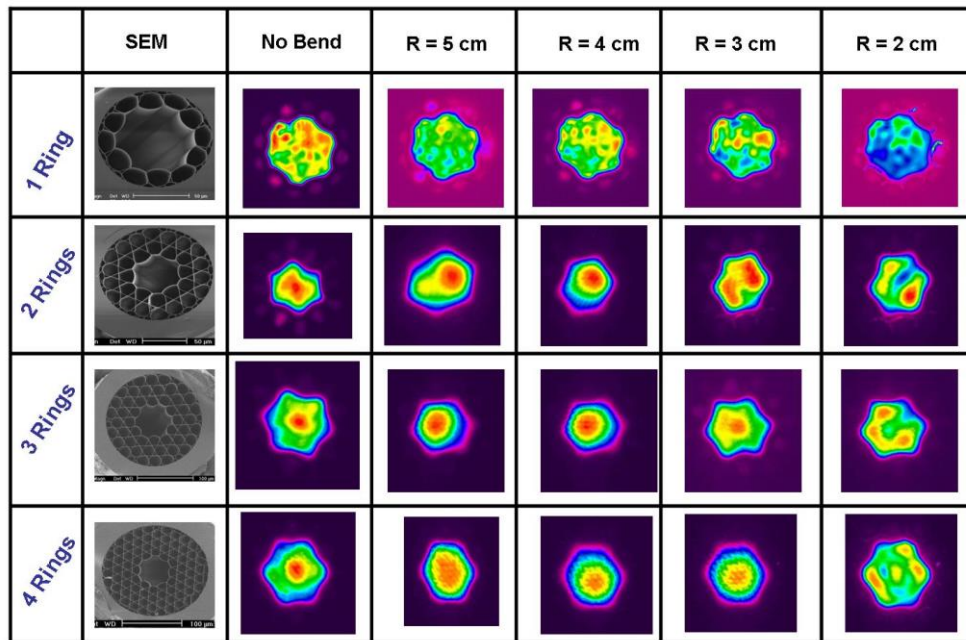
Figure 3.20: Near field mode profile for four fibres (1, 2, 3, and 4 ring) at no bend and different bend radii (5, 4, 3, and 2 cm) [24].

3.5 Summary

This chapter covered a thorough experimental and theoretical work in designing and fabricating hypocycloid core Kagome HC-PCF with state-of-the-art performances in transmission loss, modal content and optical overlap of guided light with the cladding. The results corroborate the IC model and open new prospects in HC-PCF. Of direct relevance to the long-term aim goal that underpins the scope of the present thesis is the possibility now to reconcile in one single fibre, broadband guidance and ultra-low transmission loss. This is illustrated in the FOM shown in Figure 3.21 below, where the FOM in the case of 7 cell and 19 cell Kagome HC-PCF is enhanced by a factor of 20 when the hypocycloid core contour is introduced. Moreover, what is especially remarkable is that the FOM for these new hypocycloid Kagome fibres are comparable to the one of PBG while having a larger core diameter. Furthermore, in anticipation of optical power scaling-up for Raman comb, this fibre has the advantages for high power Raman comb due to its very small optical overlap with silica.
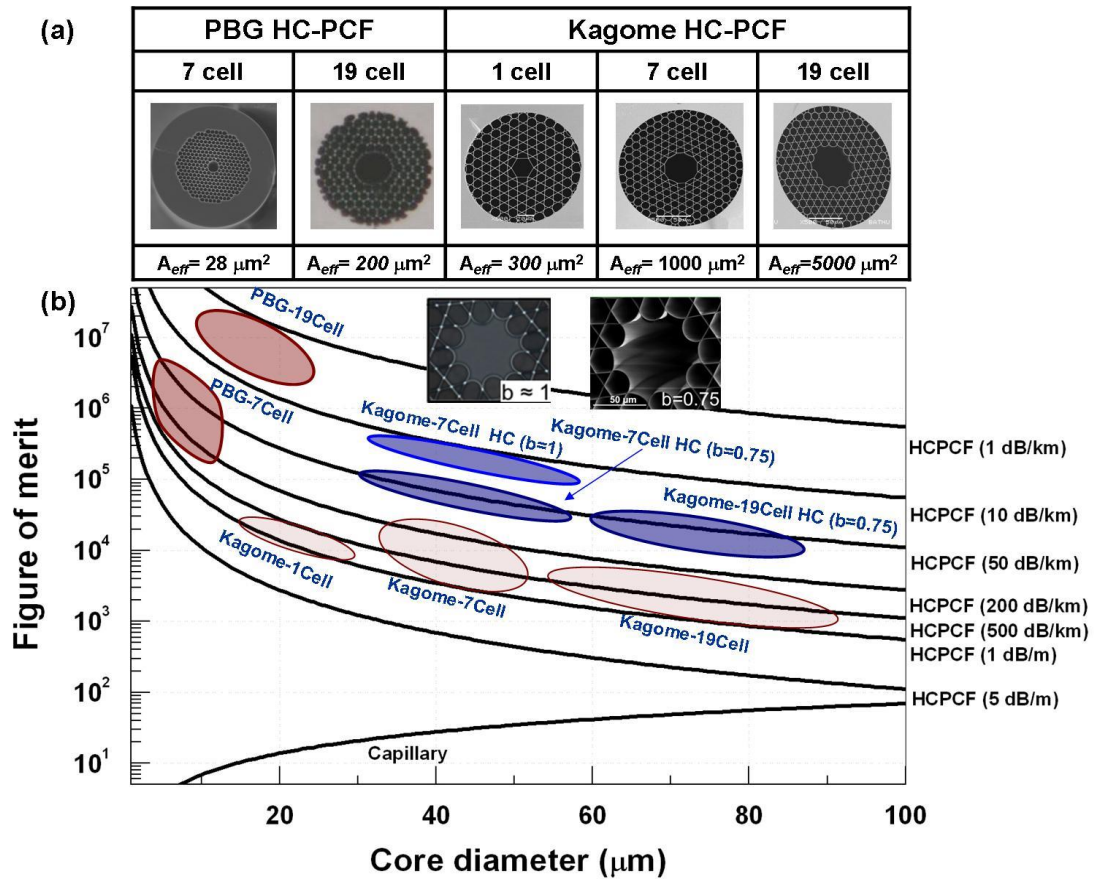
Figure 3.21: FOM of different types of HC-PCF (introduced before in Chapter 1) add to it the new fabricated hypocycloid (HC) Kagome HC-PCF with different *b* values (blue regions).

References

[1]   F. Benabid, J. C. Knight, G. Antonopoulos, and P. S. J. Russell, "Stimulated Raman scattering in hydrogen-filled hollow-core photonic crystal fibre.," *Science*, vol. 298, no. 5592, pp. 399–402, Oct. 2002.

[2]   F. Couny and F. Benabid, "Optical frequency comb generation in gas-filled hollow core photonic crystal fibres," *J. Opt. A Pure Appl. Opt.*, vol. 11, no. 10, p. 103002, Oct. 2009.

[3]   F. Couny, F. Benabid, P. J. Roberts, P. S. Light, and M. G. Raymer, "Generation and photonic guidance of multi-octave optical-frequency combs.," *Science*, vol. 318, no. 5853, pp. 1118–21, Nov. 2007.

[4]   J. von Neumann and E. Wigner. *Physik. Z*, vol. 30, no. 465. 1929

[5]   F. Couny, "Photonic Solutions towards Optical Waveform Synthesis," *University of Bath*, 2008.

[6]   F. Couny, F. Benabid, P. J. Roberts, P. S. Light, and M. G. Raymer, "Generation and photonic guidance of multi-octave optical-frequency combs.," *Science*, vol. 318, no. 5853, pp. 1118–21, Nov. 2007.

[7]   Y. Wang, F. Couny, P. J. Roberts, and F. Benabid, "Low Loss Broadband Transmission In Optimized Core-shape Kagome Hollow-core PCF," in *Conference on Lasers and Electro-Optics (CLEO)*, p. CPDB4. 2010

[8]   Y. Y. Wang, N. V Wheeler, F. Couny, P. J. Roberts, and F. Benabid, "Low loss broadband transmission in hypocycloid-core Kagome hollow-core photonic crystal fibre," *Opt. Lett.*, vol. 36, no. 5, pp. 669–671, 2011.

[9]   Y. Y. Wang, N. V Wheeler, F. Couny, P. J. Roberts, and F. Benabid, "Low loss broadband transmission in hypocycloid-core Kagome hollow-core photonic crystal fibre.," *Opt. Lett.*, vol. 36, no. 5, pp. 669–71, Mar. 2011.

[10]   B. DEBORD, M. Alharbi, T. Bradley, C. Fourcade-Dutin, Y. Wang, L. Vincetti, F. Gerome, and F. Benabid, "Cups curvature effect on confinement loss in hypocycloid-core Kagome HC-PCF," in *CLEO:* p. CTu2K.4. 2013

[11]   B. DEBORD, M. Alharbi, T. Bradley, C. Fourcade-Dutin, Y. Wang, L. Vincetti, F. Gerome, and F. Benabid, "Hypocycloid-shaped hollow-core photonic crystal fibre Part I : Arc curvature effect on confinement loss," *Opt. Express*, vol. 21, no. 23, pp. 1441–1448, 2013.

[12]   S. Selleri, L. Vincetti, A. Cucinotta, and M. Zoboli, "Complex FEM modal solver of optical waveguides with PML boundary conditions," *Opt. Quantum Electron.*, vol. 33, no. 4–5, pp. 359–371, 2001.

[13]   L. Vincetti, "Numerical analysis of plastic hollow core microstructured fibre for Terahertz applications," *Opt. Fibre Technol.*, vol. 15, no. 4, pp. 398–401, Aug. 2009.

[14]   L. Vincetti and V. Setti, "Con fi nement Loss in Kagome and Tube Lattice Fibres: Comparison and Analysis," *J. Lightw. Technol.*, vol. 30, no. 10, pp. 1470–1474, 2012.

[15]   L. Vincetti and V. Setti, "Extra loss due to Fano resonances in inhibited coupling fibres based on a lattice of tubes.," *Opt. Express*, vol. 20, no. 13, pp. 14350–61, Jun. 2012.

[16]   E. A. J. Marcatili and R. A. Schmeltzer, "Hollow Metallic and Dielectric Waveguides for Long Distance Optical Transmission and Lasers," *Bell Syst. Tech. J.*, vol. 43, no. 4, pp. 1783–1809, 1964.

[17]   T. Grujic, B. T. Kuhlmey, A. Argyros, S. Coen, and C. M. de Sterke, "Solid-core fibre with ultra-wide bandwidth transmission window due to inhibited coupling.," *Opt. Express*, vol. 18, no. 25, pp. 25556–66, Dec. 2010.

[18]   T. D. Bradley, Y. Wang, M. Alharbi, B. Debord, C. Fourcade-dutin, B. Beaudou, F. Gerome, and F. Benabid, "Optical Properties of Low Loss (70dB / km) Hypocycloid-Core Kagome Hollow Core Based Optical Applications," *J. Lightw. Technol.*, vol. 31, no. 16, pp. 3052–3055, 2013.

[19]   L. Vincetti and V. Setti, "Waveguiding mechanism in tube lattice fibres.," *Opt. Express*, vol. 18, no. 22, pp. 23133–46, Oct. 2010.

[20]   Y. Y. Wang, X. Peng, M. Alharbi, C. F. Dutin, T. D. Bradley, F. Gérôme, M. Mielke, T. Booth, and F. Benabid, "Design and fabrication of hollow-core photonic crystal fibres for high-power ultrashort pulse transportation and pulse compression.," *Opt. Lett.*, vol. 37, no. 15, pp. 3111–3, Aug. 2012.

[21]   R. F. Cregan, B. J. Mangan, J. C. Knight, T. A. Birks, P. St. J. Russell, P. J. Roberts, and D. C. Allan, "Single-Mode Photonic Band Gap Guidance of Light in Air," *Science*, vol. 285, no. 5433, pp. 1537–1539, Sep. 1999.

[22]   NKT, "Hollow core photonic crystal fibres _ NKT Photonics." [Online]. Available: http://www.nktphotonics.com/hollowcorefibres?cid=5215.

[23]   P. Roberts, D. Williams, B. Mangan, H. Sabert, F. Couny, W. Wadsworth, T. Birks, J. Knight, and P. Russell, "Realizing low loss air core photonic

crystal fibres by exploiting an antiresonant core surround.," *Opt. Express*, vol. 13, no. 20, pp. 8277–85, Oct. 2005.

[24] M. Alharbi, T. Bradley, B. Debord, C. Fourcade-Dutin, L. Vincetti, F. Gerome, and F. Benabid, "Hypocycloid-shaped hollow-core photonic crystal fibre Part II: Cladding effect on confinement and bend loss," *Opt. Express*, vol. 21, no. 23, pp. 28609–28616, 2013.

[25] A. V. V. Nampoothiri, A. M. Jones, C. Fourcade-Dutin, C. Mao, N. Dadashzadeh, B. Baumgart, Y. Y. Wang, M. Alharbi, T. Bradley, N. Campbell, F. Benabid, B. R. Washburn, K. L. Corwin, and W. Rudolph, "Hollow-core Optical Fibre Gas Lasers (HOFGLAS): a review [Invited]," *Opt. Mater. Express*, vol. 2, no. 7, p. 948, Jun. 2012.

[26] G. J. Pearce, G. S. Wiederhecker, C. G. Poulton, S. Burger, and P. St J Russell, "Models for guidance in kagome-structured hollow-core photonic crystal fibres.," *Opt. Express*, vol. 15, no. 20, pp. 12680–5, Oct. 2007.

[27] M. Heiblum and J. Harris, "Analysis of curved optical waveguides by conformal transformation," *Quantum Electronics, IEEE Journal of*, vol. 11, no. 2. pp. 75–83, 1975.

[28] L. Vincetti, M. Foroni, F. Poli, M. Maini, A. Cucinotta, S. Selleri, S. Member, and M. Zoboli, "Numerical Modeling of S-Band EDFA Based on Distributed Fibre Loss," *J. Lightw. Technol.*, vol. 26, no. 14, pp. 2168–2174, 2008.

[29] Y. Tsuchida, K. Saitoh, and M. Koshiba, "Design of single-moded holey fibres with large-mode-area and low bending losses: the significance of the ring-core region.," *Opt. Express*, vol. 15, no. 4, pp. 1794–803, Mar. 2007.

[30] V. Setti, L. Vincetti, and a Argyros, "Flexible tube lattice fibres for terahertz applications.," *Opt. Express*, vol. 21, no. 3, pp. 3388–99, Mar. 2013.

[31] A. F. Kosolapov, A. D. Pryamikov, A. S. Biriukov, V. S. Shiryaev, M. S. Astapovich, G. E. Snopatin, V. G. Plotnichenko, M. F. Churbanov, and E. M. Dianov, "Demonstration of CO_2-laser power delivery through chalcogenide-glass fibre with negative-curvature hollow core.," *Opt. Express*, vol. 19, no. 25, pp. 25723–8, Dec. 2011.

Part 2

Raman frequency comb and coherence with pulsed pump

This part of the thesis covers the study of the Raman molecular coherence whereby a theoretical and experimental investigation of the spatial and temporal dynamics of molecular Raman coherence is presented in Chapter 4. The results show that with a modest laser pump, molecular coherence persists for a duration longer than that of the molecular dephasing time. In addition, results show the coherence is distributed along a multi-metre long fibre.

Furthermore, the decay time of the calculated coherence is found to be equal to T_2. In Chapter 5, the first demonstration of the synthesis of a 17.6 THz repetition frequency of 26 fs pulse train AC waveform using Raman comb generated in hydrogen-filled Kagome HC-PCF is demonstrated. The comb is generated by exciting the medium with a 400 ps pulse pump and a Stokes seed generated under transient SRS conditions.

.

Chapter 4

Spatio-temporal mapping of Raman coherence in HC-PCF

This chapter covers the theoretical and experimental investigation of the spatial and temporal dynamics of molecular Raman coherence. This is achieved through monitoring the stimulated Raman scattering of a delayed probe in hydrogen-filled hollow-core photonic crystal fibre (HC-PCF) that has been excited by a leading pump pulse. The experimental results show Stokes scattering via the molecular coherence frequency modulation even for a delay time of 22 ns, correspondingly 129 times larger than the molecular dephasing time. More intriguingly, the decay time of the coherence induced Stokes signal was found to be 7.2 ns, which is 42 times the expected decay time.

4.1 Introduction

PBG HC-PCF filled with Raman active gas has been demonstrated to be an unprecedentedly efficient Raman converter [1]. The long interaction length and the micrometre scale core area offer an excellent platform for new Raman dynamics. Thus, this enabled the generation of SRS in the transient regime even when the pump pulse duration τ is longer than the dephasing time T_2 of the Raman resonance [2]. Furthermore, the use of Kagome HC-PCF enables the demonstration of an intra-pulse phase-locked multi-octave comb. However, these comb components are uncorrelated from pulse to pulse due to the quantum noise seeded generation process and to the faster decay of the Raman resonance (typically $T_2 = 1/2\Gamma$ is in the hundreds of picoseconds, Γ is the dephasing rate, which is dominantly collisional). This in turn drastically limits the use of such a comb. One possible solution that does not require a second laser for the generation of pulse-to-pulse coherent combs is to have a sufficiently long life Raman coherence combined with a laser that has a sufficiently high repetition rate that the coherence survives the time separation between the laser adjacent pulses. Within this context, in 1991 Smithey *et al.* [3] have previously shown that in the high gain and transient SRS regime, the molecular coherent excitation can, intriguingly, survive for much longer than T_2. They also showed that the generated Stokes pulses from two delayed pump pulses remain coherent provided the dominant spatial-temporal mode (STM) contains between 15 and 50 surviving molecular excitations (which we call for convenience, phonons) from the number of initially excited phonons. The number N_C of these coherent phonons decays as $N_C = N_0 e^{-\frac{t}{T_2}}$, with N_0 being the initially excited molecular excitation, and is equal to the number of Stokes photons in the quantum limit.

On the other hand, we know that with the use of HC-PCF, a net Raman gain exceeding 1000 can be reached with low-power pump lasers. Secondly, a quantum-limit conversion to the Stokes is now common with PBG guiding HC-PCF. And finally, because of the combination of the very high gain, the single modedness of the fibre, and the partial spontaneous emission suppression, it is expected that the dominant "vacuum generated" STM is primarily excited with enhanced extinction ratio relative to the other STM. This means that one would expect survival of the coherence with less molecular excitation per STM than the previously reported 15-50 [3].

This makes PBG HC-PCF a platform where the persistence of Raman molecular coherence should be expected to be much longer. During the duration of this coherence survival, the Raman gas-filled HC-PCF would act as a phase modulator with a frequency set by Raman shift frequency. Consequently, if this long-persistence coherence is excited with a pump pulsed laser with a repetition period being shorter than the survival time of the molecular coherence, one could use it to develop pulse-to-pulse coherent Stokes lasers, and possibly use it as a seed to excite a Raman comb, which would have a pulse-to-pulse coherence (see chapter 5). Finally, mapping the spatio-temporal distribution of the Raman coherence and exploring its dynamics throughout the whole length of the HC-PCF under extremely high gain is interesting from basic physics as it further provides a new platform for revisiting the properties of a pure quantum state with a macroscopic system.

In this chapter, we report on a pump-probe experimental set-up to examine the survival time of the Raman molecular coherence that was excited by the pump via the measurement of the strength of the Stokes from the probe that scatters off the pre-established molecular coherence, and a numerical simulation that

calculates the Raman coherence temporal and spatial distribution[2]. The chapter is split into three sections. The first section; section 4.2, describes the experiment and its rationale. Section 4.3 deals with the experimental and theoretical results. The results show that with a modest laser pump, molecular coherence persists after the pump pulse passage for as long as 42 times the molecular dephasing time. The decay of the Stokes signal was found to be 7.2 ns. Moreover, the spatial and temporal coherence dynamic underlying these results are investigated theoretically. The results show the coherence is distributed along multi-meter long fibres, and nears the fundamental maximum. The longer decay time found in the experimental results compared to theory is discussed and the explanation for the observed results is provided. This work is published in [4], [5].

4.2 Experimental setup

Figure 4.1(a) shows schematically the experimental set-up. Here, the delayed probe-pump technique is used whereby the Stokes generated by a weak pulse is monitored in function with the delay time between the two input pulses. The two pulses are generated from the same laser. The laser is a 532 nm (doubled Nd:YAG) passive Q-switch diode pumped microchip laser producing 550 ps pump pulses with 7 kHz repetition rate and an average output power of up to 25 mW (peak power 6 kw and 3.6 μJ). The laser beam is split into two pulses by sending one through a delay line. The delay between the two pulses is controlled by sending the probe pulse through a chosen length of endless single mode PCF (ESM-PCF).

---

[2] The author acknowledges that the initial work on the experiment was undertaken by YingYing Wang. The author carried out the experimental work and the data processing and analysis. The numerical simulations were carried out by Anton Husakou.
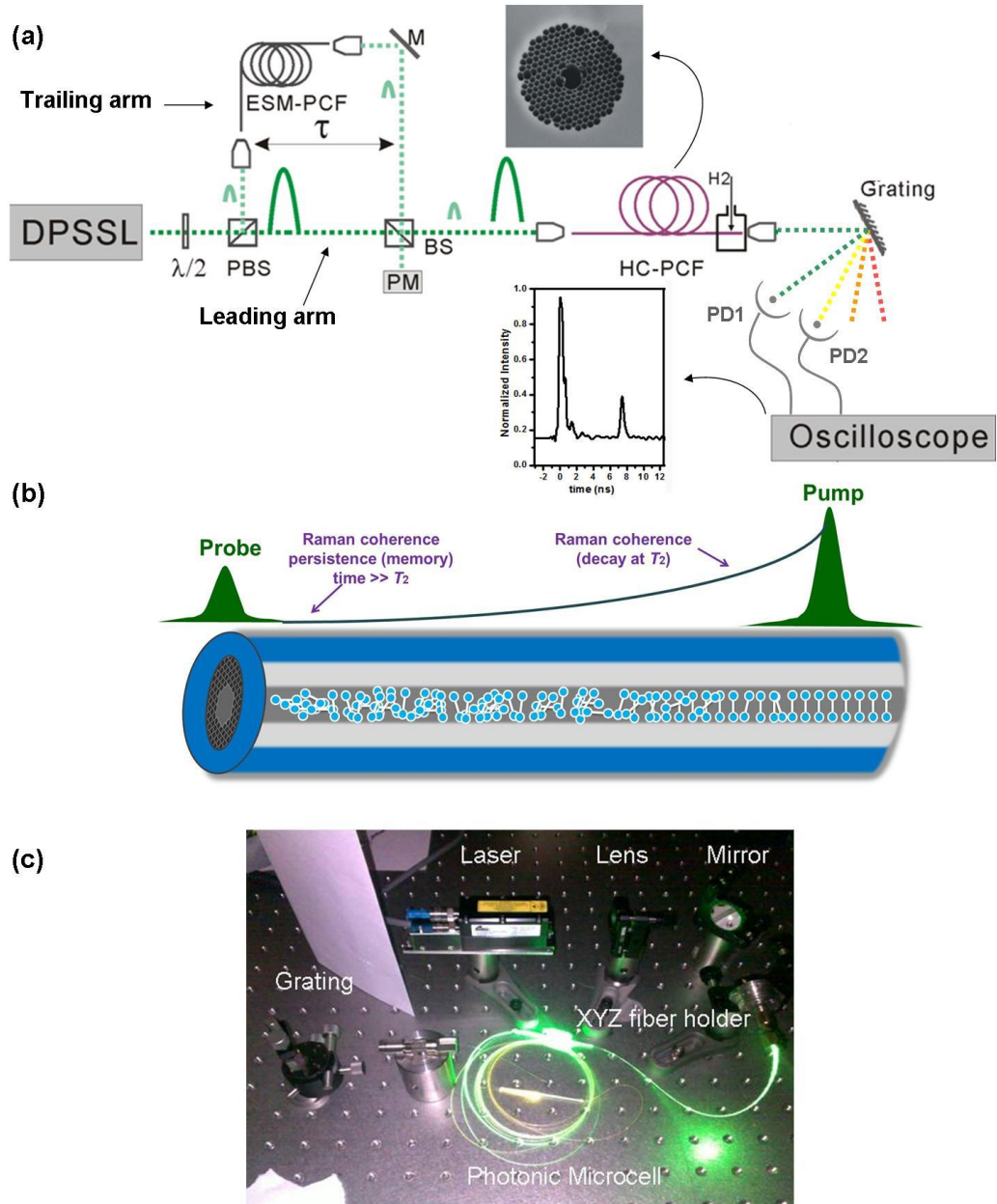
Figure 4.1: (a) Experimental setup for the molecular coherence measurement. Top image: SEM for the PBG HC-PCF; PBS: polarisation beam splitter; M: mirror; λ/2: half-wave plate; Att: attenuator; PM: power meter; BS: beam splitter; SMF: single mode fibre; PD1: photodetector for pump detection; PD2: photodetector for Stokes detection. (b) Raman coherence persistence [4]. (c) Photograph of comb generation using PBG HC-PCF as photonic microcell filled with H_2 [6].

Figure 4.2 illustrates the SEM of the HC-PCF used in this setup. It is a photonic bandgap guiding fibre with a transmission window ranging from 500 nm to 650 nm (~140THz) with an attenuation of α ~ 0.6 dB/m = 0.14m^{-1}. The fibre has a core diameter, d of 5.4 μm, hence a mode-field diameter of approximately $\left(\pi/4\right)d = 4.2\mu m$. It is ~2 m long and is filled with H_2 at a pressure

of 15 bar. With these fibre characteristics, and assuming a Raman gain coefficient of $g = 2cm.GW^{-1}$ [7], the Raman net gain is $G = gP_p \left(l_{eff} \middle/ A_{eff} \right)$, with $l_{eff} = \left(1 - e^{-\alpha l}\right) \middle/ \nu$ can reach ~34000 if the 6kW of the laser is launched into the fibre. In our experimental condition, only 6 mW average power (1.6 kW of peak power, and 857 nJ of pulse energy) from the pump pulse is sent to the fibre. Assuming 50% of fibre-coupling efficiency, this corresponds to the maximum intensity I_p that propagates inside the fibre in excess of ~ 6 GW/cm², and a Raman gain G reaches ~450 for our fibre length l of 2 m. In terms of the number of pump photons, this power corresponds to ~1x10¹². The power of the probe pulse is set so we operate just below the SRS threshold. In practice, we set the coupled average power to be less than 0.1 mW. Consequently, the net gain generated by the probe trailing pulse is G<15. This means that if the probe contains Stokes frequency at the fibre output, it is necessarily due to phase-modulation at the Raman resonance frequency, of the probe from a pre-established Raman coherence.

The output end of the fibre is attached to a gas chamber, whilst the input end is spliced to a single-mode fibre (SMF) with a cut-off wavelength around 400 nm. This SMF acts as a seal for hydrogen filled HC-PCF and as a spatial mode filter to provide exactly the same mode-coupling conditions for the two beams. The length of the sealed SMF was kept to less than 5 cm so as to avoid any nonlinear effect from the silica. The output pulses are then dispersed with a grating and the pulses at the input and the 1st order Stokes wavelengths are detected by the photodetector and recorded on the oscilloscope (see Figure 4.1(a)). It is noteworthy, that the experimental set-up is highly compact, as is illustrated in Figure 4.1(c) showing a photograph of the essential components.
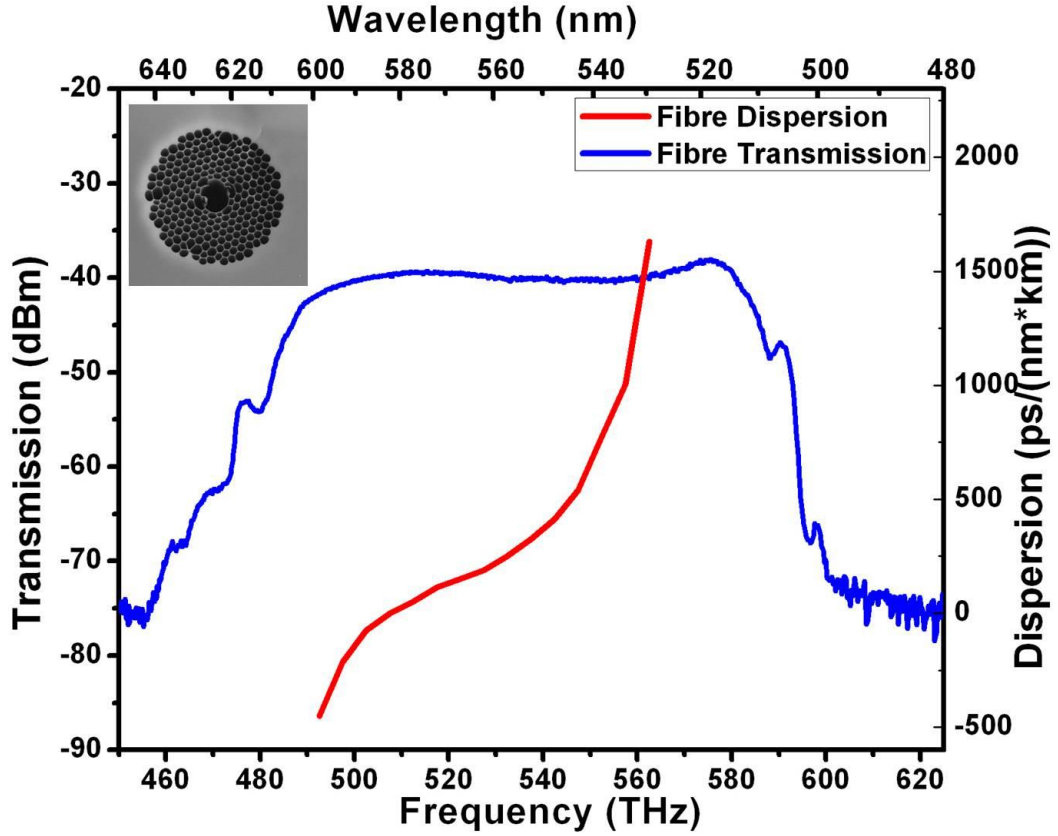
Figure 4.2: Dispersion and transmission spectrum for PBG HC-PCF measured by an optical spectrum analyser (OSA).

In order, to project the expected maximum delay line to observe frequency modulation of the probe from the pre-established Raman coherence left after the passage of the pump, we recall that for the rotational $S_{00}(1)$ transition at our operational pressure of ~10 bar, the linewidth is $\Delta v \sim 1GHz$ [8], corresponding to a dephasing rate of $\Gamma = \pi\Delta v \sim 3GHz$, and dephasing time of $T_2 = (\Gamma)^{-1} \sim 340ps$. Therefore, the SRS process generated by the pump beam is in the highly transient regime ($\Gamma\tau_p$<< G, τ_p being the pump pulse duration), and a high Raman molecular coherence is generated. The number of the available molecules in the entire fibre is thus 2×10^{10}, of which $\sim 2 \times 10^9$ are contained in the ~20 cm long pump pulse. We note that we have many more pump photons than molecules. Hence, if the quantum limit is reached (i.e. each pump photon coherently excites a molecule), Raman saturation occurs. This effect is currently ignored in our approach and in our qualitative estimate for the time after the

initial pulse for which the Raman coherence can scatter a trialling pulse at the Stokes frequency. This is reasonable as the effective SRS generation time (i.e. the Stokes pulse duration) is much shorter that pulse width, and scales with $G^{-1/2}$.

After the pump pulse, the number of coherently excited molecules, according to conventional SRS theory should decay exponentially with time τ at a rate set by the collisional dephasing; i.e. the coherence evolves as exp (-2$\Gamma\tau$) [3]. The probe pulse, whose power is set so we operate below the SRS threshold (couple average power <0.1mW, hence G<15), enters the fibre at the time τ and gets phase-modulated at the Raman resonance frequency, and thus generates a Stokes component. The intensity of this coherent Stokes is directly proportional to the modulation depth imparted by the molecular excitation to the probe laser, and hence to the amount of remaining molecules that are coherently excited. This is qualitatively formalised by stating that the nuclear displacement of the rotating molecules follow the motion of a classical harmonic oscillator [9]. Consequently, and adopting the formalism used in[10], the probe pulse field equation of motion is:

$$\frac{\partial E_{trail}}{\partial z} + \frac{1}{v_g}\frac{\partial E_{trail}}{\partial z} = i\frac{\tilde{g}}{Q_0}Q\left(t - z/v_g\right)E_{trail},$$ (4.1)

with Q_0 being the initial coherent excitation magnitude, and $\tilde{g} = Q_0\frac{2\pi N}{c}\left(\frac{\partial\alpha}{\partial Q}\right)$,

where v_g is the group velocity of the trailing probe pulse, and the right hand side includes phase mismatch Δk between pump and Stokes. Consequently, the trailing pulse field can be written as:

$$E_{trail}(z,t) = E_{trail}(0,t)Exp\left(-i\left(\tilde{g}e^{-\Gamma t}\frac{\sin(\Delta Kz)}{\Delta K}\right)\sin(\Omega_R t + \Delta Kz)\right)$$ (4.2)

This is an expression of a phase modulated field at the Raman frequency and a modulation depth of $\tilde{g}e^{-\Gamma t}\dfrac{\sin(\Delta Kz)}{\Delta K}$, which simplifies to $\tilde{g}e^{-\Gamma t}z$ if we assume $\Delta K = 0$. Using an expansion in Bessel function terms, and ignoring the higher order frequency terms, the frequency modulated signal at the Stokes frequency is given by $I_S(\tau) \propto I_{trail}Q_0^2 z^2 e^{-2\Gamma\tau}$.

The above simple derivation shows that the modulation depth of the trailing pulse field from the pre-established Raman coherence is proportional to the initial coherence magnitude Q_0^2, the interaction length z^2, and the trailing pulse field. Note, however, that higher order Stokes and anti-Stokes are neglected in the above derivation. More importantly to our experimental protocol, the measured Stokes signal is directly proportional to the initial coherence state and should show the same evolution of $e^{-2\Gamma\tau}$ as the coherence. Consequently, taking the required number of coherent molecules in the dominant STM as $N_r = 15$, the longest time one could still observe Stokes scattering from the pre-established coherence (i.e. the time duration during which the initial coherent molecules N_0 drops to N_r is given by $\tau_r = T_2 Log\left(N_0 \Big/ N_r\right) \sim 10T_2$.

4.3 Stokes intensity strength decay

Firstly, the fibre output spectrum was investigated. Figure 4.3(a) shows the generated SRS for two leading pump powers. The first spectrum is excited with a 6 mW average power, of which ~50% is coupled to the HC-PCF. The spectrum shows that the conversion is dominantly to the 1st order Stokes, and with more than 35 dB above the second order. The 6 mW was found to be maximum power for which the conversion is limited to the first order Stokes. Indeed, increasing the power to 10 mW for example results in a spectrum with several higher order Raman lines. We thus must operate at pump power of less
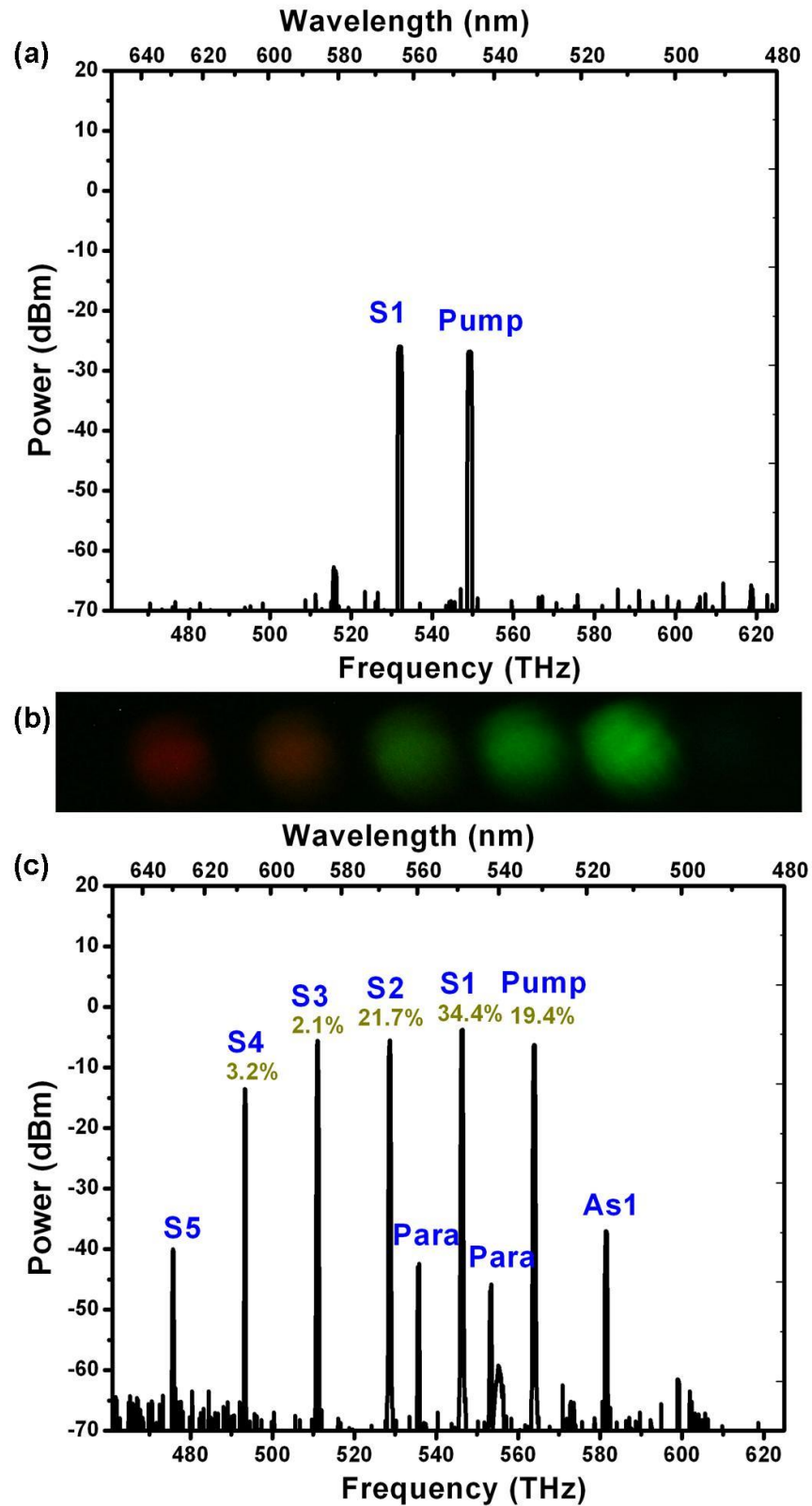
Figure 4.3: (a) The recorded spectrum for the PBG HC-PCF with input power of 6 mW (b) Photograph of the dispersed output comb lines at input power of 10 mW; (c) the output Raman comb spectrum for the PBG HC-PCF with input power of 10 mW [6].

than 6 mW so as to avoid parametric processes between the higher order Stokes and anti-Stokes, which affects both the coherence and the probed 1st Stokes as predicted in the simple model described above. Indeed, the Raman coherence $\rho_{12} \propto \sum_i E_i E_{i-1}^*$, and hence its magnitude and phase is affected by the generation of higher order Raman line. Here i corresponds to the Raman order. Similarly, and via four-wave mixing, phase of the 1st Stokes field is altered through the proportionality relation $E_{-1} \propto \sum_i E_{-i} E_{i-1}^*$.

Figure 4.4 (b and c) illustrates a typical time trace of the 1st Stokes output as recorded by a photodetector and when the time delay between the input pulses is set at τ = 7.4 ns. By blocking the probe arm (i.e. trailing arm), only the first Stokes pulse generated by the pump arm is shown on the oscilloscope (Figure 4.4(a)). To ensure that the probe arm is below threshold, the pump arm is then blocked while the probe beam is coupled into the fibre, with no Stokes pulse detected as shown in Figure 4.5(a). When, however, both pump and probe are propagating, the Stokes pulse shape changes as shown in Figure 4.4(c). The Stokes peak generated from the pump beam remains at t = 0. More interestingly, a second peak appears, delayed from the pump beam by 7.4 ns. This second peak originates from the interaction of the probe arm with the remaining molecular coherence set off by the leading strong pulse. We then examined the evolution of the Stokes from the leading pulse (Figure 4.4(d and f)) and the Stokes from the trailing pulse (Figure 4.4(e and g)) at 5ns and 13ns time delays. In the case of the leading pulse, the evolution of the Stokes is typical to that of SRS with a strong increase and then a plateauing due to conversion to higher order Raman lines. However, in contrast, the evolution of the trailing Stokes shows a different trend. This can be qualitatively explained by the fact that $I_S(\tau) \propto Q_0^2$. Knowing that $Q_0^2 \propto I_{0,P} I_{0,S}$, with $I_{0,P}$ and $I_{0,S}$ being the leading pulse pump and Stokes intensity respectively. Using the expression of $I_{0,S}$ in the transient regime (see Eq. (1.5) of Chapter 1), one should expect a trend of the

trailing Stokes with the leading pulse intensity as $I_S(\tau) \propto I_{0,P} e^{b\sqrt{I_{0,P}}}$, where a and b are constants that depend on the experimental parameters. The red curve in Figure 4.4(e and g) is a fit of the measured detected 1st Stokes signal based on the proportionality function mentioned above. The agreement is reasonable, indicating thus that the origin of our Stokes signal is dominated by the pre-established Raman coherence by the leading pulse.
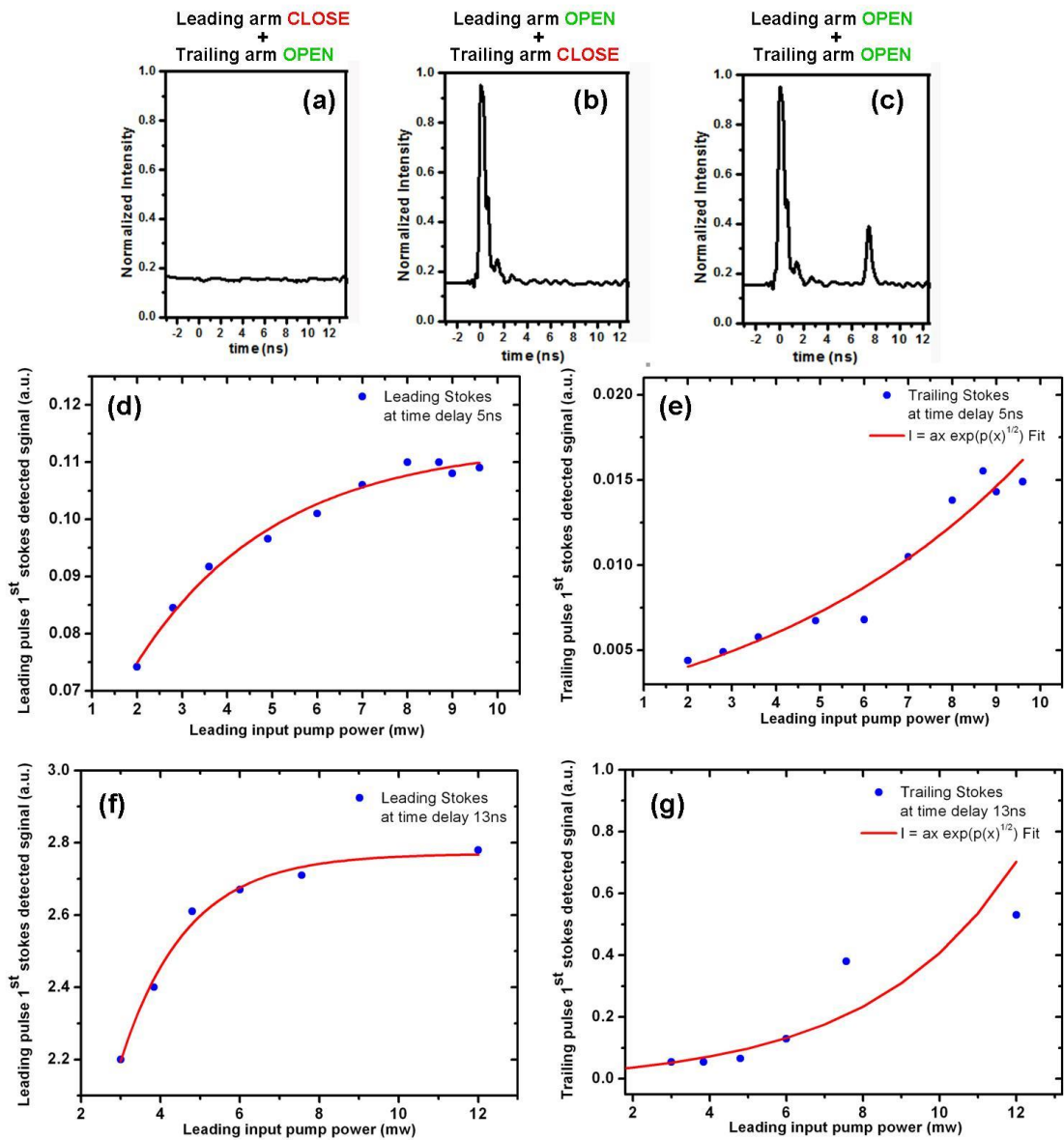
Figure 4.4: Time trace of the first Stokes recorded by PD2 (see Figure 4.1) when (a) leading pump is blocked. (b) Leading pump is present only. (c) The presents of both the leading pump and the trailing probe which is delayed by 7.4ns. First Stokes leading power as function of leading input pump power at time delay (d) 5ns and (f) 13 ns. First Stokes trailing power as function of leading input pump power at time delay (e) 5ns and (g) 13 ns.

Once these preliminary tests were done, the trailing Stokes signal was measured for different delay times. Figure 4.5 shows the Stokes temporal traces in function of delay time over a range spanning from 1 ns to 21.5 ns. The lower bound of the delay time is limited by our detector response time. The peak traces were obtained by repeating the measurements for different lengths of ESM-PCF by proceeding with a fibre cutback of 20 cm fibre-length each measurement run. A measurable Stokes peak could be detected for a time delay as long as 21.4 ns, indicating that the molecular coherence is still sufficient enough to generate Stokes. Compared to the dephasing time of 340 ps, the 21.4 ns delay is ~ 63 times the dephasing time T_2 of the molecular coherence. It is even longer than the longest time required for molecular coherence survival $\tau_r \sim 10 T_2$.

Furthermore, and although the need for realignment after every ESM fibre cut gives the measurement some uncertainty, the trailing pulse Stokes peaks show a clear exponential decay with a good fit with exp (-0.14 τ). However the time decay was found to give a decay time of 7.1 ns, which means 21 times longer than the expected $T_2 \sim 0.34 ns$. These results indicate that the theoretical model of the SRS generation we considered is not complete. A discussion on this is given later in the section.
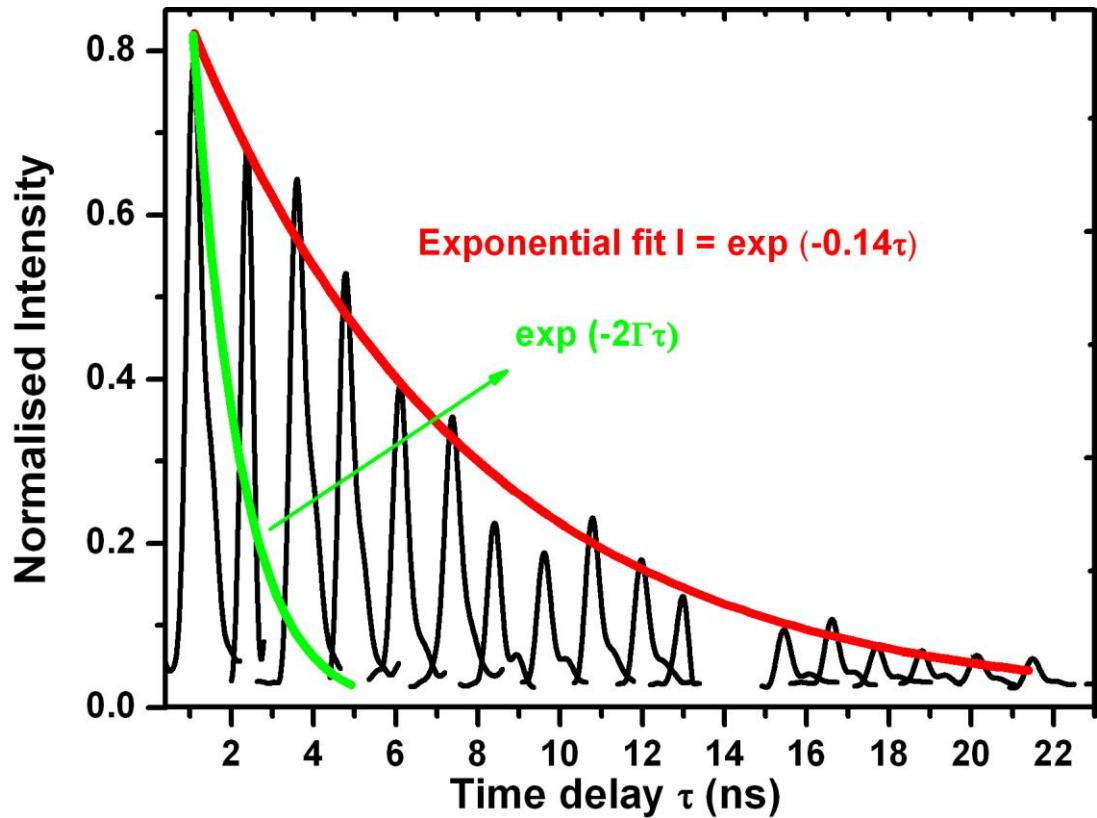
Figure 4.5: The probe Stokes intensity plotted as a function of time delay. The red curve represents the experimental fit exp (-0.14τ). The green curve is the experimental fit exp(2Γτ) for the dephasing rate (Γ~ 2GHz) rotational Raman at a pressure of ~ 10 bar [4].

In order to gain further insight on the mechanism ruling the decay of the coherence in our case, we have explored the evolution of the probe Stokes when both the delay time and the leading pump power are changed. Figure 4.6 shows, for a given time delay (here 2.4 ns), a typical evolution of the detected trace at the 1st Stokes wavelength when the leading pump is increased. The traces clearly show that the Stokes from the trailing probe pump increases with increasing leading pulse pump power. Figure 4.7 shows the measured probe Stokes intensity normalised to the probe intensity (i.e. of the trailing pulse) for different pump (leading) beam power as a function of time delay.
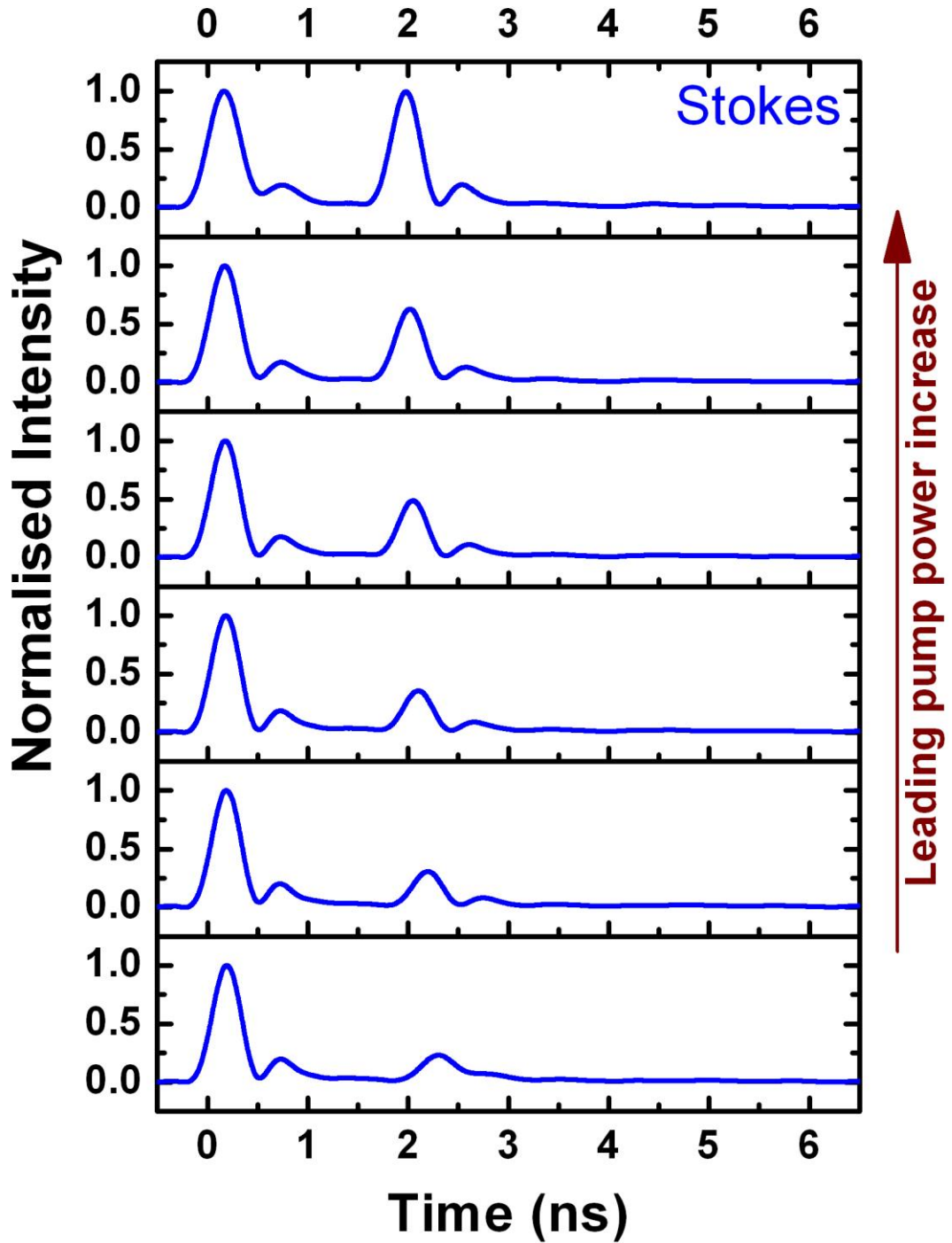
Figure 4.6: (a) First Stokes time traces evolution as the leading pump power increases recorded by PD2 photodetector; (b) Pump time traces evolution as the leading pump power increases recorded by PD1 photodetector.

One notes two major trends. Firstly, we observe two Stokes time-evolution regimes. Firstly, for delay time shorter than a given value, which decreases with the leading pulse power, the Stokes signal increases with delay time. The reason for the increase is believed to be due to the interaction between the

pre-established coherence (generated by the leading pulse) and a small amount that was generated from the trailing pulse itself. Reducing the trailing pump power was found to be hard because of the limited sensitivity of our detector. Nevertheless, this speculation was corroborated experimentally by the ~4% of Stokes signal, which is present even in the absence of a leading pulse (grey curve in Figure 4.7). Furthermore, this is corroborated with numerical simulation results presented below, and which provides the explanation of such a longer-than-T_2 decay time in the trailing pulse Stokes detected signal.
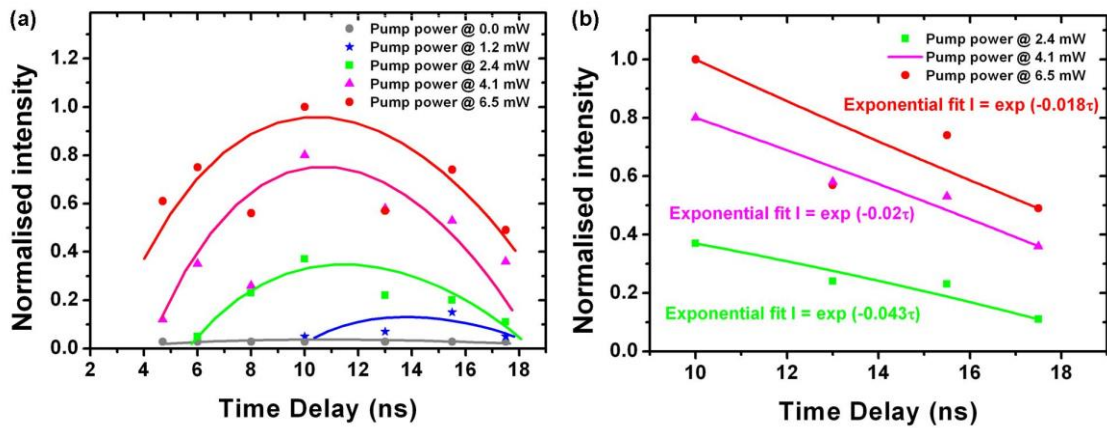
Figure 4.7: (a) Experimental measured normalised probe Stokes intensity at different pump pulse powers. (b) The decay rate at pump power 6.5 mW (55.5 ns), 4.1 mW (50 ns) and 2.4 mW (23.2 ns)[5].

To establish the governing mechanism and the dynamic of the process, theoretical simulation are performed [3] based on first-order propagation equation, see [10] for details. Figure 4.8 (a) shows the calculated spatial and temporal distribution of the Raman coherence when a single pump is considered. Here, the medium is excited with a pulsed laser with the same specifications as the one used in our experiment. After a very short length of roughly half a centimetre, which corresponds to the Raman length, a strong Raman coherence arises and reaches the quantum limit value of 1. With further propagation, this coherence drops because a fraction of the initial energy of the

---

[3] The numerical calculations were undertaken by Anton Husakou

pump is dissipated via power-conversion to higher-order Raman lines, which lie outside the bandgap window. Figure 4.8 (b) shows ρ_{12} dependence with time delay for a propagation length of 2 m. The trend confirms the decay of the coherence at the dephasing time of the Raman transition T_2 after the rapid growth ensuring the passage of the pump pulse, which even after 2 m propagation length, its maximum remains very high and a non-negligible amount persists at delay time of 5 ns. Figure 4.8 (c) shows the evolution of ρ_{12} with the fibre length 5 ns after the leading pulse. The results show that the coherence is significant over the whole fibre length.
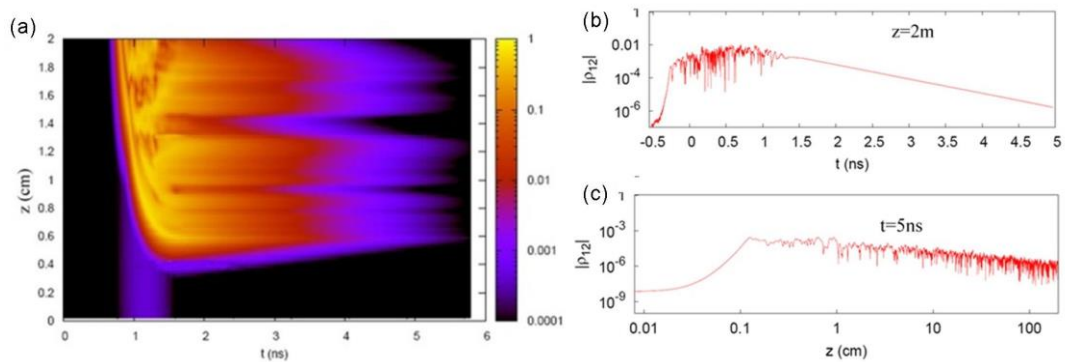
Figure 4.8: (a) Simulated spatio-temporal map of the coherence r_{12}. (b) Simulated coherence dependence on time at the output of the 2 m fibre. (c) Simulated spatial dependence of the coherence on the propagation length 5 ns after the pump pulse centre [5].

In the case of two pulses, it was too complex to reproduce the spatio-temporal map of the coherence. However, the coherence and the population difference were obtained in the case of a fixed pulse delay. Figure 4.9 shows theoretically the evolution of the Raman coherence, ρ_{12}, and the population difference, $w = \rho_{22} - \rho_{11}$, with time in the case of the leading pulse and the trailing one which are time-separated by 12 ns. This was calculated numerically using the formalism described in [11][4]. The average powers were taken to be 1.2 mW and 0.1 mW for the leading and trailing pulses respectively. This corresponds to the

---

[4] The numerical calculations were undertaken by Anton Husakou

experimental conditions of those of the black curve in Figure 4.7 (a), while taking a fibre-coupling efficiency of 50%. Furthermore, the population decay time T_1 was taken to be 10 ns [12]. Both the coherence and the population traces show an increase at the time corresponding to the passage of the trailing pulse. Furthermore, their exponential decrease after the leading pulse passage follows the expected trend with a decay time equal to T_2 and T_1 for the coherence and the population difference respectively. The Stokes energy at different time delay a long the fibre length is illustrated in Figure 4.9 (b).

Furthermore, the theoretical simulations show that for short pump-probe delays, the coherence left after the pump shifts the start of the Raman generation to earlier spatial positions, leads to larger loss during correspondingly longer subsequent propagation, as illustrated by the difference between the red and the green curves in Figure 4.9 (c). The loss occurs due to energy coupling to lossy higher order Stokes. This explains the decreasing Raman signal for decreasing delay, observed both experimentally (Figure 4.7) and numerically (Figure 4.9(c)). For larger delays the Raman generation does not develop fully. However, small coherence induced by the probe pulse and its interaction with the coherence of the leading pulse lead to notable Stokes energy from the probe. This energy decreases with increasing delay, but its slowed down by the probe pulse own coherence.

(a)

(b)

(c)
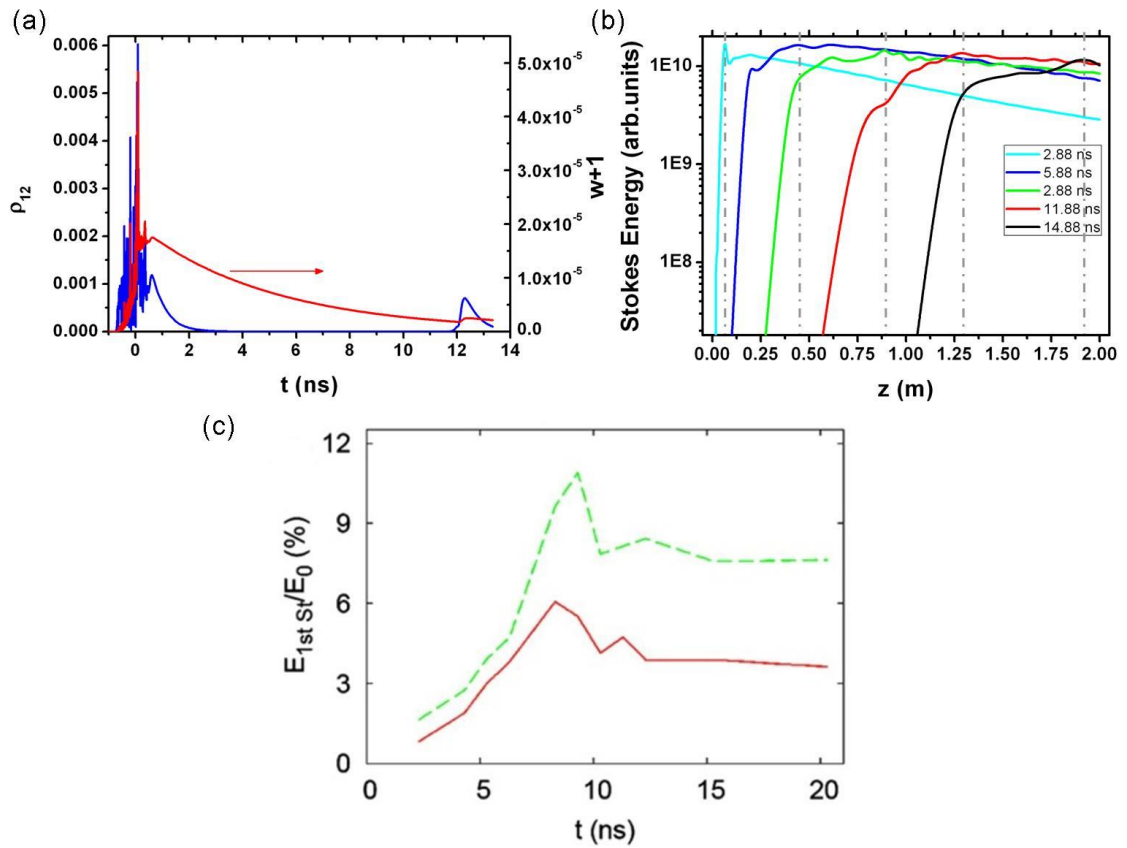
Figure 4.9: (a) Calculated Raman coherence (blue curve), and population difference between the rotational excited and ground state, expressed as w+1 (red curve) versus time, when the medium is excited by leading pump pulse and the trailing probe pulse that are time-spaced by 12 ns. Here the average power is 1.2 mW for the pump pulse and 0.1 mW. (b) Stokes energy for different time delay along the 2 m fibre. (c) The factional energy in Stokes relative to total energy of the probe pulse on the delay for 2 m propagation length (red curve) and 0.8 m propagation length (green dashed curve) [5].

4.4 Stokes visibility

In an attempt to corroborate the molecular coherence time dynamics as inferred by our measurement of the scattered Stokes from a delayed probe pulse to a stronger pulse, and also to provide further experimental data to clarify the inconsistency between the measured decay of the Stokes signal-hence of the Raman coherence, and theoretical predictions, we examine the correlation between the Stokes fields generated from the same medium but from two different time-events.
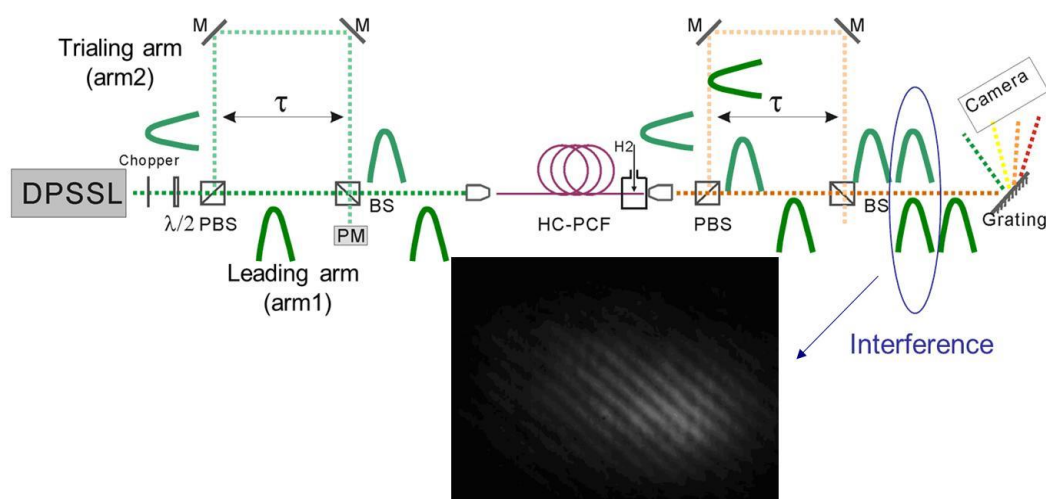
Figure 4.10: Schematic of experimental setup used for measuring the visibility. Bottom: image of the recorded interference fringes.

In other words, we examine how the Stokes fields were generated by a sequence of two delayed pulses and are correlated by measuring the interference fringes of their superimposed pulses. The set-up and rationale are similar to those reported in [3]. Figure 4.10 illustrates schematically the experimental set-up. Here, the beam from the laser source is split into two equal parts where one part is delayed with similar power (3 mw at fibre input for each arm) to generate Stokes. After that, the output from the fibre end is sent to another time delay setup. Therefore, fringes can be observed as shown in Figure 4.10. The fringes are recorded on the camera for 256 shots each time. The relative phase of the two Stokes pulse interferometric is measures. Figure 4.11 show the distribution of phase difference histogram for the pump and for the Stokes at time delay 11.3 ns and 15 ns. The histogram of phase distribution for the pump and the Stokes at delay time of 11.3 ns are illustrated in Figure 4.11 (a) and (b). The phase distribution histogram for longer delay (15 ns) is shown in Figure 4.11 (c), which shows that the molecular coherence still lasts at 15 ns. These results indicate that coherence of the pulse is transferred to the subsequent pulse for reasons which require further study.
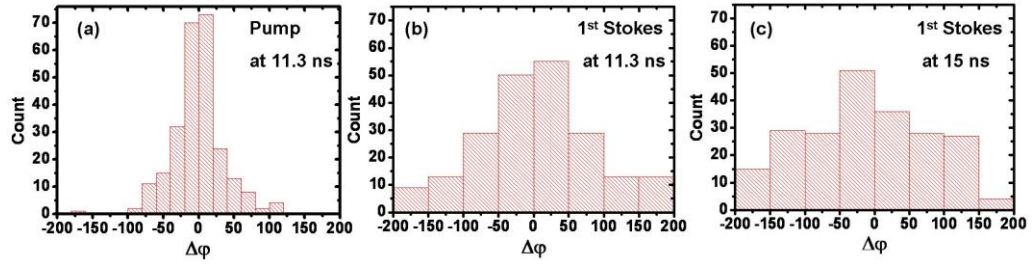
Figure 4.11: Distribution of phase difference histogram of (a) the pump at time delay 11.3 ns. (b) The first Stokes time delay 11.3 ns. (c) The first Stokes time delay 15 ns.

4.5 Summary

We report on a pump-probe experimental set-up for spatial and temporal dynamics study of molecular Raman coherence. The results show that with a modest laser pump, the molecular coherence persists after time duration as long as 42 times that of the molecular dephasing time. The decay of the Stokes signal is found to be 7.2 ns. Moreover, results show that the coherence is distributed along a multi-meter long fibre and that the coherence nears the fundamental maximum. The numerical simulations show that trailing pump has an effect on the overall coherence time and space evolution, even for pump power levels 10 times lower than the power threshold for SRS generation. This explains the longer-than-T_2 of the experimentally observed Stokes signal time decay. Cross-interference of two Stokes pulses generated by two identical delayed pulses show strong visibility (hence coherence) even at 15 ns pulse time separation. This means that pulse-to-pulse mode locking of Stokes pulses could be achieved with pump laser with a repetition rate of less than 100 MHz is possible. The cross-interference experiment is repeated in chapter 5.

Reference:

[1]   F. Benabid and P. J. Roberts, "Linear and nonlinear optical properties of hollow core photonic crystal fiber," *J. Mod. Opt.*, vol. 58, no. 2, pp. 87–124, Jan. 2011.

[2]   F. Benabid, G. Antonopoulos, J. Knight, and P. Russell, "Stokes Amplification Regimes in Quasi-cw Pumped Hydrogen-Filled Hollow-Core Photonic Crystal Fiber," *Phys. Rev. Lett.*, vol. 95, no. 21, p. 213903, Nov. 2005.

[3]   D. T. Smithey, M. Belsley, K. Wedding, and M. G. Raymer, "Near quantum-limited phase memory in a Raman amplifier," *Phys. Rev. Lett.*, vol. 67, no. 18, pp. 2446–2449, Oct. 1991.

[4]   Y. Y. Wang, F. Couny, B. J. Mangan, and F. Benabid, "Ultra-long-lived Molecular Coherence in Hydrogen Filled Hollow-core Photonic Crystal Fiber," *in Conference on Lasers and Electro-Optics 2010, OSA Technical Digest (CD) (Optical Society of America, 2010)*, paper QTuG1.

[5]   Y. Y. Wang, A. Husakou, B. J. Mangan, and F. Benabid, "Spatial and Temporal Dynamics of Raman Coherence in hydrogen-filled HC-PCF," *Lasers and Electro-Optics (CLEO), 2011 Conference on*, vol., no., pp.1,2, 1-6 May 2011

[6]   Y. Y. Wang, F. Couny, P. S. Light, B. J. Mangan, and F. Benabid, "Compact and portable multiline UV and visible Raman lasers in hydrogen-filled HC-PCF," *Opt. Lett.*, vol. 35, no. 8, pp. 1127–1129, 2010.

[7]   J. L. Carlsten and R. Wenzel, "Stimulated rotational Raman scattering in CO_2-pumped para-H_2," *Quantum Electronics, IEEE Journal of*, vol. 19, no. 9. pp. 1407–1413, 1983.

[8]   W. K. Bischel and M. J. Dyer, "Temperature dependence of the Raman linewidth and line shift for the Q(1) and Q(0) transitions in normal and para-H_2," *Phys. Rev. A*, vol. 33, no. 5, pp. 3113–3123, May 1986.

[9]   B. W. Robert, Nonlinear Optics, 4th ed. London: *Elsevier Inc.*, 2008.

[10]   A. Nazarkin, G. Korn, M. Wittmann, and T. Elsaesser, "Generation of Multiple Phase-Locked Stokes and Anti-Stokes Components in an Impulsively Excited Raman Medium," *Phys. Rev. Lett.*, vol. 83, no. 13, pp. 2560–3, Sept. 1999.

[11]   V. Kalosha and J. Herrmann, "Ultrawide spectral broadening and compression of single extremely short pulses in the visible, uv-vuv, and middle infrared by high-order stimulated Raman scattering," *Phys. Rev. A*, vol. 68, no. 2, p. 023812, Aug. 2003.

[12]   M.-M. Audibert, C. Joffrin, and J. Ducuing, "Vibrational relaxation in hydrogen-rare-gases mixtures," *Chem. Phys. Lett.*, vol. 19, no. 1, pp. 26–28, 1973.

Chapter 5

Waveform Synthesis using transient Raman comb generation in HC-PCF

In this chapter, we demonstrate the generation of a periodic train of pulse waveform with 17.6 THz repetition rate and ~ 26fs pulse duration. The waveform is achieved with a Raman comb generated using an original configuration based on transient stimulated Raman scattering using an all-fibre set-up consisting of hydrogen-filled hollow-core photonic crystal fibre (HC-PCF). The chapter covers the survival of the Raman coherence for possible pulse-to-pulse phase locking.

5.1 Historical Overview of Waveform Synthesis using Molecular Modulation

It is now established that the ability to generate ultrashort pulse lasers with adequate temporal resolution has a huge impact in science and technology as is illustrated in the emergence of the field of femtochemistry [1] or the rise of attoscience that holds the potential of probing the atomic and molecular dynamics at the single electron spatio-temporal resolution [2]–[5].

Such optical pulse temporal shaping was made possible thanks to the generation of a multiple octave wide coherent optical frequency comb. Meaning that the all comb spectral components are phase-locked together, or they share a deterministic phase relationship. This was initially achieved via high harmonic generation (HHG) and still remains the powerhouse for the field of attoscience. However, the need for optical pulses as short as 10 fs, and for peak intensities as high as 10^{15} Watt/cm^2 for noble gas excitation on one hand, and the extremely low photon conversion efficiency on the other hand make this technique far too complex and expensive for widespread or friendly use. Furthermore, HHG spectral coverage for the generation of isolated attosecond pulses is limited to XUV, which is a strong hindrance in both its accessibility by a wider scientific community and its exploration scope of matter dynamics. These constraints have led to the emergence of new alternative routes for ultra-broad and coherent spectral comb generation.

Among the techniques that have proved a potential to properly address the HHG shortcomings mentioned above, is high order stimulated Raman scattering (HSRS) in Raman media such as hydrogen or deuterium [6]–[10]. It is noteworthy that within HSRS, we count mainly three schemes with their own strengths and weaknesses, which stem from their difference in the physics involved. These schemes are (1) Molecular modulation method [11], (2) impulsive Raman method [7], and (3) transient Raman method [10].

The first method is arguably the most successful and richest in the physics involved in exciting the medium.   The principle of molecular modulation is to prepare a Raman medium to evolve adiabatically into a coherent superposition of the ground and excited states involved in the two-photon Raman transition. In other words the Raman medium is set to have maximum Raman coherence. For this to happen, the medium is preferably initially prepared so most of the molecules are in their ground state, and is excited by two narrow linewidth pulses whose frequency difference is finely controlled so it is slightly detuned from the Raman resonance. It was originally suggested and demonstrated by Harris and co-workers [11], [12], using cryogenic (Nitrogen temperature) hydrogen and/or deuterium driven by two narrow-linewidth, transform-limited pulse lasers with duration and energy in the tens of ns and 100 mJ levels respectively. The frequency difference can be tuned down to the laser linewidth limit of ~50 MHz. With this set-up several results were reported comprising generation of collinear and mutually coherent combs as broad as 1000 THz, and of pulses with a single-cycle duration [13]. More recently synthesis of several waveforms like saw tooth, square or cosine were demonstrated by Kung and co-workers[14]. Notwithstanding these major achievements, they come at the cost of a set-up that is as correspondingly complex as that of HHG, and the overall efficiency is hindered by the low gas pressure, thus requiring very powerful laser pulses. Finally, and as a side note, it is noteworthy to mention that another promising feature of molecular modulation is the fact that it is amenable to CW excitation. Raman comb generation using molecular modulation in CW regime is now turning into a goal of several research groups. The third part of the thesis (chapter 6 and 7) covers our progress towards this aim.

Impulsive Raman technique consists of exciting a Raman medium with a pulsed laser, which is sufficiently short that its spectrum comprises components whose frequency difference is larger than that of the Raman resonance to impulsively excite the medium. This means that the latter must be exposed to an intense laser pulse with a duration shorter than the period of Raman

oscillation (i.e. $\tau < \Omega_R^{-1}$ with Ω_R being the natural frequency of the Raman resonance). This was demonstrated by Nazarkin *et al.* [7] in SF₆ using 30 fs Ti:sapphire laser at 800 nm. They experimentally illustrated the generation of high order Stokes and anti-Stokes sidebands in impulsively excited medium. This technique has been able to produce pulses as short as 3.8 fs in the near UV region [15]. However, "clean" Raman sidebands were only demonstrated with a second weak delayed pulse, which experienced frequency modulation via the generated coherence from the initial pulse. Indeed, because of the extremely high peak power of the initial pulse, other Kerr related optical nonlinearities, such as self-phase modulation and self-steepening, compete with the SRS process to generate a super continuum like spectrum. In addition to the complexity of the set-up, which compares with those for HHG, the overall optical conversion efficiency is comparatively poor. Indeed, because of the non-adiabatic coherence generation, and the intrinsic Raman gain reduction because of the short pulse duration, the conversion is much lower than what one could expect from an adiabatic excitation. This conversion is further reduced by the use of an initial strong pulse to prepare the medium.

The third technique relies on transient Raman scattering. This initially consisted of the excitation of the Raman medium with pulses whose duration is shorter than the dephasing time of the medium molecules T_2. Within this context, a broad comb based on rotational SRS in hydrogen was demonstrated using an 800 fs Ti:sapphire laser by Iamasaka and co-workers [8], who also speculated on the possible phase-locking of such a spectrum, but with no theoretical or experimental demonstration. More recently, and owing to the recent development of HC-PCF, our group demonstrated that transient regime of SRS could be accomplished using much longer pulses compared to T_2 and with much lower pumping powers [16]. A pure-rotational Raman comb of ~ 70THz bandwidth was generated, and whose bandwidth was limited to the transmission window of the PBG HC-PCF used [17]. A multi-octave hydrogen ro-vibrational SRS, from 325 nm to 2300 nm, was generated afterwards using the broadband guiding Kagome HC-PCF and 12 ns laser pulses [10]. Finally,

because in such a configuration the Raman spectral lines are initiated from the quantum noise induced spontaneous emission, legitimate concerns on the coherence of the generated comb were raised, and which were clarified by a set of experiments and theory [18], [19]. The results show that these comb lines exhibit intra-pulse strong self-coherence and mutual coherence. This remarkably counter-intuitive result was simply explained by the modal description of the quantum noise, whereby the initial zero-point motion of the molecular polarization or its associated Stokes field can be decomposed in a linear superposition of coherent spatio-temporal modes (STM). Under proper excitation; ultra-high gain, Raman net gain and the tight and long confinement of the Raman medium in HC-PCF, temporal and spatial filtering of the multi-mode vacuum Stokes field can occur so only one single pure quantum state is amplified to the macroscopic level. The net result is transform-limited Stokes and anti-Stokes pulses are generated in a correlated fashion, which then frequency modulate the Raman medium to generate higher order sidebands. However, the expected pulse train is yet to be demonstrated. Secondly, in light of the results in chapter 4, the possibility for this coherent comb to be pulse-to-pulse phase-locked is yet to be addressed.

The work presented in this chapter describes the first demonstration, to the best of our knowledge, of the synthesis of a 17.6 THz repetition frequency of 26 fs pulse train AC waveform using Raman comb generated in hydrogen-filled Kagome HC-PCF. The comb is generated by exciting the medium with a 400 ps pulse pump and a Stokes seed generated under transient SRS conditions. The results are corroborated with the theoretical model reported in [10], [18], [19], and the role of the "transiency" of seed Raman generation is demonstrated. Finally, in anticipation of extending this technique to a pulse-to-pulse waveform synthesis, we performed cross-interference between two Stokes generated by exciting the hydrogen filled fibre with two delayed identical pulses. The results corroborate the results of chapter 4, with a decay time of the measured visibility of 28 ns.

5.2 Experimental setup and rationale

Figure 5.1 shows the experimental setup, which consists of two stages. The first stage (Figure 5.1(a)) is the pure rotational Raman comb generator. The second consists of a set-up to measure the comb components mutual coherence via sum frequency generation (Figure 5.1 (b)), and a waveform trace recorder using an auto-correlator (Figure 5.1 (c)).

The schematic of the comb generator setup comprises two stages: (i) one stage, coined the Raman frequency down-shifter (RFDS), is set to generate 1st order Stokes under the transient SRS regime, (ii) a second stage is set to generate the pure rotational coherent comb (PRCC). The set-up architecture is described as follows. A microchip laser operating at 1064 nm with total output energy of 90 μJ and pulse duration of ~ 400 ps is split into two beams. The first part of the beam (~12 μJ) is sent to the RFDS by coupling 75% of its energy to a 50 cm long photonic bandgap (PBG) HC-PCF (first stage), to generate favourably, and under a highly transient regime, the first order rotational Stokes[16]. The second beam (~75 μJ), along with the frequency-down shifted one, is directed to the PRCC. This is done by recombining temporally and spatially the second beam with the generated Stokes from the RFDS, using a delay line and a beam splitter (BS). The PRCC consists chiefly of a 4 m long piece of hypocycloid core Kagome (HC-PCF)[20], [21]. Figures 5.3 and 5.4 show the properties of the two HC-PCFs used here. The PBG fibre has a core diameter of 7.5 μm, a transmission window spanning from 1000 to 1200 nm, and a loss figure of ~ 75dB/km at 1064 nm (Figure 5.3). The detail of the guidance and the fabrication process of the fibre are described in chapter 2. The narrow transmission window will be exploited to selectively generate the 1st Stokes [16]. The IC guiding HC-PCF is a hypocycloid core Kagome (HC-PCF)[20], [21], which has a core diameter of 34 μm, a broad transmission bandwidth wider than the used range 700 nm -1700 nm shown here, and with a loss figure of ~ 250 dB/km, as

shown in Figure 5.4. The two fibres are filled with H_2 at a pressure of 10 bars so that the frequency difference between the pump and the seed is equal to the Raman resonance. To ensure that the pressure remains the same in both fibres, the fibre ends were attached to the same gas-supply manifold.

The rationale of the set-up architecture is summarised in the following points: (I) the use of a single and small laser is motivated by the desire to make out of this set-up a fibre-based compact and portable coherent comb generator. Secondly, the set-up is uniquely frequency-scalable because of the difficulty in finding a Stokes seed laser whose frequency can easily match the difference of any chosen pair of pump laser frequencies and Raman resonance. (II) The dual pump scheme is motivated by the need to suppress the vibrational lines so as to have a singly frequency-spaced comb, unlike the ro-vibrational comb which is obtained with a single pump [10], [22]. This was identified as a limitation towards the generation of pulse train using transient SRS in HC-PCF [10]. (III) The generation of the Stokes under the transient regime is dictated by the necessity of having a transform-limited pulse. This is the most crucial feature of the set-up. Below we recall how the spectral and temporal content of the Stokes is determined under the transient regime, and how this affects the mutual coherence of the generated comb.

We recall that the spatio-temporal content of Stokes field that is spontaneously emitted by a Raman medium can go, in some cases of transient SRS, through an amplification process, from a thermal-like distribution of independent spatio-temporal modes (STM) to a macroscopic transform limited pulse with a well defined phase, frequency and envelope [18], [19], [23]–[25]. In other words, and using classical language, the expression of Stokes field at the output of a Raman medium $E_{-1}(\rho, z, t)$, transforms from a Karhunen-Loeve expansion [26] of a set of individual and uncorrelated coherent modes or wavepackets:

$$\hat{E}_S^{(-)}(\rho, L, \tau) = \sqrt{(2\pi\hbar\omega_S n_S / c)} \left(\sum_n \left(\sum_k \hat{b}_k^{(n)} \psi_k(\tau) \right) \sqrt{\beta_n} \, \Phi_n(\rho) \right) \qquad (5.1)$$

to a field $E_o(\rho, z, t)$: $E_{-1}(\rho, L, \tau) = \alpha_0^* E_0(r, z, t) p(\Delta\beta_0, z, t) E^{i\theta} + \varepsilon$, with a deterministic phase θ and an envelope set by the molecular polarization, $p(\Delta\beta_0, z, t) E^{i\theta}$ and the laser pump field. Variable ε represents residual small random terms that stem from other amplified STM. In Couny *et al.* [10] experimental conditions corresponded to the net gain G was ~ 180 and the pulse duration equal to 12 ns, the amplitude of higher order STM relative to the transform-limited pulse amplitude was estimated to be about 0.1%. This noise contribution could be further decreased by increasing the Raman net gain and by reducing the ratio between the pulse duration to the dephasing time, τ/T_2 [26]–[29]. Compared to Couny et al. the present net gain for the Stokes generation was about 1100 and is thus 6 times larger than in[10]. This is chiefly due to the larger FOM which one can obtain with smaller core fibres (see Chapter 1). The present pump pulse duration of 400 ps is 30 times shorter. Consequently, one should expect a much larger extinction ratio between the dominant STM that was amplified to a macroscopic transform-limited pulse and noise. This STM filtering enhancement is even further boosted by the use of PBG HC-PCF, which results in a reduction of spontaneous emissions over a significant solid angle [17].

Furthermore, the single conversion to the Stokes which, through the use of PBG HC-PCF, enabled a higher conversion is achieved even with low pump power. Secondly the generated coherence could survive for a much longer time (see Chapter 4). This point, even though, as we will see below, is not necessary for the generation of auto-correlation waveforms; it would undoubtedly open the exciting possibility for pulse-to-pulse phase locking. This possibility is discussed in the last section of the chapter.

Once the Stokes pulse is generated, its field ε_{-1} and that of the pump ε_0 drive the molecular coherence Q of the same Raman medium contained in the second fibre via the relation $\partial_\tau Q \propto E_0^* E_{-1}$. This in turn, frequency-modulates the Stokes and pump field at the Raman frequency, leading the total electric field amplitude of the pump-plus-sidebands with the following form:

$$E = \sum_{n=-N}^{N} E_n \exp\left[-i(\omega_0 + n\Omega_R)t + i\beta_n z + in\theta\right] \tag{5.2}$$

where n is the order for Stokes (negative integers) and anti-Stokes (positive integers). β_n is the propagation constant of the nth order Raman line. A salient feature of the comb is how the Stokes deterministic phase θ is now "disseminated" throughout the comb components. The effect of this phase on the autocorrelator waveform traces is discussed in a later section of the present chapter. Consequently, the current set-up is a novel scheme to synthesise intra-pulse optical waveform at a few femtoseconds time-resolution.

Now that the motivations of the set-up of the comb generator are described, we continue the description of the second stage of the set-up. Figure 5.1(b) and (c) schematically show the two detection schemes we explored. The first one is an interferometer to measure the degree of mutual coherence via sum-frequency. The detail of the measurement protocol is given below. The second scheme is an autocorrelator (AC) for the measurement of AC waveform.
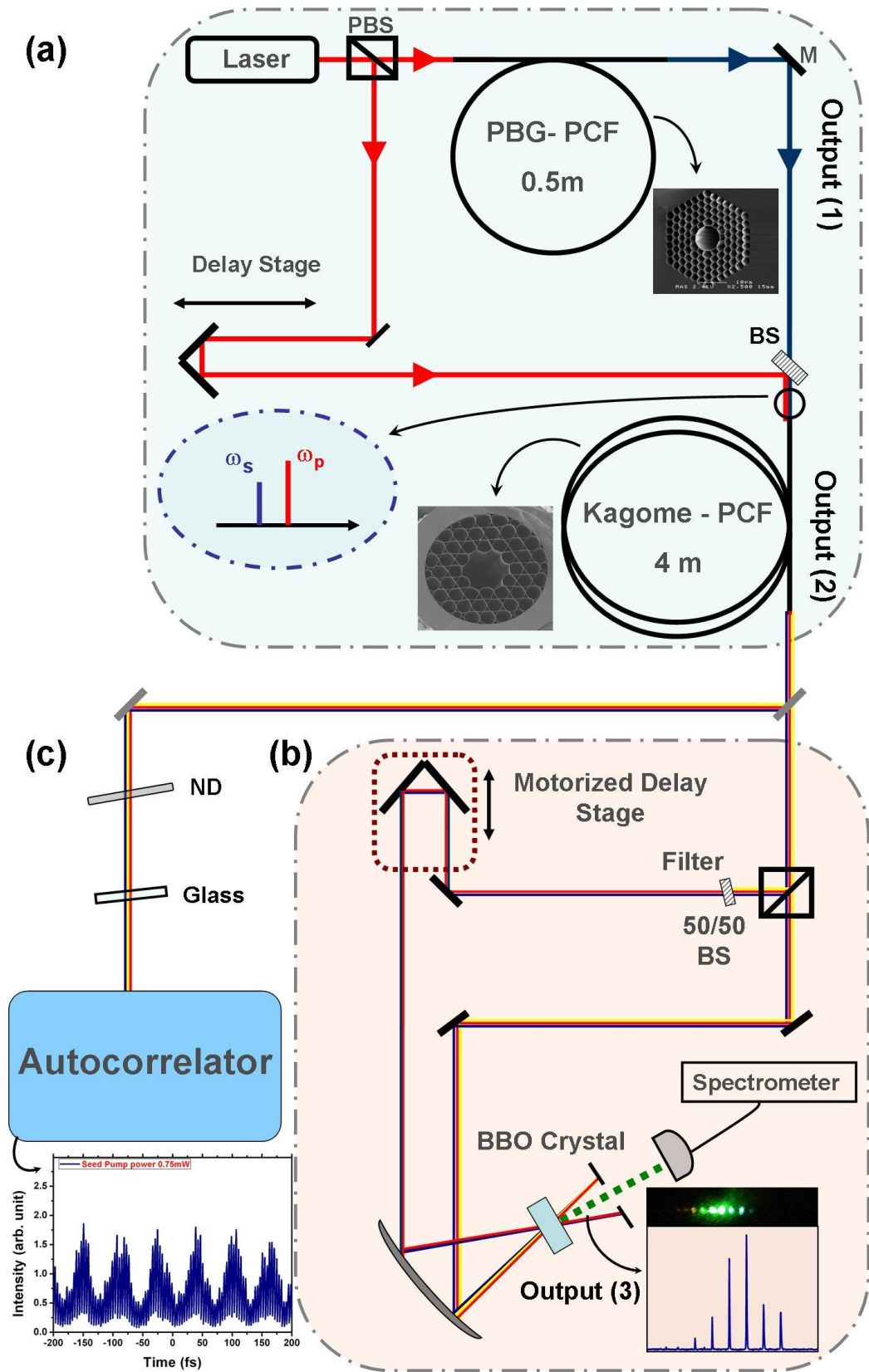
Figure 5.1: Schematic of experimental setup (a) the Raman comb generation set up; (b) Interferometer setup for phase detection of Raman lines; (c) Setup for Temporal profile of the comb.
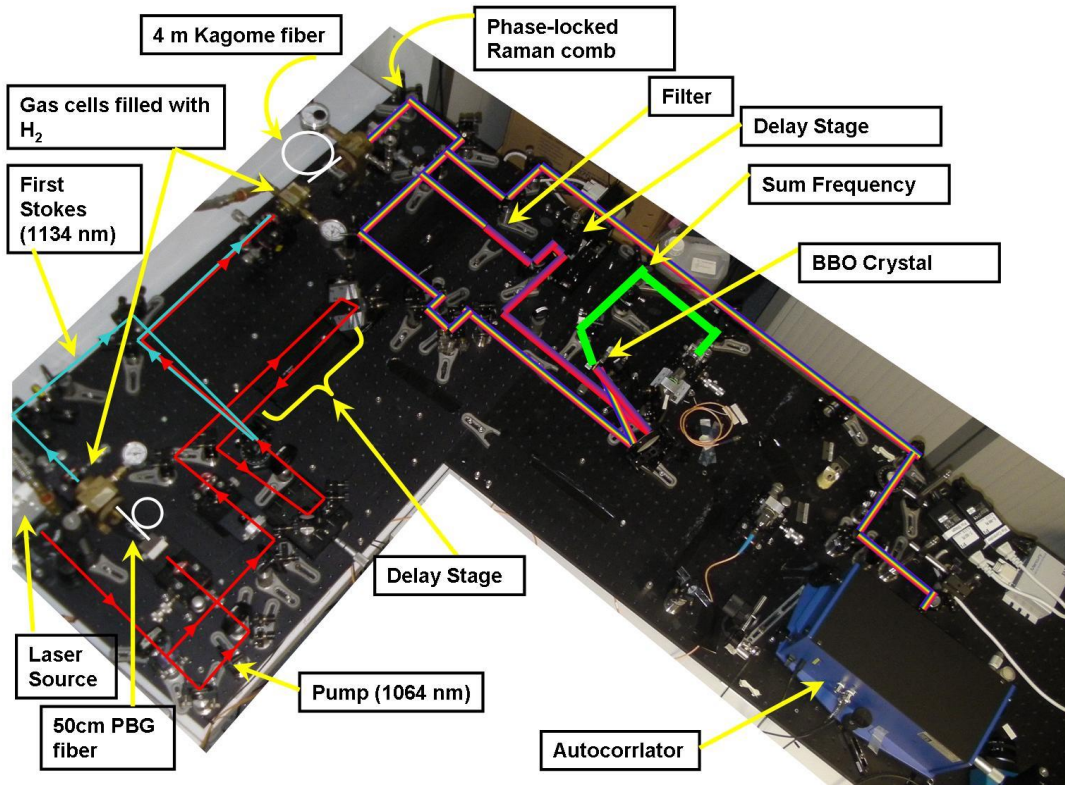
Figure 5.2: Photograph of the experimental setup.
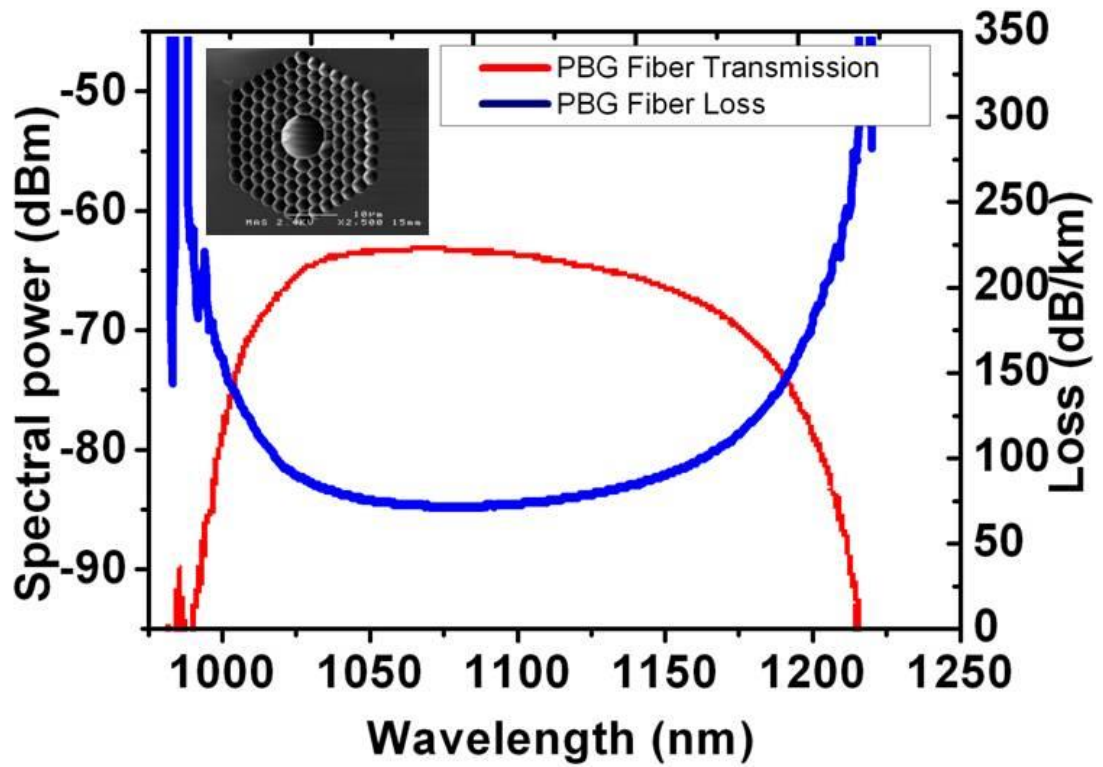
Figure 5.3: The PBG fibre transmission and loss measurement, inset is SEM image of the fibre.
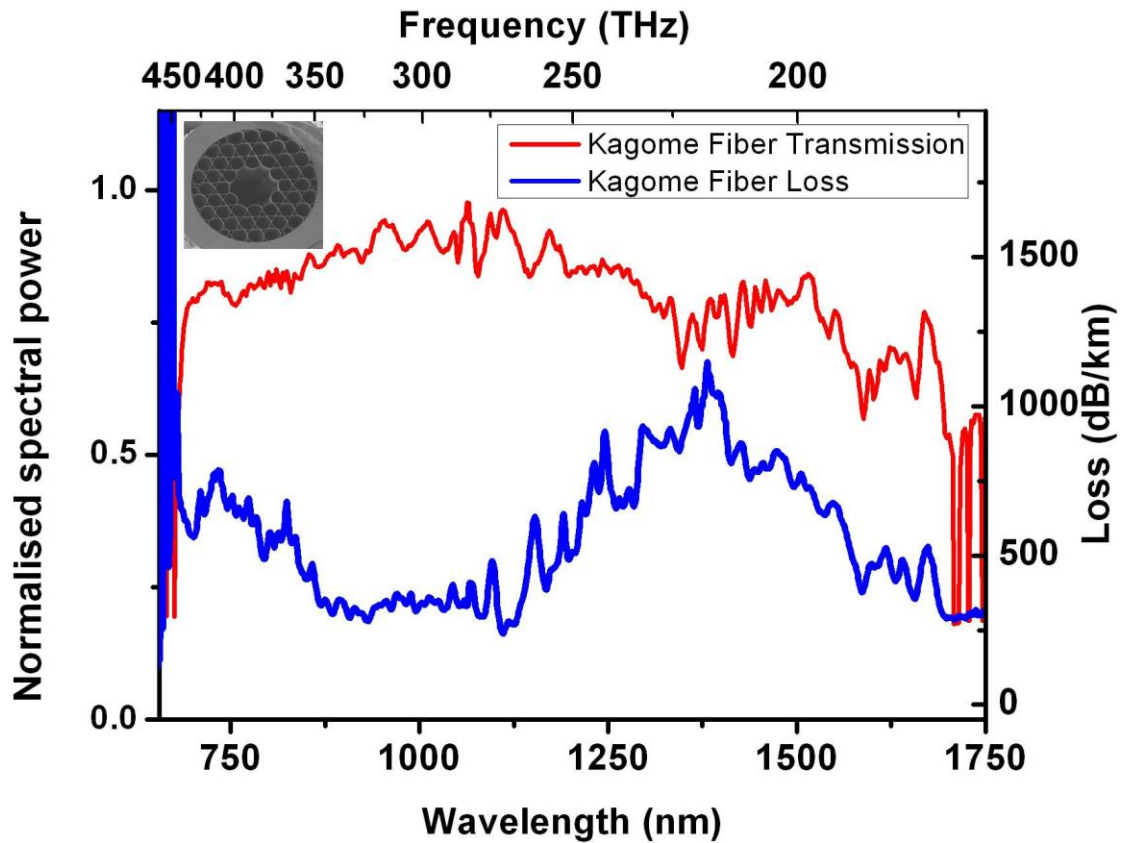
Figure 5.4: Kagome HC-PCF transmission and loss measurement, inset is SEM image of the fibre.

5.3 Experimental Results and Analysis

5.3.1   Pure Rotational Raman Generation

We have seen above the advantage of using the PBG HC-PCF for an efficient and selective generation of the 1st rotational Stokes. Figure 5.5, which shows the transmitted spectrum from H_2 filled PBG HC-PCF, corroborates this. Figure 5.5(a) shows that more than 98% of the pump was converted to the rotational Stokes at 1134 nm. Despite the large Raman net gain of over 1000, no other Raman lines are generated. This is because the second stokes (1219 nm) lies outside the transmission window, and the anti-Stokes is suppressed via pump

polarization control [16] (Figure 5.5(b)). A fraction of the Stokes power is sent to the PRCC and acts as a seed for the next part (output (1) - see Figure 5.5(a)).

Figure 5.5: (a) Pump source and first Stokes generated in PBG fibre recorded by optical spectrum analyser. (b) PBG fibre transmission and first Stokes Raman sideband spectra.
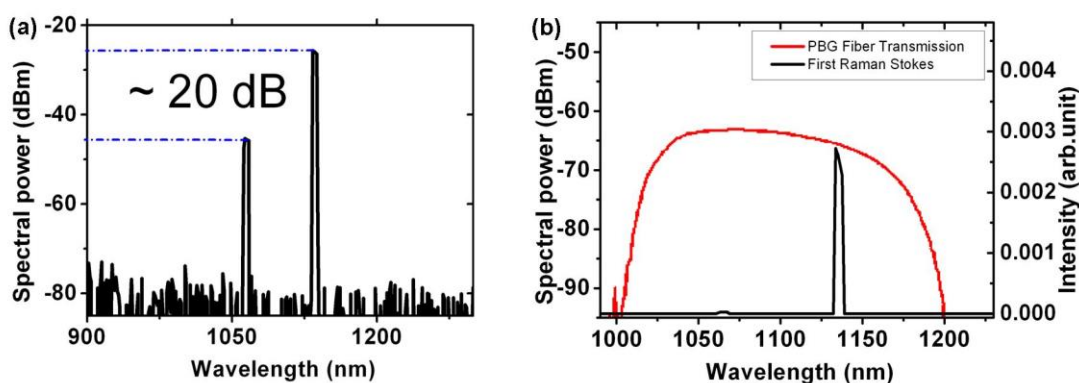
Figure 5.6 show the SRS spectra generated in and transmitted through a 6 m long H_2 filled hypocycloid core Kagome HC-PCF. The fibre was excited either with a single pump at 1064 nm or in the presence of a seed at the Stokes frequency generated from the RFDS. The average power that was sent to the Kagome HC-PCF was measured to be ~30 mW (pulse energy of 60 μJ), with a coupling efficiency estimated to be 50%. The seed power that was sent to the fibre was varied using a neutral density filter to range from 0.01 mW to 0.45 mW. For the example shown in figure 5.6, the seed power was measured to be 0.04 mW (i.e. 0.1% of the pump power). It is noteworthy to mention that varying the seed power within the above-mentioned range has little effect on the generated comb line strength.

Figure 5.6(a) is the spectral comb when the hydrogen filled fibre is excited with the pump alone. The spectrum contains the typical ro-vibrational sidebands. Figure 5.6(b) shows the generated comb when the fibre is excited by both laser pulses. The average power of the comb was measured to be 16 mW. Here, it is readily noticeable that the rotational sidebands of the vibrational anti-Stokes were suppressed, as is shown in Figure 5.6(c) where both spectra are super-imposed. The red comb is the ro-vibrational one and generated from the

pump. The blue one is a pure rotational comb, resulting from the presence of the Stokes pulse. The presence of the first rotational Stokes seed also enhances the generated sidebands power.
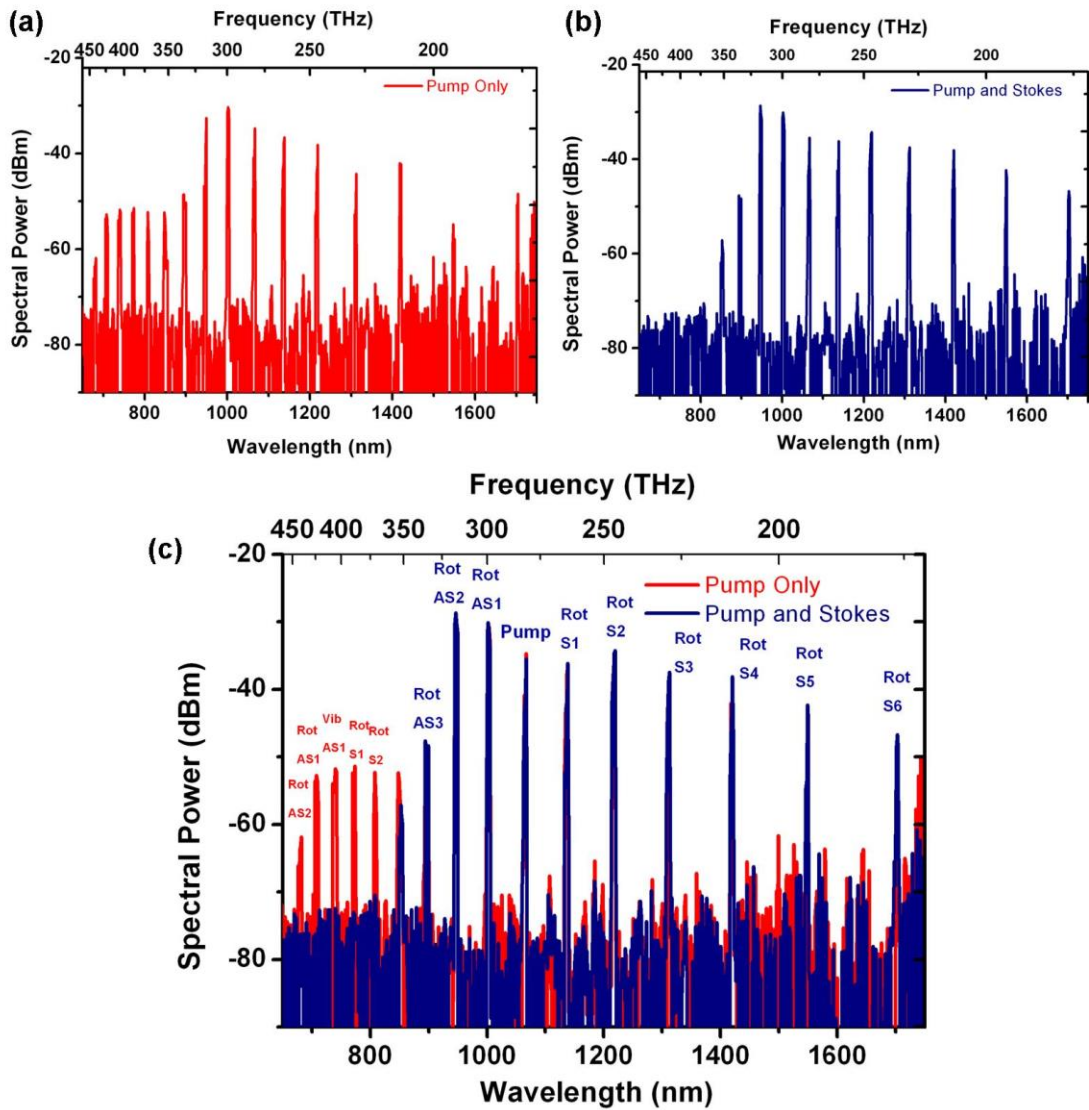

Figure 5.6: (a) Raman sideband spectrum lines generated in HC-PCF without the seed Stokes introduced. (b) The spectrum after coupling the Stokes seed (c) Spectra of Raman sideband with and without Stokes seed superimpose.
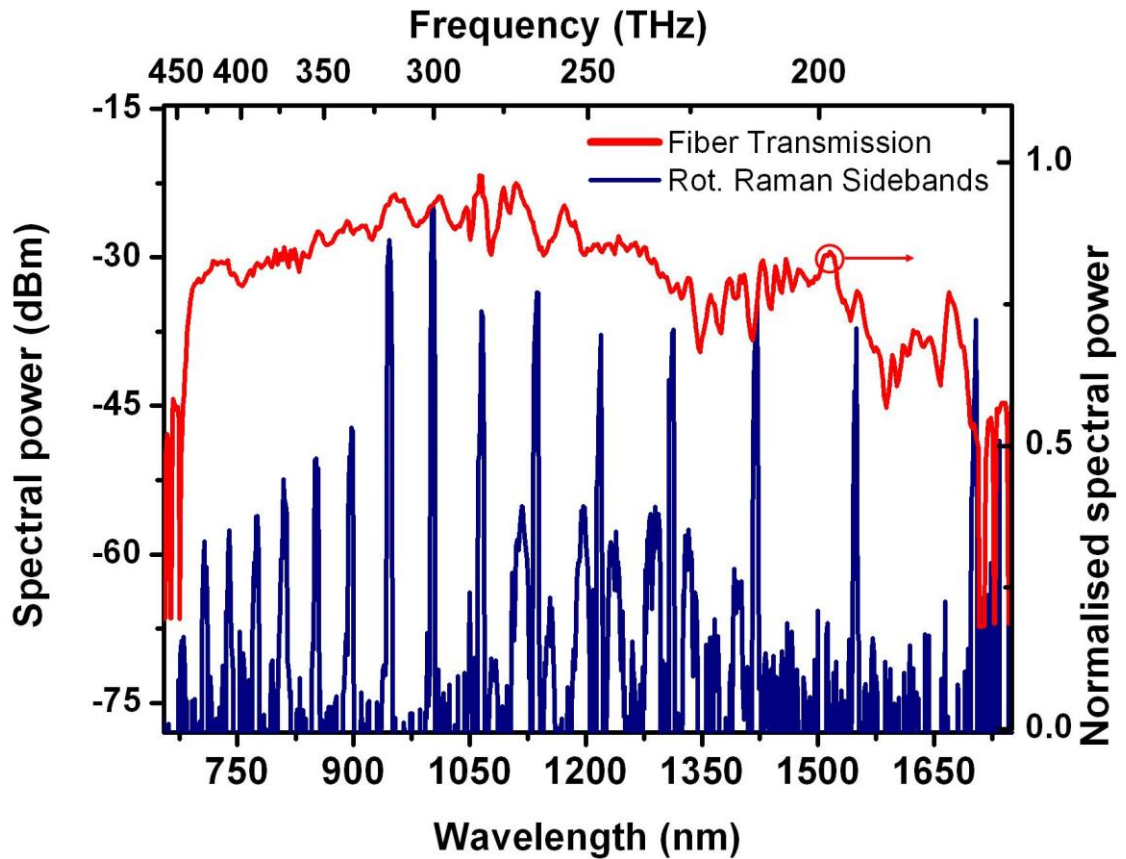
Figure 5.7: Pure rotational Raman comb generation within the Kagome transmission bandwidth.

Once the above preliminary work was finished, the fibre length was cut to 4 m as it is a sufficient length for the comb generation. Figure 5.7 shows a 4 m long HC-PCF generated Raman comb covering almost the whole of one of the Kagome HC-PCF transmission bands and spanning from 650 nm to 1700 nm. This comb is sent to the detection stage of the set-up to undertake sum-frequency generation (SFG) and auto-correlation measurements.

5.3.2   Sum frequency generation

The first part of the detection set-up stage is a sum-frequency generator set-up (see Figure 5.1(b)). It consists of a spectral interferometer for spectral phase measurement, whose principle is introduced in [30]. The comb is first split by a non-polarizing beamsplitter.   In one arm (arm I) of the interferometer, a

bandpass filter is used to extract the pump and the first-order Stokes. The pump and 1st Stokes beam passes through a delay line using a single axis precision stage. In the second arm (arm II), we pass the whole comb. Both beams from arm I and arm II are then focused on to a 300 μm thick β-barium-borate (BBO) crystal using a concave mirror. As a result, a sum-frequency spectrum is generated (output (3)). The SFG comb lines are recorded using a fast photo spectrometer. From the spectrum both the power and a relative phase of each SFG component is deduced, thus demonstrating the phase coherence between the comb spectral lines. Figure 5.8(a) and 5.8(b) shows a photo of the dispersed SFG comb lines on a black screen, and the measured spectrum respectively. Each line is labelled with its corresponding sum frequency. The spectrum also shows the measured relative phase of each SFG comb line. This was deduced from the trace of each line power with delay time. Here, the intensity of five spectral components, chosen from the sum-frequency spectrum, was simultaneously measured when the delay line was varied. The results clearly show sinusoidal variation with fixed period of 17.6 THz as a function of the delay-time over a span of ~400 fs. This is evidence that our comb spectral components are mutually coherent, or put differently, phase-locked.

However, it is noteworthy to emphasise that such compelling experimental evidence of phase-locking applies to intra-pulse components only. This means that our SFG scheme demonstrates single shot coherence and not pulse-to-pulse coherence. This is easily deduced from the theory reported by our group [10], [18], [19]. Indeed, the electric field of a given comb line can be written as $E_n(t) = A_n e^{i\omega_n t} e^{i\phi_n}$. Here, A_n and ϕ_n are the real amplitude and phase of the nth order Raman respectively. The frequency of each comb line is $\omega_n = \omega_0 \pm n\Omega_R$, where Ω_R is the rotational frequency shift of H_2. In addition, we have seen that $\phi_n = \beta_n z + n\theta$, with θ being the intra-pulse deterministic phase of the

amplified Stokes from the quantum noise. In our SFG experimental conditions, each component of the measured SFG spectrum, labelled by an integer m, is the result of sum-frequency generation by two pairs of lines. One pair results from the mixing of the pump (i.e. $n=0$) with a given m^{th} order Raman line from the unfiltered arm (arm II), and the other pair results from mixing the 1st Stokes ($n=-1$) with the $(m+1)^{th}$ order line from the unfiltered portion. Therefore the intensity of the SFG signal at frequency ω_m is:

$$
\begin{aligned}
\langle I_m(\tau) \rangle &\propto \left\langle \left| A_0 A_m e^{i(\Omega_{Raman}\tau + \phi_0 - \phi_{-1} + \phi_m - \phi_{m+1})} + A_{-1} A_{m+1} \right|^2 \right\rangle \\
&= \left\langle A_o^2 A_m^2 + A_{-1}^2 A_{m+1}^2 + 2 A_0 A_m A_{-1} A_{m+1} \cos(\Omega_{Raman}\tau + \phi_0 - \phi_{-1} + \phi_m - \phi_{m+1}) \right\rangle
\end{aligned}
\tag{5.3}
$$

Recalling that the phase of the nth order Raman is $\phi_n = \beta_n z + n\theta$, we get $\Delta\phi_m = \phi_0 - \phi_{-1} + \phi_m - \phi_{m+1} = (\beta_0 - \beta_{-1} + \beta_m - \beta_{m+1})z$. We see that the pulse-to-pulse random phase θ is suppressed from the SFG comb line intensity. Consequently, the average intensity of mth line of SFG spectrum, $\langle I_m(\tau) \rangle \propto (1 + V_m \cos(\Omega_R \tau + \Delta\phi_m))$ is a modulated signal at the Raman frequency with phase and visibility set by the fibre dispersion and the power at the Raman lines of the Stokes and the pump from arm I and the mth and $(m+1)^{th}$ order Raman lines from arm II. Furthermore, even when we proceed with averaging over several shots (which is the closest representation to the experimental conditions), and add residual random phase noise, which could be either due to technical noise such as thermal and/or vibration stress on the fibres or other optical components, and laser phase jitter, or it can rise from the inherent quantum noise of our SRS process, we can write the phase of each comb line as $\phi_n = \beta_n z + n\theta + \varepsilon_n$. Consequently, the phase measured in SFG signal is $\Delta\phi_m = (\beta_0 - \beta_{-1} + \beta_m - \beta_{m+1})z + \varepsilon$, where ε is the uncorrelated sum of the different comb line residual random phase. Since our experimental results show robust intra-pulse phase locking, we conclude that firstly the fibre dispersion induced phase noise is negligible from pulse to pulse, and secondly

that the high order STM phase noise "ε" is sufficiently small to state that we have amplification of a single dominant STM. Consequently, we have, to a phase constant offset, $\Delta\phi_m \approx 0$. This also means that the generated 1st Stokes is indeed amplified from a single dominant STM and a strong extinction ratio with other possible amplified STM.
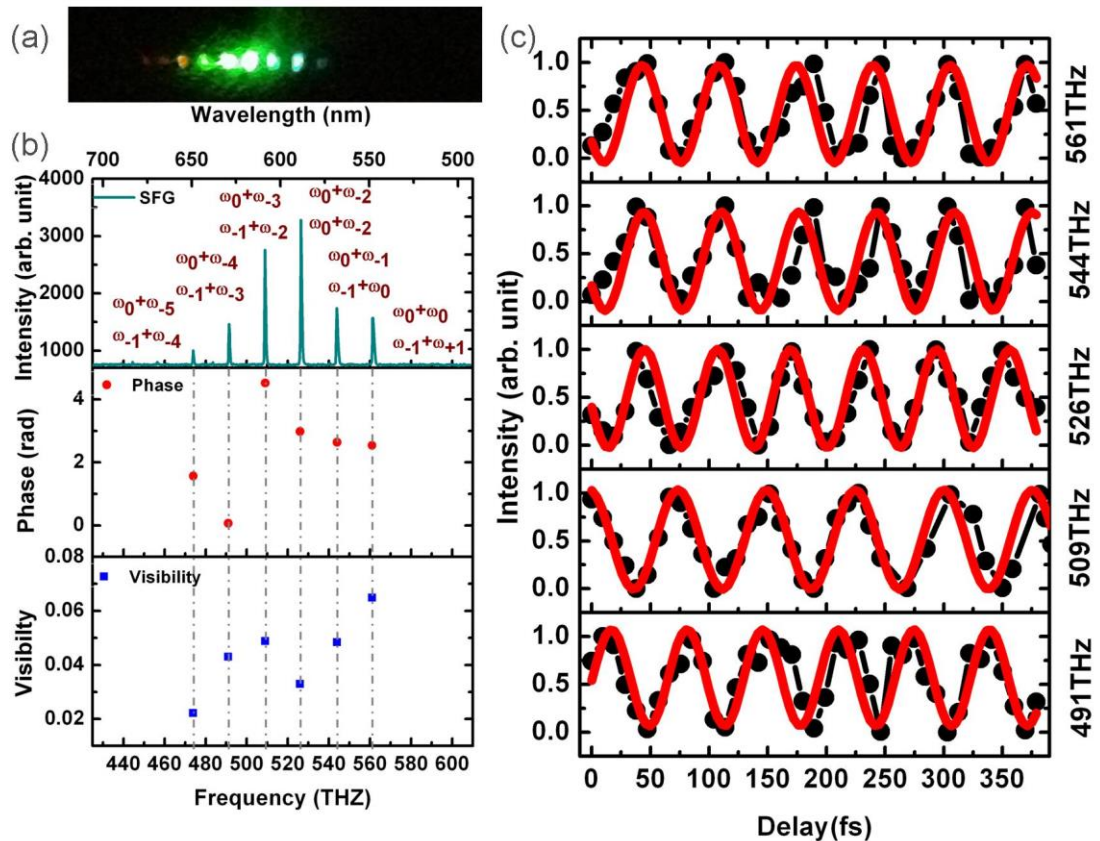

Figure 5.8: (a) Photo of the sum-frequency generated by BBO crystal. (b) Sum frequency spectrum from BBO crystal (top), phase measurements (middle) and visibility measurement (bottom). (c) Intensity variation of the sum-frequency as function of delay (black circle) and their fitting (red curve).

5.3.3 Temporal profile of phase-locked Raman comb

This section further explores the robustness of the intra-pulse phase-locking of transient SRS comb generation. This is carried out by synthesising the temporal profile of the comb by controlling the magnitude and the relative phase of a selective comb component. In our case, however, because of the lack of adequate equipment to have a line-by-line control, we limit our demonstration to the generation of a pulse train, which is expected from the fibre dispersion.

The schematic of the waveform trace recorder is shown in Figure 5.1 (c). The resulting comb "output (2)" from Figure 5.1(a) is directed towards a commercially available Autocorrelator (AC). Figure 5.9 (a) illustrates again the set-up with the typical AC traces we obtain when the seed laser beam is on and off. The resulting AC trace shows a train of pulses with a period of 17.6 THz, which matches that of the rotational Raman resonance, and pulse duration of 26 fs, as illustrated. In the absence of the Stokes seed, Figure 5.9 (b), the AC trace remarkably shows no pulse train as illustrated. Figure 5.9(c) shows a A snapshot of a recorded video of AC trace of train of pulses when the Stokes seed is on and off. This result can easily be explained by the relatively lower Raman net gain with the H_2-filled Kagome HC-PCF than in the case of the PBG HC-PCF. In the case of the Kagome fibre the Raman net gain is estimated to be ~260 when 30 µJ pulse energy is coupled into the fibre compared to ~1100 in the case of the PBG fibre. As a matter of fact the gain of 260 is an upper value, as the higher order Raman sideband generation reduces the gain. Consequently, the amplification of a dominant single STM with a sufficiently high extinction ratio relative to the other STM (noise) is weakened, and $\Delta\phi_m$ is no longer pulse-to-pulse stable. The filtering effect of the gain is further explored later.
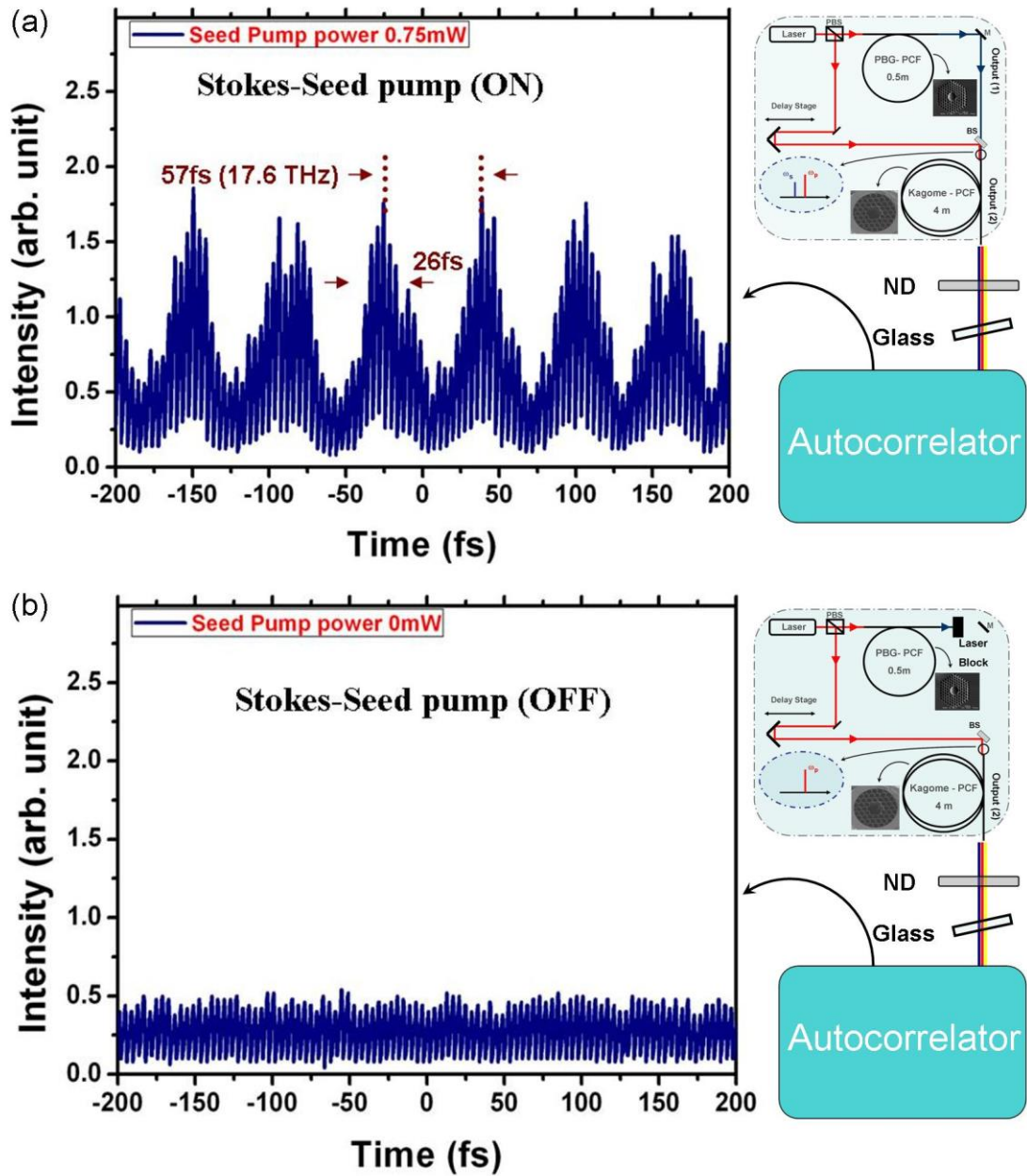
Figure 5.9 (a-b): Experimental set-up for temporal profile measurements of the Raman comb, and a typical AC trace when (a) the Stokes seed is (ON), and (b) the Stokes seed is (OFF).
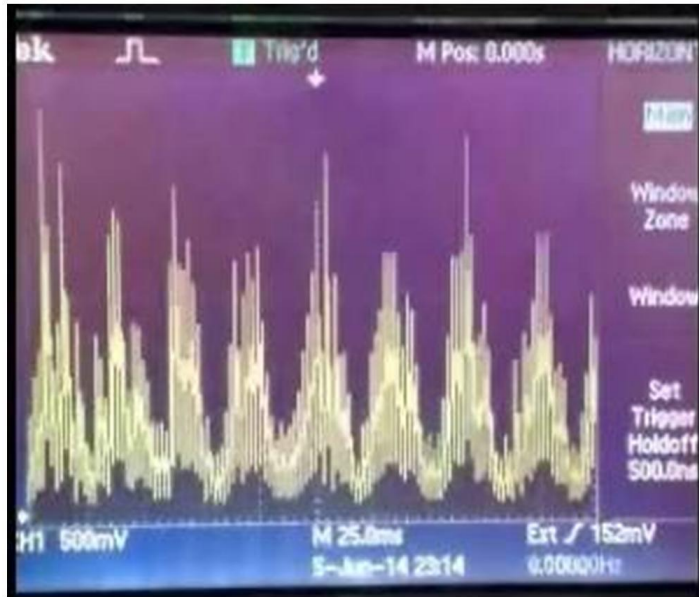
(c)

Figure 5.9(c): (video available upon request[5]). A snapshot of a recorded video of AC trace of train of pulses when the Stokes seed is ON or OFF. The seed pump average power was 0.75mW.

Figure 5.10(a) shows the measured AC waveform superimposed to the calculated temporal profile using the transient SRS theory mentioned. The agreement is very good. The reconstruction of the temporal profile is done by extracting the phase and the amplitude from the relative power of the spectra lines of the comb, and the fibre dispersion. The effective refractive index n_{eff} of the H_2 hosted in the Kagome fibre is numerically calculated. The fibre induced-phase difference is deduced from $\Delta\beta l = (\beta_i - \beta_0)l$, where $\beta_i = 2\pi n_{eff}/\lambda$, l is the Kagome fibre length. Figure 5.10(b) plots the $\Delta\beta \times l$ spectrum along with the synthesised Raman comb. It is noteworthy that we had similar good agreement between the calculated waveform and experiment when the phase and amplitude were extracted from the SFG spectrum and temporal traces

[5] This video could be provided upon your request. Please email: ma302@bath.ac.uk or f.benabid@xlim.fr.

(Figure 5.8(b)). Figure 5.8(b), shows a snapshot of a recorded video of the intra-pulse waveform measured using AC.
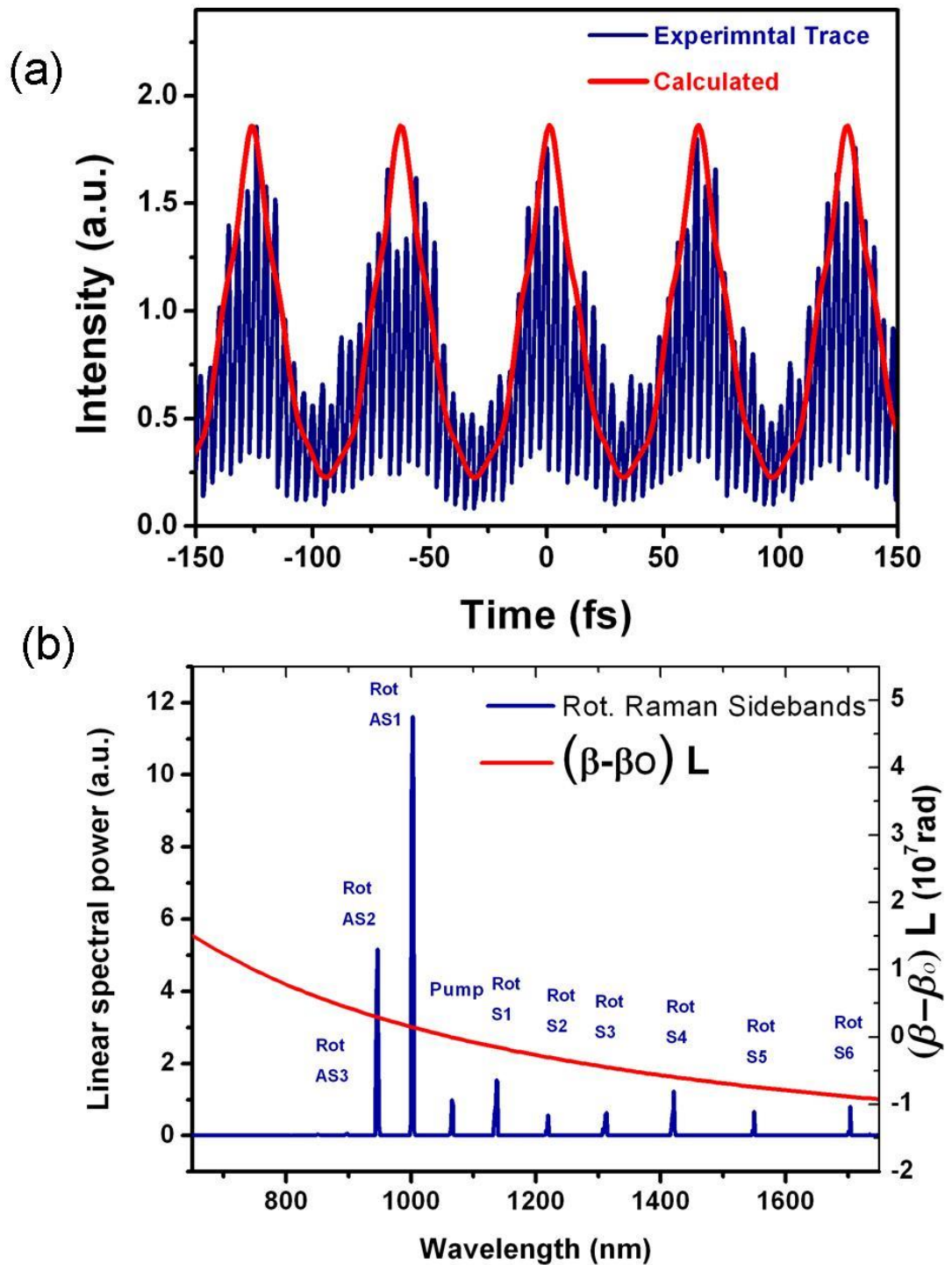

Figure 5.10: (a) The experimental AC trace showing a train of pulses (blue curve) for Raman comb and the calculated temporal profile based on the amplitude and phase of these Raman comb. (b) The $\Delta\beta l$ (red curve) spectrum calculated from the effective refractive index of the H_2 in the fibre. The linear scaled spectrum Raman comb is shown in blue curve.

In order to have an idea of the shortest pulse, this generated train waveform could be achieved by simply controlling the average intensity of the comb lines. We superimposed, on the same measured waveform shown above, a temporal profile with the same extracted phase by setting the amplitude of all the lines to being equal. Figure 5.11 shows the results of such a procedure. The pulse width (FWHM) is now ~10 fs, indicating thus that with our simple apparatus and no line-by-line amplitude-phase control such as with a spatial light modulator, a train of 10 fs pulse is possible. Remarkably, the measured waveform that remains stable over the whole few hours of monitoring, is achieved despite the strong energy and time jitter of our pump laser.
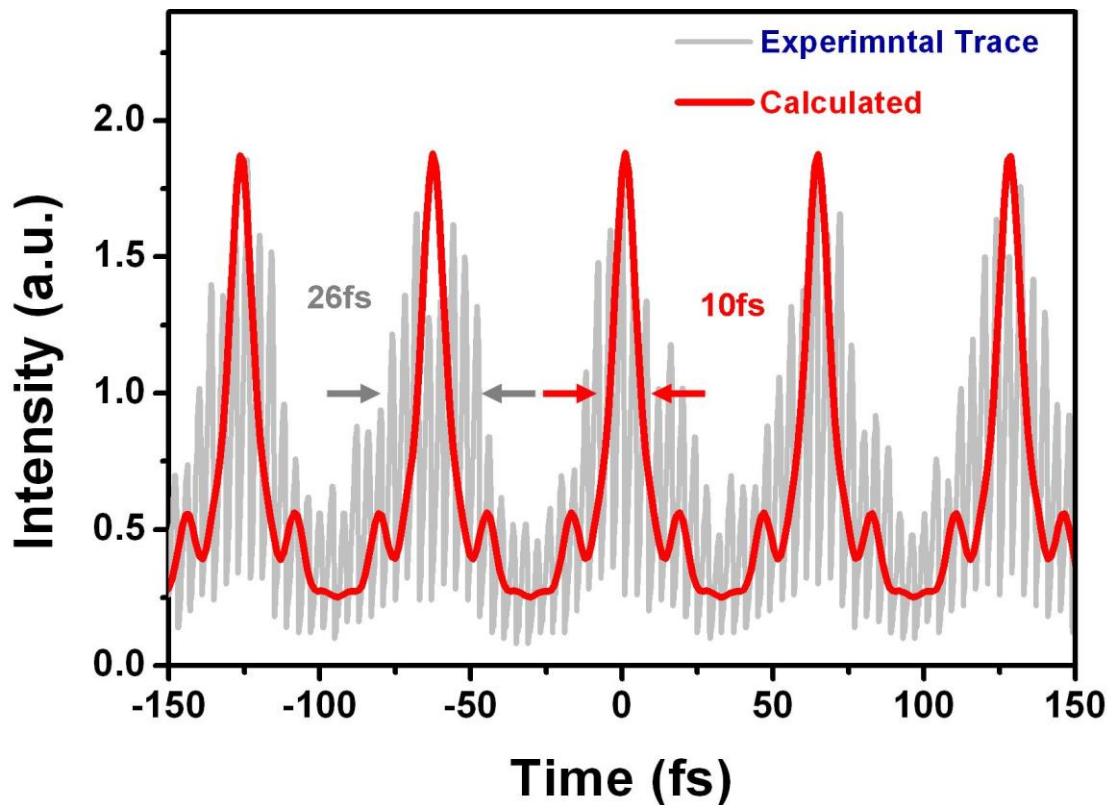

Figure 5.11: The experimental AC trace showing a train of pulses (grey curve) for Raman comb and the calculated temporal profile based on phase of these Raman comb whereas the amplitude of each Raman lines assumed to have the same value.

5.3.4   The effect of Stokes-Seed Pump level variation

This section aims to further examine the prediction of the transient SRS modal description in filtering quantum noise STM by increasing the Raman gain. This is done by monitoring the change in the AC waveform with the level of "transiency" under which the Stokes seed (SS) is generated. We carry this out by using two experimental protocols. Firstly, we change the pump power that generates the seed (PS), and we maintain the generated Stokes power to a constant by using a variable neutral density filter wheel. Consequently, the only change in the pumping pulses of the H_2-filled Kagome HC-PCF is that the SS pulse is generated under different Raman gain. Secondly, and in contrast with the first protocol, PS power is kept constant, however, we change SS power. This means that the SS spectral and spatio-temporal content remains the same, but its power coupled to a Kagome fibre is varied.

Figures 5.12 and 5.13 show the evolution of the AC waveforms with PS when the first protocol is used for a fixed Stokes seed power of 0.01 mW and 0.045 mW respectively. Figure 5.14 relates to the second protocol, and shows the evolution of the AC waveform with SS power. The results clearly show the crucial role of the SS level of "transiency" on the AC waveform and hence on the mutual coherence of the comb. When the PS power is varied from 0 mW to 1.75 mW, we observe the same evolution regardless of the SS power. Firstly, for PS powers less than 1 mW (i.e. $G{\sim}150$, assuming 60% fibre coupling efficiency), no AC waveform is generated. On the other hand, when the PS power is increased from 1 mW to 1.75 mW we have a clear formation of pulse train waveforms with increasing contrast. This indicates that for a net gain of 150, the gain is low enough for the required level of "transiency" to amplify only a single dominant STM (DSTM). Instead several STM are amplified to form the Stokes pulse, and the extinction ratio of the DSTM and the other STM must be increased further. Put differently, the phase of each comb component should be

written as $\phi_n = \beta_n z + n\theta + \delta$ where δ is an intra-pulse random phase that stems from the presence of sufficiently amplified STM. The higher the extinction ratio between the DSTM and these STM, the smaller δ and hence a stronger comb mutual coherence. This is consistent with the evolution of the AC waveform with the PS when the gain is larger than 150. Further evidence of this model is given with the results of the second measurement protocol. Figure 5.14 shows the evolution of the AC waveform at PS power fixed above the "sufficiently high transiency level" by setting it to 1.86 mW (G ~270) with different SS power levels. The results show that even though the SS power has been increased almost 35 fold from 0.01 mW to 0.35 mW, the AC waveform still exist.

Figure 5.12: (a) Schematic of the setup. (b) Waveform of pulse train traces while fixing the Stokes seed at 0.01 mW and varying the pump seed couples to the PBG HC-PCF.
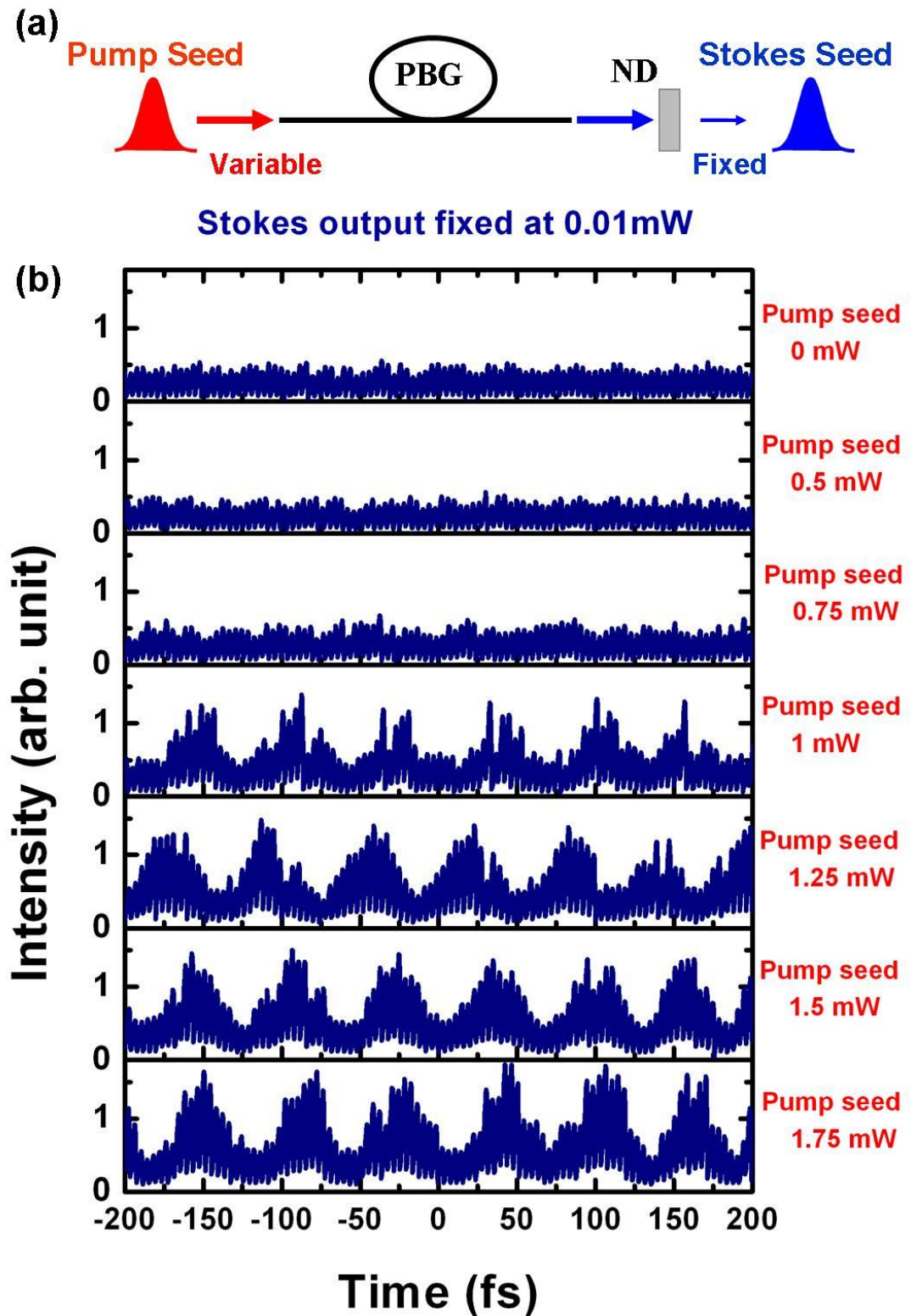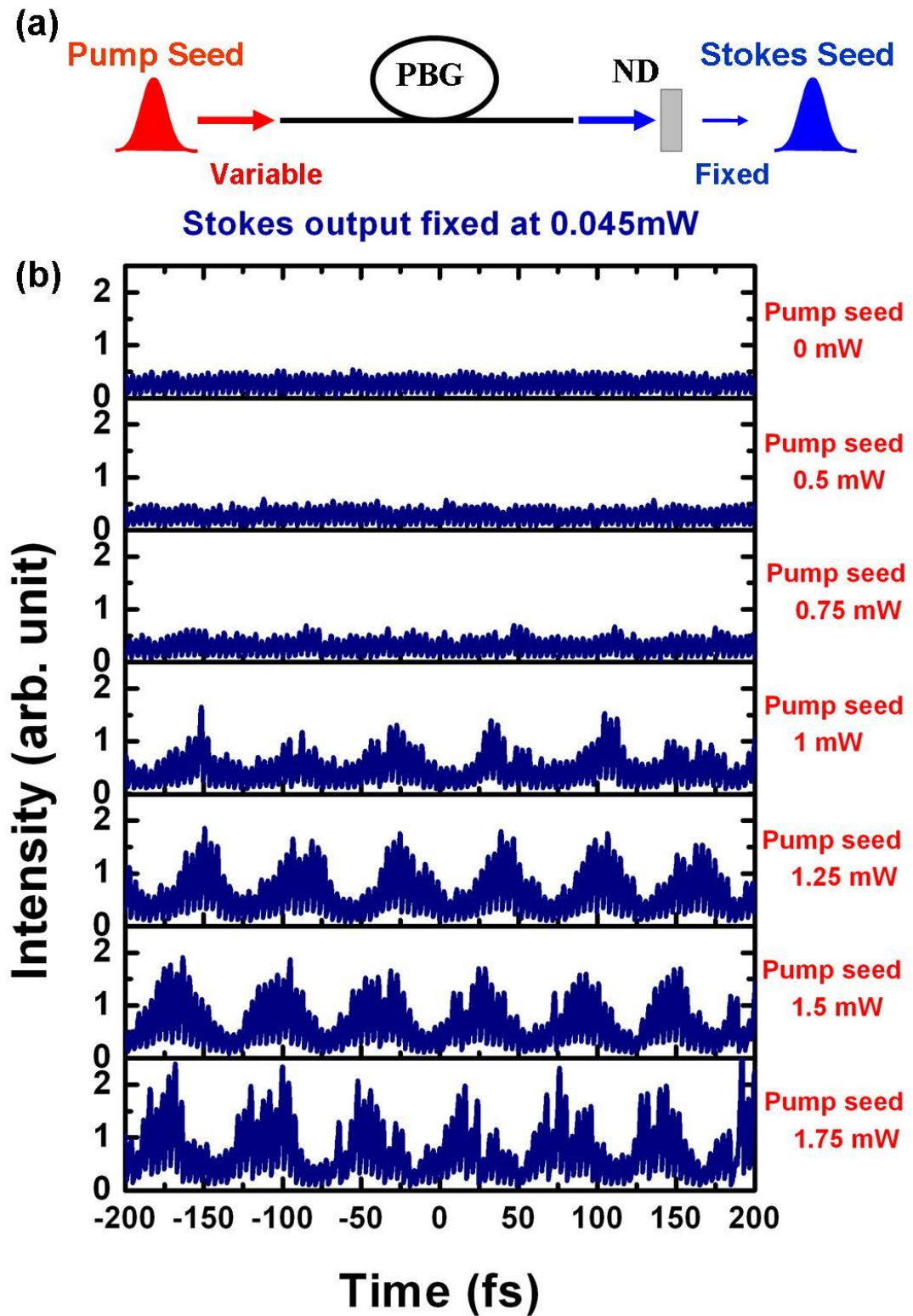
Figure 5.13: (a) Schematic of the setup. (b) Autocorrelator traces while fixing the Stokes seed at 0.045 mW and varying the pump seed couples to the PBG HC-PCF.
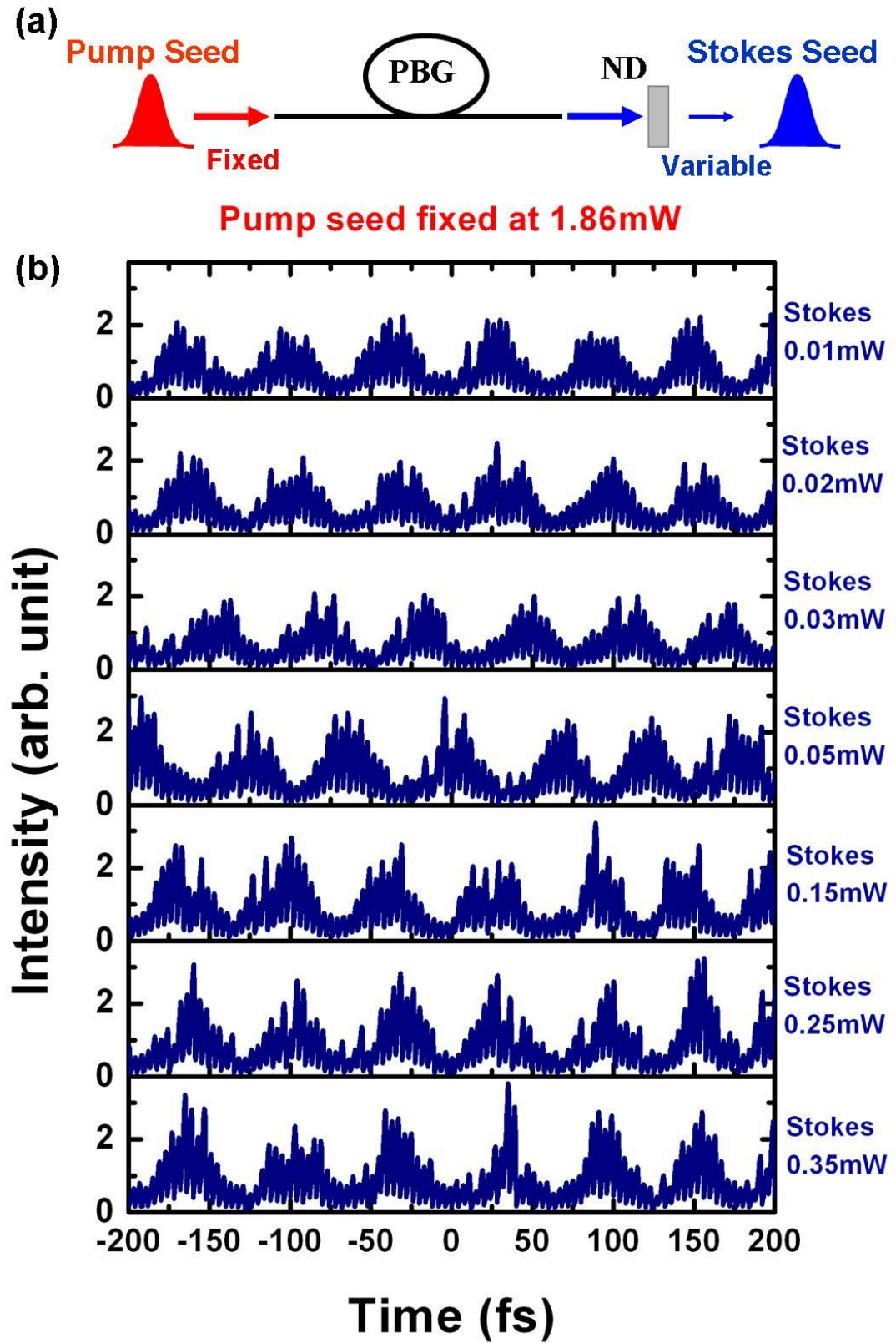
Figure 5.14: (a) Schematic of the setup. (b) Autocorrelator traces while fixing the pump seed at 1.86 mW and varying the Stokes seed.

5.3.5 Visibility Measurement

The preceding sections demonstrated the intra-pulse phase locking of a Raman comb that resulted from the amplification of a Stokes seed generated under transient SRS regime. This has led to a robust pulse train AC waveform. This section aims to give further clues on whether the AC waveform we generated is the result of pulse-to-pulse stable waveform. In other words, is our comb pulse-to-pulse phase-locked? This question is raised in light of the results of the preceding chapter, which show that the probe was frequency modulated by a pre-established Raman coherence even if the probe arrives at the Raman medium at 22 ns, which is 129 times larger than T_2, after the passage of the leading pump which generated the Raman coherence. We also find that the decay of this coherence is dependent on the pump power (i.e. to the net Raman gain), indicating a novel physical mechanism that is not addressed by the conventional SRS generation model.

Here in this chapter, we repeat the visibility measurement described in the preceding chapter. Figure 5.15 recalls schematically the principle. The beam of the same 1064 nm microchip laser used so far is divided into two equal pulses using 50/50 beam splitter. One pulse is then delayed with a variable delay-time second pulse τ_d. The two pulses are then coupled into the 0.5 m long H_2 filled PBG HC-PCF, thus generating a pair of delayed 1st rotational Stokes pulses. The residual pumps are filtered out using a narrow bandpass filter. The resulting Stokes pulses are then split into two parts with one part delayed, and then recombined so the first pulse is superposed with the delayed one. The superposed pulse beam is sent to CCD for possible interference fringes. The resulting interference is recorded and processed to extract the visibility. Note that in order to extend the delay arms up to 28 ns, two pieces of 7 m long HC-PCF are used. The fringes are recorded for the longest delay first and then the fibres in the delay arms are cut down to different required lengths. Care

was taken to make sure that the coupling to the PBG fibre remains the same at different delay lengths.

The visibility between the interfering Stokes is shown in Figure 5.18. In consistency with the results obtained in Chapter 4, we observe visibility even with a delay of 28 ns. More remarkably the exponential decrease of the visibility shows a decay time of 28 ns.
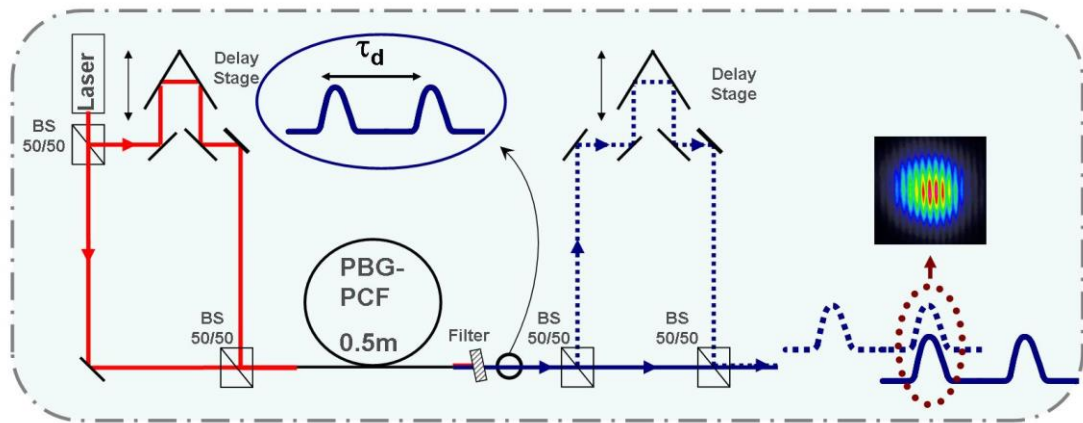
Figure 5.17: Schematic setup for visibility measurements.
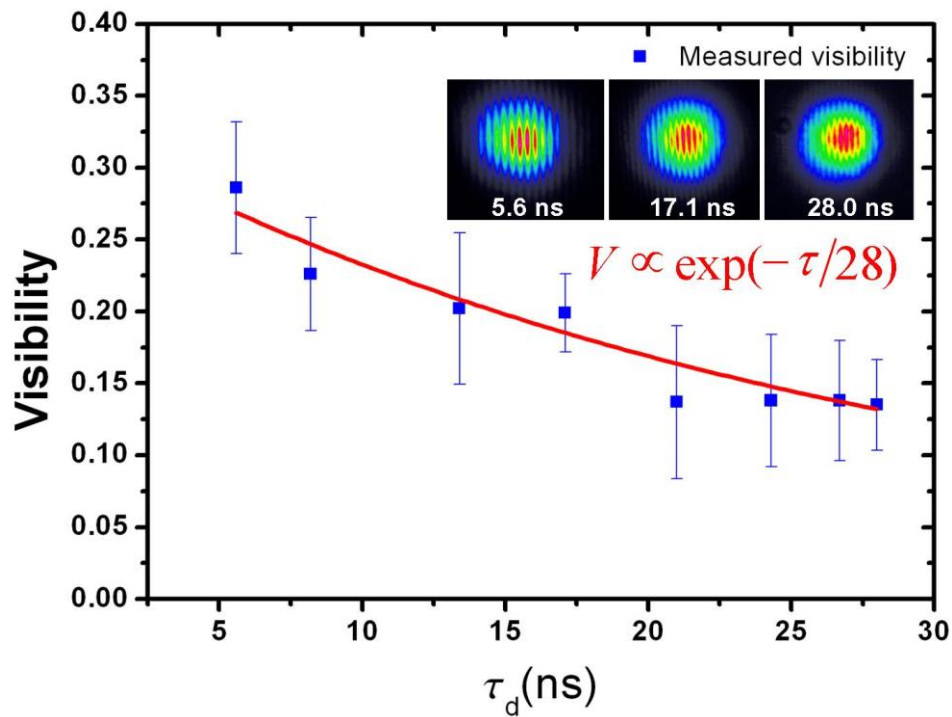
Figure 5.18: visibility recorded as a function of the delay τ_d.

5.4 Summary

An AC waveform of 26 fs pulse train with a repetition rate set by a rotational resonance of molecular hydrogen was demonstrated. Role of the transiency of the Stokes generation is shown to play a central role in the waveform formation and hence in the phase-locking of the spectral comb. Raman coherence is shown to decay at a much slower rate than that of the dephasing time. Indicating that a new mechanism is involved in the process. One possible route is that there is a velocity-selective SRS generation where only slow molecules participate in the Stokes emission. This route would be similar to the mechanism in CW SRS that we cover in Chapter 7.

References

[1] A. H. Zewail, "Laser Femtochemistry," *Sci.* , vol. 242 , no. 4886 , pp. 1645–1653, Dec. 1988.

[2] N. A. Papadogiannis, B. Witzel, C. Kalpouzos, and D. Charalambidis, "Observation of Attosecond Light Localization in Higher Order Harmonic Generation," *Phys. Rev. Lett.*, vol. 83, no. 21, pp. 4289–4292, 1999.

[3] P. Corkum, "Attosecond pulses at last," *Nature*, vol. 403, no24 FEBRUARY, pp. 845–846, 2000.

[4] M. Hentschel, R. Kienberger, C. Spielmann, G. A. Reider, N. Milosevic, T. Brabec, P. Corkum, U. Heinzmann, M. Drescher, and F. Krausz, "Attosecond metrology," *Nature*, vol. 414, no. 6863, pp. 509–513, Nov. 2001.

[5] P. M. Paul, E. S. Toma, P. Breger, G. Mullot, F. Auge, P. Balcou, H. G. Muller, and P. Agostini, "Observation of a train of attosecond pulses from high harmonic generation.," *Science*, vol. 292, no. 5522, pp. 1689–92, Jun. 2001.

[6] a V Sokolov, D. R. Walker, D. D. Yavuz, G. Y. Yin, and S. E. Harris, "Raman generation by phased and antiphased molecular states.," *Phys. Rev. Lett.*, vol. 85, no. 3, pp. 562–5, Jul. 2000.

[7] A. Nazarkin, G. Korn, M. Wittmann, and T. Elsaesser, "Generation of Multiple Phase-Locked Stokes and Anti-Stokes Components in an Impulsively Excited Raman Medium," *Phys. Rev. Lett.*, vol. 83, no. 13, pp. 2560–3, Sep. 1999.

[8] H. Kawano, Y. Hirakawa, and T. Imasaka, "Generation of high-order rotational lines in hydrogen by four-wave Raman mixing in the femtosecond regime," *IEEE J. Quantum Electron.*, vol. 34, no. 2, pp. 260–268, 1998.

[9] E. Sali, K. J. Mendham, J. W. G. Tisch, T. Halfmann, and J. P. Marangos, "High-order stimulated Raman scattering in a highly transient regime driven by a pair of ultrashort pulses.," *Opt. Lett.*, vol. 29, no. 5, pp. 495–7, Mar. 2004.

[10] F. Couny, F. Benabid, P. J. Roberts, P. S. Light, and M. G. Raymer, "Generation and photonic guidance of multi-octave optical-frequency combs.," *Science*, vol. 318, no. 5853, pp. 1118–21, Nov. 2007.

[11] S. E. Harris and a. V. Sokolov, "Broadband spectral generation with refractive index control," *Phys. Rev. A*, vol. 55, no. 6, pp. R4019–R4022, Jun. 1997.

[12] S. E. Harris and A. V Sokolov, "Subfemtosecond Pulse Generation by Molecular Modulation," *Phys. Rev. Lett.*, vol. 81, no. 14, pp. 2894–2897, Oct. 1998.

[13] S. F. Sokolov, a. V. Harris, "Ultrashort pulse generation by molecular modulation," *J. Opt. B Quantum Semiclassical Opt.*, vol. 5, 2003.

[14] H.-S. Chan, Z.-M. Hsieh, W.-H. Liang, A. H. Kung, C.-K. Lee, C.-J. Lai, R.-P. Pan, and L.-H. Peng, "Synthesis and Measurement of Ultrafast Waveforms from Five Discrete Optical Harmonics," *Sci.* , vol. 331 , no. 6021 , pp. 1165–1168, Mar. 2011.

[15] N. Zhavoronkov and G. Korn, "Generation of Single Intense Short Optical Pulses by Ultrafast Molecular Phase Modulation," *Phys. Rev. Lett.*, vol. 88, no. 20, p. 203901, May 2002.

[16] F. Benabid, G. Bouwmans, J. Knight, P. Russell, and F. Couny, "Ultrahigh Efficiency Laser Wavelength Conversion in a Gas-Filled Hollow Core Photonic Crystal Fiber by Pure Stimulated Rotational Raman Scattering in Molecular Hydrogen," *Phys. Rev. Lett.*, vol. 93, no. 12, p. 123903, Sep. 2004.

[17] F. Benabid, G. Antonopoulos, J. Knight, and P. Russell, "Stokes Amplification Regimes in Quasi-cw Pumped Hydrogen-Filled Hollow-Core Photonic Crystal Fiber," *Phys. Rev. Lett.*, vol. 95, no. 21, p. 213903, Nov. 2005.

[18] Y. Y. Wang, C. Wu, F. Couny, M. G. Raymer, and F. Benabid, "Quantum-Fluctuation-Initiated Coherence in Multioctave Raman Optical Frequency Combs," *Phys. Rev. Lett.*, vol. 105, no. 12, p. 123603, Sep. 2010.

[19] C. Wu, M. G. Raymer, Y. Y. Wang, and F. Benabid, "Quantum theory of phase correlations in optical frequency combs generated by stimulated Raman scattering," *Phys. Rev. A*, vol. 82, no. 5, p. 053834, Nov. 2010.

[20] Y. Y. Wang, N. V Wheeler, F. Couny, P. J. Roberts, and F. Benabid, "Low loss broadband transmission in hypocycloid-core Kagome hollow-core photonic crystal fiber.," *Opt. Lett.*, vol. 36, no. 5, pp. 669–71, Mar. 2011.

[21] T. D. Bradley, Y. Wang, M. Alharbi, B. Debord, C. Fourcade-dutin, B. Beaudou, F. Gerome, and F. Benabid, "Optical Properties of Low Loss (70dB / km) Hypocycloid-Core Kagome Hollow Core Based Optical Applications," *J. Lightwave Technol.*   31, 3052-3055 (2013).

[22] Y. Y. Wang, F. Couny, P. S. Light, B. J. Mangan, and F. Benabid, "Compact and portable multiline UV and visible Raman lasers in hydrogen-filled HC-PCF," *Opt. Lett.*, vol. 35, no. 8, pp. 1127–1129, 2010.

[23] M. G. Raymer and J. Mostowski, "Stimulated Raman scattering: Unified treatment of spontaneous initiation and spatial propagation," *Phys. Rev. A*, vol. 24, no. 4, pp. 1980–1993, Oct. 1981.

[24] M. Belsley, D. T. Smithey, K. Wedding, and M. G. Raymer, "Observation of extreme sensitivity to induced molecular coherence in stimulated Raman scattering," *Phys. Rev. A*, vol. 48, no. 2, pp. 1514–1525, Aug. 1993.

[25] M. G. Raymer, "Qunatum state entanglement and readout of collective atomic-ensemble modes and optical wave-packets by stimulated Raman scattering," *Jounal of Modern Optics*, vol.51, pp. 1739–1759, 2004.

[26] M. G. Raymer, I. A. Walmsley, J. Mostowski, and B. Sobolewska, "Quantum theory of spatial and temporal coherence properties of stimulated Raman scattering," *Phys. Rev. A*, vol. 32, no. 1, pp. 332–344, Jul. 1985.

[27] M. D. Duncan, R. Mahon, L. L. Tankersley, and J. Reintjes, "Control of transverse spatial modes in transient stimulated Raman amplification," *J. Opt. Soc. Am. B*, vol. 7, no. 7, pp. 1336–1345, 1990.

[28] I. A. Walmsley and M. G. Raymer, "Experimental study of the macroscopic quantum fluctuations of partially coherent stimulated Raman scattering," *Phys. Rev. A*, vol. 33, no. 1, pp. 382–390, Jan. 1986.

[29] I. A. Raymer, M.G. Walmsley, "The quantum coherence properties of stimulated Raman scattering." *E. Wolf, Progress in Optice*. Vol 28, 1990.

[30] T. Suzuki, N. Sawayama, and M. Katsuragawa, "Spectral phase measurements for broad Raman sidebands by using spectral interferometry.," *Opt. Lett.*, vol. 33, no. 23, pp. 2809–11, Dec. 2008.

Part 3

Part of the ongoing progression towards the realisation of an optical waveform synthesiser using hollow-core photonic crystal fibres (HC-PCF) is to study Stokes generated in the CW regime. This Stokes is used as a second seed along with the original pump to form the synthesiser. The output power stability of the generated Stokes is one of the concerns that are essential for the frequency comb generation which is covered in chapter 6. A further characterisation of the generated Stokes is performed in chapter 7. This is based on the study of the forward and backward Stokes linewidth. An impressive sub-natural linewidth was measured for both Stokes. This has led to more information on the motion of the molecule. In this chapter, we report on a novel molecular confinement whereby the Raman activity of an ensemble molecule is restricted to a very thin section.

Chapter 6

Continuous Wave Stimulated Raman Scattering in Hydrogen-filled HC-PCF

In this chapter, we recall the long term objective of developing an optical waveform synthesiser using CW stimulated Raman scattering in HC-PCF and the prior work achieved towards this. The chapter covers the generation of first rotational Stokes emission in the CW regime with output power in excess of 50 W using PBG HC-PCF. We characterise the power stability of the emitted Stokes and the thermal distribution along the fibre input. This plays an essential role in the ongoing procedure towards the realisation of arbitrary optical waveform synthesiser.

6.1 Introduction

Efforts to develop an arbitrary optical waveform synthesiser, akin to electronics, are an on-going effort, and have recently attracted a lot of attention. By waveform synthesiser akin to electronics, we mean Fourier synthesis of a multi-octave optical comb with CW spectral components instead of pulsed ones, and where amplitude and phase could be controlled with the same degree of flexibility as in electronics. So far generation of a multi-octave comb and their temporal synthesis have been achieved in the pulsed regime using HHG [1], [2] or molecular modulation [3] (see Chapter 1). Significantly, the molecular modulation is amenable to comb generation even when the Raman medium is excited with CW lasers. However, this task turned out to be extremely challenging as it would require lasers exhibiting large intensity (GW/cm² level) and narrow linewidth. In addition, one needs a Raman excitation scheme that offers exceptional conversion efficiency.

Indeed, whilst off-resonance stimulated Raman scattering (SRS) in gaseous media was well identified as a very promising method for the generation laser sources at unconventional wavelengths. For example, if CW SRS could be achieved at low power levels the combination of a CW tunable laser and a set of Raman media would cover a very large band of the electromagnetic spectrum with CW lasers. Traditionally, two techniques were developed to this objective. The first method is based on enhancing the effective length of the Raman medium using multi-pass cells [4], [5]. However, the resulting threshold reduction has remained extremely modest. The second method is called resonance enhancement, where the power is enhanced by increasing the effective length using an optical resonant cavity filled with Raman active medium. Carlsten and co-workers have reported in [6], [7] the use of a high-finesse cavity filled with H_2 and resonates at the pump and Stokes frequencies. An extraordinary low power threshold was reported using this

method. Meng *et al.* in 2002 [7] reported on a milli-Watt level threshold power for the Raman effect to take place using a pump laser source at 800 nm. This has led to the realization of the first CW Raman laser in H_2 [6], [7]. However, this method suffers from a number of limitations such as low power handling, limited bandwidth, and poor conversion efficiency.

An alternative method to the two mentioned above is the use of HC-PCF. Couny *et al.* [8] reported CW rotational SRS in H_2-filled HC-PCF, with results combining low power threshold for SRS generation, strong power handling (8 W were generated at the Stokes line), and a frequency conversion reaching the quantum-limit which is an order of magnitude larger than the high finesse cavity techniques [13]. This is achieved using a single-pass configuration due to the high efficiency laser-matter interaction inside the hollow core fibre. The Raman power threshold in this study was 2.25W with 50% conversation efficiency into the first rotational Stokes line, as illustrated in Figure 6.1. This clearly illustrates the advantage of using HC-PCF as the excellent host for Raman wavelength converter, with up to 99.99% of the output power at the first rotational Stokes, even at gas operating pressure as low as 1 bar (Figure 6.2). This shows the potential that this technique holds to bring the comb generation technique to the CW regime. It is this technique that is used in the present work.
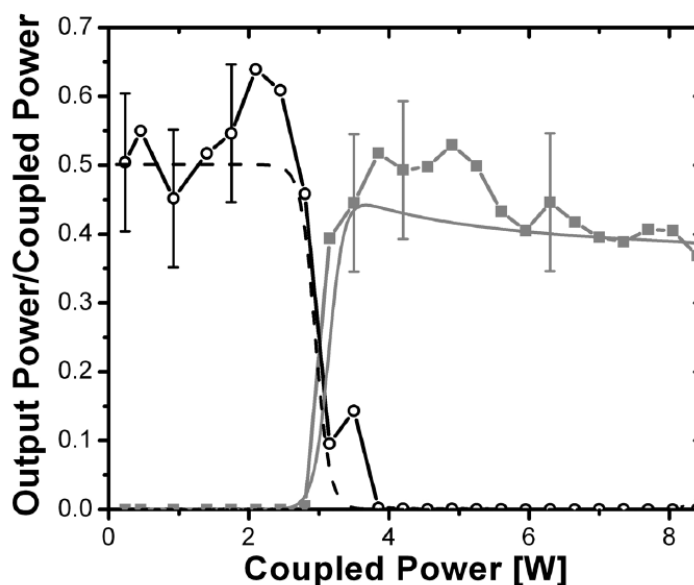
Figure 6.1: Experimental output/input power ratio for the pump (circles and black line) and first Stokes (grey squares and line) at 5bars H2 pressure. Theoretical calculations for the pump (dashed black line), the first Stokes (solid grey line) [8].
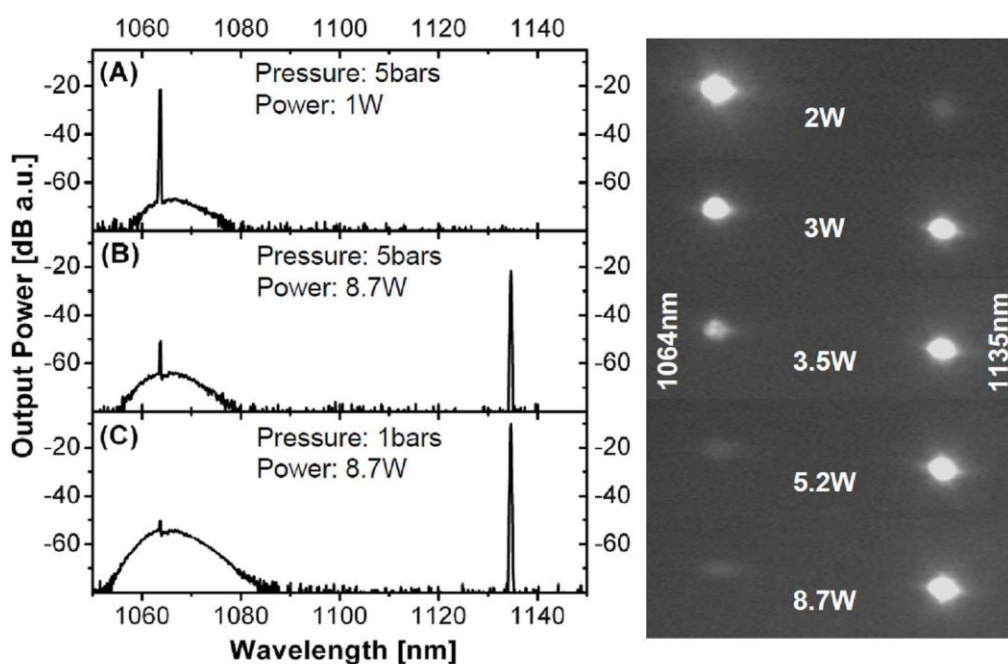
Figure 6.2: LHS; Output optical spectrum for (A) 1W and (B) 8.7W input power at 5bar pressure. (C) Higher conversion efficiency is achieved at 1bar pressure. RHS; evolution of the dispersed output spectrum as a function of input power: (Left) Pump (1064 nm) and (right) Stokes (1135nm) at 5bars pressure [12].

This work is part of the proposed all fibre optical waveform synthesiser (AFOWS) based CW Raman sideband generator system (see Chapter 1), and

which schematically reproduced in Figure 6.3 [11]. It is considered to be the first CW-based optical waveform synthesiser and attosecond pulse generator in an integrated all-optical system based on hollow-core photonic crystal fibre (HC-PCF) filled with hydrogen gas. The device would generate and synthesise almost any optical intensity waveform with a frequency as high as several tens of THz and with any central wavelength from UV to IR. It would be able to generate ultra-short laser pulses with tuneable duration from a few femtoseconds down to a few hundreds of attoseconds.

In principle, the AFOWS can be excited with a single laser. One fraction of its power is sent to the first part of the set (Device 1) to generate a single Stokes line. Once the first Stokes is generated through, it is coupled together along with the pump part into the second part of the setup (Device 2). This is where the Raman comb is generated either by using branches of PBG HC-PCF filled with H_2 or simply using a single Kagome HC-PCF.

With the new developments we reported in Chapter 3, and where Kagome HC-PCF exhibit now comparable or better transmission performance than state-of-the-art PBG HC-PCF, it is now clear that a single Kagome HC-PCF will be favoured. Implementing the second stage of the AFOWS is beyond the scope of the current work. However, the results shown in chapter 3 represent a major milestone towards its realisation.
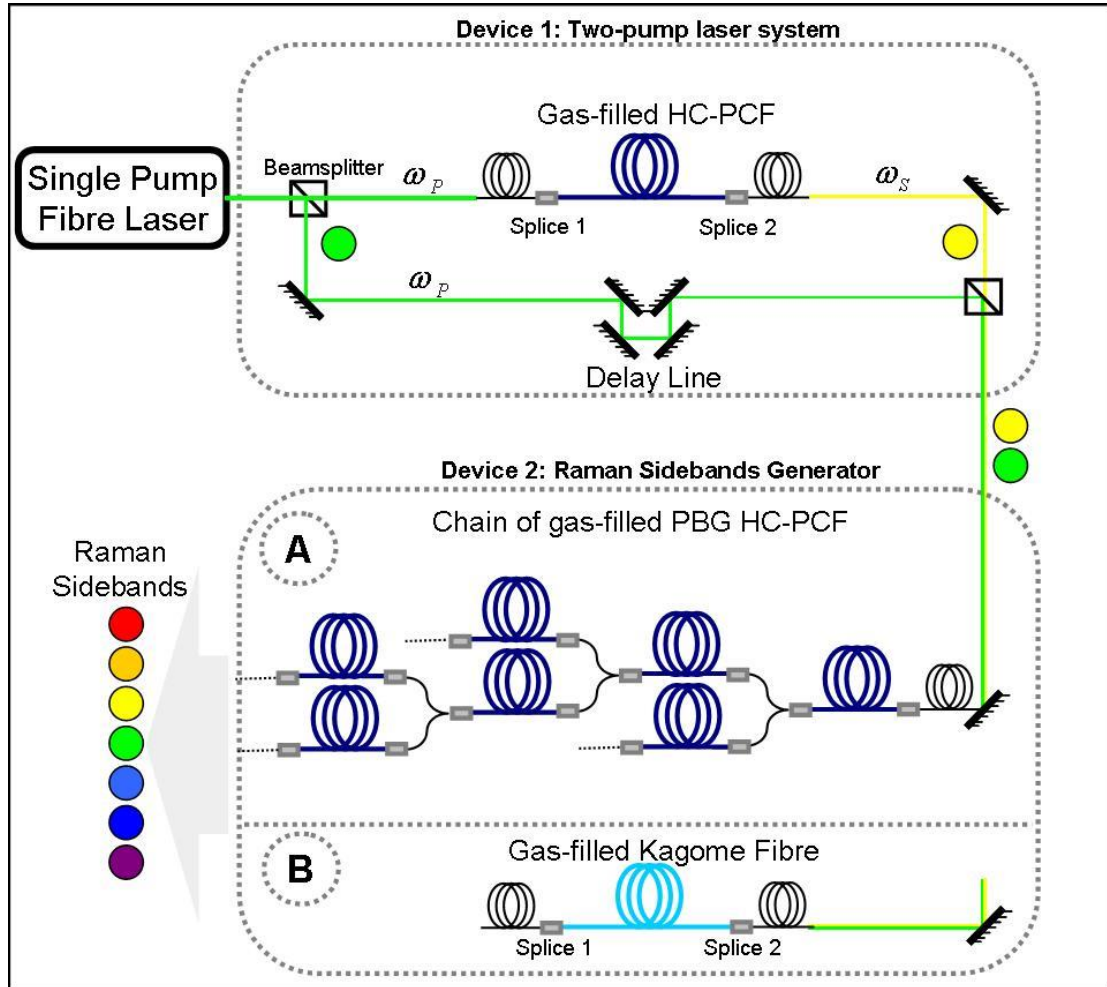
Figure 6.3: Schematic of proposed Raman sidebands generator based on gas-filled HC-PCF. A single laser is coupled into Device 1 to generate the required Stokes radiation. The resulting two-pump laser system is then coupled onto Device 2 for the generation of the sidebands by (A) a chain of gas filled PBG HC-PCF, (B) a single Kagome-lattice HC-PCF [10], [11].

The process of achieving such a broad frequency comb using CW laser, which is described above, consists of many stages. The generation of first rotational Stokes is one of the key technological milestones towards the realisation of the synthesiser. This first rotational Stokes acts as a second pump source along with the original pump, as illustrated in Chapter 1. The first demonstration of high Raman fibre-gas laser is reported by Couny *et al.* in 2010 [14]. They have reported on high power Stokes generation of 55W and around 99.9% conversion efficiency to first rotational Stokes (1131 nm) using high power CW fibre-laser source (Figure 6.4). This illustrates the potential and efficiency that this technique holds for high power laser conversion. The quality of the

Stokes output in the near-field is high due to the spatial mode filtering that is offered by HC-PCF.
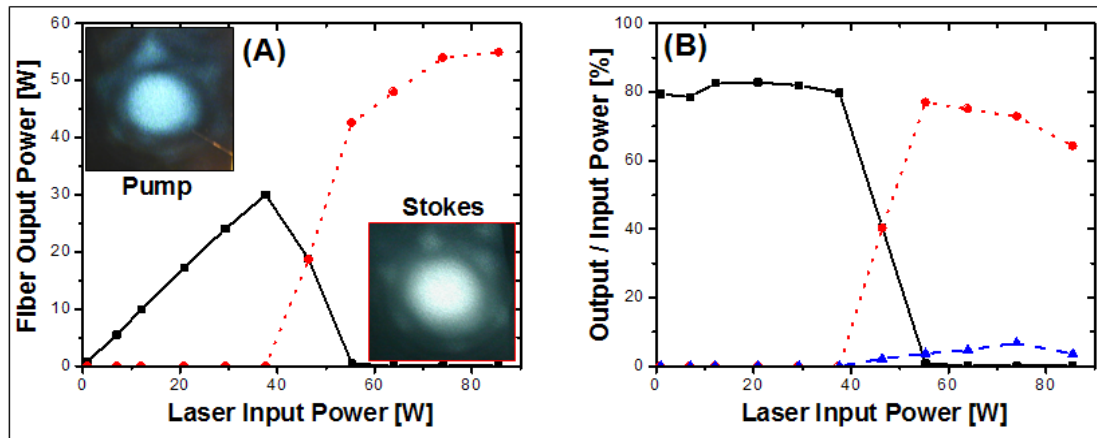
Figure 6.4: (A) Output power from HC-PCF at pump (black line) and Stokes (red dotted line) wavelength as a function of laser source input power. Insets: Images of the fibre output's far-field for the pump and Stokes. (B) Output/input power ratio versus laser input power for the pump (black line) and Stokes (red line). The backscattered Stokes is represented in blue dashed line [14].

In this chapter, we continue on the work reported in [14] through characterising this second pump source (i.e. the high power Stokes) . Here, the stability of the generated CW Stokes is studied. Furthermore, the effect heat distribution along the fibre input end and how its effect the coupling is considered in this chapter.

6.2   Experimental setup

The experimental setup, illustrated in Figure 6.5(a), depends mainly on coupling high power CW fibre laser source to HC-PCF filled with H_2 molecules in a similar configuration as reported in [8], [14]. Figure 6.5 (a) presents a schematic of the experimental setup. The pump source is an IPG CW fibre-laser delivering up to 100 Watt at 1061nm with a narrow linewidth. The fibre used here is 8 m of PBG HC-PCF (see Chapter 2) with guiding transmission bandwith at the pump and the first rotational Stokes wavelength with loss figure of ~ 75dB/km. The output end of the fibre is placed inside a cell filled with 10 bar of H_2. A high power Semrock MaxLine laser line filter is placed in front of the fibre other end to prevent any backward Stokes from causing any damage to the laser source. The filter is designed for 1064nm and is tilted to transmit the 1061nm laser whilst effectively reflecting the backward Stokes to a power meter. Figure 6.5(b) shows the optical spectrum recorded using optical spectrum analyser at the output of the PBG HC-PCF. Furthermore, due the short HC-PCF length used here, no anti-Stokes or high-order Stokes components are observed. The output power for pump source, forward Stokes and backward Stokes are measures using high power thermopile sensor.
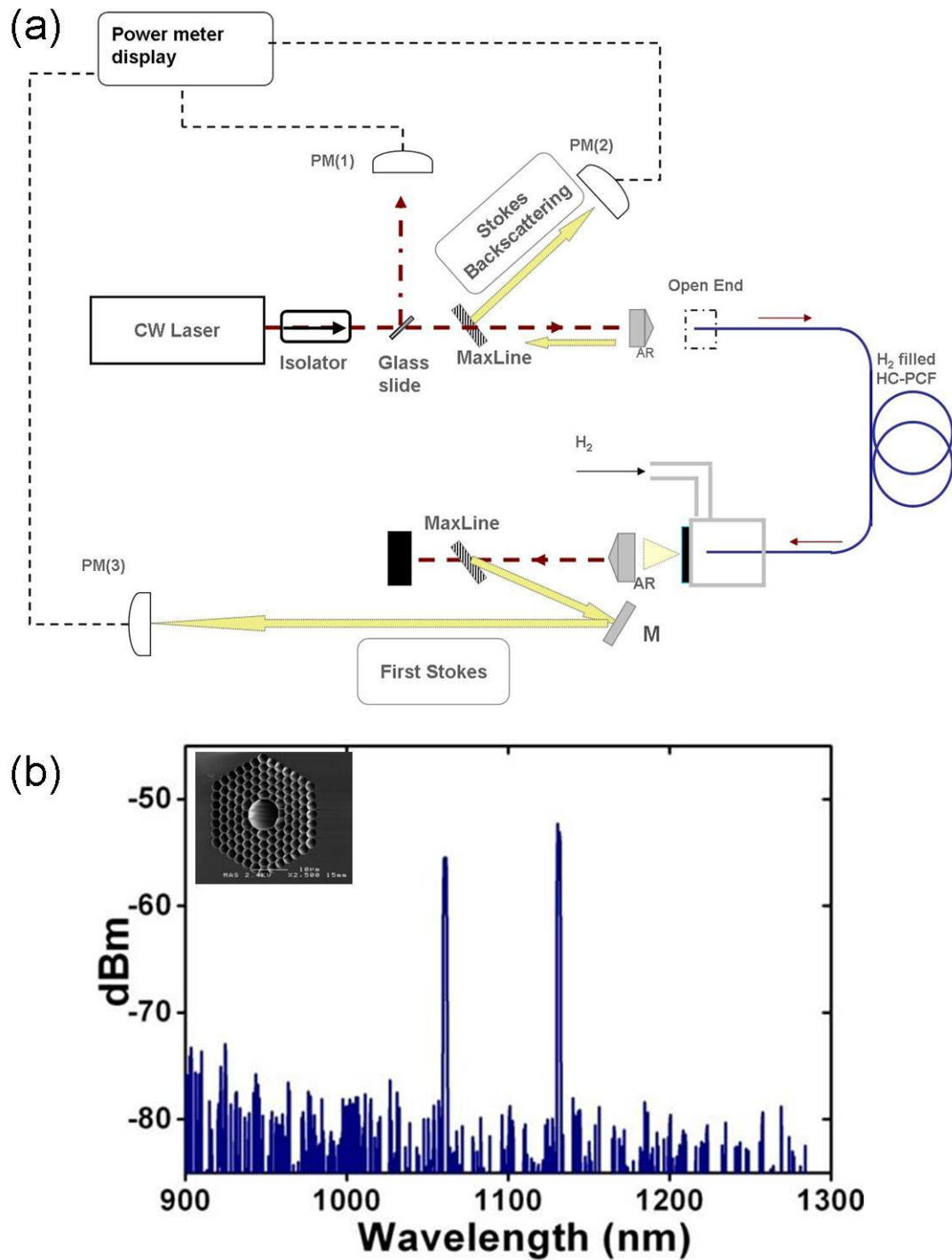
Figure 6.5: (a) Experimental setup for output stability measurements. PBS: Polarized beam splitter, MaxLine: High power filter, M: High power mirror, MO: Microscope objective, AR: Antireflection coated window, PM: power meter. (b) Pump source and first Stokes spectrum generated in PBG fibre and recorded by optical spectrum analyser. Inset the SEM of the fibre.

6.3   Results

6.3.1 Stokes output stability

The stability in terms of power fluctuation of the generated first rotational Stokes is vital as a first step for the realization of an optical waveform synthesizer.   Figure 6.6 illustrates the power stability as a function of time for the pump source, the first generated forward Stokes, and the backscattering Stokes using 8 meters of photonic bandgap HC-PCF filled with H_2 at 10 bar pressure. The measurements are acquired over a continuous time period of three hours. Each plotted point is an average of five measured data points that were acquired at two minutely time slots. The data are obtained after operating the laser for two hours to ensure that the output from this laser is stable enough to run the experiment. The output of the laser source is shown in Figure 6.6 (Black square). A small power drift of the laser output is noticed at the end of the experiment. At the start of the experiment the laser output is fixed at around 60 W and by the end of the experiment the power measure was approximately 64 W. The forward Stokes (red circle) and the backward Stokes (blue triangle) are plotted in the same figure. It was noticed during the entire time of the experiment that the forward Stokes power from the fibre output was fluctuating with no obvious fixed value for a reasonably long time. The back-scattering Stokes generated in this process is around 1 W as shown in the same figure. The Stokes output fluctuation might be due to the thermal accumulation at the fibre-coupling end that might cause the change of the coupling efficiency. The following examine the heat distribution along the fibre coupling end.
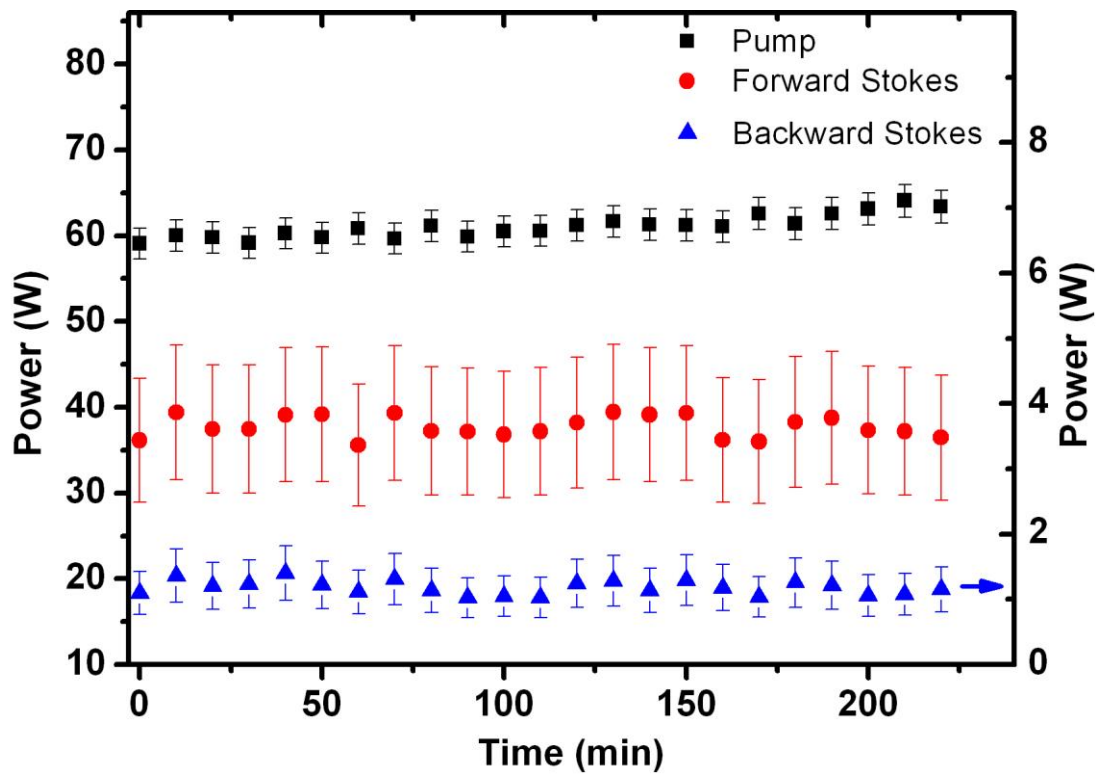
Figure 6.6: The output stability for the source, forward Stokes and backward Stokes as function of time.

6.3.2 Thermal effect

In order to have a better understanding of the effect of thermal accumulation along the beginning of the fibre-coupling end, two thermocouples at two different distances from the fibre-coupling end are used as illustrated schematically in Figure 6.7. A 10 mm length of PBG HC-PCF is used in this setup is stripped from its jacket polymer protector and placed on top of two V-groove fibre holders. The thermocouples are then attached to the stripped fibre and are distanced 15 mm and 75 mm away from the fibre-coupling end. The laser power coupled to the fibre is increased in steps using the control panel of the laser. Results are illustrated in Figure 6.8, where an increase of fibre temperature from around 50°C to 100°C occurs as the coupling power reaches around 50 W. For the longer distance location (L_2 = 75 mm), a slight gradual increase up to 50°C occurs at a coupling power of 75 W.

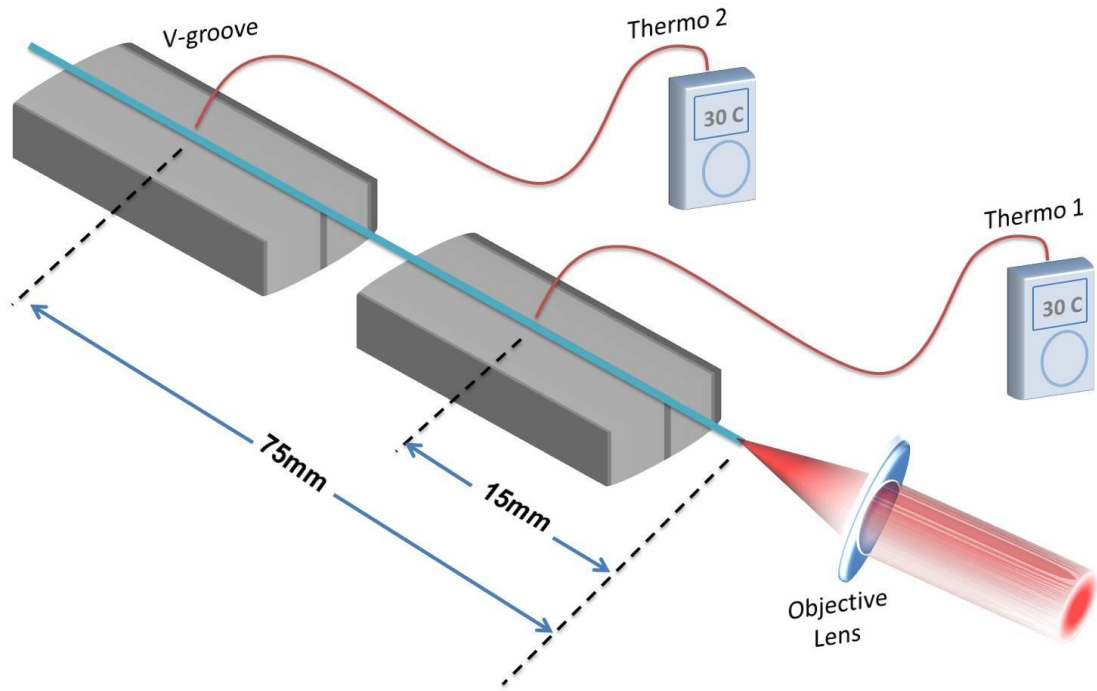Figure 6.7: Schematic setup for measuring temperature of the fibre at L_1=15mm and L_2=75mm. Thermo: Thermocouples. V-groove: V-groove Fibre holders.
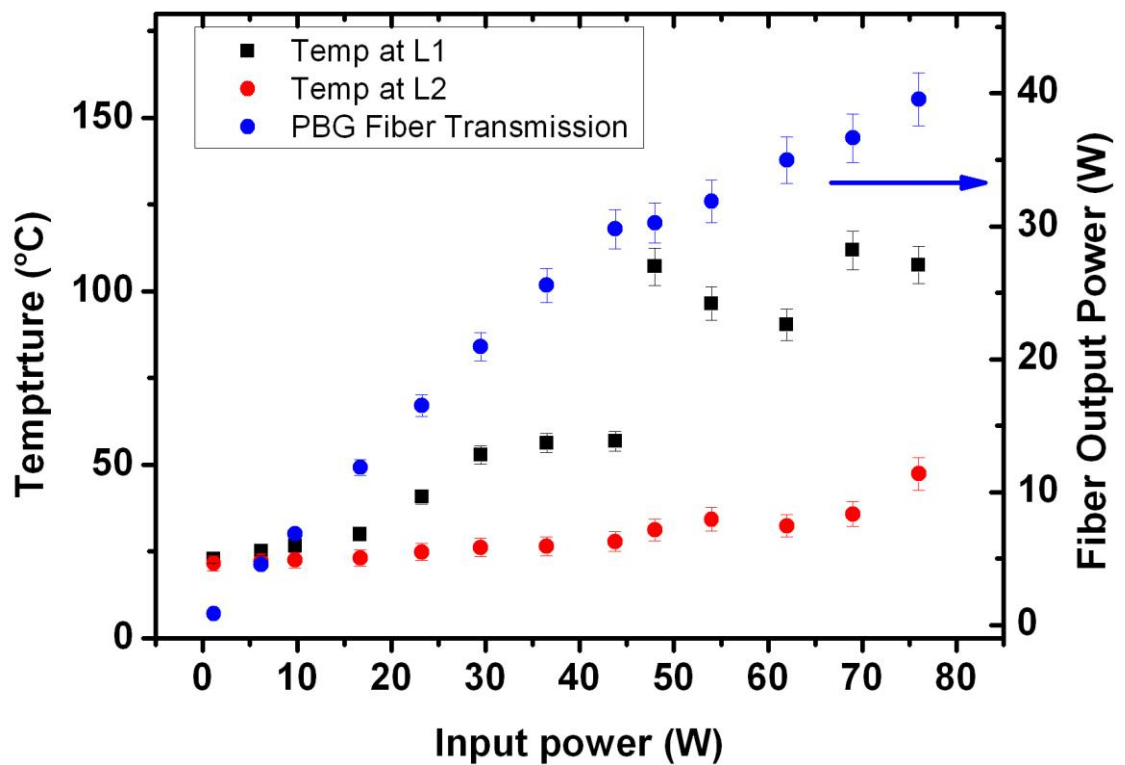

Figure 6.8: The temperature evaluation at two different distances away from fibre input tip (L_1= 15 mm (Black squares) and L_2= 75 mm (Red circles)). Fibre output power at pump wavelength (1061 nm) as a function of laser input power shown in blue circles.

In addition, the output power as a function of the input power is shown in the same figure. It can be seen from this plot that the fibre transmission drops slightly at input power ~ 50 W. At this level of power, an increase in the fibre temperature to ~ 100°C is observed. This might explain the drop of the coupling transmission of the fibre. One of the possible reasons for coupling transmission drop at high operating input powers could be explained in Figure 6.9.
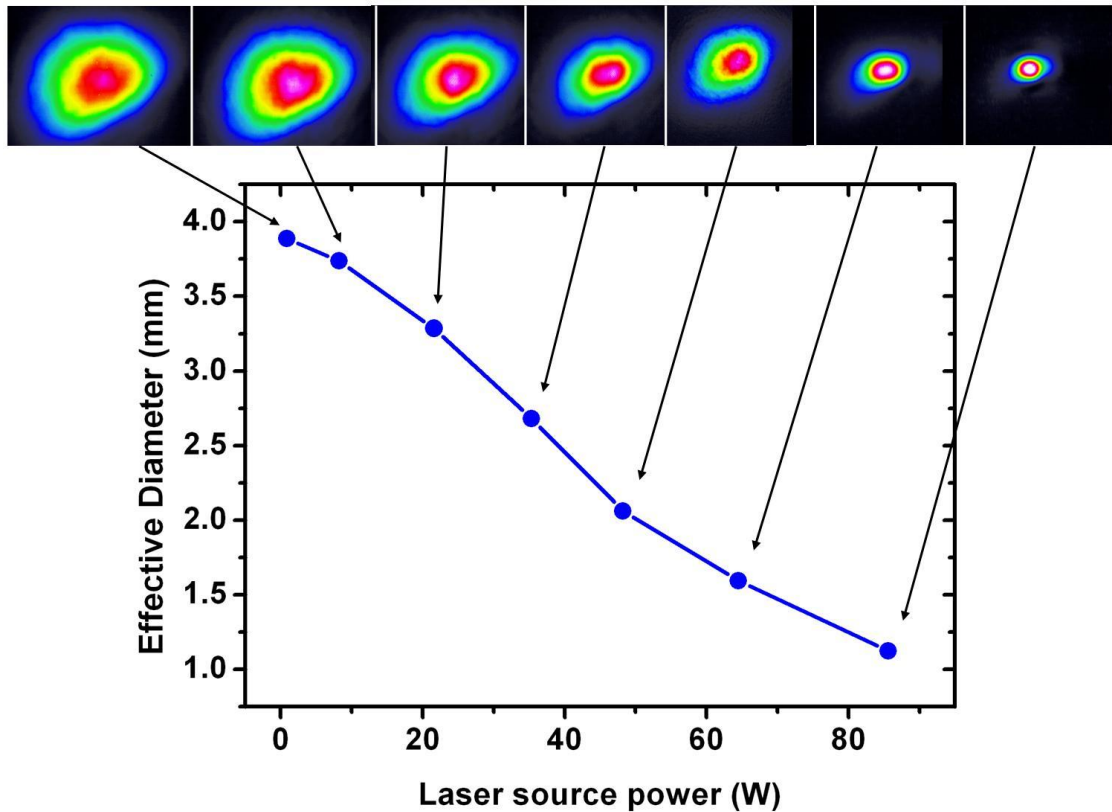
Figure 6.9: The effective beam diameter of the laser source output as function of laser source power output. Top penal; the far-field modes of the source output as the power increase.

Figure 6.9 illustrate the effective beam diameter of the laser source output as a function of laser source power output. The beam diameter is recorded and measured using a CCD camera located 1 m from the laser source output. The plot clearly illustrates a significant reduction in the beam diameter from ~ 3.8 mm at 1 W to ~ 1mm at 85 W. The far-field for the source output as a function of the laser output power is shown in the top panel in Figure 6.9. It clearly shows how the beam mode from the laser source head changes as the source power increases. This, consequently, affects the coupling efficiency in the PBG

HC-PCF as illustrated in Figure 6.8 where the transmission of the fibre dropped at high power levels.

6.4   Summary

The generation of first rotational Stokes in the CW regime in HC-PCF filled with H_2 has been reported. A further characterizing in terms of stability for forward and backward Stokes has been performed at fixed operating pump power (~ 60 W). Although the forward Stokes output power at this level is not particularly stable for short time measurements, the averaged values for prolonged periods show a comparatively steady output. This output fluctuation led to the study of thermal accumulation at the fibre coupling end. This plays an essential role in the ongoing procedure towards the realisation of arbitrary optical waveform synthesiser.

Reference

[1]   P. Antoine, a L'Huillier, and M. Lewenstein, "Attosecond Pulse Trains Using High-Order Harmonics.," *Phys. Rev. Lett.*, vol. 77, no. 7, pp. 1234–1237, Aug. 1996.

[2]   Y. Mairesse, a. de Bohan, L. Frasinski, H. Merdji, L. Dinu, P. Monchicourt, P. Breger, M. Kovačev, T. Auguste, B. Carré, H. Muller, P. Agostini, and P. Salières, "Optimization of Attosecond Pulse Generation," *Phys. Rev. Lett.*, vol. 93, no. 16, p. 163901, Oct. 2004.

[3]   S. E. Harris and A. V Sokolov, "Subfemtosecond Pulse Generation by Molecular Modulation," *Phys. Rev. Lett.*, vol. 81, no. 14, pp. 2894–2897, Oct. 1998.

[4]   P. Rabinowitz, A. Kaldor, R. Brickman, and W. Schmidt, "Waveguide H2 Raman laser," *Appl. Opt.*, vol. 15, no. 9, pp. 2005–2006, 1976.

[5]   B. Perry, R. O. Brickman, a Stein, E. B. Treacy, and P. Rabinowitz, "Controllable pulse compression in a multiple-pass-cell Raman laser.," *Opt. Lett.*, vol. 5, no. 7, pp. 288–90, Jul. 1980.

[6]   J. K. Brasseur, K. S. Repasky, and J. L. Carlsten, "Continuous-wave Raman laser in H(2).," *Opt. Lett.*, vol. 23, no. 5, pp. 367–9, Mar. 1998.

[7]   L. S. Meng, P. a Roos, and J. L. Carlsten, "Continuous-wave rotational Raman laser in H(2).," *Opt. Lett.*, vol. 27, no. 14, pp. 1226–8, Jul. 2002.

[8]   F. Couny, F. Benabid, and P. Light, "Subwatt Threshold cw Raman Fiber-Gas Laser Based on H2-Filled Hollow-Core Photonic Crystal Fiber," *Phys. Rev. Lett.*, vol. 99, no. 14, p. 143903, Oct. 2007.

[9]   F. Benabid, "Optical Wave Generator," Patent: GB 0615541.02006.

[10]   F. Couny, "Photonic Solutions towards Optical Waveform Synthesis," *University of Bath*, 2008.

[11]   F. Couny, F. Benabid, and P. Light, "Subwatt Threshold cw Raman Fiber-Gas Laser Based on H2-Filled Hollow-Core Photonic Crystal Fiber," *Phys. Rev. Lett.*, vol. 99, no. 14, p. 143903, Oct. 2007.

[12]   J. T. Green, D. E. Sikes, and D. D. Yavuz, "Continuous-wave high-power rotational Raman generation in molecular deuterium.," *Opt. Lett.*, vol. 34, no. 17, pp. 2563–5, Sep. 2009.

[13]   F. Couny, B. J. Mangan, A. V. Sokolov, and F. Benabid, "High Power 55 Watts CW Raman Fiber-Gas-Laser," *Conf. Lasers Electro-Optics (CLEO)*, p. CTuM3, 2010.

[14]   F. Benabid, J. C. Knight, G. Antonopoulos, and P. S. J. Russell, "Stimulated Raman scattering in hydrogen-filled hollow-core photonic crystal fiber.," *Science*, vol. 298, no. 5592, pp. 399–402, Oct. 2002.

[15]   F. Couny, B. J. Mangan, A. V. Sokolov, and F. Benabid, "High Power 55 Watts CW Raman Fiber-Gas-Laser," *Conf. Lasers Electro-Optics 2010*, p. CTuM3, 2010.

Chapter 7

Ultra-narrow linewidth and molecular motion resolved spectrum of Stokes emission in spatially nano-structured Raman gain

In this chapter, a novel configuration of stimulated Raman scattering is reported. The model is based on optically induced nanostructured Raman gain, whereby the population difference is saturated but in 1D periodic sub-wavelength sections over a long interaction length. The results show a multi-watt forward and backward Stokes emission with structured spectrum and linewidth as narrow as ~ 10 KHz (>5 orders of magnitude shorter than the Raman linewidth). Observation of rich dynamics that include Rabi splitting, molecular motional sideband and inter-sideband four wave mixing, and finally AC stark induced molecule acceleration is reported

7.1   Introduction

In the preceding chapters, we have seen that among the requirements in building our optical waveform synthesiser based on molecular modulation in gas filled HC-PCF, we count CW lasers which frequency difference must match that of the Raman resonance, and that they have to exhibit high power and narrow linewidth. The power requirement is set by the necessity to exceed the MW/cm² intensity level to drive the molecule. With PBG HC-PCF we have seen that this intensity level is reached with laser power as low as 1W, and that with SRS we can emit at our desired wavelength with power as high as 50 W. This chapter examines the linewidth of CW Stokes. The results show a novel SRS dynamic with linewidth reaching unprecedentedly low values with a minimum being measured to be 14 kHz, which is over 5 orders of magnitude lower than the 1 GHz collisional linewidth predicted by conventional SRS for 20 bar of gas pressure. In addition to the narrow linewidth, the Stokes scattered-spectrum exhibits: (1) sidebands due to the motion of trapped molecules by the fields induced potential well, (2) Mollow triplet due to Rabi-splitting, and (3) higher-order sidebands due to four wave mixing (FWM). Notably, the results of this rich dynamic are scalable, as one could suppress the sidebands by only changing the pumping power and the gas pressure. A theoretical model, developed by F. Benabid, explains all the observed spectral features. It shows that because of Raman saturation over its effective length, the molecular gas only scatters from one-dimensional periodic array of sub-wavelength wide sections and spaced by half the Stokes optical wavelength. In turn, the emission spectral signature features properties analogous to a single molecule fluorescence or a quantum electrodynamic cavity (QED).

The impact of this chapter results overarches the sole objective of developing an optical waveform synthesiser. Indeed, in addition to having a powerful output and narrow linewidth laser at tailored wavelengths, the results achieved provided us within a single photonic component several sub-Doppler spectral

signatures of a dynamics that comprises molecular motions, Dicke-like narrowing, Rabi-splitting and inter-sideband nonlinear interactions. These results indicate that our system is an original platform to observe phenomena that were thought to usually be in the realm of cold atoms or Bose-Einstein condensate (BEC).

In the first section, we describe the experimental set-up. The second section describes the different spectral traces of the backward and forward Stokes emission in varied conditions of input power and gas pressure. The spectra were presented with two spectral spans. The first presentation is a resolved spectrum around the central peak, which we call "fine structure". The second presentation spans a larger bandwidth to show the sideband properties, and will be coined "broad structure". The third section describes the theoretical model and analyses the different results. Finally, we show yet another feature of the novel dynamics by observing AC Stark acceleration of the molecules inside the HC-PCF.

7.2   Experimental set-up

The experimental set-up is schematically shown in Figure 7.1. A home-made PBG guiding HC-PCF (see chapter 2) is filled with molecular hydrogen at a controllable pressure, using the set-up described in [1]. Here, the gas cells housing the two fibre ends are equipped with AR coated windows at both sides to avoid laser back reflection. The fibre has a core diameter of 6.5 μm, corresponding to a HE_{11} guided core mode field diameter of ~ 5μm and guides from 1000 nm to 1200 nm with a loss of 70 dB/km (see figure 7.1 (c)).   The hydrogen-filled fibre is excited with a randomly polarised CW laser that could emit up to a maximum of 100 W of optical power, with a linewidth of only ~400

kHz, and at a wavelength of 1061 nm. The optical spectrum from both fibre-ends is monitored using an optical spectrum analyser.
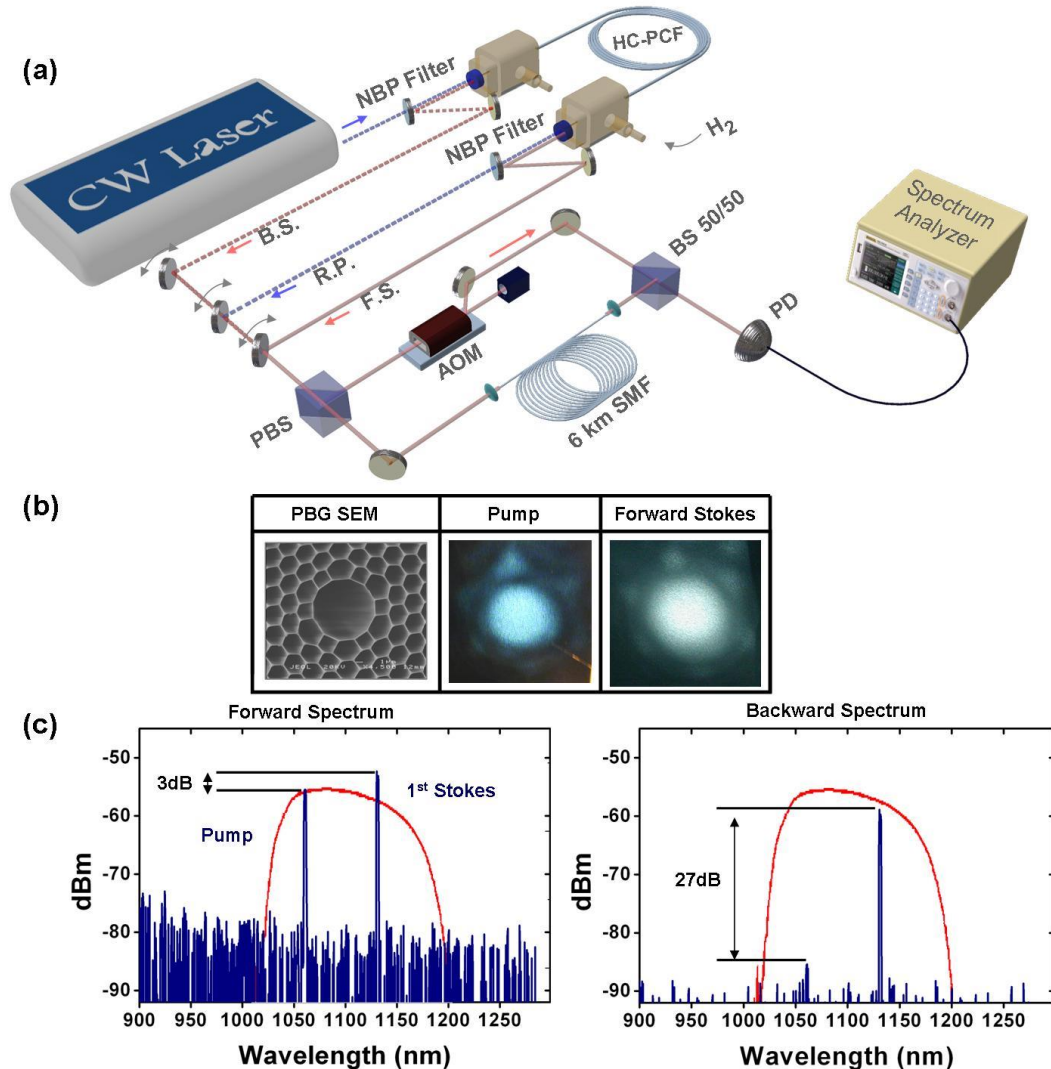

Figure 7.1: (a) Schematic of experimental setup consisting of Raman generation through PBG HC-PCF and self-heterodyne linewidth measurement technique. NBP Filter: narrow bandpass filter; B.S: Backward Stokes; F.S: Forward Stokes; R.P: residual pump, AOM: acousto-optic modulator; PBS: polarisation beam splitter; BS: beam splitter; SMF: single mode fibre; PD: photodetector. (b) Pump source and first Stokes spectrum generated in PBG fibre and recorded by optical spectrum analyser. Inset the SEM of the fibre. (c) The recorded linewidth trace for pump, forward Stokes and backward Stokes. F.S: forward Stokes; B.S: backward Stokes; R.P: residual pump.

Figure 7.2 shows the typical recorded spectra of the transmitted (forward spectrum) and back-reflected (backward spectrum) beams when 29 W of pump

power is sent into the fibre. The fibre-coupling efficiency was estimated to be 60%, and is considered the same throughout the chapter unless otherwise specified. The forward spectrum shows two spectral lines; one at 1061 nm from the pump laser, and a second at 1131 nm from forward 1st order Stokes (FS). The FS line shows an 8 dB extinction ratio above that of the pump. The backward spectrum is composed mainly of the backward Stokes (BS) line, with residual light from the pump, which is back reflected off the fibre input end. Such a reflection off the fibre tip results from a residual optical overlap between the core-guided mode and the cladding silica, and ranges typically around 1% of the total coupled power. Except for wavelength near anti-crossing between surface mode and core mode where the power fraction in the silica reaches ~10%. Figure 7.2 shows the typical fibre output beam profile at the pump and the Stokes wavelength. With this system, as we have seen it in the preceding chapter, we have successfully coupled up to 85 W into the fibre, and generated a maximum of 55 W power in the forward Stokes and 5 W power in the backward Stokes.

The set-up also comprises a portion with a self-heterodyne interferometer to measure the linewidth of both forward and backward propagating beam spectral components. The self-heterodyne system consists of a delay arm made of a 6 km long optical single-mode fibre (SMF), and a short modulation arm comprising an acousto-optic modulator (AOM) operating ~211 MHz. The beat signal between the delayed optical beam and the AOM-frequency down-shifted signal is detected using a fast photo-detector and recorded using an RF spectrum analyser. The linewidth traces of the pump, FS and BS are then analysed for different pump lasers and gas pressures.

7.3 Stokes linewidth and spectral structure

7.3.1 Transmitted pump and Stokes linewidth

Figures 7.2 (a), (b) and (c) show typical linewidth traces over 4 MHz spectral span of the forward Stokes (FS), backward Stokes (BS), and the pump respectively for 30 bar of pressure and 16 W of pump power sent into the fibre (i.e. 6 W of coupled power assuming the estimated fibre-coupling efficiency of 60%). As mentioned above, unlike what one would expect from the conventional picture of SRS process, whereby the Stokes linewidth is expected to be around 1 GHz for a gas pressure of 20 bar [2], the present emitted Stokes lines are outstanding with a linewidth that is over 5 orders of magnitude narrower. The measured linewidth of both FS and BS are below 20 kHz, which is well below the Doppler limit linewidth (FWHM) of 153 MHz and 300 MHz for H_2 rotational Raman transition in forward and backward configurations respectively [3]. The linewidth of the fibre transmitted pump was measured to be ~ 400 kHz, and is consistent with the manufacturer specifications. However, the FS and BS exhibit both a non-Gaussian and structured linewidth-trace profile with a pair of sidebands at 200 kHz and ~1 MHz respectively. The origin of these sidebands is discussed later.

It is noteworthy that the pump linewidth value and the trace spectral profiles remain unchanged when both the fibre-coupled power, and the gas pressure are varied (see Figure 7.3).   In contrast, FS and BS linewidth and trace strongly depend on the pump power coupled to the fibre and to the gas density.
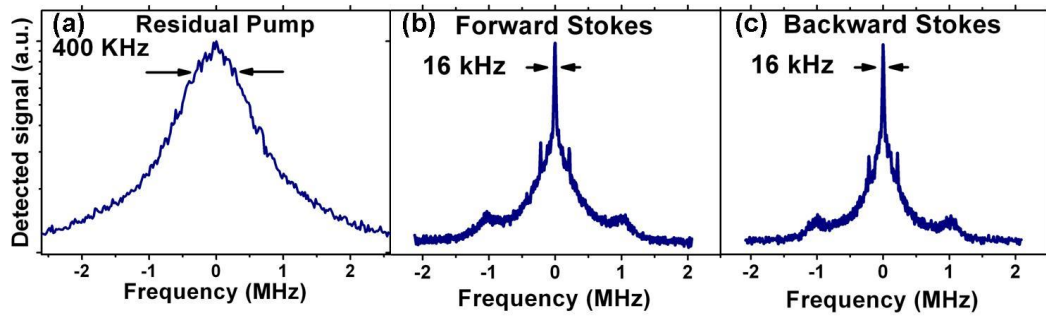
Figure 7.2: The recorded linewidth trace for (a) pump, (b) forward Stokes and (c) backward Stokes.
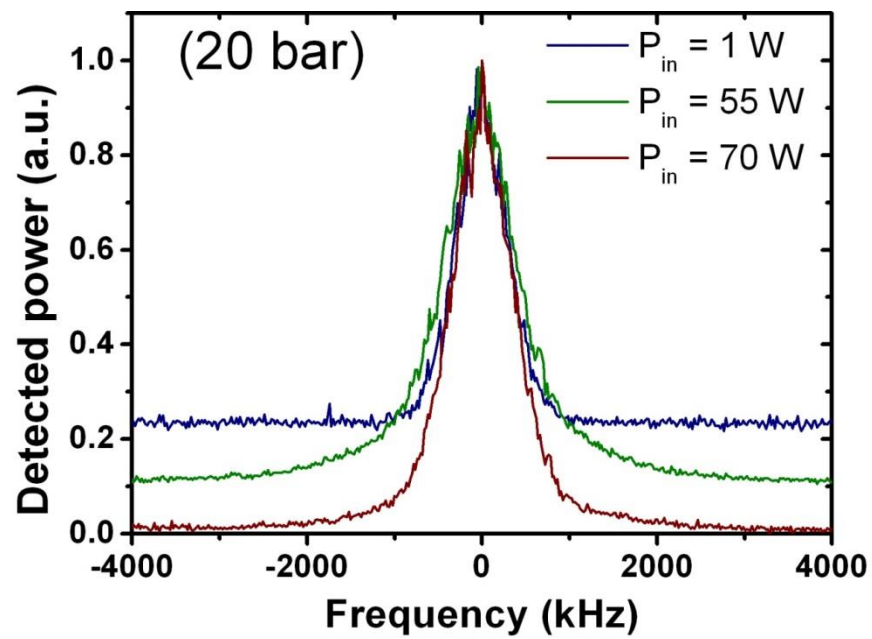

Figure 7.3: The recorded linewidth trace for residual pump at different power levels.

7.3.2 Stokes Linewidth and line-shape evolution with pump power and gas pressure

7.3.2.1 Linewidth "fine" structure

The trend of the spectral linewidth and profile evolution with the input power and the gas pressure for FS and BS is summarised in Figures 7.4 (a)-7.4 (d). Each figure shows, for a given fixed gas pressure, the evolution with the pump input power of both the optical spectrum of the transmitted beam, and that of 6 MHz-span RF spectrum of the forward and backward Stokes lines. Here, the input power ranges from 9 W (i.e. coupled power of 5.4 W) to 42 W. Given the necessity of resetting the laser fibre-coupling for each power level due to the change of its beam size and divergence, the number of input power runs was limited to 3 or 4 power-values of 9 W, 16W, 29W and 42 W. The rest of the figure series show the same content but at a different pressure. Four pressure values of 20 bar, 30 bar, 40 bar and 50 bar were investigated.

All figures of the series show broadly the same qualitative trend. For a relatively low input power range, the linewidth traces of both FS and BS show a central peak with an ultra-narrow linewidth that slowly decreases with pressure increase. For example, in the case of 9 W input power, the FS linewidth exhibits a minimum value of 14 kHz at 50 bar, and increases to 42 kHz at 20 bar. Similarly for BS, the linewidth is 16 kHz at 40 bar and increases to 44 kHz when the pressure is dropped to 20 bar. At higher pump power levels, corresponding to $P_{in} \geq 29W$, the linewidth increases and the line shape is altered. The linewidth increase is observed to be stronger at low pressure (here 20 bar) than with high pressure. Furthermore, for higher pressure (>30 bar) the spectral structure of the emission trace is significantly altered. The line shape exhibits a "triangular" profile with the sidebands no longer resolved. This is correlated with the generation of the second order Stokes as is shown in the

transmitted optical spectrum. The theoretical explanation will be provided in the following section.

Finally, the rather intricate evolution of FS and BS with pressure and pump power become much clear when the linewidth is shown in a more condensed manner by plotting against the product of the pump power and the gas pressure. This is illustrated in Figure 7.5 (a) and (b). The results show for both FS and BS that linewidth is relatively constant for a $P_{in} \times \Pr essure$ range between ~125 W·bar and 1200 W·bar, and then broaden rapidly when this product is larger than 1200 W·bar. This broadening coincides with the generation of the second order Stokes.
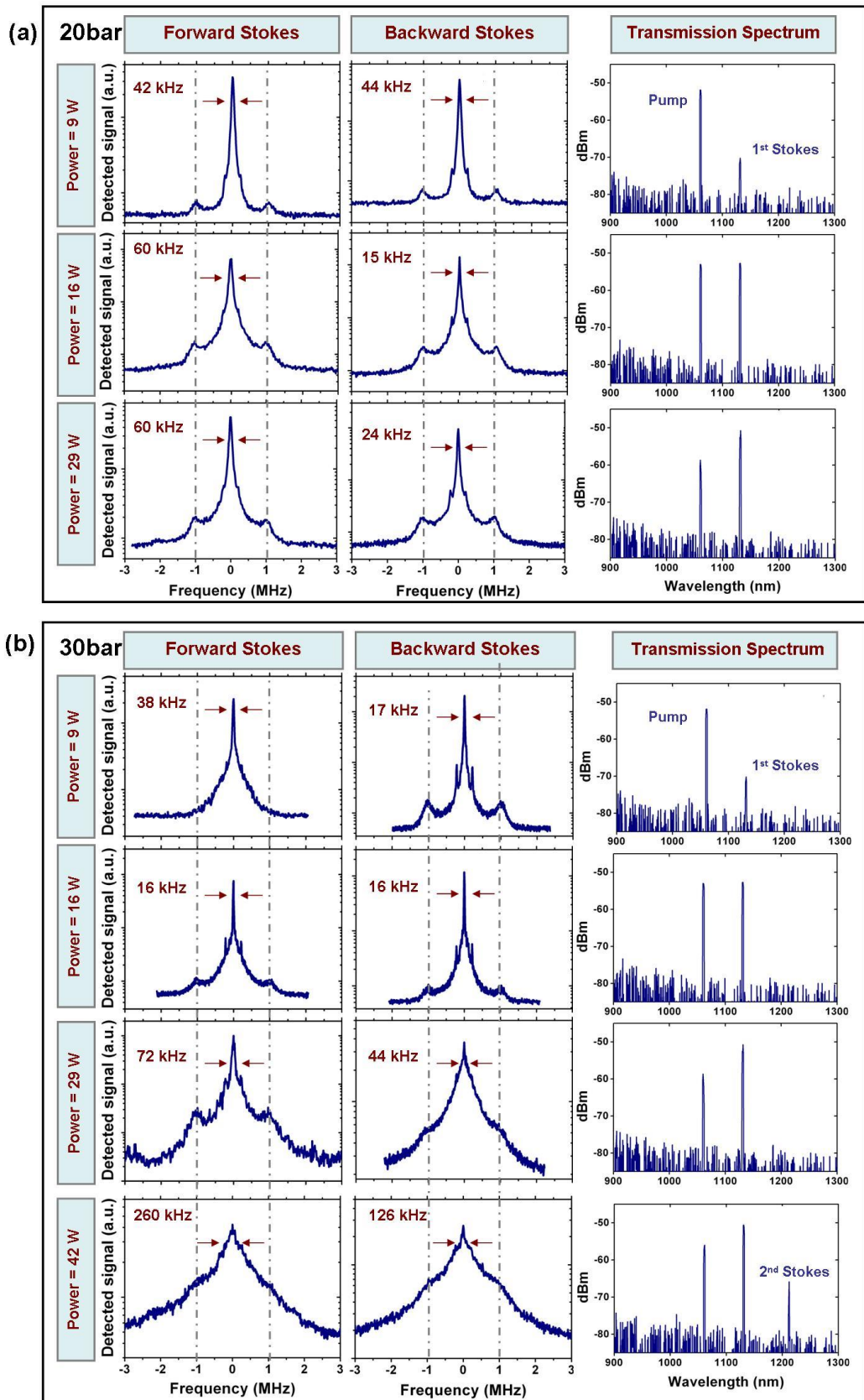
Figure 7.4 (a-b): Spectral linewidth evolution with the input power for FS and BS at gas pressure of (a) 20 bar and (b) 30 bar.
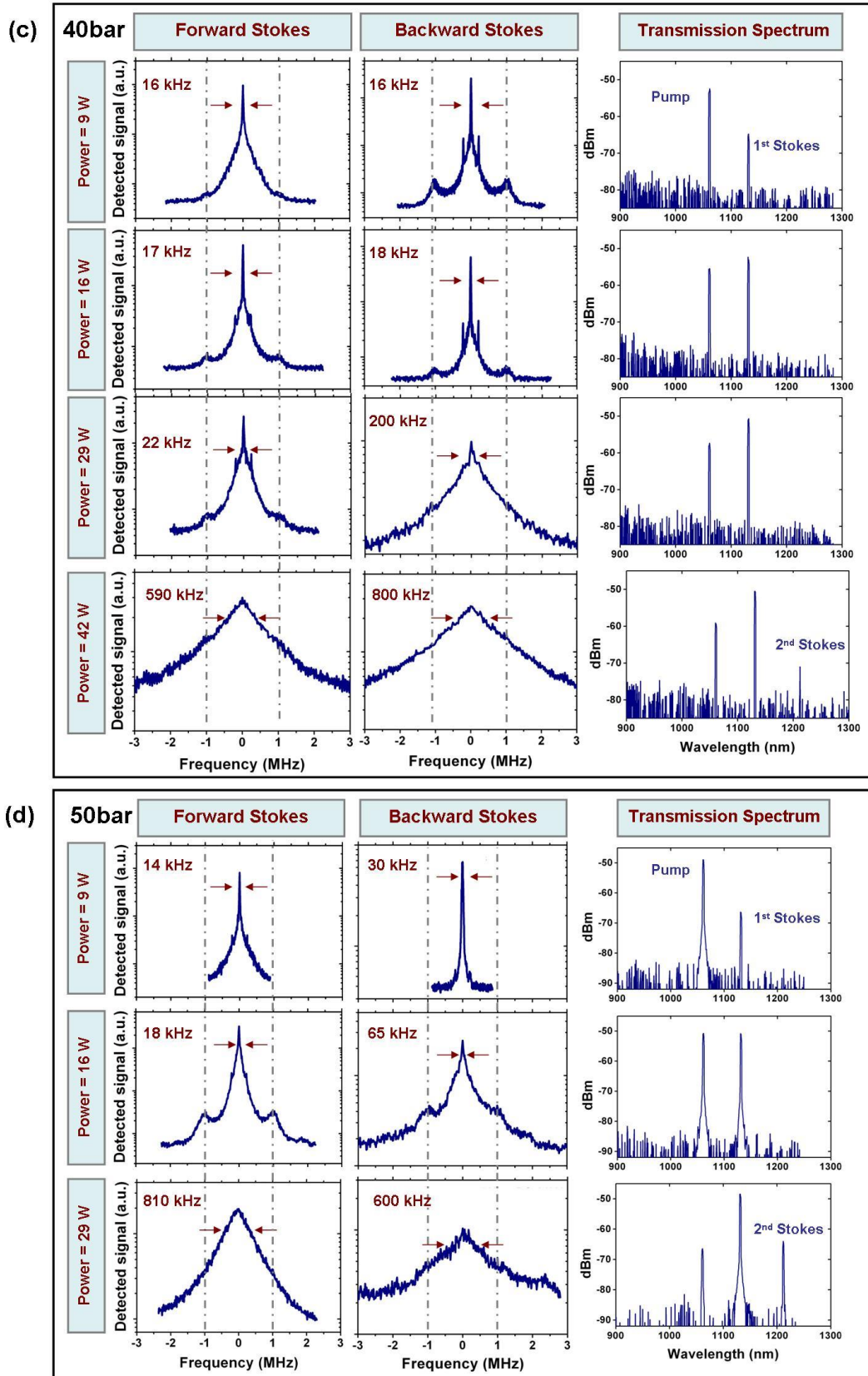
Figure 7.4 (c-d): Spectral linewidth evolution with the input power for FS and BS at gas pressure of (c) 40 bar and (d) 50 bar.
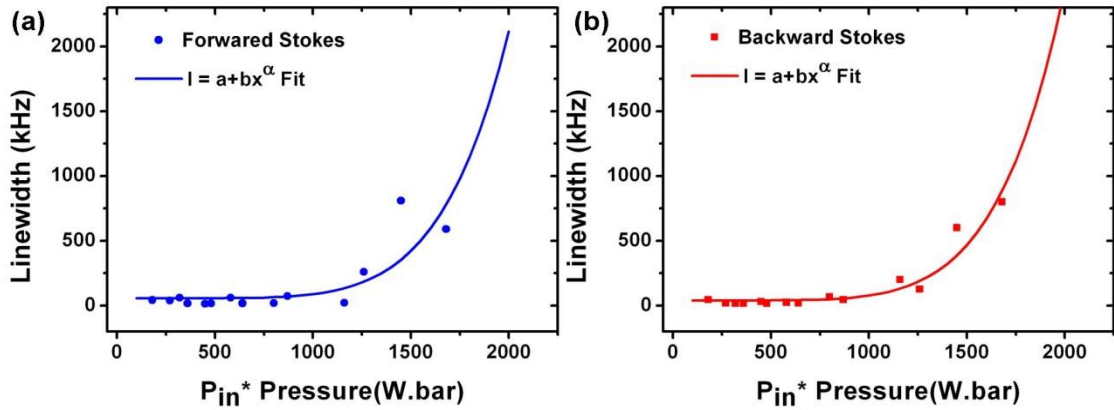
Figure 7.5: linewidth versus the product of the pump power and the gas pressure for forward and backward Stokes.
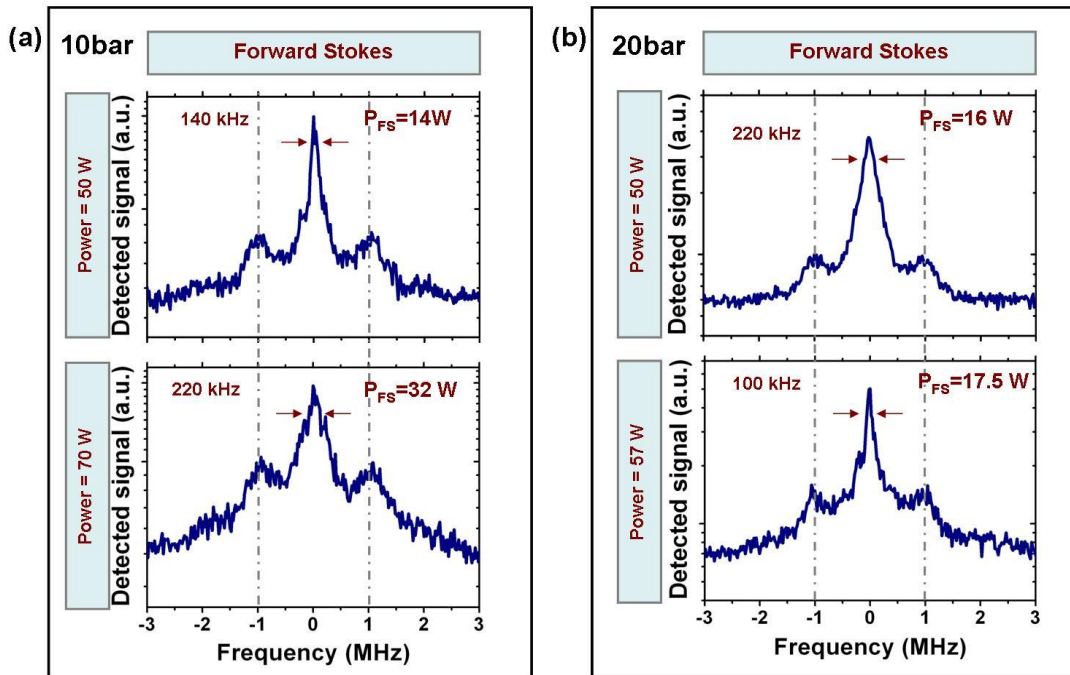
Figure 7.6: Spectral linewidth evolution with the input power for FS and BS using 7 m of PBG HC-PCF at gas pressure of (a) 10 bar and (b) 20 bar.

These results were also observed with a shorter fibre, and in a slightly different pressure range. Figure 7.6 shows the linewidth traces of FS and BS generated from a 7 meter long PBG HC-PCF. The fibre is similar to the one used so far. The input power was increased to 70 W, and the gas pressure was set to 10 bar and 20 bar. This indicates that one could obtain a laser with an ultra-narrow

linewidth at high power by simply lowering the pressure. For example with a pressure of 10 bar, a generated and transmitted Stokes with a power level in the range of 30-50 W and a linewidth of ~100 kHz was achieved. Consequently, we have achieved the requirements in developing the pair of lasers for the future CW Raman comb generation. Furthermore, the above and the following results show that our Stokes generation holds a broader potential than that of Raman comb generation.

In addition to an unconventionally narrow linewidth and a distinctive evolution of pressure compared to conventional pressure broadening, the linewidth trace exhibits two broad sidebands at ~1 MHz. The spectral position of these sidebands (indicated by vertical dashed grey lines in the different figures above) doesn't significantly vary in the range of $P_{in} \times \mathrm{Pr}essure$ below ~1200 W·bar. It is noteworthy that above this range, the sidebands are no longer observable.

Figure 7.7 (a) corroborates the above and shows the sideband evolution with input power for three different pressures. For a pressure of 20 bar and 30 bar the sideband frequencies shift from the central peak, increases very slowly when the input power is increased from 10 W to 16 W, and then decreases again when the input power is further increased. The sideband frequencies are also plotted against the product $P_{in} \times \mathrm{Pr}essure$ as shown in Figure 7.7 (b). The origin of these sidebands, as discussed later, is due to a transverse motion of the molecule. Finally, second pair of sidebands around 200 kHz are also observed when the linewidth is sufficiently narrow. The source of these sidebands are currently undefined.
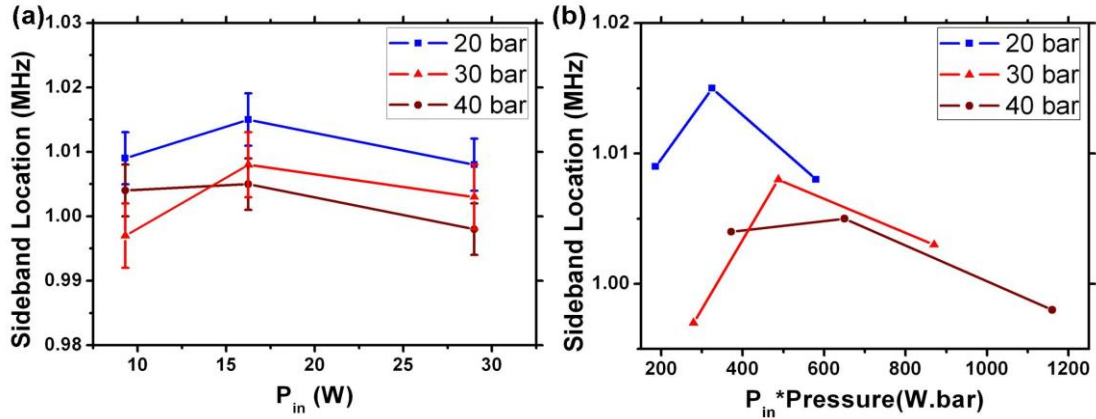
Figure 7.7: Sidebands evolution at ~1 MHz with (a) input power and (b) product $P_{in} \times \mathrm{Pr}\,essure$, for different gas pressures.

7.3.2.2 Linewidth "broad" structure

In this section, we re-examine the linewidth traces and their evolution with input power and gas pressure, but over a larger RF frequency span of 160 MHz. The recorded spectral traces are displayed in a similar fashion to those of the linewidth fine structure. Four figures (Figure 7.8(a)-(c)) contain the evolution of the spectral traces with input power for a given fixed pressure. The pressure values are the same as in the preceding sections. For the lower-range pressure (20 bar), the spectral traces of both FS and BS are dominated by a single narrow peak, which are accompanied by mainly two families of small sidebands. The first family of sidebands are located in the range of ~7-8 MHz and their higher order harmonic frequencies. We call these sidebands longitudinal motion sidebands. The reason for this terminology will be given in the following section. It is noteworthy, that these longitudinal motion sidebands are observed for lower power levels. As a matter of fact for higher pressures, the sidebands are completely suppressed when the input power is increased. Figure 7.8(d) clearly illustrates this evolution. Here, the longitudinal motion sidebands, which are indicated by the red vertical lines, are clearly much stronger at a

power of 9 W than 16 W. When the power is 29 W, the signal strength of the sideband is even further decreased to be hardly above the baseline signal of the linewidth trace. This effect will be explained theoretically in the following section. Figure 7.10, illustrate the motional sidebands for the FS at different pressures as function of the input power.

The second sidebands are located in the range of ~12-15 MHz and their harmonic frequencies. These sidebands will be coined Rabi-splitting sidebands. Figure 7.9 (a) shows the frequency location of the 1st order Rabi sideband of the ~12-15 MHz for the FS as a function of input power. The frequency difference between the FS and BS at 1st order Rabi sideband is illustrated in Figure 7.9 (b). The ratio between the power level of the 1st order Rabi sideband to central peak is defined here as "*R*". Figure 7.9 (c) and (d) show the ratio *R* for 1st order Rabi sideband as a function of input power for the FS and BS. Moreover, the 2nd order Rabi sideband ratio is plotted for both FS and BS in Figure 7.9 (e) and (f). The evolution of the 2nd order Rabi sideband is typical of a nonlinear optical effect. We attribute this effect to four wave mixing (FWM) [4] between Stokes central peak and the two sidebands and with a frequency given by $\omega_{2nd} = \omega_S + (\omega_S \pm \Omega_{Rs}) - (\omega_S \mp \Omega_{Rs}) = (\omega_S \pm 2\Omega_{Rs})$. The 2nd order Rabi sideband signal will be determined by the nonlinear susceptibility at its frequency $\chi(\omega_{2nd})$ via the relation $E_{2nd} = \chi(\omega_{2nd})E_S(\omega_S)E_{Rs}(\omega_S \pm \Omega_{Rs})E_{Rs}^*(\omega_S \mp \Omega_{Rs})$.
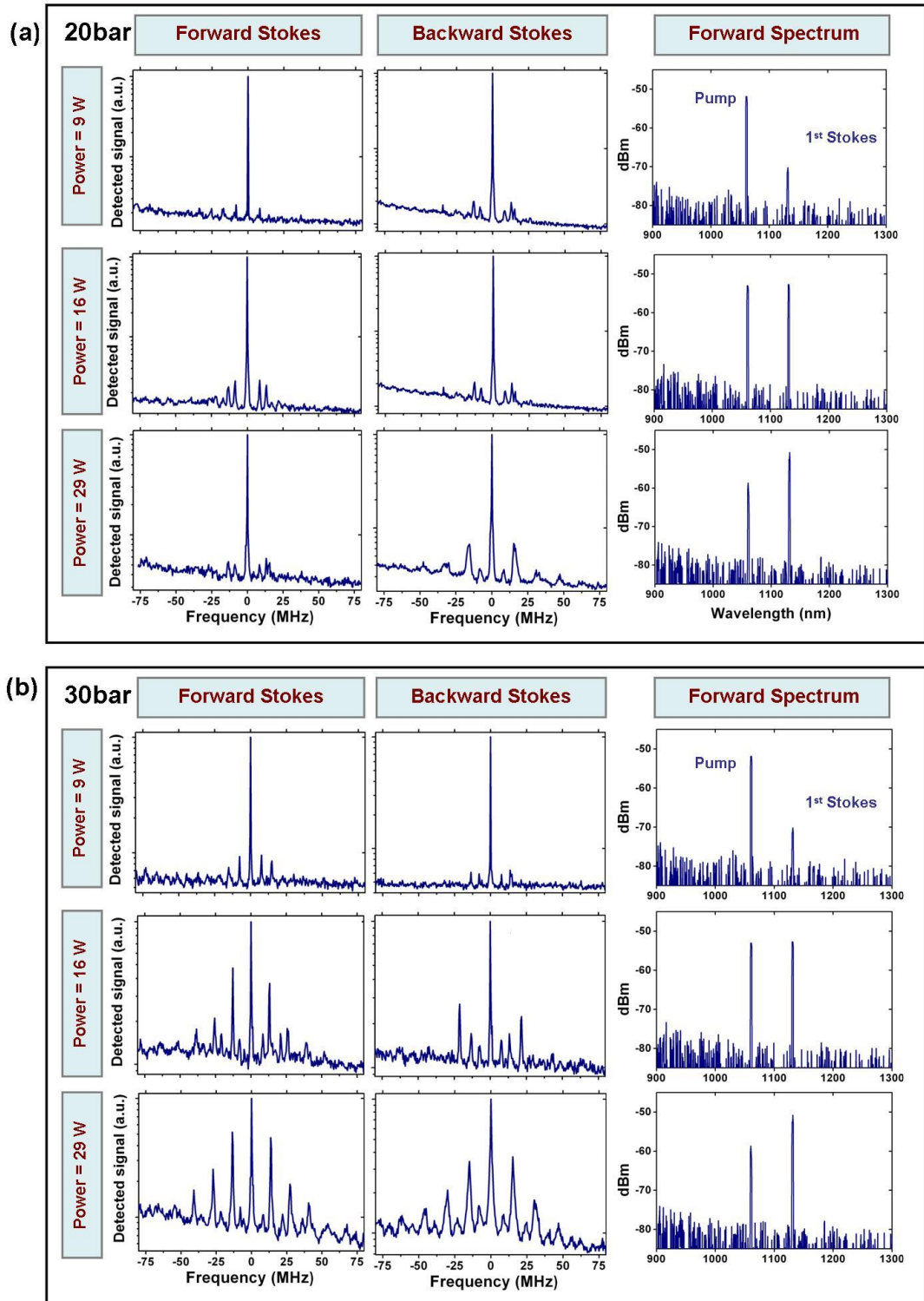
Figure 7.8 (a-b): Evolution with the input power for FS and BS at gas pressure of (a) 20 bar and (b) 30 bar.
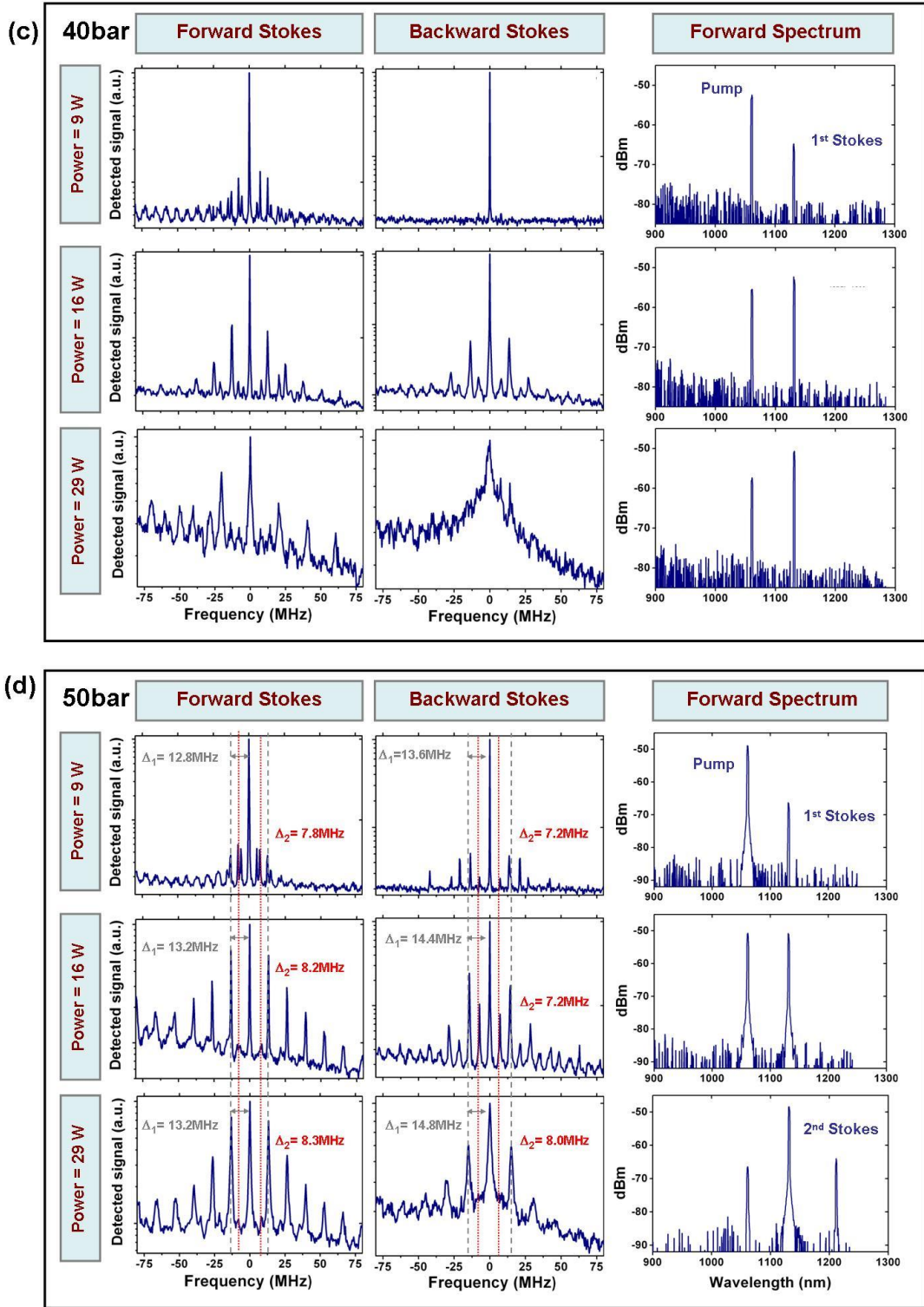
Figure 7.8 (c-d): Evolution with the input power for FS and BS at gas pressure of (c) 40 bar and (d) 50 bar.
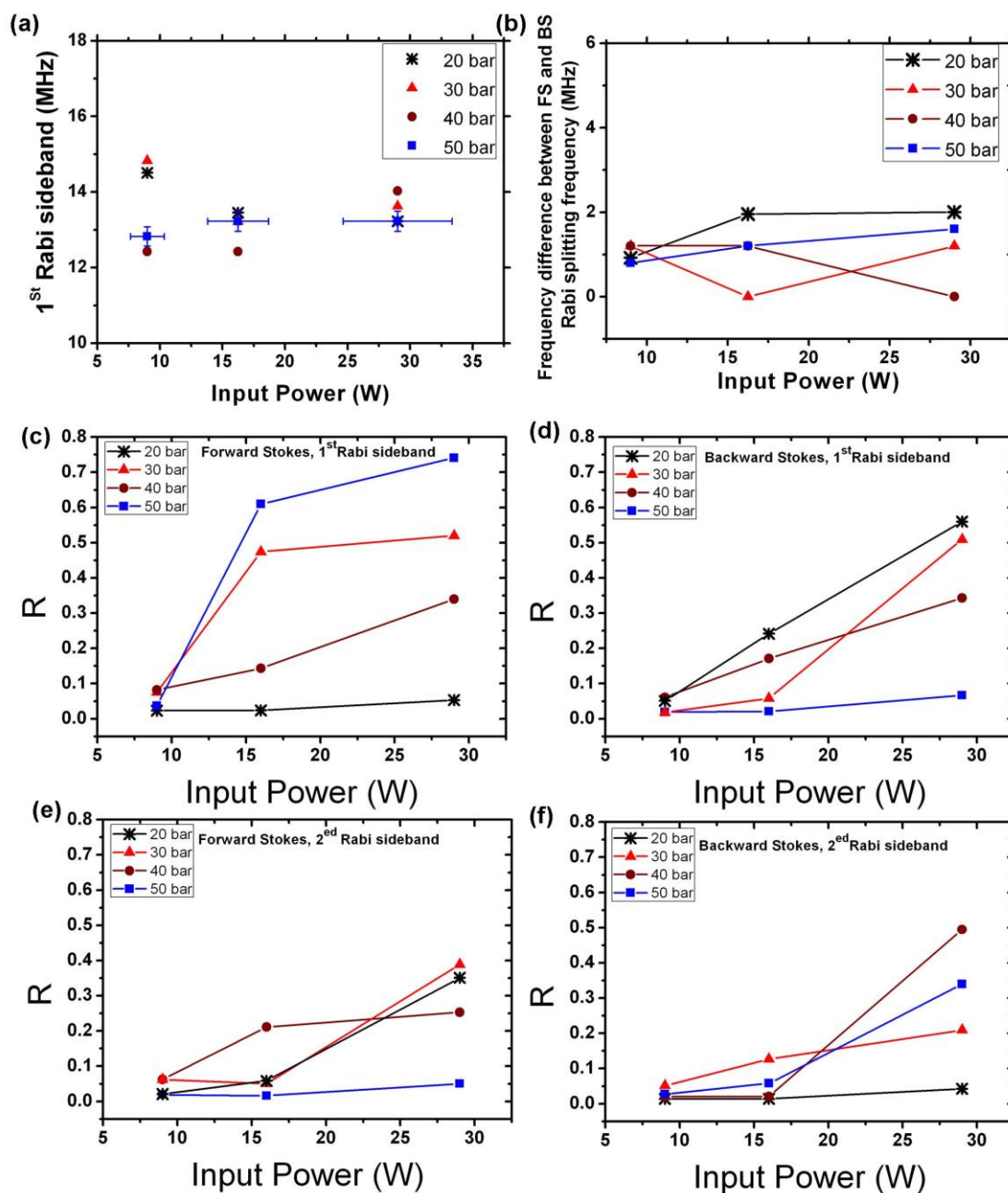
Figure 7.9: (a) The 1st order Rabi sideband frequency location for the FS as function of the input power at different gas pressures. (b) The frequency difference 1st order Rabi sideband between the FS and BS. The ratio *R* for the 1st order Rabi sideband as function of input power for (c) FS and (d) BS. The ratio *R* for the 2ed order Rabi sideband as function of input power for (e) FS and (f) BS.
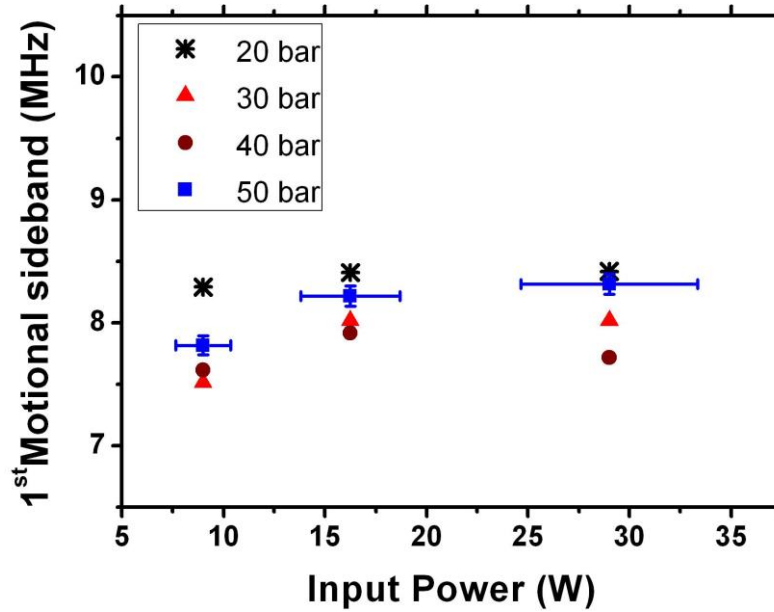
Figure 7.10: The 1st order motional sideband frequency location for the FS as function of the input power at different gas pressures.

7.4 Theoretical model and data analysis

7.4.1 Theoretical model

In order to explain the above experimental results, we use a theoretical model[6] that can be summarised as follows. Firstly, we treat the Raman medium as a two-level system. Using the density matrix formalism we deduce a steady-state expression for the population, coherence and subsequently the Raman gain. Secondly, we numerically solve the Raman coupled motion equation to extract the Stokes and pump field distribution along the fibre. Notably, we take into account the field reflection at the fibre tips. In PBG HC-PCF, the power reflectivity ranges are typically between 10^{-4} and 10^{-3}.

---

[6] The theoretical model was conceived and developed by Fetah Benabid. The numerical calculations were undertaken by Anton Husakou

The two level states $\{|1\rangle, |2\rangle\}$ of the system represent the ground and excited states of the molecule rotation (see Figure 7.11 (a)). The effective interaction Hamiltonian in the rotating wave approximation (RWA) and after the adiabatic elimination of the upper electronic states $\{|i\rangle\}$ [5]–[7], the effective Hamiltonian can be written as:

$$H_{eff} = \frac{\hbar}{2} \begin{pmatrix} \Omega_{11} & \Omega_{12} \\ \Omega_{21} & \Omega_{22} \end{pmatrix} + h.c., \tag{7.1}$$

Here, $\Omega_{11} = a_{-1} E_S E_S^* + a_0 E_P E_P^*$ and $\Omega_{22} = d_{-1} E_S E_S^* + d_0 E_P E_P^*$ are the Stark shift of the ground and the excited state respectively. E_P and E_S are the pump and Stokes fields with angular frequency of ω_P, and ω_S respectively. In our case both fields are highly dependent on z (position along the propagation direction). $\Omega_{12} = \Omega_{21}^* = b_0 E_P E_S^*$ is the two-photon Rabi frequency. Here a_i, b_i and d_i are the coupling coefficients related to the dipole moments between the two rotational levels and the different states involved (including the electronic upper states) [7].
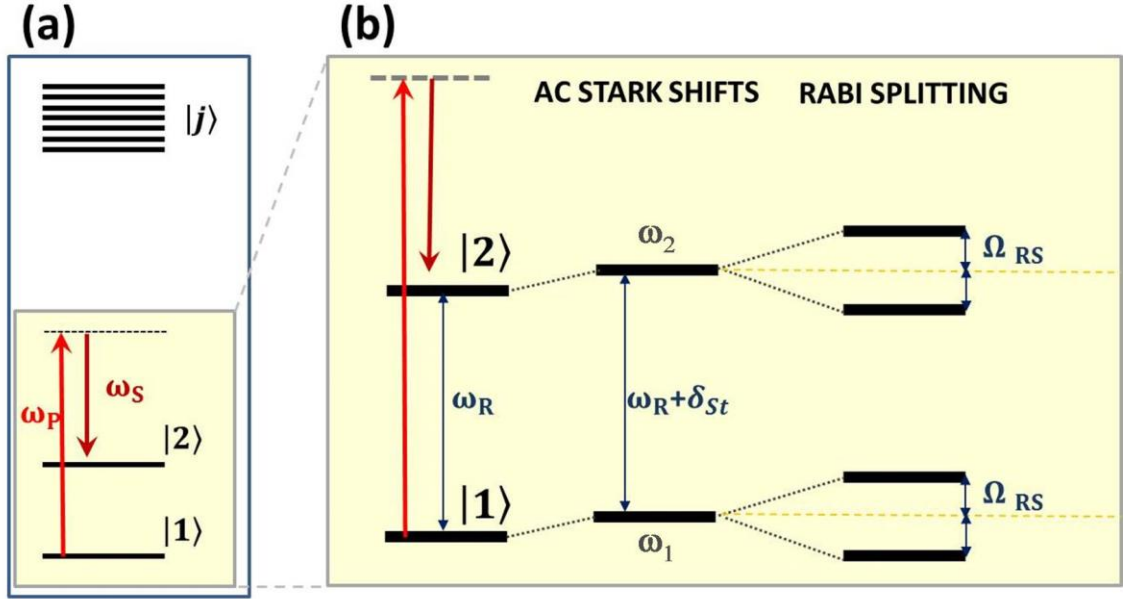
Figure 7.11: (a) The two level system. (b) Evolution of the two-level system in the presence of the fields E_p and E_s.

Figure 7.11 (b) shows the evolution of the two-level system when the molecule is in the presence of the fields E_P and E_S. For sufficiently strong fields, the energy levels get shifted by the AC Stark effect and split by the Rabi splitting effects. The fields are written in function of their forward, $E_{P,S}^{(f)}$ and backward, $E_{P,S}^{(b)}$ propagating components as

$$E_P = E_P^{(f)} + E_P^{(b)} = E_P^{(f)}(1 + r_P) \tag{7.2}$$

$$E_S = E_S^{(f)} + E_S^{(b)} = E_S^{(f)}(1 + r_S) \tag{7.3}$$

Here, $r_{P,S}$ are defined by $E_{P,S}^{(b)} = r_{P,S} E_{P,S}^{(f)}$. It noteworthy that in our experimental conditions of SRS generation in a HC-PCF, the field is highly dependent on z, and hence $r_{P,S}$ is also z-dependent.

Solving the Bloch equations within the density matrix formalism, we get the following steady-state expressions for the normalised population difference,

$\rho_{22} - \rho_{11}$, the Raman coherence, ρ_{12} and, the systems potential expectation value, U_{tot} (expressed in Hz) are:

$$\rho_{11} + \rho_{22} = 1 \quad \rho_{22}^{(0)} - \rho_{11}^{(0)} = -1$$

$$\rho_{22} - \rho_{11} = A = \left(\rho_{22}^{(0)} - \rho_{11}^{(0)}\right) \frac{1}{1 + 4\dfrac{|\Omega_{12}|^2}{\Gamma_{12}\gamma_{12}}} \tag{7.4}$$

$$\rho_{12} = i\left(\rho_{22} - \rho_{11}\right) \frac{\Omega_{12}}{\gamma_{12} - i(\tilde{\delta})}$$

$$\left\langle \hbar^{-1} U_{tot} \right\rangle = Tr(\rho H_{int})$$

$$= \left(\rho_{21}\Omega_{12} + \rho_{12}\Omega_{21}\right) + \left(\frac{1 - (\rho_{22} - \rho_{11})}{2}\Omega_{11} + \frac{1 - (\rho_{22} - \rho_{11})}{2}\Omega_{22}\right) + \frac{1 - (\rho_{22} - \rho_{11})}{2}\omega_R$$

$$\tag{7.5}$$

Here, $\rho_{22}^{(0)} - \rho_{11}^{(0)}$ is the initial normalised population difference where we assume that all the molecules are initially in the ground state. The detuning of the pump and the Stokes frequency is determined by the Stark shift as $\Omega_{11} - \Omega_{22} = \tilde{\delta}$. γ_{12} is the Raman dephasing rate, Γ_{12} the population decay rate. Γ_{12} is taken to be approximately $2\pi \times 10kHz$, γ_{12} is $\sim 2\pi \times 1GHz$ for a pressure of 20 bar [3]. ω_R is the Raman shift resonance in the absence of driving field.

Substituting the field expression in the different Hamiltonian frequencies, we get the expression for the two-photon Rabi frequency:

$$|\Omega_{12}|^2 = \left|d_{-1}\overline{E}_P^{(f)}\overline{E}_S^{(f)}\right|^2 \begin{bmatrix} 1 + r_P^2 + r_S^2 + 2r_P^2 r_S^2 + 2r_P^2(1 + r_P^2 r_S^2)\cos(2\beta_P z) + \\ 2r_S^2(1 + r_P^2 r_S^2)\cos(2\beta_S z) + 2r_P^2 r_S^2 \cos(s(\beta_S + \beta_P)z) \end{bmatrix} \tag{7.6}$$

Here, $E_i = \overline{E}_i e^{i\beta z}$ and β_i is the propagation constant. The subscript p for the pump field and S for the Stokes field.

Similarly, we get the following expressions for the Stark shift frequency, the population difference and the Raman gain coefficient:

$$\tilde{\delta} = (a_0 - b_0)\left(\left|(\overline{E}_P^{(f)})\right|^2 (1 + r_P^2 + 2r_P^2 \cos(2\beta_P z))\right) +$$
$$(a_{-1} - b_{-1})\left(\left|(\overline{E}_S^{(f)})\right|^2 (1 + r_S^2 + 2r_S^2 \cos(2\beta_S z))\right) \tag{7.7}$$

$$\rho_{22} - \rho_{11} =$$
$$\frac{(\rho_{11}^{(0)} - \rho_{11}^{(0)})}{1 + \dfrac{\left|d_{-1}\overline{E}_P^{(f)}\overline{E}_S^{(f)}\right|^2 \left[1 + r_P^2 + r_S^2 + 2r_P^2 r_S^2 + 2r_P^2(1 + r_P^2 r_S^2)\cos(2\beta_P z) + 2r_S^2(1 + r_P^2 r_S^2)\cos(2\beta_S z) + 2r_P^2 r_S^2 \cos(s(\beta_S + \beta_P)z)\right]}{\Gamma_{12}\gamma_{12}}} \tag{7.8}$$

$$g_R = \left[\frac{2\omega_S}{n_S n_P c^2 \varepsilon_0^2} N\hbar d_S^2 (\rho_{22}^{(0)} - \rho_{11}^{(0)})\right] \frac{\gamma_{12}^2 + \delta^2}{(\gamma_{12}^2 + \delta^2) + 4\dfrac{|\Omega_{12}|^2}{\Gamma_{12}}\gamma_{12}} \cdot \frac{1}{\gamma_{12}^2 + \tilde{\delta}^2}$$

$$= g(0)\frac{\gamma_{12}^2 + \delta^2}{(\gamma_{12}^2 + \delta^2) + 4\dfrac{|\Omega_{12}|^2}{\Gamma_{12}}\gamma_{12}} \cdot \frac{1}{\gamma_{12}^2 + \tilde{\delta}^2} \tag{7.9}$$

Here, N is the number for molecule density, $n_{S,p}$ is the refractive index for the Stokes or the pump.

In our case r_p and r_s are due to back reflection off the end of the hollow-core, and are determined from the solution of the Raman coupled equations, which we solve numerically. However, for the sake of demonstration, we firstly start by setting r_s as a free constant parameter, and take $r_p = 0$ as it is experimentally extremely small. Furthermore, it is noteworthy that a reflection grating is also established during Raman generation. Here, the reflection r_s kept constant for simplicity.

Figure 7.12 shows the Raman gain coefficient, the population difference and the total average potential in function of z over a distance of twice the Stokes wavelength (i.e. $2 \times \lambda_S \sim 2.2\mu m$) and for four pairs of pump and Stokes power values. Here, we consider the power in the backward Stokes to be equal to the forward Stokes (i.e. $r_S = 1$). The results show a periodic structure with z for both three physical quantities. We can distinguish two regions in this

z-distribution; one corresponds to high gain region (HGR), and a second with low gain, which we coin saturating region (SR). The HGR is characterised by a narrow region centred at an odd multiple of $z = \dfrac{\lambda_S}{4}$, and wherein the gain and the population difference are at their maximum. As the power of the Stokes and the pump are increased the HGR width gets narrower, whilst the gain in SR is strongly decreased to reach zero, corresponding to full population saturation in SR.
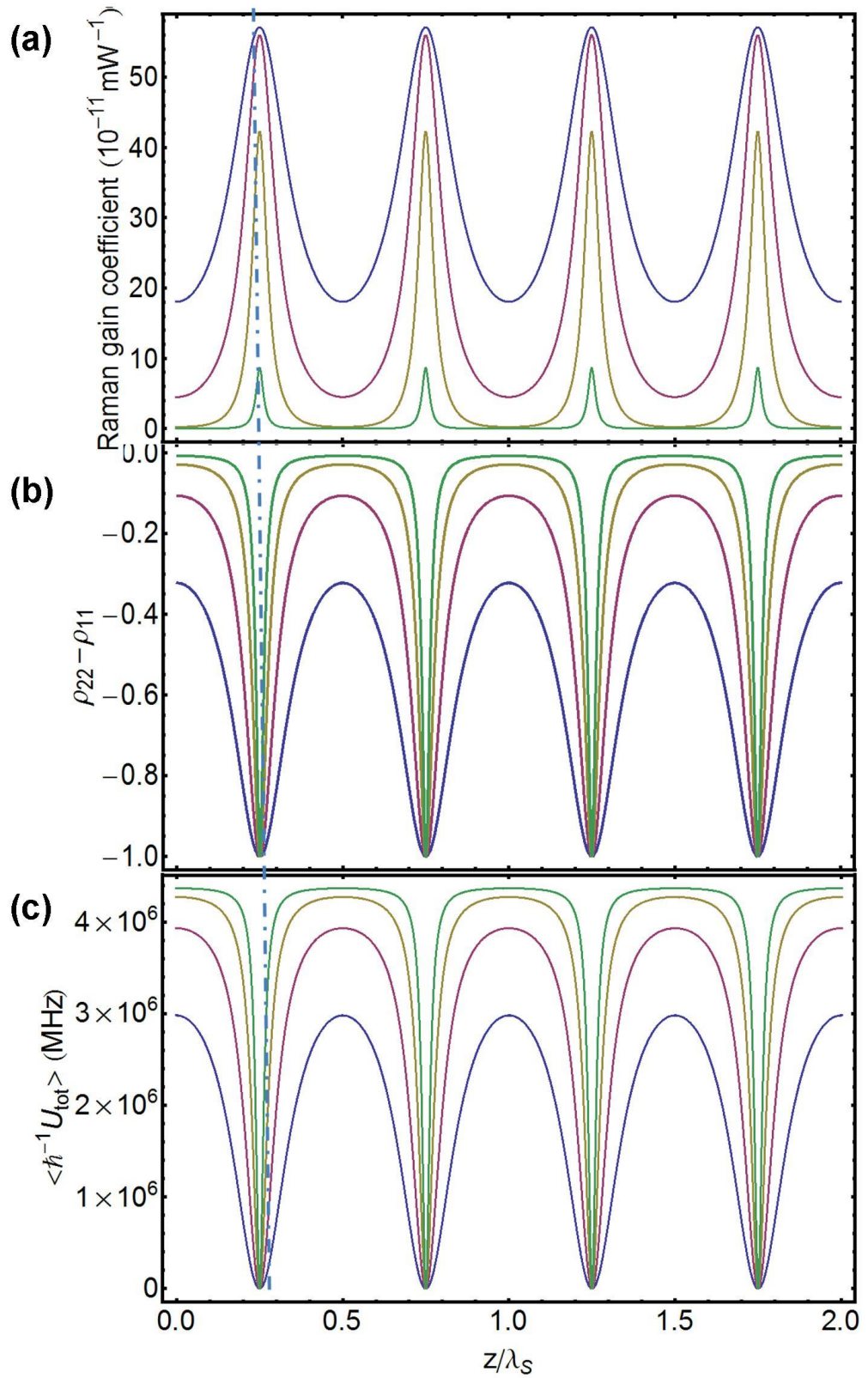
Figure 7.12: (a) Raman gain coefficient. (b) The population difference (c) The total average potential as function of z/λ_s. Power level of pump, FS and BS are as follow: 0.5, 0.125,0,125 (blue curve); 1, 0.25, 0.25 (red curve); 2,0.5,0.5 (brown curve); 4; 0.5,0.5 (green curve) respectively.

Remarkably, this gain and population spatial structure is achieved for relatively lower power levels of Stokes and pump. For example, full saturation (green curves in Figure 7.12) is reached even with 4W of pump power, and 1 W for FS and BS. This is so because the strong transverse confinement of the PBG HC-PCF guided mode reaches the saturation intensity (i.e. intensity level for which $\Omega_{12} \geq \Omega_{12}^{(sat)} = \sqrt{\gamma_{12}\Gamma_{12}}$ with low power levels. In our case $\Omega_{12}^{(sat)} \sim 2\pi \times 3MHz$ is reached even with the case of pump power =0.5 W (i.e. intensity of 3.3 MW/cm²), FS power =0.125W, and BS power =0.125 W, (here $\Omega_{12} \sim 10MHz$).

Furthermore, with such a spatially structured gain, it is noticeable that the scattering molecules are dominantly located in sub-wavelength wide regions, where FWHM reaches the outstanding figure of $0.05\lambda_S \sim 50nm$ in the case of 4W of pump power, and 1 W for FS and BS. In the case of r_S=1, the expression of the thickness of the Raman active region can be expressed as the spatial FWHM of the gain or the population difference. This gives a width:

$$\delta z = \frac{\lambda_S}{2\pi}\sqrt{\frac{\gamma_{12}\Gamma_{12}}{2\Omega_{12}^2}} = \frac{\lambda_S}{2\pi}\frac{\Omega_{12}^{(sat)}}{\Omega_{12}\sqrt{2}} \tag{7.10}$$

Consequently, their scattered spectrum deviates strongly from that of a Doppler-limited spectrum or a pressure broaden spectrum. Instead, as the experimental results show, one would expect a rather spectral signature analogous to those in Dicke regime [8] with a Lorentzian shape whose width is determined by the transit time of the molecule inside the Raman active region.

In our case, among the molecules that cross the Raman active nanometre wide sections, only those which have a sufficiently large "dwell time" could scatter. The characteristic times involved here are: (1) the population decay time of molecular rotation ($T_1 = \Gamma_{12}^{-1}$), and the excitation rate (i.e. Ω_{12}). This sets a limit on the velocity of molecules that are participating in the scattering process,

which is $v_{mol} < \max(T_1, \Omega_{12}^{-1})$. In our case the two-photon Rabi frequency is larger than 1 MHz, whilst T_1 is of the order of ~100 µs [9]. Consequently, the maximum velocity of the "active" scattering molecules is given by $v_{mol,\max} = \delta_Z / T_1$. In the case of 4W, 1W, 1W, we get the maximum velocity of the scattering molecules in the Raman active region of 0.1 mm/s. Therefore, for a transit-time of T_1, one would expect a Stokes emission spectrum with Lorentzian shape and a FWHM linewidth of 3.2 kHz. Interestingly, scaling this velocity of 0.1 mm/s with respect to the recoil velocity $v_R = \hbar k / M$ of the hydrogen molecule (~200 mm/s), the result gives a sub-recoil linewidth. This is only encountered in an ultra-cold atom, whilst here the molecules are thermal, but there is a velocity selection allowing only very slow molecules to scatter. The number of the molecules is rendered sufficiently large thanks to an extremely deep potential well, which keeps these molecules localised within the HGR. Figure 7.12(c) shows z distribution of this potential. The potential $\langle \hbar^{-1} U_{tot} \rangle$ exhibits a nanostructure wide HGR (δ_z) well and is centred at an odd even multiple of $\frac{\lambda_S}{2}$. The well depth strongly depends on the laser power of both Stokes and pump. Figure 7.12 (c) shows that this potential depth reaches a staggering figure of changes ~3 THz even for 0.5 W pump power and 0.125W for FS and BS, to 4.5 THz for 1 W pump power and 1W for FS and BS. The latter case corresponds to a velocity capture (i.e. the maximum velocity of the trapped molecules), $v_{cap} = \sqrt{2 \frac{U_{tot}}{m}}$, of ~217m/s. Consequently, a large fraction of the thermal molecules will be trapped in the HGR, and will be scattering Stokes light exhibiting not only a Lamb-Dicke spectral linewidth signature but also motional sidebands. A longitudinal one because of the above z-oscillation, and a transvers one because of the Gaussian-like beam of the fibre guided mode radial profile.

The frequency of such motions can be deduced by expanding the potential near the anti-nodes and using the approximation of a harmonic oscillator. This gives the following approximated expressions for the longitudinal and transverse motional frequencies:

$$\upsilon_{l,vib} = \frac{1}{\pi}\sqrt{\left\langle \hbar^{-1}U_{l,\max} \right\rangle \omega_{recoil}} ,$$ (7.11)

and

$$\upsilon_{\tau,vib} = \frac{1}{\pi}\frac{1}{r_{mf}}\sqrt{\frac{\left\langle \hbar^{-1}U_{tr,\max} \right\rangle}{m}}$$ (7.12)

Here, $\omega_{recoil} = \left(\hbar\beta_S^2\right)/2m$ is the frequency recoil. r_{mf} is the mode field radius of the guided mode. $U_{l,\max}$ and $U_{tr,\max}$ are the local maximum of the potential near the r= 0 and $z = (m+1/2)\lambda_S$. For a case of P_P = 4 W, P_{FS} = 1 W, P_{BS} = 1 W, the transverse natural frequency is approximately equal to ~ 657 MHz and the transverse one was found to be ~ 430 MHz. These values are too large for our RF spectral span. Furthermore, we believe that the experimentally observed of around 1MHz and 8 MHz are, however, motional sideband because of fine structure in z distribution in Hamiltonian that due to the Raman Hamiltonian (the first term right-hand-side of Eq. (7.5)).

This theoretical model also predicts the Mollow triplet we observe experimentally (Rabi splitting). Indeed, given the sub-Doppler signature of the scattered spectrum on one hand, and the large intensities involved on the other, the two-level energy structure of the rotational Raman transition experiences Rabi splitting. As a result, the emission will exhibit a central peak with a pair of sidebands to form a Mollow triplet. Figure 7.11 (b) shows schematically the energy level using the dressed picture. Each of the states is split into states with eigenfrequencies $\omega_{\pm} = \omega_i \pm \Omega_{Rs}$. Given our sub-wavelength field structure, we

have $\Omega_{Rs} = \langle \Omega_{12} \rangle_Z$ where $\langle \Omega_{12} \rangle_Z$ is the two-photon Rabi frequency, averaged over one Stokes wavelength.

For the case of 4W, 1W, 1W powers for the pump, FS and BS, the frequency splitting is found to be ~12 MHz, which corresponds with the experimental results. Furthermore, harmonics of these sidebands can be generated via four wave mixing [4].

In conclusion, the model does describe all the presented experimental features of the linewidth traces. In addition, we also observed a strong velocity drift of the molecules along several meters inside the fibre, which is described below. An inspection of the optical force generated by the potential using $\vec{F} = -\vec{\nabla}(U_{tot})$, and recalling the negative slope of pump power along the propagation, predicts such a phenomenon. Below, we confront the numerical results with the experiment.

We list the experimental evidence that shows that the Stokes scattering is indeed occurring dominantly in the HGR. Firstly, in addition to the high gain in the "saddle" potential point, the Stokes evolution with the input shows an increase of the emitted Stokes power with that of the pump until the onset of the 2nd Stokes around 15-20W of input power. If the emission is dominated by scattering molecules in SR, one should observe a quick Stokes decrease because of the quick gain saturation. Secondly, the strong decrease of the longitudinal motional sidebands with the pump power increase rules out that the SRS from SR. Instead, the longitudinal sideband suppression is consistent with the saturation increase with input power.

7.4.2 Numerical simulations

In the above model, the field values were free parameters. In order to develop and assess the above model, one needs to take into account the complex field distribution along the fibre due to stimulated Raman scattering in HC-PCF. Here, we use numerical methods to calculate the fields and the potential energy of the system[7]. We consider the propagation of a continuous-wave pump and Stokes radiation in the fundamental mode of the HC-PCF. The simulation neglects the excitation of higher-order Stokes band and of anti-Stokes. Furthermore, we will ignore mode coupling between the core fundamental mode and the higher-order modes. The propagation characteristics of Stokes and pump, such as the propagation constants β_p, β_s and the loss coefficients α_p, α_s, were calculated using the JCMwave finite-element Maxwell solver.

To derive the propagation equations, we first consider the steady-state values of the density matrix ρ, mentioned above. Secondly, we deduce the following polarisation expressions P_{FS}, P_{BS} and P_P:

$$P_{FS} = 2N\hbar(a_{-1}\rho_{11} + b_{-1}\rho_{22})E_{FS} + i\frac{N\hbar_S^2(\rho_{22} - \rho_{11})}{\gamma_{12} - i(\Omega_{11} - \Omega_{22})|E_P|^2 E_{FS}} \tag{7.13}$$

$$P_{BS} = 2N\hbar(a_{-1}\rho_{11} + b_{-1}\rho_{22})E_{BS} + i\frac{N\hbar_S^2(\rho_{22} - \rho_{11})}{\gamma_{12} - i(\Omega_{11} - \Omega_{22})|E_P|^2 E_{BS}} \tag{7.14}$$

$$P_P = 2N\hbar(a_0\rho_{11} + b_0\rho_{22})E_P + i\frac{N\hbar_S^2(\rho_{22} - \rho_{11})}{\gamma_{12} - i(\Omega_{11} - \Omega_{22})|E_S|^2 E_P} \tag{7.15}$$

The propagation equations then are written as:

$$\partial_Z E_{FS} = -\frac{\omega_S}{2c\varepsilon_0}P_{FS} - \alpha_S E_{FS} \tag{7.16}$$

---

[7] The numerical simulations were undertaken by Anton Husakou.

$$\partial_Z E_{BS} = -\frac{\omega_S}{2c\varepsilon_0} P_{BS} + \alpha_S E_{BS} \qquad (7.17)$$

$$\partial_Z E_P = -\frac{\omega_P}{2c\varepsilon_0} P_P - \alpha_P E_P \qquad (7.18)$$

The boundary conditions for the Stokes field are:

$$E_{FS}(0) = \sqrt{r} E_{BS}(0) \qquad (7.19)$$

$$E_{FS}(L) = \sqrt{r} E_{BS}(L) \qquad (7.20)$$

where r is the power reflection coefficient and L is the fibre length.

The above equations were solved self-consistently with the propagation equations, using the numerical shooting method to determine $E_{SF}(0)$. No reflection of the pump field was considered, since the values of the pump field at the fibre output were typically quite low. The following input parameters were assumed: $a_0 = 3.854\mathrm{x}10^{-7}$ J/m/V^2, $a_{-1} = 3.849\mathrm{x}10^{-7}$ J/m/V^2, $b_0 = 3.85831\mathrm{x}\,10^{-7}$ J/m/V^2, $b_{-1} = 3.8536\mathrm{x}10^{-7}$ J/m/V^2, $d_{-1} = 3.8538\mathrm{x}10^{-7}$ J/m/V^2, $\gamma_{12} = 2\pi(2\mathrm{x}10^9)$Hz, $\Gamma_{12} = 2\pi\,\mathrm{x}10^5$ Hz, $N = 4.86\mathrm{x}10^{26}$ 1/m^3 corresponding to the experimental pressure of 20 bar [3]. Furthermore, we take $L = 7$ m, and a fibre core radius is taken to 3.5 μm.

Figure 7.13 shows the numerically obtained results of the z-distribution of the pump, FS, BS and the Raman gain for input power of 10 W (Figure 7.13 (a)) and 25 W (Figure 7.13(b)). The z-distribution is typical for that of SRS with a concomitantly pump depletion and FS and BS rise, and with a Raman gain effective length increase with input power decrease (Figure 7.13 (c) and 7.13(d)). However, a close-up of the distribution centred at the position of the gain and over a length of $2\lambda_S$ shows a periodic gain and population difference in accordance with the analytical model mentioned above. The results also show that even with 10 W the population difference is essentially saturated. For 25 W of input power the medium is fully saturated over the whole length but periodic nanometer wide sections.
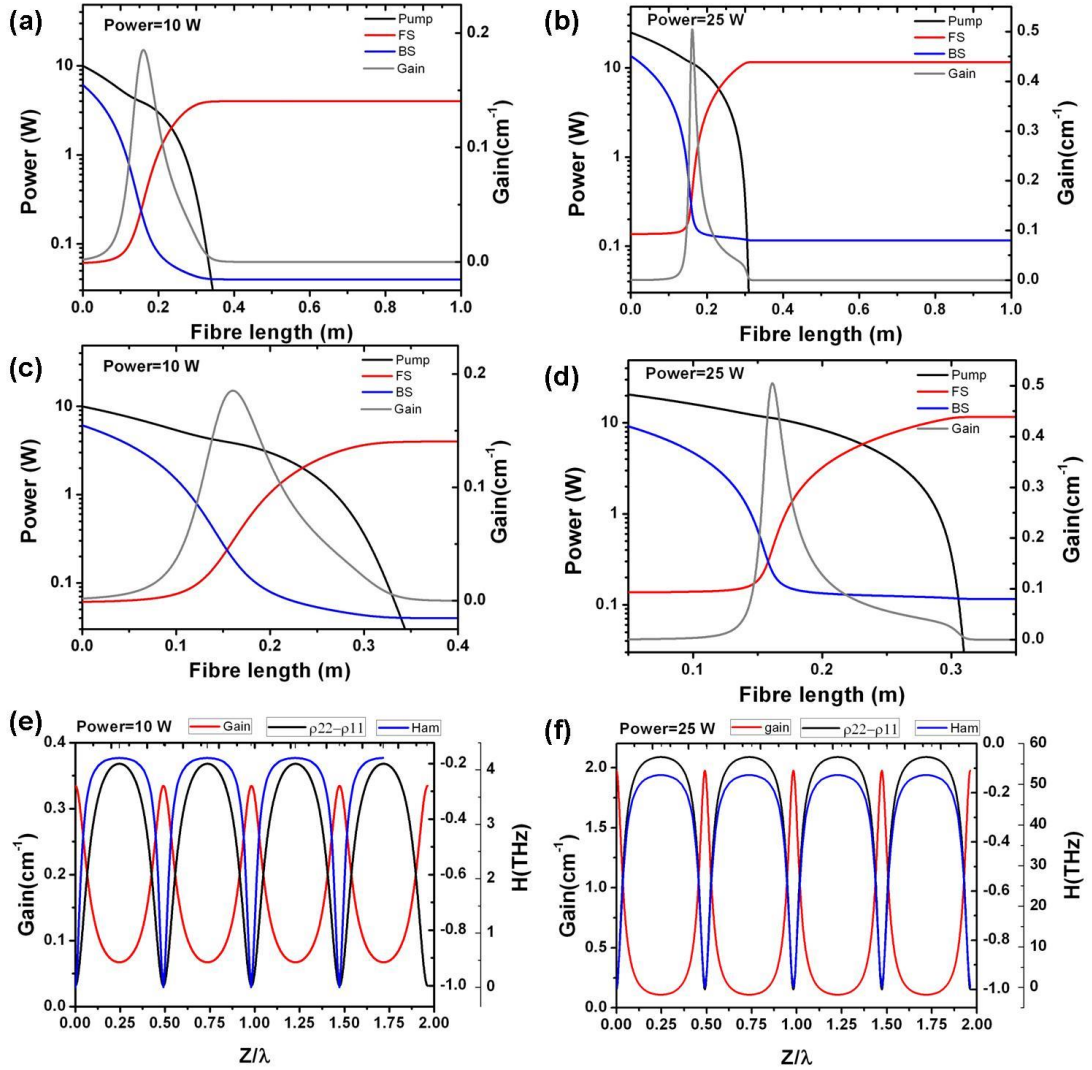
Figure 7.13: Pump, FS and BS power along the propagation direction for input power of (a) 10 W and (b) 25 W. A zoom-in of the power distribution for (c) 10 W, and (d) 25 W. (e) Raman gain coefficient, the population difference and the total average potential (H=U_{tot}) as function of z/λ_s. for (e) 10 W and (f) 25 W.

After the fields as a function of the propagation coordinates were obtained, we use the Hamiltonian (potential) to determine numerically the Rabi frequency, the motional sidebands frequencies and the linewidth.

Figure 7.14 shows the spatial profile of the potential, expressed in THz, for the case of 25 W coupled power. In accordance with the above, the Hamiltonian exhibits transverse and longitudinal minima. Figure 7.15(d) shows the calculated T_1 transit-time limited linewidth for different pressures along with

the experimental data. The results show that for power medium range (~10 W input power) the measured linewidth are close to the theoretical limit for the whole pressure range. For higher power, the higher order Raman process start to play an important role, which is not considered in the theoretical model.

Comparison of the calculated frequencies and the experimental ones reveal a typical deviation of 10% to 20%, and the slow variation of the sidebands with varying power and pressure is also qualitatively reproduced by theory. The deviation between the calculated and experimental data come from several factors. First, in the theoretical model, we disregard of higher order Raman components. Second in the experiment, we have a limited range and resolution in input power due to unstable coupling, which limited the experimental data with sufficient resolution. Third, the interaction light-gas dynamics is intrinsically complex.

Given the above, and the fact that the calculated results are obtained with a fit parameter free theoretical model, this is a very good agreement.
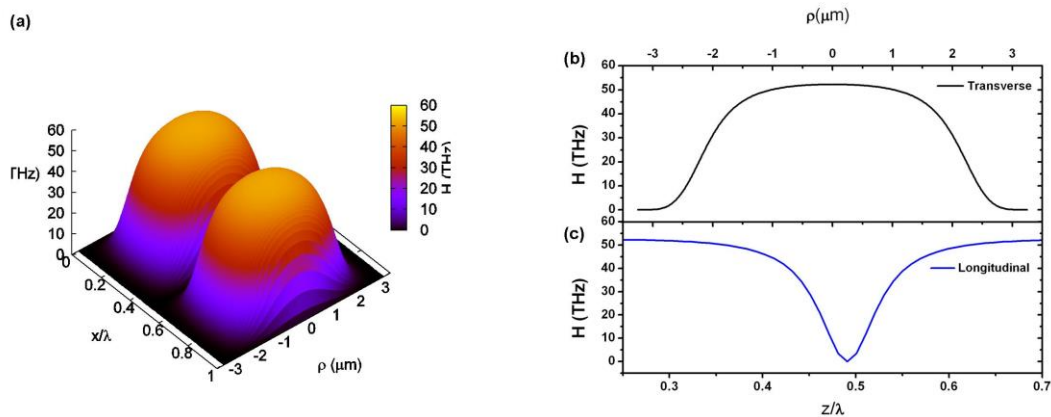

Figure 7.14: (a) The total average potential (H=U_{tot}) as function of z/λ_s and ρ for 50 W potential. (b) H longitudinal profile. (c) H transverse profile.
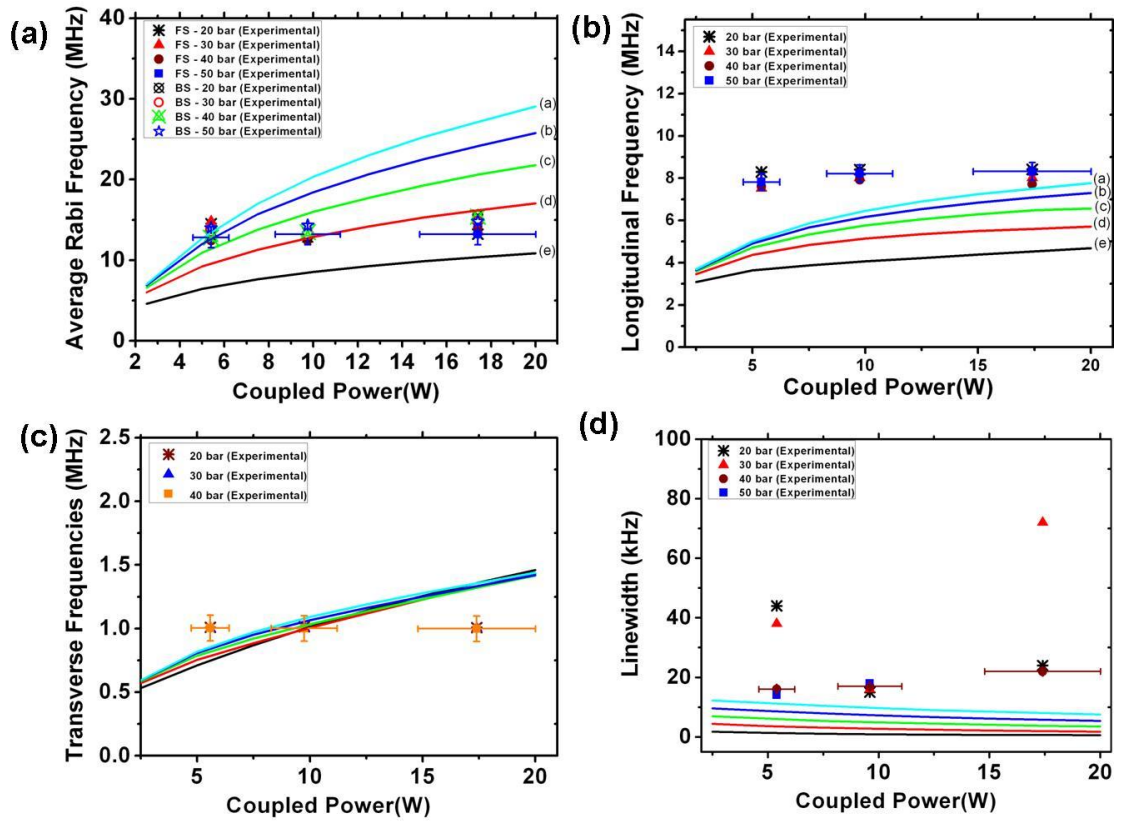
Figure 7.15: Experimental and theoretical of (a) the average Rabi frequency [inset: (a) gas pressure at 10 bar, (b)20bar, (c) 30bar, (d)40bar, (e)50bar] (b) longitudinal frequency (c) transverse frequency, and (d) Stokes linewidth versus coupled power.

7.5   AC Stark force

Another salient feature of the configuration is that the sequence of this SRS process starts with a strong Stark acceleration of the molecules. This is experimentally observed with a naked eye though the fluorescence of the molecular motions moving along the fibre, as shown in Figure 7.16. These molecular motions are recorded in real-time through a CCD camera. A 5 m length of PBG fibre is shaped as a spiral to capture as many frames as possible via the camera. A snapshot of the moving molecules at different times is illustrated in Figure 7.16 (c). The location of the motional molecules is plotted in Figure 7.16 (a) as a function of time for different input powers. The velocity of

these motional molecules as a function of input power is illustrated in Figure7.16 (b).
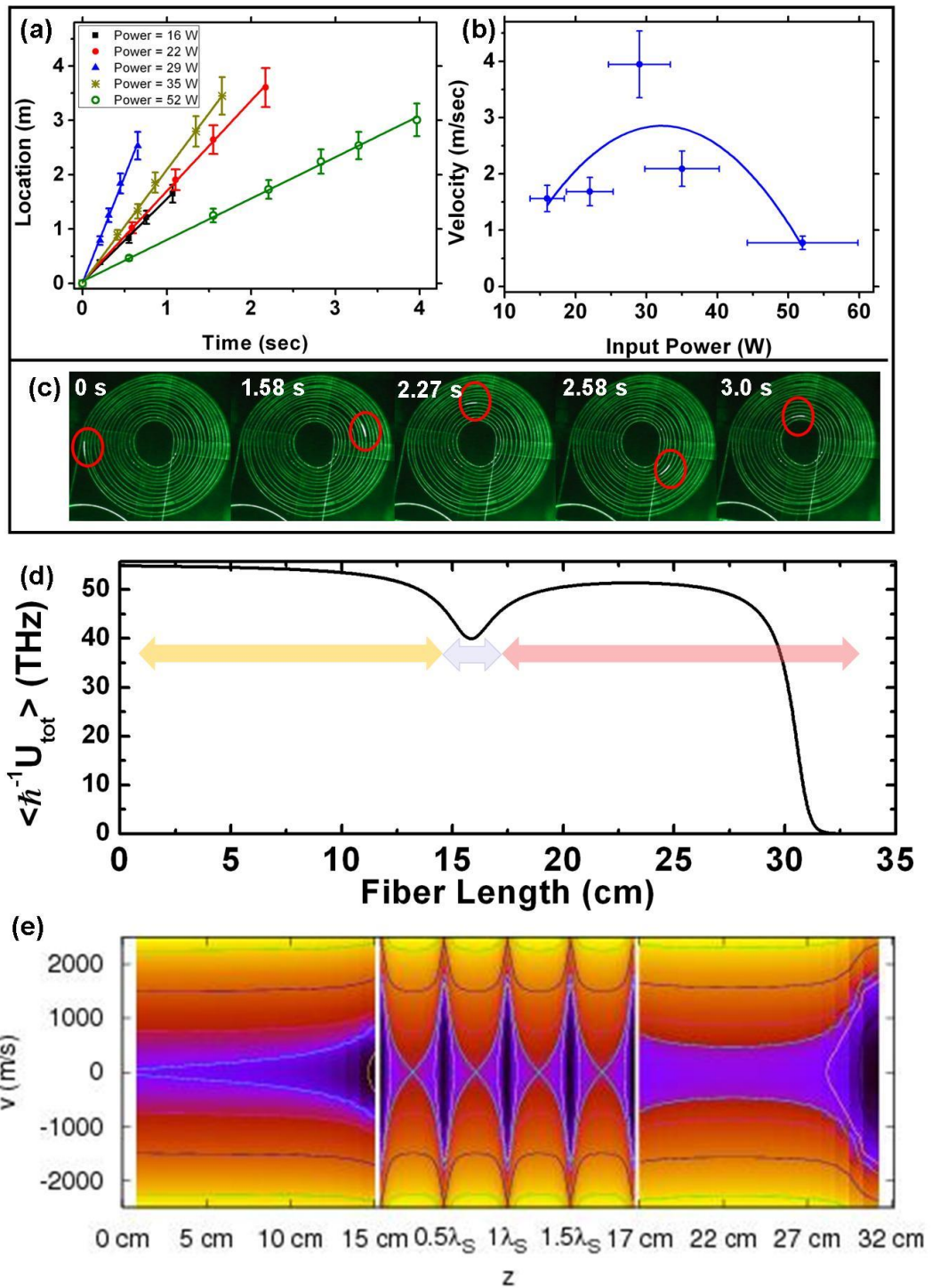

Figure 7.16: Stark acceleration along the fibre length (a) the position floruence of moving molecules as function of time at different input pump powers. (b) The velocity of moving molecules as function of input pump powers. (c) Snapshots of the moving molecules at different time. (d) The total average potential as function of fibre length (e) The velocity-phase diagram.

It can be noticed that the velocity reaches a maximum of around 4 m/sec at 29 W input power and then drops as the input power increases. We contribute this drop to the fact that at this level of power we are reaching the threshold level for the second order Stokes, as shown early in section 7.3.2. This molecular acceleration can readily be predicted by the distribution along z of the macroscopic Hamiltonian. Indeed, Figure 7.16 (d) shows, for the case of coupled power of 25 W, that the Hamiltonian exhibits a nearly constant gradient of $1.5\hbar THz$ over the first 10 cm of propagation, which is due to onset of the pump depletion. This in turn gives a constant acceleration along z to the molecules by virtue of the relation $a = -m^{-1}\partial\left(U_{tot}\right)/\partial z$. These accelerated molecules then enter the Raman generation section, which is represented by a potential well of depth of $11\hbar THz$ and spatial width of ~4 cm. Within this section, the molecules experiences the presence of an optical lattice mentioned above, and a significant fraction of them are trapped.

It is noteworthy that this optical lattice is also accelerating as it is depends on the molecular density as well. However, treating this complex dynamics is beyond the scope of the current work. Instead we keep using the above mentioned model where the molecules are considered to be initially stationary. However, one could extract qualitatively the molecules kinetic dynamics by considering the velocity-phase diagram. Figure 7.16 (e) shows this diagram for the pressure of 20 bar with pump power of 25 W. The figures captured the molecule acceleration, which corresponds to the fibre section before the Raman generation section, and the molecule trapping. If we consider only the longitudinal motion of the molecules, for any velocity, the colour map indicates the positions in the velocity-coordinate space a molecule can occupy. The velocities at the position of the maximum gain are used as a reference. One can see that there exists closed trajectories in the velocity-coordinate space near the minima of the Hamiltonian ($z/\lambda = 0.5 + N$, N is an integer), which correspond to the trapping of molecules with velocities below roughly 1000 m/s in the

vicinity of the minimum. The trapping is a result of the space-dependent Stark shift terms. The motion of such molecules both in the longitudinal direction as well as in the normal direction can result in the generation of the motional sidebands, as explained before.

Molecules with the velocities in the range from 0 to roughly 1500 m/s at the positions of the maximum gain ($z/\lambda = N$) experience a significant influence of the Stark shift, while faster molecules (>1500 m/s) are not influenced, however, such molecules do not significantly contribute to the emission due to the fact that they do not spend a long enough time in the region of high gain and are strongly saturated. Therefore, it is the dynamics of the initially slower molecules with velocities below several 1000 m/s, which determines the experimentally observed spectra. A more rigorous account will take into account of the trapped molecule ballistic dynamics which is not considered here.

Furthermore, Figures 7.16 (d) and 7.16 (e) also explains the observed moving scattering entities recorded in the video of Figure 7.17. These scatters are due the sudden acceleration and deceleration experienced by the molecules in the Raman active region (z= 15 cm and z= 17cm in Figure 7.16(d)-(e)), and at the full pump depletion (z= 27 cm and z= 30cm in Figure 7.16(d)-(e))). Such accelerations create local pressure gradients, which in turn, results in local molecular density increase. These high density molecules exhibit stronger scattering emission which can be observed by the naked eye.
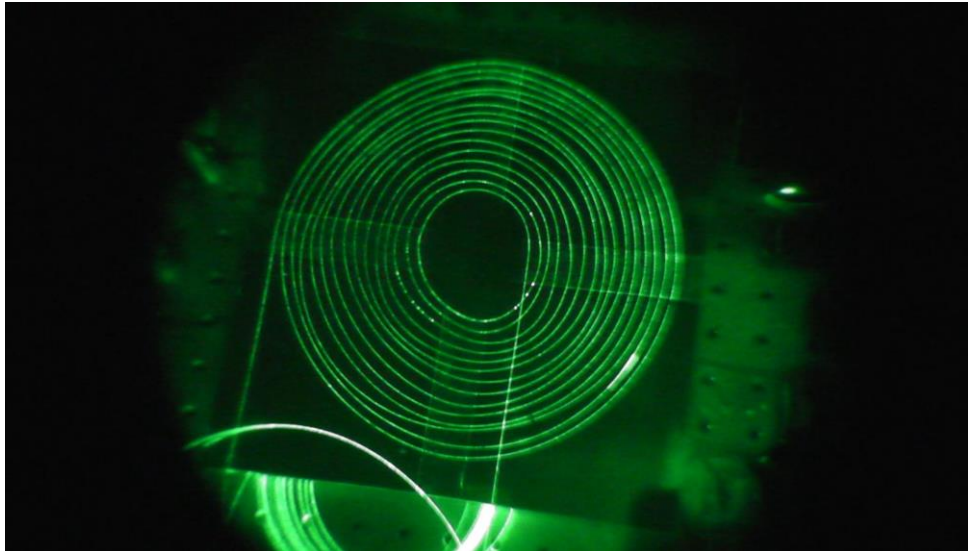
Figure 7.17: (video available upon request[8]) a snapshot of a recorded video for moving molecules at input power of ~ 29W.

7.5   Summary

A novel mechanism of SRS is reported, where the model is based on optically induced nanostructured Raman gain, whereby the population difference is saturated but in 1D periodic sub-wavelength sections over a long interaction length. The results show a multi-watt forward and backward Stokes emission with structured spectrum and linewidth as narrow as ~ 10 KHz (6 orders of magnitude shorter than the Raman linewidth). Observations of rich dynamics that include Rabi splitting, molecular motional sideband and inter-sideband four wave mixing, and finally AC stark induced molecule acceleration is reported.

---

[8] This video could be provided upon your request. Please email: ma302@bath.ac.uk or f.benabid@xlim.fr.

References

[1]   F. Benabid, J. C. Knight, G. Antonopoulos, and P. S. J. Russell, "Stimulated Raman scattering in hydrogen-filled hollow-core photonic crystal fiber.," *Science*, vol. 298, no. 5592, pp. 399–402, Oct. 2002.

[2]   G. C. Herring, M. J. Dyer, and W. K. Bischel, "Temperature and density dependence of the linewidths and line shifts of the rotational Raman lines in N_2 and H_2," *Phys. Rev. A*, vol. 34, no. 3, pp. 1944–1951, Sep. 1986.

[3]   W. K. Bischel and M. J. Dyer, "Temperature dependence of the Raman linewidth and line shift for the Q(1) and Q(0) transitions in normal and para-H_2," *Phys. Rev. A*, vol. 33, no. 5, pp. 3113–3123, May 1986.

[4]   D. J. Harter, P. Narum, M. G. Raymer, and R. W. Boyd, "Four-Wave Parametric Amplification of Rabi Sidebands in Sodium," *Phys. Rev. Lett.*, vol. 46, no. 18, pp. 1192–1195, May 1981.

[5]   F. Kien, J. Liang, M. Katsuragawa, K. Ohtsuki, K. Hakuta, and a. Sokolov, "Subfemtosecond pulse generation with molecular coherence control in stimulated Raman scattering," *Phys. Rev. A*, vol. 60, no. 2, pp. 1562–1571, Aug. 1999.

[6]   F. Kien, K. Hakuta, and a. Sokolov, "Pulse compression by parametric beating with a prepared Raman coherence," *Phys. Rev. A*, vol. 66, no. 2, p. 023813, Aug. 2002.

[7]   S. F. Sokolov, a. V. Harris, "Ultrashort pulse generation by molecular," *J. Opt. B Quantum Semiclassical Opt.*, vol. 5, 2003.

[8]   R. H. Dicke, "The Effect of Collisions upon the Doppler Width of Spectral Lines," *Phys. Rev.*, vol. 89, no. 2, pp. 472–473, 1953.

[9]   M.-M. Audibert, C. Joffrin, and J. Ducuing, "Vibrational relaxation in hydrogen-rare-gases mixtures," *Chem. Phys. Lett.*, vol. 19, no. 1, pp. 26–28, 1973.

Chapter 8

Summary and Future Work

8.1 Summary

In this thesis we presented several milestones towards the development of an all-fibre photonic waveform synthesiser. The synthesiser design relies on the generation of multiple-octave wide coherent Raman comb in hydrogen confined in hollow-core photonic crystal fibres (HC-PCF), with the ultimate aim to generate the comb of continuous wave (CW) spectral components, thus paving the way to optical waves like electronics.

In chapter 2 and 3, we reported on the design and fabrication of state-of-the-art PBG HC-PCF type and Kagome HC-PCF type. Those types of fibres are an important element towards the development of an optical waveform synthesiser based on the generation and the synthesis of optical frequency combs using stimulated Raman scattering (SRS) process in gas filled HC-PCF. The guidance mechanism of the Kagome type of fibre, known as Inhibited Coupling (IC), is examined in chapter 3 through experimental and theoretical study of the effect of the hypocycloid core shape on confinement loss, and which led to a reduction in optical loss figures from a typical value of ~100

dB/km down to ~17 dB/km. In addition, a systematic theoretical and experimental study on the effect of the number of cladding rings upon the confinement and bending loss in Kagome HC-PCF is performed to gain a profound understanding of the IC guidance mechanism.

In chapter 4, we reported on theoretical and experimental investigation of the spatial and temporal dynamics of molecular Raman coherence. The results show that with a modest laser pump, molecular coherence persists for a duration 129 times longer than that of the molecular dephasing time. Furthermore, the decay time of the coherence induced Stokes found to be 7.2 ns, which is 42 times more than that of the expected decay time. In chapter 5, we demonstrated the generation of a periodic train of pulse waveform with 17.6 THz repetition rate and ~ 26fs pulse duration. This is achieved through Raman comb generation under transient SRS conditions and by using all-fibre based system consisting of hydrogen-filled HC-PCF.

The developments and breakthroughs made to Kagome HC-PCF design will provide a real boost to a successful ultra-broad Raman comb in the CW regime, and subsequently to the long-term objective of developing and arbitrary optical waveforms synthesiser. In chapter 6, we reported on the first milestone achievement by generating first-order rotational Stokes with over 50W power in the CW regime using SRS in HC-PCF has already been achieved recently. In chapter 7, we reported on novel mechanism of SRS. The model is based on optically induced nanostructured Raman gain, whereby the population difference is saturated but in 1D periodic sub-wavelength sections over a long interaction length. The results show a multi-watt forward and backward Stokes emission with structured spectrum and linewidth as short as ~ 10 kHz (6 orders of magnitude shorter than the Raman linewidth). In addition, the recorded linewidth trace shows a rich dynamics that include Rabi splitting, molecular motional sideband and inter-sideband four wave mixing, and finally observation of AC-stark-induced molecule acceleration.

8.2 Future work

New prospect in designing better fibre performance have been now opened up by the new negative curvature design for HC-PCF. Further reduction on loss figure and optical bandwidth broadening would make a huge improvement.

We also mapped the spatio-temporal the coherence. Intriguing results found on the decay indicating that both theoretical and experimental work on this is very promising.

Furthermore, we demonstrated the waveform synthesis for the first time in the transient regime. Immediate improvement could be considered through the use of spatial light modulator (SLM) for better phase and amplitude control to synthesis intra-pulses.

Stable pulse-to-pulse synthesis should be explored. Giving the fact that the decay of the visibility that we observed is sufficiently long to consider a new type of mode-locked laser.

Generating first order rotational Stokes with sufficient power and sufficient linewidth has been demonstrated. Completely and radically new rich dynamics in the interaction between light and hydrogen molecules enabled the generation of high power Stokes with ultra-narrow linewidth. Due to the novelty of both the experimental results and theoretical model, a further investigation is recommendable on the velocity distribution of thermal molecule inside optical lattice.

Finally, two major milestones have been now reached for developing a comb and subsequently waveform synthesis based on CW excitation.